Departament d'Enginyeria Mecànica

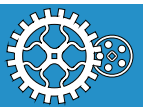

UNIVERSITAT POLITÈCNICA DE CATALUNYA

# A model for railway induced ground vibrations in the frame of preliminary assessment studies

by

Robert Arcos Villamarín

directed by

Jordi Romeu Garbí

A thesis submitted in partial fulfilment for the
degree of Doctor of Philosophy of Mechanical Engineering

in the

Escola Tècnica Superior d'Enginyeries Industrial i Aeronàutica de Terrassa
Mechanical Engineering Department

May 23, 2011

# Declaration of Authorship

I, Robert Arcos Villamarín , declare that this thesis titled, 'A model for railway induced ground vibrations in the frame of preliminary assessment studies' and the work presented in it are my own. I confirm that:

- This work was done wholly or mainly while in candidature for a research degree at this University.
- Where any part of this thesis has previously been submitted for a degree or any other qualification at this University or any other institution, this has been clearly stated.
- Where I have consulted the published work of others, this is always clearly attributed.
- Where I have quoted from the work of others, the source is always given. With the exception of such quotations, this thesis is entirely my own work.
- I have acknowledged all main sources of help.
- Where the thesis is based on work done by myself jointly with others, I have made clear exactly what was done by others and what I have contributed myself.

Signed: _____

Date: _____

*"After having spent years trying to be accurate, we must spend as many more in discovering when and how to be inaccurate"*

Ambrose Bierce

Departament d'Enginyeria Mecànica

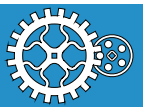

UNIVERSITAT POLITÈCNICA DE CATALUNYA

# *Abstract*

Escola Tècnica Superior d'Enginyeries Industrial i Aeronàutica de Terrassa
Mechanical Engineering Department

Doctor of Philosophy in Mechanical Engineering

by Robert Arcos Villamarín

This thesis focuses on the development of an analytical model for the generation and propagation parts of a global model of ground induced vibrations to be used in preliminary assessment studies for the case of at-grade railway infrastructures. The model is designed prioritising its speed, simplicity and usability ahead its accuracy modelling the real railway system. This model takes into account the subgrade as a viscoelastic and homogeneous half-space, the superstructure as a 2-layer supporting model and the vehicle as 1DOF system. With the aim of simplify the model, the superstructure/subgrade interaction is studied in terms of the wheel/rail contact dynamics, bounding in what cases this interaction can be neglected. The adaptation of this model when a far field semi-analytical model is desired to be used as the propagation model is fully developed, by means of the dimensioning of the near field and far field regions.

# *Acknowledgements*

Són moltes les persones que durant aquest llarg camí que ha estat per mi el doctorat han posat de la seva part per que aquesta tesi pogués veure la llum. Sigui d'una forma directa o indirecta (ambdues totalment inestimables) aquestes persones són també partícips d'aquesta petita (qualificatiu sens dubte massa extens) aportació a la ciència.

Primer de tot m'agradaria agrair l'infinit esforç realitzat per el meu director de tesi, el doctor Jordi Romeu Garbí, el qual ha estat sempre disposat a ajudar, a discutir, proposar i/o revisar cada idea, cada text, cada equació... sempre amb l'afany d'aconseguir un resultat final òptim. M'agradaria destacar que ha estat fantàstic poder treballar amb algú tan tolerant amb les idees dels altres.

I que puc dir de la resta de companys del grup de recerca, el Laboratori d'Enginyeria Acústica i Mecànica (LEAM): sense el seu coneixement, ganes i dedicació aquesta tesi no hagués estat possible. I, sobretot, sense el bon ambient existent, sempre fomentat, encara menys. I no em refereixo només als companys professors i investigadors, també em refereixo a tota la tropa de becaris i projectistes que han passat per el LEAM que ens han ajudat tan amb la seva feina com amb la seva amistat. També voldria fer especial èmfasi en tots els meus companys o excompanys de despatx, als quals planyo per tenir-me que aguantar tan sovint.

També m'agradaria agrair a d'altres persones fora de l'àmbit del meu grup de recerca per la seva més que significativa aportació a aquest treball: als doctors Salvador Cardona i Jordi Martínez, companys del  per les seves inestimables classes de vibracions mecàniques, les quals van servir per introduir-me en aquest camp tan interessant de l'enginyeria mecànica, i a tots els companys de AV Enginyers, Vibcon, i de la secció d'acústica i vibracions de Sener per donar-me la possibilitat de treballar amb ells i poder aprendre tant.

Finalment, i sobretot, m'agradaria donar les gràcies a tota la meva família, especialment als meus pares, i a tots els meus amics i companys per el fet d'haver estat sempre allà.

Moltes gràcies a tots i totes per fer-ho possible.

# Contents

# List of Figures

# List of Tables

# Symbols

| | | |
|---|---|---|
| $\alpha$ | P-wave velocity | [m/s] |
| $\alpha_B$ | Ballast stress distribution angle | [°] |
| $\beta$ | S-wave velocity | [m/s] |
| $\delta(.)$ | Delta Dirac function | |
| $\epsilon(t)$ | Joint wheel and rail irregularities in time domain | [m] |
| $\epsilon(\omega)$ | Joint wheel and rail irregularities in frequency domain | |
| $\epsilon_r(t)$ | Roughness of the rail in time-domain | [m] |
| $\epsilon_w(t)$ | Roughness of the wheel in time-domain | [m] |
| $\varepsilon$ | Radius of the $C_\varepsilon$ integration contour | |
| $\varepsilon_0$ | Radius of the $C_{\varepsilon_0}$ integration contour | |
| $\varepsilon_{\mathrm{i}k_x}$ | Radius of the $C_{\varepsilon_{\mathrm{i}k_x}}$ integration contour | |
| $\zeta$ | $x$ position of the vertical point load applied on the track | [m] |
| $\eta_B$ | Ballast structural damping coefficient | [-] |
| $\eta_F$ | Fasteners structural damping coefficient | [-] |
| $\kappa$ | Wavenumber associated to the Rayleigh waves | [rad/m] |
| $\kappa'$ | Holzlöhner adimensional wavenumber associated to the Rayleigh waves | [rad/m] |
| $\lambda$ | Complex Lamé's second constant | [N/m$^2$] |
| $\lambda_{\mathrm{Rayleigh}}$ | Wavelength associated to the Rayleigh waves | [m] |
| $\mu$ | Complex Lamé's first constant | [N/m$^2$] |
| $\nu$ | Poisson ratio | [-] |
| $\rho$ | Density | [kg/m$^3$] |
| $\tau$ | Stresses | [N/m$^2$] |

| | | |
|---|---|---|
| $\upsilon$ | Wavenumber dependent constant related to the P-waves | [rad/m] |
| $\upsilon'$ | Wavenumber dependent constant related to the S-waves | [rad/m] |
| $\upsilon_{xy}$ | 2D wavenumber dependent constant related to the P-waves | [rad/m] |
| $\upsilon'_{xy}$ | 2D wavenumber dependent constant related to the S-waves | [rad/m] |
| $\omega$ | Angular frequency | [rad/s] |
| $\tilde{\omega}$ | Angular frequency of a moving source on its point of view | [rad/s] |
| $\omega'_n$ | Natural frequency of the nth-mode of the track for the case of no superstructure/subgrade coupling | [rad/s] |
| $\Phi(.)$ | Holzlöhner power series | |
| | | |
| $c$ | Half the width of the superstructure/subgrade interaction area | [m] |
| $c_B$ | Ballast viscous damping | [Ns/m] |
| $c'_B$ | Ballast viscous damping of the equivalent model | [Ns/m] |
| $c_F$ | Fasteners viscous damping | [Ns/m] |
| $c'_F$ | Fasteners viscous damping of the equivalent model | [Ns/m] |
| $c_{PS}$ | Primary suspension viscous damping | [Ns/m] |
| $d_B$ | Depth of the ballast | [m] |
| $f$ | Frequency | [Hz] |
| $f_g(x,t)$ | Superstructure/subgrade coupling force in the spatial-time domain | [N] |
| $\bar{f}_n$ | Resonant frequency of the nth-mode of the track for the case of superstructure/subgrade coupling | [Hz] |
| $\bar{f}'_n$ | Resonant frequency of the nth-mode of the track for the case of no superstructure/subgrade coupling | [Hz] |
| $f_{w/r}$ | Wheel/rail contact force in the time domain | [N] |
| $h$ | Ratio between P-wave and S-wave velocities | [-] |
| $h_0$ | Static joint deformation of the wheel and the rail | [-] |

| | | |
|---|---|---|
| $h(t)$ | Joint deformation of the wheel and the rail | [m] |
| $h_B$ | Ballast structural damping | [Ns/m] |
| $h'_B$ | Ballast structural damping of the equivalent model | [Ns/m] |
| $h_F$ | Fasteners structural damping | [Ns/m] |
| $h'_F$ | Fasteners structural damping of the equivalent model | [Ns/m] |
| i | Imaginary unit | [-] |
| $k$ | Wavenumber | [rad/m] |
| $k'$ | Holzlöhner adimensional wavenumber | [rad/m] |
| $k_0$ | Wavenumber associated to the bending waves in a Bernoulli-Euler beam | [rad/m] |
| $k_\alpha$ | Wavenumber associated to the P-waves | [rad/m] |
| $k_\beta$ | Wavenumber associated to the P-waves | [rad/m] |
| $k_B$ | Ballast complex stiffness | [N/m] |
| $k'_B$ | Ballast stiffness of the equivalent model | [N/m] |
| $\bar{k}_B$ | Ballast stiffness (not complex) | [N/m] |
| $k_F$ | Fasteners complex stiffness | [N/m] |
| $k'_F$ | Fasteners stiffness of the equivalent model | [N/m] |
| $\bar{k}_F$ | Fasteners stiffness (not complex) | [N/m] |
| $k_{\text{Hertz}}$ | Non-lineal elasticity constant of the Hertz elliptical contact | [N/m$^{3/2}$] |
| $k_{\text{Hertz}}^{\text{lin}}$ | Linearised elasticity constant of the Hertz elliptical contact | [N/m] |
| $k_{PS}$ | Primary suspension stiffness | [N/m] |
| $k_x$ | Wavenumber in the $x$ direction | [m] |
| $k_y$ | Wavenumber in the $y$ direction | [m] |
| $k_{\text{lim}}$ | Truncated limit of integration | [rad/m] |
| $l_c$ | Distance between the centres of the rail heads | [m] |
| $l_e$ | Effective supporting length of half sleeper on the ballast | [m] |
| $l_e s$ | Effective supporting length of half sleeper on the subgrade | [m] |
| $m'_r$ | Equivalent rail mass | [kg] |
| $m_s$ | Sleepers distributed mass | [kg] |

| | | |
|---|---|---|
| $m'_s$ | Equivalent sleepers mass | [kg] |
| $m_{\text{sprung}}$ | Sprung mass associated to a single wheel | [kg] |
| $m_w$ | Unsprung mass associated to a single wheel | [kg] |
| $r$, $\theta$, $z$ | Cylindrical coordinates | [m] |
| $\bar{r}$ | Holzlöhner adimensional radial distance | [-] |
| $r_g$, $\theta_g$, $z_g$ | Ground vibration displacements at a $\{r, \theta, z\}$ position in the spatial-time domain | [m] |
| $r_{g0}$, $\theta_{g0}$, $z_{g0}$ | Ground surface vibration displacements at a $\{r, \theta, z\}$ position in the spatial-time domain | [m] |
| $r_{\text{norm}}$ | Adimensional radial distance with respect to a point source | [-] |
| $v_{\text{train}}$ | Train velocity | [m/s] |
| $v_P^{\min}$ | Smallest phase velocity of the complete problem | [m/s] |
| $x$, $y$, $z$ | Cartesian coordinates | [m] |
| $x_g$, $y_g$, $z_g$ | Ground vibration displacements at a $\{x, y, z\}$ position in the spatial-time domain | [m] |
| $x_{g0}$, $y_{g0}$, $z_{g0}$ | Ground surface vibration displacements at a $\{x, y, z\}$ position in the spatial-time domain | [m] |
| $x_{\text{norm}}$ | Adimensional horizontal distance with respect to a line source | [-] |
| $z_r$ | Rail vertical vibration displacement in the spatial-time domain | [m] |
| $z_s$ | Sleepers vertical vibration displacement in the spatial-time domain | [m] |
| $z_w$ | Wheel vertical vibration displacement in the spatial-time domain | [m] |
| $z'_r$ | Rail vertical vibration displacement for the case of no superstructure/subgrade coupling in the spatial-time domain | [m] |
| $z'_s$ | Sleepers vertical vibration displacement for the case of no superstructure/subgrade coupling in the spatial-time domain | [m] |

| | | |
|---|---|---|
| $z'_w$ | Wheel vertical vibration displacement for the case of no superstructure/subgrade coupling in the spatial-time domain | [m] |
| $z_{g0}^{(0)}$ | Subgrade surface vertical vibration displacement at a $\{x, 0, 0\}$ position in the spatial-time domain | [m] |
| $C$ | Lamb's propagation model constant | [-] |
| $C_1$ | Lamb's propagation model constant | [-] |
| $C_\varepsilon$ | Integration contour around a $\varepsilon$ radius semicircle | |
| $C_{\varepsilon_0}$ | Integration contour around a $\varepsilon_0$ radius semicircle | |
| $C_{\varepsilon_{\mathrm{i}k_x}}$ | Integration contour around a $\varepsilon_{\mathrm{i}k_x}$ radius semicircle | |
| $C_R$ | Integration contour around a $R$ radius semicircle | |
| $D$ | Lamb's propagation model constant | [-] |
| $D_1$ | Lamb's propagation model constant | [-] |
| $D_P$ | P-wave damping coefficient | [-] |
| $D_S$ | S-wave damping coefficient | [-] |
| $E$ | Complex Young modulus | [N/m$^2$] |
| $\bar{E}$ | Young modulus (not complex) | [N/m$^2$] |
| $F(k)$ | Rayleigh function | [rad$^4$/m$^4$] |
| $F_g(x,t)$ | Superstructure/subgrade coupling force in the spatial-frequency domain | |
| $\bar{F}_g(x,t)$ | Superstructure/subgrade coupling force in the wavenumber-frequency domain | |
| $F_R(k_x, k_y)$ | 2D Rayleigh function | [rad$^4$/m$^4$] |
| $F_{w/r}$ | Wheel/rail contact force in the frequency domain | |
| $G(\omega)$ | Frequency dependent constant of the superstructure | [N/m] |
| $G'(\omega)$ | Frequency dependent constant of the superstructure | [N/m] |
| $H$ | Lamb's propagation model constant | [-] |
| $H(.)$ | Heaviside step function | |
| $H_n^{(2)}(.)$ | nth-order Hankel function of the second kind | |
| $I$ | Rail second moment of inertia | [m$^4$] |
| $I_q(k,\omega)$ | Integral of the Lamb's point source solution for the radial displacement | [m/rad] |

| | | |
|---|---|---|
| $\tilde{I}_q(k,\omega)$ | Integrand of the Lamb's point source solution for the radial displacement | [-] |
| $I_u(k,\omega)$ | Integral of the Lamb's line source solution for the horizontal displacement | [m/rad] |
| $\tilde{I}_u(k,\omega)$ | Integrand of the Lamb's line source solution for the horizontal displacement | [-] |
| $I_w(k,\omega)$ | Integral of the Lamb's line or point source solution for the vertical displacement | [m/rad] |
| $\tilde{I}_w(k,\omega)$ | Integrand of the Lamb's line or point source solution for the vertical displacement | [-] |
| $I_{k_y}(k_x,\omega)$ | Superstructure/subgrade coupling integral | [m$^2$/N] |
| $\tilde{I}_{k_y}(k_x,k_y,\omega)$ | Superstructure/subgrade coupling integrand | [m$^3$/N] |
| $\tilde{I}'_{k_y}(k_x,k_y,\omega)$ | Superstructure/subgrade coupling integrand after Apsel's technique application | [m$^3$/N] |
| Im(.) | Imaginary part of a complex expression or number | |
| $J_n(.)$ | nth-order Bessel function | |
| $K$ | Lamb's propagation model constant | [-] |
| $L$ | Concentrated load of a point source | [N] |
| $M_X^{\text{Line}}$ | Near field distance factor related to the horizontal displacement induced by a line load | [dB] |
| $M_Z^{\text{Line}}$ | Near field distance factor related to the vertical displacement induced by a line load | [dB] |
| $M_R^{\text{Point}}$ | Near field distance factor related to the radial displacement induced by a point load | [dB] |
| $M_Z^{\text{Point}}$ | Near field distance factor related to the vertical displacement induced by a point load | [dB] |
| $M_{\text{nfd}}$ | Assumed error in the determination of the near field distance | [dB] |
| $\mathcal{P}$ | Cauchy principal vale | |
| Phase(.) | Phase of a complex expression or number | |
| $Q$ | Distributed load of a line source | [N/m] |
| $Q(\omega)$ | Frequency dependent constant of the superstructure | [N/m] |
| $Q'(\omega)$ | Frequency dependent constant of the superstructure | [N/m] |

| | | |
|---|---|---|
| $R$ | Radius of $C_R$ integration contour or a constant of the superstructure in the non-coupled case | [m] or [$kg^4/s^4$] |
| $R_g$, $\Theta_g$, $Z_g$ | Ground vibration displacements at a $\{r, \theta, z\}$ position in the spatial-frequency domain | |
| $R_{g0}$, $\Theta_{g0}$, $Z_{g0}$ | Ground surface vibration displacements at a $\{r, \theta, z\}$ position in the spatial-frequency domain | |
| $\bar{R}_g$, $\bar{\Theta}_g$, $\bar{Z}_g$ | Ground vibration displacements at a $\{r, \theta, z\}$ position in the wavenumber-frequency domain | |
| $\bar{R}_{g0}$, $\bar{\Theta}_{g0}$, $\bar{Z}_{g0}$ | Ground surface vibration displacements at a $\{r, \theta, z\}$ position in the wavenumber-frequency domain | |
| Re(.) | Real part of a complex expression or number | |
| Res(.) | Residue of a pole | |
| $S$ | Rail cross-sectional area | [$m^2$] |
| $T(\omega)$ | Frequency dependent constant of the superstructure | [N/m] |
| $X_g$, $Y_g$, $Z_g$ | Ground vibration displacements at a $\{x, y, z\}$ position in the spatial-frequency domain | |
| $X_{g0}$, $Y_{g0}$, $Z_{g0}$ | Ground surface vibration displacements at a $\{x, y, z\}$ position in the spatial-frequency domain | |
| $\bar{X}_g$, $\bar{Y}_g$, $\bar{Z}_g$ | Ground vibration displacements at a $\{x, y, z\}$ position in the wavenumber-frequency domain | |
| $\bar{X}_{g0}$, $\bar{Y}_{g0}$, $\bar{Z}_{g0}$ | Ground surface vibration displacements at a $\{x, y, z\}$ position in the wavenumber-frequency domain | |
| $Z_r$ | Rail vertical vibration displacement in the spatial-frequency domain | |
| $Z_s$ | Sleepers vertical vibration displacement in the spatial-frequency domain | |
| $Z_w$ | Wheel vertical vibration displacement in the spatial-frequency domain | |
| $Z'_r$ | Rail vertical vibration displacement for the case of no superstructure/subgrade coupling in the spatial-frequency domain | |

| | |
|---|---|
| $Z'_s$ | Sleepers vertical vibration displacement for the case of no superstructure/subgrade coupling in the spatial-frequency domain |
| $Z'_w$ | Wheel vertical vibration displacement for the case of no superstructure/subgrade coupling in the spatial-frequency domain |
| $\bar{Z}_r$ | Rail vertical vibration displacement in the wavenumber-frequency domain |
| $\bar{Z}_s$ | Sleepers vertical vibration displacement in the wavenumber-frequency domain |
| $\bar{Z}_w$ | Wheel vertical vibration displacement in the wavenumber-frequency domain |
| $Z_{g0}^{(0)}$ | Subgrade surface vertical vibration displacement at a $\{x, 0, 0\}$ position in the spatial-frequency domain |
| $\bar{Z}_{g0}^{(0)}$ | Subgrade surface vertical vibration displacement at a $\{x, 0, 0\}$ position in the wavenumber-frequency domain |

*Dedicada a la meva mare i al meu pare*

# Chapter 1

# Introduction

## 1.1 Justification

In recent years there has been growing interest by the authorities to control the vibrations induced by train infrastructures due to an increase in preoccupation by the general population about the effects on their comfort and quality of life. The appearance of high speed lines and/or the increase in urban and intercity networks of railways has caused an increment in the perception of this phenomenon, to which the administrators of infrastructures have to face in at least two different situations: in the design of new infrastructures and when an action plan to reduce population exposure to vibrations must be drawn up.

When designing new infrastructures, three types of ground-borne vibration prediction model should be considered, according to the stage of system's development [4]:

- Scoping model: to be used at the very earliest stages of development of a rail system to identify whether ground-borne vibration is an issue.
- Environmental assessment model: to be used to quantify more accurately the location and severity of ground-borne vibration effects for a rail system and the generic form and extent of mitigation required to reduce the effects.
- Detailed design model: to be used to support the detailed design and specification of the generic mitigation identified as being required by the environmental assessment model.

When making action plans for reducing population exposure to vibrations, it is necessary to define which areas of territory are affected and also to quantify the affected population [5]. This could allow to define priority criteria for the application of vibration mitigation measures, for example, as is established for environmental noise caused by railways [6].

Both in making action plans for reducing population exposure to vibrations as well as in the first stages in the development of new infrastructures, large scale undertakings must be faced and a wide variety of situations can be found. In these situations, the calculation model applied should be the simplest and most adaptable possible, in order to avoid unnecessary effort at these stages. This simple model should be divided, as shown in Fig. 1.1, into three main parts [4]:

- **Generation**. This should comprise of the quasi static and dynamic excitations induced by the train passage. Static and dynamic properties of the rolling stock, superstructure and subgrade should be used to compute an output value that characterises the source.

- **Propagation**. This should use the output value of the generation model as an input and calculate, from this reference, the vibration amplitude at any point on the ground.
- **Reception**. Finally, this part of the global model should compute the vibration inside a building from the vibration amplitudes calculated by the propagation model.

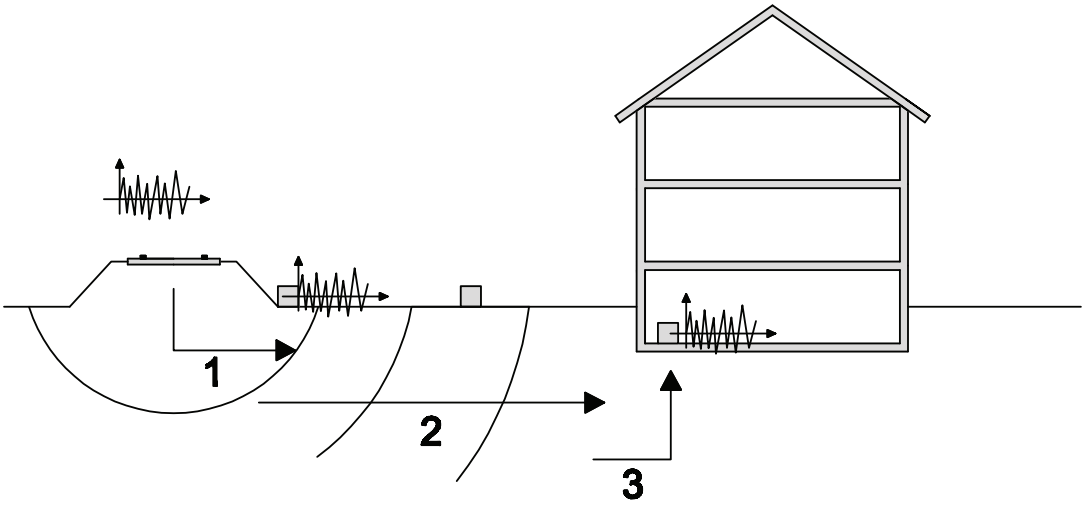


FIGURE 1.1: Parts of a global model of vibration assessment: Generation (**1**), Propagation (**2**) and Reception (**3**).

Therefore, any global model of vibration assessment should yield the ground-borne vibration at the required location and should be a function of the source, the propagation path and the receiver [7–13].

Within this global model, the algorithms involved in the propagation model are the most computationally intensive. There are many models of propagation for train infrastructures, which can be classified into three main types [4, 14]: analytical models, numerical models and empirical models (Section 2.2).

- **Analytical models** are quite adaptable and require a computational effort that depends on its complexity.
- **Numerical models** usually require huge computational capacities and their adaptation to other cases is less efficient since it usually requires rebuilding the model of elements. However, they allow for the calculation of unusual or complex cases, usually unattainable by using any other model type.

- Finally, **empirical models** are extremely fast but, when based entirely on experimental measures, are not usually very adaptable. However, they can contemplate analytical concepts, becoming **semi-analytical models** and allowing for higher adaptability [15].

Therefore, semi-analytical or fast analytical propagation models are the best choices to ensure high computational efficiency and high adaptability at the preliminary stages of the project, in scoping global models for example [4]. More precise analytical models or numerical models are more appropriate in more advanced stages of the project development.

This thesis focuses on the development of a model for the generation and propagation parts of a global model (see Fig. 1.1) to be used in preliminary assessment studies for the case of at-grade infrastructures. Other kinds of infrastructures, like underground railways or viaducts, are outside the scope of this investigation. Two different ways are followed:

- **Develop a fast analytical model for both generation and propagation parts**. As this model needs high computational efficiency and high adaptability at the preliminary stages of the project, time consumption (engineering and computational time consuming) is the most important aspect while the accuracy modelling the real railway system moves to the background.
- **Use the previous model only as a generation model to feed adequately semi-analytical propagation models**. In semi-analytical propagation models, the train source is usually characterized by a frequency-dependent reference vibration amplitude at a reference distance (see Section 2.2.9 for more details). If these reference values are taken from experimental measurements the generation/propagation model becomes very inflexible. In contrast, if these reference values are obtained by using an analytical generation model, the model becomes quite adaptable.

## 1.2 Objectives of this thesis

As can be inferred from the previous section, the objective of this thesis is to develop a generation/propagation model for an at-grade train source, which would be used to evaluate railway-induced ground vibrations in preliminary assessment studies. To achieve this main objective, three partial objectives are defined:

- Bound the region of the ground surface on the surroundings of an at-grade train source that allows for the use of typical semi-analytical propagation models.
- Implement a simple and fast analytical model of the superstructure, which would allow for economic calculations of the track receptance and the wheel/rail contact force in terms of the computational effort. This model must allow for the computation of any particular case, composed of any combination of rolling stock, superstructure and subgrade kinds. The influence of the subgrade on the system response will be studied, with the aim of simplifying the model if this influence is not significant.
- Expand the previous model to determine ground surface vibration levels in the surroundings of the train infrastructure induced by a train passage, obtaining a complete generation/propagation model. Again, any combination of subsystems involved must be carried out. This model can also be used to obtain a reference vibration amplitude at a reference distance (calculated in the first partial objective) to use semi-analytical propagation models.

## 1.3 Structure of this thesis

In Chapter 2 one can find a state of the art for generation and propagation models, Sections 2.1 and 2.2 respectively. Propagation models can be classified, as stated above, in analytical models (2.2.1), numerical models (2.2.8) and empirical or semi-analytical models (2.2.9)

Chapter 3 is structured as follows. In Section 3.1 the definition of Lamb's solutions for line (Section 3.1.1) and point (Section 3.1.2) sources are recalled and the numerical solution approach used is also presented (Section 3.1.3) as well as a methodology to calculate the near field distance (Section 3.1.4). In Section 3.2 the relationship between the parameters of the problem and the near field distance for the case of infinite line source (Section 3.2.1) and point source (Section 3.2.2) is explained. A calculation example of near field distances (Section 3.2.3) is also presented. Section 3.3 contains the conclusions of this chapter.

Chapter 4 presents a complete model of superstructure coupled with its subgrade, which is assumed to be a viscoelastic and homogeneous half-space. The analytical formulation of this model is developed in Section 4.1, showing the subgrade model (Section 4.1.1), the superstructure/subgrade coupling (Section 4.1.2) and the numerical integration approach used to solve the integral solutions of the problem (Section 4.1.3). The influence of the subgrade parameters on the track receptance is shown in Section 4.2, where the

particular effects of damping (Section 4.2.1), density (Section 4.2.2), Poisson ratio (Section 4.2.3), Young's modulus (Section 4.2.4) and superstructure width (Section 4.2.5) are investigated. In view of these results, a fast method to obtain the track receptance is presented in Section 4.3. Additionally, an equivalent 2DOF model of the track is developed in Section 4.4 assuming frequency non-dependent (Section 4.4.1) and dependent (Section 4.4.2) parameters.

Chapter 4 also presents a methodology to evaluate the wheel/rail contact force with the aim of investigating the effects of the subgrade in this variable. First, in Section 4.5, a rolling stock model and its coupling with the superstructure model are defined (Sections 4.5.1 and 4.5.2). An approach to evaluate the wheel/rail contact force using the complete model and a methodology to work with roughness information are presented in Sections 4.5.3 and 4.5.4 respectively. Finally, the influence of the subgrade parameters on the wheel/rail contact force are investigated in Section 4.6. Section 4.7 contains the conclusions for this chapter.

Chapter 5 presents a general model for a train passage, generalising the complete model developed in Chapter 4 to a moving force arbitrarily varying in time which simulates a single wheel-set pass-by (Section 5.1). A methodology to obtain the response of the ground using the previously evaluated wheel/rail contact force as this moving source is presented in Section 5.2.

Finally, Chapter 6 presents the conclusions of this work, summarising the principal contributions of this thesis (Section 6.1) and proposing future research ideas that the author considers interesting as a continuation for this research line.

# Chapter 2

# State of the Art

In this chapter, a review of the most relevant studies and investigations developed about railway-induced ground vibrations is presented. This review is subdivided into generation models, which concerns about the rolling stock, the track and their contact; propagation models, where the most used models of the ground are explained; and railway-induced ground vibrations models, which contains the most renowned complete models (only generation and propagation parts) of train infrastructures at-grade.

## 2.1 Generation models

The generation of vibrations in railway infrastructures is due to loads generated in the wheel-rail contact. Excitations that generate these loads can be classified into two very distinct kinds [16]:

- The static component of the axle loads generates an excitation due to its displacement along the track. It is called the **quasi-static excitation**. It has a "low" frequency content in general ($< 20Hz$), which shifts to lower frequencies with increasing distance from the track and to high frequencies with increasing train speed [17].
- The dynamic component of the wheel-rail contact forces generates an excitation basically due to the spatial variation of the support stiffness and the wheel and track roughness. It is called the **dynamic excitation**. It has a "high" frequency content in general: between 20 Hz and 250 Hz, as a loose range.

For the case of sub-Rayleigh train velocities, Lombaert, Gupta and Degrande [16, 17] show, as well as Sheng, Jones and Thompson [18] did, that the quasi-static excitation dominates the track response and, by contrast, the dynamic excitation dominates the ground-borne vibration. Therefore, an inclusion of these two kinds of excitation is mandatory for any superstructure model that will be used to quantify its attenuation between, for example, the rail and the surrounding ground. In contrast, for ground-borne vibration assessment the quasi-static excitation can be neglected in most cases, with the exception of the trans-Rayleigh trains [19].

### 2.1.1 Track models

In 1993 Knothe and Grassie published a review of dynamic track models and contact force models at high frequencies [20]; this work has become a reference for most of the investigations carried out later in this topic. They considered "high" frequency as those above 20 Hz, where track dynamics become increasingly important and vehicle dynamics less important. With regard to the frequency range of interest, many authors show that it lies between 0 Hz and 1500 Hz for the case of superstructure response [20–24], and between 20 Hz and 250 Hz for the case of ground-borne vibration for mid-speed trains [16, 25–32]. Low frequency excitations (in the frequency range below 20 Hz) do not excite significantly the superstructure, unlike what happens with rolling stock [20]. Only for the case of high speed trains and soft grounds, therefore, when the high speed trains become trans-Rayleigh trains, the quasi-static excitation is sufficiently important to be

significant in the surface response of the surrounding ground and, thus, to induce low frequency vibrations on this response [19]. In buildings, technical standards [4, 33, 34] set the frequency range to evaluate human exposure to vibrations between 1 Hz and 80 Hz. Therefore, any kind of vibration mitigation measure must to act mainly in the frequency range between 20 Hz and 80 Hz.

Knothe and Grassie also state that up to 500Hz the rail can be modelled as an Euler beam. For higher frequencies the rail must be modelled as a Timoshenko beam [35–41]. The use of an Euler beam is thus justified for models dedicated to the propagation of vibrations on the ground.

There are two main types of track models with respect to the modelling of rail supports:

- Discrete support model. Sleepers or blocks (depending on the type of superstructure) are considered discrete supports.
- Continuous support model. Sleepers or blocks are considered a support which is uniformly distributed along the rail.

Both model types contemplate the possibility of one, especially two, and even three layers of support. The track model types used most frequently in the bibliography are presented in figures 2.1 and 2.2, to which some authors have added variants such as the use of elastic sleepers instead of rigid sleepers [42], or subgrade models which are not entirely rigid such as elastic or viscoelastic and homogeneous or stratified media [30].

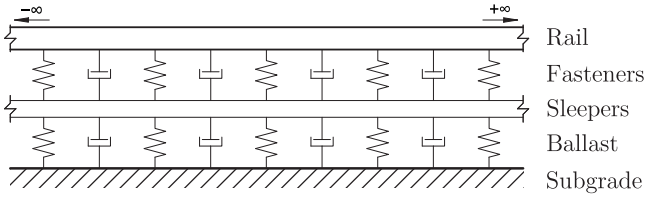


(a) 2-layer continuous support model

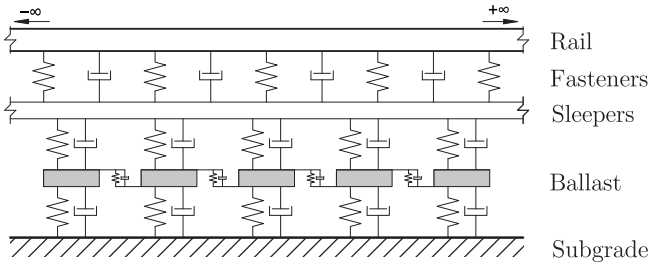


(b) 3-layer continuous support model

FIGURE 2.1: Types of superstructure models. (a) Continuous support model with two layers of support. (b) Continuous support model with three layers of support where ballast mass and its internal friction is considered.

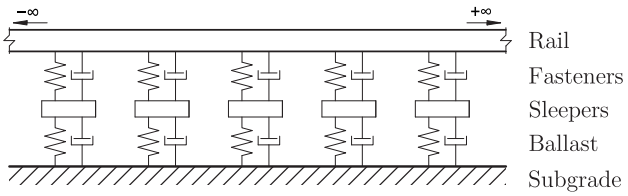


(a) 2-layer discrete support model

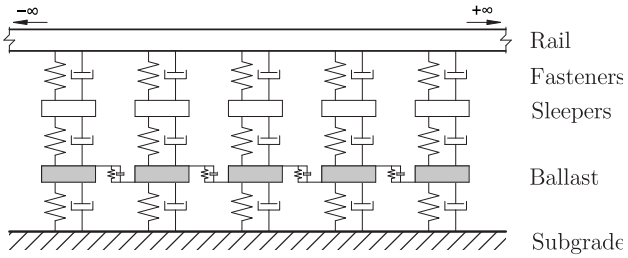


(b) 3-layer discrete support model

FIGURE 2.2: Types of superstructure models. (a) Discrete support model with two layers of support. (b) Discrete support model with three layers of support where ballast mass and its internal friction is considered.

Regarding the different existing possibilities of modelling the subgrade and ground supporting the track, it is interesting to cite the works of Knothe and Wu in 1998 [30] in which it was demonstrated that for frequencies below 200Hz correct modelling of the subgrade of the track is needed, thus ruling out the assumption that it is entirely rigid in most cases. As also demonstrated in [43], the ground must be adequately modelled to consider the coupling between sleepers. The need of a good subgrade model has been contrasted by other authors [44–47].

It is also important to stress the work carried out by A. V. Metrikine [48–54] in this field, who demonstrated the possible instability of a mass circulating on a track (a quasi-static excitation model) caused by the proximity of circulation speed to the minimum propagation speed of the waves in the rail. Metrikine carried out this investigation for different types of rail supports thus contributing to the improvement of the modelling of the superstructure and subgrade supporting it, such as the concept of the equivalent stiffness of a half-space [49, 50]. He has also recently carried out a study in which he added the viscoelastic theory in the modelling of the half-space [54].

Many authors demonstrate the existence of 2 natural frequencies in the case of the continuous support model and 3 for the discrete support model [20, 55]. The first two resonances coincide exactly with both models and are found from 50 to 200 Hz and 300 to 600 Hz approximately: In first mode the sleepers and track oscillate in-phase and in second mode oscillate in counter-phase. The third natural frequency, which appears only in the discrete support model, corresponds to the pinned-pinned mode. This resonance, found between 700 Hz and 1000 Hz [56], is excited when the wavelength coincides with

the distance between sleepers and will thus never appear in a continuous parameter model. It is therefore negligible for the frequency range mentioned above.

One of the most applied models is that proposed by Grassie, Gregory, Harrison and Johnson in 1983 [55]. This model is lineal, it uses a point mass to model the unsprung mass of the vehicle and it represents the wheel/rail contact by a lineal spring, contemplating the contact deformation according to the Hertz theory [57]. Both the point mass and the Hertz spring move along the track, which is modelled according to the Euler and Timoshenko theories. Using this approach, the authors are able to determine the response of the system of both the rail and the wheel.

Another method of interest is that presented by Clark, Dean, Elkins, Newton [42]. In this method the wheel/rail contact force is calculated on the basis of a modal analysis of the track and integrating this force according to the displacement of the wheel along the corrugated surface of the rail. Using this method, the solution of the problem to various irregularities of the rail and the wheel was found in the time domain: specifically, a wheel flat and a uniform irregularity of the rail. Wu and Thompson [58] more recently used a similar model to those aforementioned to determine the response of multiple wheels based on the superposition principle.

The objective of all these models is to determine the response of the track under the passing of the train; therefore the contact force should be adequately characterized.

### 2.1.2 Contact force models

A good wheel/rail model is that which generates an adequate, inherently non-lineal, response for all types of rail irregularities. The track is subjected to a wide diversity of loads and, in consequence, the types of irregularities are thus also diverse [59]. The irregularities not caused by the passing of the train, such as joints [60], factory irregularities [61], etc..., must be also taking into account.

Regarding to the normal contact problem, the contact force model most often applied is the Hertz theory of elliptical contact mechanics [57]. There are, however, other procedures such as the Boussinesq theory and the distributed point reacting spring (DPRS) [62, 63]. These methodologies allow a more adequate characterisation of stress distribution on the contact surface. Regarding to the tangential contact problem, Kalker's programs (CONTACT or FASTSIM) or their subsequent simplifications are the most used solutions [20].

The roughness of a rail or wheel is commonly modelled following to a random process. It has been demonstrated that in a wide range of measures, in the space domain,

roughness obeys an isotropic Gaussian distribution [64–66]. This process is transformed into the time domain according to vehicle speed, thus converting it into a stationary ergodic process [67]. Being a random variable, the roughness is usually described in the wavenumber domain. Within this domain, one of the most widespread descriptors of the roughness is its power spectral density (PSD) [64, 65, 68], which is the accepted spectral representation for random stationary processes [67]. It is therefore usual to describe a roughness typology (classified according to irregularity types, when previous maintenance took place, type of steel, etc...) according to a PSD generally calculated based on the large amount of measurements of the same roughness type. As the standards stay [69, 70], the roughness PSD should be presented in the form of one-third octave bands in the wavenumber domain [18, 41, 45, 61, 71, 72].

Nevertheless, to feed track models such as those aforementioned, the time roughness history (based on spatial roughness history and vehicle speed) must be known. Therefore, the spectral information in one-third octave bands describing the roughness typology applied must be transformed to the spatial domain. A commonly used approach to solve this problem is the reconstruction of the signal, based on its power spectral density, through a combination of triangular series [16, 45, 68, 73]. The result will be one of an infinite number of stochastic signals which have the same spectral content as the initial spectral roughness data.

An effective approach to determine this contact force is that presented by Cardona, Otero, de los Santos and Martínez [1, 74, 75] in which a simplification into a 2DOF system of the 2-layer continuous parameter track model (Figure 2.1(a)) is proposed by adjusting its parameters through modal analysis requiring the receptances of the rail to be precisely equal. The spatial dependence of the expressions is thus eliminated and, adding the model of the rolling stock and contact force, the time history of the contact force can be obtained based on the numerical integration of the one-dimensional motion expressions. The same authors propose a convolution method of variable kernel in [76, 77], for which the time evolution of the rail vertical displacement in a certain point is calculated based on the contact force previously determined.

## 2.2 Propagation models

### 2.2.1 Analytical propagation models

The theory of elastic wave propagation in continuous media demonstrates that when an elastic and homogeneous half-space is excited basically 4 wave types arise, which can be classified into volumetric and surface waves [78]

- Volumetric waves:
  - Compression waves or P-waves.
  - Shear waves horizontally and vertically polarized waves (SH-waves and SV-waves respectively).
- Surface waves:
  - Rayleigh waves.

Lamb, specifically, was one of the first investigators to demonstrate that the propagation on a homogeneous elastic half-space is composed by these different wave types [79], for the case of line and point sources. If a half-space is considered to be divided into horizontal layers of homogeneous thickness and properties, which is a model of ground frequently used in literature (see Section 2.2.3), two additional wave types arise: Love waves and Stoneley waves [80, 81]. These six wave types are not the only ones but are the most significant with respect to its contribution to the vibration levels of the ground; other kinds of waves, such as leaky surface waves [82], have been demonstrated to transport only a very small amount of excitation energy.

For the homogeneous elastic half-space problem and for the case any surface source, the waves which propagate more and more energetically are Rayleigh surface waves [79], as carefully demonstrated by the point source case in [83] and [84]. Specifically, Lamb showed that, taking into account only the geometrical attenuation of the waves, Rayleigh wave and volumetric waves amplitudes induced for a point source decrease proportionally to $r^{-1/2}$ and $r^{-2}$ on the far field (see Section 2.2.4), respectively. In the case of a line source, the Rayleigh wave has no geometrical attenuation and the volumetric waves decrease proportionally to $r^{-3/2}$. It is also demonstrated in [83, 84] that energy distribution varies according to source type (point load, multi-point load, line load, strip load, etc...) but, in any case, the Rayleigh wave is the most powered wave.

For the layered elastic half-space problem, Rayleigh wave dominates the propagation of vibrations induced by surface source, generally. However, there are some special cases for those the body waves dominate the surface motion, for example when the excitation frequency approaches to a natural frequency of the upper layer [85].

A summary of the principal ground vibration propagation models is presented below. These range from the most theoretical, developed in the field of seismology and geomechanics, to the most empirical, attained typically in civil engineering and/or mechanical engineering, through to numerical models based on finite, infinite or contour elements.

### 2.2.2 Homogeneous and elastic half-space

The first author to solve the surface vibration propagation in an isotropic, homogeneous and elastic half-space was Lamb in 1904 [79]. Lord Rayleigh [86] had previously discovered the existence of surface waves, later named Rayleigh waves, which restricted their propagation close to the half-space surface.

Lamb solves the problem of forced vibrations both by line source and point source, acting in both cases vertically on an isotropic, homogeneous and elastic half-space. He specifically finds a solution for an impulsive source from the harmonic source solution previously derived by him. All surface displacement expressions attained contain integrals, the complexity of which led him to the need to use asymptotic expansions to evaluate them. Another approach used was the steepest descent method [87]. All these approximation approaches are valid only if the distance of study with respect to the source is sufficiently high. They are, therefore, expressions which adequately characterise the far field [88].

Later on Holzlöhner [88] studied the applicability zone of the expressions proposed by Lamb for Rayleigh waves in the case of an harmonic point source. He observed that for sufficiently large distances the applicability of the Rayleigh waves term of the Lamb expressions, named by the author as the Lamb expression for the far field, is strong. To carry this out, he compared this expression with an exact solution of the problem proposed by him, which is derived from the formulation for rectangular surface source [89], transforming it to square and then making its dimension tend to zero. The results obtained show that for sufficiently high $\bar{r}$, where $\bar{r} = r\omega/\beta$ ($r$ is the distance between the receptor and the source, $\omega$ is the angular frequency and $\beta$ is the S-wave propagation speed), the Holzlöhner model approaches exactly to Lamb's far field model. This is logical considering the aforementioned studies by Miller and Pursey [83, 84]: Rayleigh waves propagate much more and more energetically than others and therefore predominate at larger distances. For shorter distances Barkan [90] had already suggested possible interference by compression and shear waves.

Later, Jones and Petyt, as detailed in Section 2.3.1, solve the problem of rectangular loads and strip loads acting on the surface of different half-space models. They also observed and commented the interference of the volumetric waves in the near field (see Section 2.2.4) in all these investigations.

### 2.2.3 Half-space stratified in homogeneous and elastic layers

In the section above, the ground has been assumed as an isotropic, homogeneous and elastic half-space. This model is generally only valid in finding an initial approximation

to the problem: the ground is in general predominantly heterogeneous and not perfectly elastic.

The most accepted model regarding heterogeneousness is the division of the ground into horizontal and isotropic layers, each with a certain thickness, up to a final layer considered semi-infinite. The pioneering investigators in this field were Thomson [91] and Haskell [92]. Thomson proposed a matrix method, later named the **matrix propagator method**, which allows the relation of the boundary conditions of all interfaces of a stratified medium from the surface down to the final layer. Haskell implemented this method in the case of free vibrations thus obtaining dispersion curves (variation of phase velocity with respect to the frequency and for each vibration normal mode) for Rayleigh and Love waves through a computational algorithm. This model has been used by several authors to find forced ground responses. [81, 93, 94] are examples.

In 1964 Professor Leon Knopoff [95] proposed a new matrix method to calculate the free response of a stratified half-space more efficient in terms of the computational calculation time in comparison to the Thomson-Haskell formalism. Dunkin demonstrated to [96], almost simultaneously to the investigations of Knopoff, that low efficiency in calculation time of this formalism also brought about a problem of precision at high frequencies. Dunkin proposed a further new method to solve this problem, named the loss-of-precision problem, and certified that it was also solved by the Knopoff's method.

With their relevant improvements, both methods were compared by Schwab in [97] concluding that the most efficient method regarding calculation time was the Knopoff's method [95, 98, 99]. The Dunkin method, named the $\delta$-matrix method and then changed to the reduced $\delta$-matrix method thanks to contributions by subsequent investigators about its computational efficiency [100, 101], turned out to be slightly slower.

Subsequently, in 1983, Kausel and Roësset [102] presented a new matrix formalism for the resolution of stratified media through the stiffness matrix of each layer. These stiffness matrices were taken from the Thomson-Haskell formulation thus it is therefore important to stress that, as in previous cases, this new method is not more powerful. It does, however, provide a series of advantages regarding computation and applicability. Specifically these advantages are:

- The stiffness matrices obtained are symmetrical.
- Fewer operations are required for analysis.
- An easy adaptation to multiple excitations is allowed.
- Substructuring techniques [103] can be applied to stiffness matrices, which can be interpreted and applied as stiffness matrices in the structural analysis.

- Asymptotic expressions follow naturally from the expressions: problems involving high frequencies or very thin layer can be solved without loss of precision

The structural approach of this method makes it ideal for all types of ground-structure interaction analysis. A very similar method had already been proposed previously by Biot, as stated in [104].

Many studies have recently appeared which introduce the concept of Green's functions in the calculation of a stratified half-space response. An investigation carried out by Luco and Apsel [105, 106] is one of the most widely used and accepted. In this investigation Green's functions are present allowing the calculation of the dynamic and 3D response of a stratified half-space for any underground or surface source. This method also considers certain modifications if a large number of waves are being worked with, which in turn opens the door to other applications such as infrastructures instead of seismology. In [106] the authors present a very interesting integration method to overcome the problems related to the oscillatory behaviour of the typical integrands those appear in elastodynamics expressions and compare its solution with some already existing ones proving, therefore, a high credibility.

It must also finally be highlighted that the near field problem (see Section 2.2.4) is more complicated and unpredictable than in the homogeneous case (due to reflections and refractions of the waves in the interface between layers) [85]. Likewise, the stratified case adds a new particularity to this problem: Love waves also appear in the surface far-field [81].

### 2.2.4 Near field and far field regions

As can be seen in Sections 2.2.2 and 2.2.3, the using of Rayleigh waves expressions as a solution of the vibration propagation problem in a half-space is not always an acceptable assumption. To bound this applicability, the near field and far field regions are defined as [107]:

- **Near field region.** Region where volumetric waves that either propagate on or affect the surface significantly influence the levels of vibration, together with surface waves.
- **Far field region.** Region where the only waves that bring movement to surface of the ground in a significant way are the surface waves, specifically those of Love and Rayleigh.

Therefore, there is a distance with respect to the source that confines the border between these two regions and is called **near field distance** throughout this paper.

As is mentioned above, several authors, as Lamb [79], Barkan [90], Holzlöhner [88], Jones [108] and many more have demonstrated the existence of this interference region but they did not quantify it. Only Holzlöhner gives indicative figures for this distance but does not precise ($\bar{r} \approx 40$). He finds, only for rectangular source, that the geometrical diminishing of the near field is proportional to a $r^{-1}$, as also stated in [108].

A more precise modelling of the ground, such as the well known horizontal and homogeneous strata model, can imply the existence of more waves [81, 91], keeping the inherent problems of near field [85]. More complex sources which more accurately model the superstructure/ground interaction, as will be seen in Section 2.3, are also affected for this problem.

### 2.2.5 Other models of heterogeneous half spaces

There are also model types which try to contemplate the anisotropy of the real grounds. One of the most widely studied models is transverse isotropy. A transversely isotropic material is one with physical properties which are symmetric about an axis that is normal to a plane of isotropy. This transverse plane has infinite planes of symmetry and thus, within this plane, the material properties are same in all directions. It is, hence, a particular case of anisotropy. An accurate state of the art can be found for this model in [109], for the case of a non-layered half-space.

With regard to the heterogeneousness of the ground, a different modelling approach with respect to the layered half-space (see Section 2.2.3) is to consider that ground properties vary according to a continuous function with depth [104, 110, 111]. A summary of most studies carried out with this model can be found in [112], taking both isotropic and anisotropic media into account.

It is also important to point out studies carried out on the effect of curvature or, in general, irregularities on the free surface of the half-space [113]. It has been demonstrated that these irregularities (curvature or surface corrugation) generate large distortions in the far field response of the ground.

### 2.2.6 Viscoelastic or anelastic theory

Up until here, the ground has been modelled as a completely elastic medium. This hypothesis has been demonstrated non-valid in most cases for vibration propagation in

any ground type. Only in extra low frequency range, the completely elastic assumption can be adopted successfully.

In 1950, Read [114] studied viscoelastic (also known as anelastic) material behaviour from also considering the derivatives of tension-deformation relationships. He thus proposed a model where Lamé constants (or Young modulus and Poisson's ratio) are considered complex which therefore leads to complex propagation speeds. Material attenuation in the medium is represented by the imaginary term of these speeds. This damping model was named the correspondence principle [115–121] and has been used in the modelling of different kinds of materials.

This theory was also assumed in the study of vibration propagation in the ground [122]. Haskell had already suggested the possibility of using his method considering the correspondence principle and it was Knopoff who introduced it formally in the expressions proposed by Thomson [91], therefore finding the formulation for a stratified and anelastic half-space. Recent studies still use this method to model the material attenuation in the ground [123], assuming, as in propagation speeds, a disperse character in the attenuation linked to surface waves and a non-dispersed character (albeit variable in depth) to that linked to compression and shear waves.

### 2.2.7 Numerical integration of the elastodynamic integrals

For the ground models presented in Sections 2.2.2, 2.2.3 and 2.2.5, or in most other elastodynamics problems, the Green's functions related to the displacements and stresses can be obtained as a summation of the following two canonical forms [124, 125]:

$$I(r,\omega) = \int_a^b \tilde{I}(k,\omega)\mathrm{e}^{-\mathrm{i}kr}\mathrm{d}k \tag{2.1}$$

$$I(r,\omega) = \int_a^b \tilde{I}(k,\omega)J_n(kr)\mathrm{d}k \tag{2.2}$$

where $I$ are integrals, $\tilde{I}$ are integrands (without taking into account the kernels), $a$ and $b$ are the integration limits (in general, $a = -\infty$ or $a = 0$ and $b = +\infty$), $r$ is some kind of distance associated to the model type (normally the receptor-source distance) and $J_n(.)$ is the nth-order Bessel function of the first kind.

The numerical integration of these integrals is normally fully applicable because, if the model assumes some kind of material attenuation of the ground, there are no poles along

the required integration path [105, 106, 126]. In contrast, the integrands inside has a strong oscillatory behaviour, whatever the ground model, causing two kind of problems:

- Low attenuation of the integrand with the integration variables causes low attenuation of the oscillations [126]. In this cases, to ensure accuracy on the evaluation a small truncated limit of integration can not be used, inducing the need of very much more integration points again.
- High values of $r$ generate dense oscillations and, therefore, too much integrations points are required to obtain an accurate solution [124].

An approach to solve the first problem was shown by Apsel and Luco [105, 106, 126], following an analytical procedure based on the solutions of the static integrands and integrals. This method must be used before the numerical integration. Different versions of this approach are used for other authors to improve the computational efficiency of some elastodynamic problems, as for example Schevenels [127]. The Apsel's technique is described more extensively in Appendix A.

With regard to the numerical integration process, there are some specific methods developed to compute this kind of integrals:

- Numerical integration following a Gauss-Kronrod quadrature allows to deal with low oscillatory integrands [128, 129]. It provides a good accuracy but its computational efficiency decreases too much significantly with the density of the oscillations.
- Filon's method is one of most used, being its quadrature very efficient with high oscillatory integrands [124, 125, 130–134].
- Fast Fourier and Logarithmic Fast Fourier Transform algorithms are used when the integral can be rewritten in terms of Eq. (2.1). Logarithmic Fast Fourier Transform algorithms have a good efficiency for solve the first problem because they allows for a precise evaluation of the integral at very low wavenumbers also taking into account the spectral information at very high wavenumbers [135, 136]. Another approach is the Nonuniform Fast Fourier Transform, which allows to perform an adaptive integration, with its obvious benefits [137].
- Fast Hankel and Logarithmic Fast Hankel Transform algorithms [138–142] are used when the integral can be rewritten in terms of Eq. (2.2). Logarithmic Fast Hankel Transform algorithms [135, 136] have the same advantage as the Logarithmic Fast Fourier Transform algorithms. Another approach is the Nonuniform Fast Hankel Transform, which allows to perform an adaptive integration [143, 144] in a similar manner as the Nonuniform Fast Fourier Transform.

### 2.2.8 Numerical propagation models

Three of the most widely used methods for structural dynamics in ground modelling are the finite element method (FEM), the infinite elements method (IFEM) and the boundary element method (BEM). In the field of vibration propagation in railway infrastructures, specifically, these numerical solutions are now widely used in the case of underground infrastructures.

One of the most successful models is the so-called coupled periodic FE/BE model [145–150]. This discretises a periodic cell (see Section 2.3.2) of the tunnel-superstructure system using FEM and the surrounding ground using BEM. The BEM applied for the ground modelling allows its stratification, making each interface between strata a further boundary element surface. This model has now been shown to be one of the most efficient in terms of results, even though it is, as any other numerical model, extremely time-consuming [147].

Many other authors, such as [149, 151], have created complete models of the infrastructure in FEM which have always resulted in being extremely time-consuming in calculation and very little generalising. In other words, they were used to characterise specific locations.

Another current numerical ground modelling technique is the Thin-Layer Method (TLM) [27, 152]. This is a semi-discrete numerical tool which combines the advantages of finite elements with the rigour of analytical solutions. It consists of a partial discretisation of the medium, only in the normal direction to the surface and interfaces of the stratified medium.

A similar method to TLM is the Spectral Finite Element Method (SFEM) [153], which is also able to calculate vibration propagation though a stratified medium. This method can calculate wave propagation through waveguides, which are typically structures which guide waves. Assuming each layer of the stratified medium behaves as a waveguide, this method can be satisfactorily applied for stratified ground. This is a very good approach for very high frequency excitation problems.

### 2.2.9 Empirical or semi-analytical propagation models

Finally, the simplest kind of propagation models, very used by the civil engineers, are the empirical or semi-analytical models, which are based completely or partially in experimental measurements respectively.

One of the most used semi-analytical models is Barkan's law [15, 90]. Before Barkan, Bornitz had already introduced a similar model in the field of vibrations induced by infrastructures [154]. Later, several authors have proposed laws analogous to Barkan's in order to model the propagation of vibrations [7, 155–159].

The relationship between the function of generation and of propagation is usually a reference amplitude calculated or measured at a determined distance from the track [69]. From this reference, empirical models of propagation can be used to calculate the vibration at any point on the ground, applying an attenuation law that comprises properly the effects of geometric and material attenuations. Using these laws with the geometric and material attenuations as a free parameters (empirical way), one can predict the propagation of vibrations for a specific placement site. These attenuation parameters are fitted with experimental measurements [157, 159]. Therefore, they can not be used as predictive models, unless an exactly similar placement site is found, which is very unlikely, or that a huge number of experimental measures are carried out.

On the other hand, if these laws are used in a completely theoretical way it is possible to use them as predictive models [9, 160]. In this case it is necessary to know precisely the ground's properties and, especially, which waves predominate at the reference position and at the prediction points, in order to be able to apply proper values of the geometric attenuation coefficient. For a case on the surface, it is clear that the most significant waves are the surface ones; specifically the Rayleigh waves when the ground is modelled as an infinite and homogeneous half-space [78, 83, 84]. However, volumetric waves P and S also appear, but they have a geometric attenuation higher than the Rayleigh waves.

One solution to these problems can be to superpose different kind of travelling waves models [155, 161], although this procedure does not take into account constructive or destructive interference between waves. Another option is to apply a far field model in which the Rayleigh waves would clearly predominate. In this case the amplitude of reference vibration which relates the generation function to the propagation function has to be located at a sufficient distance with respect to the source, so that it assures that the amplitude under consideration is specifically due to surface waves [9, 15, 90], and therefore outside of the near field region.

## 2.3 Train-induced ground vibration models

As previously seen in Section 2.1.2, there are a large number of models able to determine wheel/rail contact force. To find the levels reaching the ground based on this force, many authors have presented complete superstructure/ground coupling and propagation

models; in some a generation model has also been introduced. The most important interaction models which have been presented until now are described in this section.

It must also be pointed out that, as in this case, the superstructure acts as an exciter. The reverse case, such as the excitement of buildings due to vibrations propagating along the ground (zone 3 in Fig. 1.1), is not included in the study.

### 2.3.1 Analytical models

Probably the best-known analytical model of train-induced ground vibrations is the model formulated by Victor V. Krýlov [31, 162–167]. This model considers each sleeper as a point source, as the wavelengths of the generated waves are much greater than one sleeper dimensions. The deflection of the track is calculated assuming the circulation of a constant mobile force along the track and taking into account the sleepers, fasteners, ballast and subgrade [168]. Though this deflection Krýlov calculated the force acting on each sleeper and, based on this force of each sleeper, he generates a multi-point source model which uses the Lamb solution for Rayleigh waves as a propagation model [79, 80], expressed in the form of Green's function [165].

Later on, ground stratification was included in this formalism, modifying the Green's functions of the half-space for it to be considered [165]. Degrande and Lombaert, specifically, proposed a formulation based on the dynamic reciprocity theorem, for which the necessary computational effort is improved significantly [26].

A priori, this method was deficient for not incorporating the dynamic excitation generated in wheel/rail contact. Krýlov, however, discovered that when train speed approaches to propagation speed of the Rayleigh waves in the ground, the vibrations induced by quasi-static excitation increased significantly [19, 31, 162, 164–166]. This approximation of speeds only occurs on some sections of high-speed lines where the ground is very soft (low speed Rayleigh wave propagation) or when the train speed is sufficiently high, as commented in section 2.1.1. For high-speed trains, it was thus demonstrated that a good approximation of the problem is to assume only the quasi-static excitation, especially when the track rests on a low stiffness subgrade.

Another prominent investigation was that published by C.J.C. Jones and M. Petyt, in collaboration in some cases with other authors. It initially discusses the modelling of a strip source acting on a half-space as a two-dimensional problem, considering the half-space as an elastic and homogeneous medium [169], as a 1-layer stratum over a rigid medium [170] and as a 1-layer stratum over an elastic medium [171]. Later they

studied the case of a rectangular source also applied on a half-space, considering the half-space as an elastic and homogeneous medium [108] as well as considering a viscoelastic (see Section 2.2.6) stratum over a rigid foundation [172] and the source moving in the case of an homogeneous medium [173]. In all these cases the formalism of the previously explained dynamic stiffness matrix is used [102]. Other authors have studied this subject in depth proposing new cases such as that of a distributed line load in movement [174] or that of a rectangular load of a variable time width [175].

With the collaboration of X. Cheng, Jones and Petyt subsequently adapted these first investigations for the case of a railway track. They considered a moving load acting on a two-layer continuous support model of the superstructure, which rests on the ground from a infinite strip contact. They used this inherent idea in the 2.5D models [176] (see Section 2.3.2). The harmonic point load excitation were investigated, for the case of static [29] and moving load [28, 177, 178], considering an elastic stratified half-space in both cases. This model was more recently adapted to include dynamic excitation [18, 45].

### 2.3.2 Numerical models

The aforementioned analytical models are normally efficient computationally. They are not, however, able to tackle certain problems with complex geometries, such as underground infrastructures.

In a recent article, written by the aforementioned Jones, Petyt and Thompson, the main approaches carried out up to now regarding numerical models of railway infrastructures are presented [179]. As seen earlier on, these authors have presented analytical models (see previous section) but recognize the need to apply numerical models to adequately resolve problems involving infrastructures of complex geometries. According to this review, the most widely used numerical approach is the hybrid FE/BE model. As already seen in Section 2.2.8, the BEM is widely used in ground modelling. The FEM is used, on the other hand, to model the infrastructure and subsequently links up with the BE ground model to reach the global system. The following alternatives or variants exist within these hybrid FE/BE models:

- **2D FE/BE model**. This is a very efficient method regarding calculation time but does not take into account wave propagation in a longitudinal direction along the track.

- **3D FE/BE model**. This method allows a precise characterization of the problem but requires a great length of time to mesh the system and, above all, to carry out the calculation at high frequencies [180, 181].

- **2.5D FE/BE model**. This type of model is based on the supposition that the infrastructure is homogeneous in the direction of the track. From this supposition the problem linked to the waves circulating in the direction of the track is divided into a sequence of 2D FE/BE models, each calculating the system response of a specific wavenumber. The total system response can be calculated from the different components obtained from each wavenumber using the inverse Fourier transform. What is good, therefore, about these models is that they allow the modelling of a 3D case with 2D meshes with suitable precision. These methods, in which calculations are made per discrete value of the longitudinal wavenumber, are named wavenumber FEMs/BEMs or two-and-a-half dimensional methods (2.5D). One of the first articles presenting this method is that by Aubry, Cloteau and Bonnet in 1994 [176].

- **3D periodic FE/BE model**. Unlike the previous type of (2,5D) models, this model supposes that the infrastructure is periodic and not homogeneous in the track direction. The method is based on the division of the infrastructure into exactly equal 3D cells, which are equal because of the periodicity of the track. This periodic cell, named the reference cell, is solved by a coupled FEM/BEM and the Floquet theory [182] is later used to obtain the total response of the system [183–185]. The model has been validated experimentally for different cases [16, 47, 186], including certain improvements such as in the case of the doppler effect, detected in experimental measures by A. Ditzel [187].

# Chapter 3

# Near field distance determination

This chapter presents a methodology to determine an approximation of the near field distance at the surface of the ground, both for an infinite line source and for a point source, with the aim of obtain a reference distance to use semi-analytical propagation models in preliminary assessment studies. The near field distance is the distance with respect to the source that confines the border between the far field and the near field regions. Precise quantification of this distance will bound the applicability of Rayleigh wave expressions as valid solutions of the problem. The ground is modelled as an homogeneous viscoelastic half-space: this model allows to evaluate a first approximation of the near field distance with low geotechnical information and, therefore, low time/economical cost, which is the most important aspect in preliminary assessment studies. In order to measure the near field distance, an analytical approach is followed, which compares the exact solutions of the problem with Rayleigh waves expressions proposed by Lamb [79]. The effects of the excitation frequency and mechanical properties of the ground on the dimensions of this interference region, characterized here the near field distance, are also investigated. The results show near field distances for both infinite line and point sources and for five different real grounds, typical of the Barcelona (Spain) metropolitan area.

## 3.1 Theoretical background and methodology

In this section, a methodology to determine the near field distance for the case of infinite line source and point source is presented. The analytical expressions for these two kinds of sources are presented, together with a numerical integration procedure to solve them and expressions that define the near field distance from analytical expressions solutions.

### 3.1.1 Infinite line source

The complete expressions derived by Lamb [79] in the case of infinite vertical line source, for an elastic and homogeneous half-space, are

$$X_{g0} = \frac{\mathrm{i}Q}{2\pi\mu}\int_{-\infty}^{+\infty}\frac{k(2k^2-k_\beta^2-2\upsilon\upsilon')}{(2k^2-k_\beta^2)^2-4k^2\upsilon\upsilon'}\mathrm{e}^{-\mathrm{i}kx}\mathrm{d}k \tag{3.1}$$

$$Z_{g0} = -\frac{Q}{2\pi\mu}\int_{-\infty}^{+\infty}\frac{k_\beta^2\upsilon}{(2k^2-k_\beta^2)^2-4k^2\upsilon\upsilon'}\mathrm{e}^{-\mathrm{i}kx}\mathrm{d}k \tag{3.2}$$

where $Q$ represents load amplitude, $k$ is the wavenumber, $\mu$ is the shear modulus, $X_{g0}$ and $Z_{g0}$ are the horizontal and vertical displacements in the spatial-frequency domain of a point on the surface separated by a distance $x$ from the line source. The other parameters are

$$\upsilon^2 = k^2 - k_\alpha^2 \qquad \upsilon'^2 = k^2 - k_\beta^2 \tag{3.3}$$

$$k_\alpha^2 = \frac{\omega^2}{\alpha^2} \qquad k_\beta^2 = \frac{\omega^2}{\beta^2} \tag{3.4}$$

where $\omega$ is the angular frequency and $\alpha$ and $\beta$ are the velocities of propagation of the P-waves and S-waves respectively:

$$\alpha^2 = \frac{\lambda+2\mu}{\rho} \qquad \beta^2 = \frac{\mu}{\rho} \tag{3.5}$$

From these Eqs. (3.1) and (3.2) Lamb derived the following Eqs. (3.6) and (3.7), assuming large distances

$$X_{g0} = -\frac{QH}{\mu}\mathrm{e}^{-\mathrm{i}\kappa x} + \frac{\mathrm{i}QC}{2\pi\mu}\frac{\mathrm{e}^{-\mathrm{i}k_\alpha x}}{(k_\alpha x)^{\frac{3}{2}}} + \frac{\mathrm{i}QD}{2\pi\mu}\frac{\mathrm{e}^{-\mathrm{i}k_\beta x}}{(k_\beta x)^{\frac{3}{2}}} \tag{3.6}$$

$$Z_{g0} = -\frac{\mathrm{i}QK}{\mu}\mathrm{e}^{-\mathrm{i}\kappa x} - \frac{QC_1}{2\pi\mu}\frac{\mathrm{e}^{-\mathrm{i}k_\alpha x}}{(k_\alpha x)^{\frac{3}{2}}} - \frac{QD_1}{2\pi\mu}\frac{\mathrm{e}^{-\mathrm{i}k_\beta x}}{(k_\beta x)^{\frac{3}{2}}} \tag{3.7}$$

where the constants $H$, $K$, $C$, $D$, $C_1$ and $D_1$ are

$$H = -\frac{\kappa(2\kappa^2 - k_\beta^2 - 2\sqrt{\kappa^2 - k_\alpha^2}\sqrt{\kappa^2 - k_\beta^2})}{16\kappa^3 - 8\kappa k_\beta^2 - 4\kappa^3\left(\frac{\upsilon^2 + \upsilon'^2}{\upsilon\upsilon'}\right) - 8\kappa\upsilon\upsilon'} \tag{3.8}$$

$$K = \frac{k_\beta^2\sqrt{\kappa^2 - k_\alpha^2}}{16\kappa^3 - 8\kappa k_\beta^2 - 4\kappa^3\left(\frac{\upsilon^2 + \upsilon'^2}{\upsilon\upsilon'}\right) - 8\kappa\upsilon\upsilon'} \tag{3.9}$$

$$C = -2\sqrt{2\pi}\frac{k_\alpha^3 k_\beta^2(k_\beta^2 - k_\alpha^2)^{\frac{1}{2}}}{(k_\beta^2 - 2k_\alpha^2)^3}\mathrm{e}^{-\mathrm{i}\frac{\pi}{4}} \tag{3.10}$$

$$D = -2\mathrm{i}\sqrt{2\pi}\sqrt{1 - \frac{k_\alpha^2}{k_\beta^2}}\mathrm{e}^{-\mathrm{i}\frac{\pi}{4}} \tag{3.11}$$

$$C_1 = -\mathrm{i}\sqrt{2\pi}\frac{k_\alpha^2 k_\beta^2}{(k_\beta^2 - 2k_\alpha^2)^2}\mathrm{e}^{-\mathrm{i}\frac{\pi}{4}} \tag{3.12}$$

$$D_1 = -4\mathrm{i}\sqrt{2\pi}\left(1 - \frac{k_\alpha^2}{k_\beta^2}\right)\mathrm{e}^{-\mathrm{i}\frac{\pi}{4}} \tag{3.13}$$

and where $\kappa$ is the root of the Rayleigh function (Eq. (3.14)) analogous to the real root of this function when the medium is completely elastic, i.e. the so-called Rayleigh root.

$$F(k) = (2k^2 - k_\beta^2)^2 - 4k^2\upsilon\upsilon' \tag{3.14}$$

Lamb demonstrated that each term of the Eqs. (3.6) and (3.7) is the contribution of each kind of wave to the displacement of the chosen point. So the first term represents the contribution of the Rayleigh waves, the second term represents the contribution of the P-waves and the last term represents the contribution of the S-waves.

The terms for the volumetric P-waves and S-waves are not exact because they are taken from the approximation for large $k_\alpha x$ or $k_\beta x$ respectively of the branch line integrals of the branch cuts, generated by the Rayleigh function at the complex plane. On the other hand, the term for Rayleigh waves derived by Lamb is exact.

Finally, it is also demonstrated, from observation of the Eqs. (3.6) and (3.7), that the geometric attenuation of the volumetric waves is much greater than the Rayleigh waves. Therefore, for large distances, Lamb's approximate expressions can be reduced to the Rayleigh wave expressions

$$X_{g0} = -\frac{QH}{\mu}\mathrm{e}^{-\mathrm{i}\kappa x} \tag{3.15}$$

$$Z_{g0} = -\mathrm{i}\frac{QH}{\mu}\mathrm{e}^{-\mathrm{i}\kappa x} \tag{3.16}$$

In order to convert the elastic medium assumed by Lamb into a viscoelastic medium, the Lamé constants are transformed into complex constants, from the expressions

$$\lambda^* + 2\mu^* = (\lambda + 2\mu)(1 + 2D_P\mathrm{i}) \tag{3.17}$$

$$\mu^* = \mu(1 + 2D_S\mathrm{i}) \tag{3.18}$$

where $D_P$ and $D_S$ are the damping of P-waves and S-waves, respectively.

### 3.1.2 Point source

Lamb also formulated the expressions that govern the propagation of vibrations of a point source in an homogeneous and elastic half-space,

$$R_{g0} = \frac{L}{2\pi\mu}\int_0^\infty \frac{k^2(2k^2 - k_\beta^2 - 2\upsilon\upsilon')}{(2k^2 - k_\beta^2)^2 - 4k^2\upsilon\upsilon'}J_1(kr)\mathrm{d}k \tag{3.19}$$

$$Z_{g0} = -\frac{L}{2\pi\mu}\int_0^\infty \frac{k\upsilon k_\beta^2}{(2k^2 - k_\beta^2)^2 - 4k^2\upsilon\upsilon'}J_0(kr)\mathrm{d}k \tag{3.20}$$

and he found an approximate solution for large distances also separated into three terms: Rayleigh waves, P-waves and S-waves (Eqs.(3.21) and (3.22))

$$R_{g0} = -\frac{\mathrm{i}\kappa LH}{\mu}\sqrt{\frac{1}{2\pi\kappa r}}\mathrm{e}^{-\mathrm{i}(\kappa r + \frac{\pi}{4})} + \frac{Lk_\alpha C}{2\pi^2\mu}\frac{\mathrm{e}^{-\mathrm{i}k_\alpha r}}{(k_\alpha r)^2} + \frac{Lk_\beta D}{2\pi^2\mu}\frac{\mathrm{e}^{-\mathrm{i}k_\beta r}}{(k_\beta r)^2} \tag{3.21}$$

$$Z_{g0} = \frac{\kappa LK}{\mu}\sqrt{\frac{1}{2\pi\kappa r}}\mathrm{e}^{-\mathrm{i}(\kappa r+\frac{\pi}{4})} - \frac{\mathrm{i}Lk_\alpha C_1}{2\pi^2\mu}\frac{\mathrm{e}^{-\mathrm{i}k_\alpha r}}{(k_\alpha r)^2} - \frac{\mathrm{i}Lk_\beta D_1}{2\pi^2\mu}\frac{\mathrm{e}^{-\mathrm{i}k_\beta r}}{(k_\beta r)^2} \tag{3.22}$$

where $L$ is the amplitude of the point force and where $R_{g0}$ and $Z_{g0}$ are the radial and vertical displacement respectively from a point on the surface at a distance $r$ to the source.

Given the small contribution of volumetric waves at large distances also for a point source, Lamb eventually proposed the Rayleigh wave expression as the solution to the far field of a point source, represented by the Eqs. (3.23) and (3.24).

$$R_{g0} = -\frac{\mathrm{i}\kappa LH}{\mu}\sqrt{\frac{1}{2\pi\kappa r}}\mathrm{e}^{-\mathrm{i}(\kappa r+\frac{\pi}{4})} \tag{3.23}$$

$$Z_{g0} = \frac{\kappa LK}{\mu}\sqrt{\frac{1}{2\pi\kappa r}}\mathrm{e}^{-\mathrm{i}(\kappa r+\frac{\pi}{4})} \tag{3.24}$$

The derivation of the Eqs. (3.21) and (3.22) come from the Eqs. (3.6) and (3.7), therefore they accumulate the approximation errors made for a line source, and adding others, such as that caused by steepest descent method. Here the term for Rayleigh waves is not the exact solution because it is also obtained from an approximation process for large $r$. As a conclusion:

- The Eqs. (3.21) and (3.22) are not adequate for the near field.
- The Eqs. (3.23) and (3.24) cannot be considered exact expressions of Rayleigh waves for short distances.

The exact solution for the Rayleigh waves can be calculated from residue theorem, obtaining

$$R_{g0} = \frac{\mathrm{i}\kappa LH}{2\mu}H_1^{(2)}(\kappa r) \tag{3.25}$$

$$Z_{g0} = -\frac{\mathrm{i}\kappa LK}{2\mu}H_0^{(2)}(\kappa r) \tag{3.26}$$

where $H_1^{(2)}(.)$, $H_0^{(2)}(.)$ are first-order and zeroth-order Hankel functions of the second kind, respectively. Later, Holzlöhner [88] worked with the integral Eqs. (3.19) and (3.20)

deriving some exact solutions (Eqs. (3.27) and (3.28)) that allow for an approachable numerical calculation for small $r$.

$$R_{g0} = \frac{L}{\mu r}\left[\frac{\mathrm{i}\bar{r}\kappa'}{2} H H_1^{(2)}(\mathrm{i}\bar{r}\kappa') + \right. \\ \left. + \frac{\mathrm{i}\bar{r}}{\pi}\int_h^1 \frac{k'^2(2k'^2-1)\sqrt{k'^2-h^2}\sqrt{1-k'^2}}{(2k'^2-1)^4+16(k'^2-h^2)(1-k'^2)k'^4} H_1^{(2)}(\bar{r}k')\mathrm{d}k'\right] \tag{3.27}$$

$$Z_{g0} = \frac{L}{\mu r}\left[2\int_0^h \frac{\sqrt{h^2-k'^2}}{(2k'^2-1)^2+4k'^2\sqrt{h^2-k'^2}\sqrt{1-k'^2}}\Phi(\bar{r}k')\mathrm{d}k' + \right. \\ + 8\int_h^1 \frac{(k'^2-h^2)k'^2\sqrt{1-k'^2}}{(2k'^2-1)^4+16(k'^2-h2)(1-k'^2)k'^4}\Phi(\bar{r}k')\mathrm{d}k' + \\ \left. + \frac{2\pi(2\kappa'^2-1)^2\sqrt{\kappa'^2-h^2}}{8\kappa'[1-(6-4h^2)\kappa'^2+6(1-h^2)\kappa'^4]}\Phi(\bar{r}k')\right] \tag{3.28}$$

where the variables $k'$ $\kappa'$ i $\bar{r}$ relate to the Lamb variables $k$, $\kappa$, $r$ according to

$$k' = \frac{k}{k_\beta} \qquad \kappa' = \frac{\kappa}{k_\beta} \qquad \bar{r} = rk_\beta$$

and where $h = (1-2\nu)/(2-2\nu)$ and $\Phi(\bar{r}\kappa')$ is a power series that can be found at [88] or [89].

Both the direct numerical integration of the exact Eqs. (3.19) and (3.20) [188] and the expressions proposed by Holzlöhner (Eqs. (3.27) and (3.28)) allow, a priori, to carry out an exact calculation of propagation for the point source. The differences between the two methods basically lie in the calculation time and in the range of distances numerically approachables. Lamé's constants are also reconverted into complex constants according to the correspondence principle, from the Eqs. (3.17) and (3.18).

### 3.1.3 Numerical solution

In order to calculate all the exact solutions for both cases, line and point sources, numerical integration along the real axis of the integrals appearing in Eqs. (3.1), (3.2), (3.19), (3.20), (3.27) and (3.28) is necessary. This numerical integration is unapproachable for the case of a completely elastic and homogeneous half-space, because the Rayleigh root resides always in the real axis. But the incorporation of damping to Lamb's propagation

model means that neither of the poles of Rayleigh function, nor the branch points $k_\alpha$ and $k_\beta$, reside in the real axis [80]. Thus, the integrands of Lamb's expressions, both for a point and line sources, are not discontinuous along the real axis, since it does not contain poles or traverse branch cuts, and therefore numerical integration can be carried out avoiding singularities [126].

On the other hand, integrals that appear in Lamb's exact solutions have an important problem related with the computational evaluation cost of their numerical integration: Their integrands have a high oscillatory behaviour which can cause huge increments in the computational cost of their numerical integration, if more specific methods are not used [106, 124–126]. This problem is more significant in the evaluation of the ground response at large distances from the source, because the oscillations become more dense, but it still remains significantly at short distances.

In this thesis, the approach presented in the work of Luco and Apsel [106, 126] is adopted to reduce the high calculation time generated by this oscillatory behaviour of the integrands. In Appendix A this approach is described and the static integrands and integrals needed for its implementation are derived.

The application of this method for the case of infinite line source solutions (Eqs. (3.1), (3.2)) results in

$$X_{g0} = \frac{\mathrm{i}Q}{2\pi\mu}\left[-\frac{\pi\mathrm{i}\beta^2}{2(\beta^2-\alpha^2)}+ \right. \\ \left. + \int_{-k_{lim}}^{+k_{lim}} \left[\frac{k(2k^2-k_\beta^2-2\upsilon\upsilon')}{(2k^2-k_\beta^2)^2-4k^2\upsilon\upsilon'} - \frac{\beta^2}{2k(\beta^2-\alpha^2)}\right] \mathrm{e}^{-\mathrm{i}kx}\mathrm{d}k\right] \tag{3.29}$$

$$Z_{g0} = -\frac{Q}{2\pi\mu}\left[-\frac{\pi\mathrm{i}\alpha^2}{2(\beta^2-\alpha^2)}+ \right. \\ \left. + \int_{-k_{lim}}^{+k_{lim}} \left[\frac{k_\beta^2\upsilon}{(2k^2-k_\beta^2)^2-4k^2\upsilon\upsilon'} - \frac{\alpha^2}{2k(\beta^2-\alpha^2)}\right] \mathrm{e}^{-\mathrm{i}kx}\mathrm{d}k\right] \tag{3.30}$$

This new integrands tends to $+\infty$ approaching to zero from the right and to $-\infty$ from the left. To avoid this problem the following new expressions are proposed:

$$X_{g0} = \frac{\mathrm{i}Q}{2\pi\mu}\left[-\frac{\pi\mathrm{i}\beta^2}{2(\beta^2-\alpha^2)} - \right. \\ \left. - 2\int_0^{k_{lim}}\left[\frac{k(2k^2-k_\beta^2-2\upsilon\upsilon')}{(2k^2-k_\beta^2)^2-4k^2\upsilon\upsilon'} - \frac{\beta^2}{2k(\beta^2-\alpha^2)}\right]\mathrm{i}\sin(kx)\mathrm{d}k\right] \tag{3.31}$$

$$Z_{g0} = -\frac{Q}{2\pi\mu}\left[-\frac{\pi\mathrm{i}\alpha^2}{2(\beta^2-\alpha^2)} + \right. \\ \left. + \int_0^{k_{lim}}\left[2\left[\frac{k_\beta^2\upsilon}{(2k^2-k_\beta^2)^2-4k^2\upsilon\upsilon'}\right]\cos(kx) + \left[\frac{\alpha^2}{k(\beta^2-\alpha^2)}\right]\mathrm{i}\sin(kx)\right]\mathrm{d}k\right] \tag{3.32}$$

For the case of point source (Eqs. (3.19), (3.20)) the application of this technique results in

$$R_{g0} = \frac{L}{2\pi\mu}\left[\frac{\beta^2}{2r(\beta^2-\alpha^2)} + \right. \\ \left. + \int_0^{k_{lim}}\left[\frac{k^2(2k^2-k_\beta^2-2\upsilon\upsilon')}{(2k^2-k_\beta^2)^2-4k^2\upsilon\upsilon'} - \frac{\beta^2}{2(\beta^2-\alpha^2)}\right]J_1(kr)\mathrm{d}k\right] \tag{3.33}$$

$$Z_{g0} = -\frac{L}{2\pi\mu}\left[\frac{\alpha^2}{2r(\beta^2-\alpha^2)} + \right. \\ \left. + \int_0^{k_{lim}}\left[\frac{k\upsilon k_\beta^2}{(2k^2-k_\beta^2)^2-4k^2\upsilon\upsilon'} - \frac{\alpha^2}{2(\beta^2-\alpha^2)}\right]J_0(kr)\mathrm{d}k\right] \tag{3.34}$$

where $k_{lim}$ is a truncated limit of integration. Since the oscillatory behaviour disappears almost entirely in the integrands of Eqs. (3.31), (3.32), (3.33) and (3.34) the limits of integration can be truncated at a certain value, called $k_{lim}$, without loss of accuracy. This truncated limit of integration must be calculated for each integral to ensure that

$$\int_{-k_{lim}}^{k_{lim}} \gg \int_{-\infty}^{-k_{lim}} + \int_{k_{lim}}^{\infty} \qquad \text{or} \qquad \int_0^{k_{lim}} \gg \int_{k_{lim}}^{\infty} \tag{3.35}$$

Finally, the Gauss-Kronrod quadrature are used to estimate the integrals by a numerical integration. This quadrature minimises Gauss's integration error with very little additional computational cost [129]. The algorithm used to implement this numerical

integration is `quadgk`, that is provided by MATLAB. This algorithm is chosen because it provides a good accuracy but it is not the best solution with respect to the computational efficiency: fastest integration methods must be used when this model will be implemented in a real computational algorithm (it can be seen a review of this methods in Section 2.2.7).

For the case of a infinite line source, Eqs. (3.31), (3.32) are used in the following section to estimate the displacements exact solution. For the case of a point source, Holzlöhner's solution is chosen for the radial displacement (Eq. (3.27)), and Eq. (3.34) is chosen for the vertical displacement. In the case of radial displacement Holzlöhner's expression provides better computational efficiency; however, in the case of vertical displacement Holzlöhner's expression (Eq. (3.28)) is computationally inefficient at relatively large distances due to the large amount of significant terms in the power series $\Phi(\bar{r}\kappa')$.

### 3.1.4 Near field determination procedure

Having defined the expressions that characterise the near field (exact solutions) and the far field (Rayleigh wave solutions), it is necessary to apply a methodology to relate them, in order to determine the near field distance.

Specifically in the case of a line source, the near field region is extracted from the comparison of the solution of Rayleigh waves $X_{g0\,\text{Rayleigh}}$ and $Z_{g0\,\text{Rayleigh}}$ (Eqs. (3.15) and (3.16)) and the exact solution $X_{g0\,\text{Exact}}$ and $Z_{g0\,\text{Exact}}$ (Eqs. (3.31) and (3.32)), using the factors $M_X^{\text{Line}}$ and $M_Z^{\text{Line}}$ described as

$$M_X^{\text{Line}} = 20\log\left(\frac{X_{g0\,\text{Rayleigh}}}{X_{g0\,\text{Exact}}}\right) \qquad M_Z^{\text{Line}} = 20\log\left(\frac{Z_{g0\,\text{Rayleigh}}}{Z_{g0\,\text{Exact}}}\right) \tag{3.36}$$

which give the difference in dB between Rayleigh's solution and the exact one for every distance. Thus, it is simple to find the distance from which both $\left|M_X^{\text{Line}}\right|$ and $\left|M_Z^{\text{Line}}\right|$ remain under a limit $M_{\text{nfd}}$, which defines the bearable error (e.g. 2 dB). This distance will be directly the near field distance, because for higher distances the only use of Rayleigh waves will produce an error under $M_{\text{nfd}}$.

In the case of a point source the following factors are defined

$$M_R^{\text{Point}} = 20\log\left(\frac{R_{g0\,\text{Rayleigh}}}{R_{g0\,\text{Exact}}}\right) \qquad M_Z^{\text{Point}} = 20\log\left(\frac{Z_{g0\,\text{Rayleigh}}}{Z_{g0\,\text{Exact}}}\right) \tag{3.37}$$

which define the difference in dB between the exact Rayleigh solutions (Eqs. (3.25) and (3.26)) and the exact solutions (Eqs. (3.27) and (3.33)).

## 3.2 Results

In this section the results of the determination of near field distance are shown for the two types of source presented. Results are shown as a function of normalised adimensional distances Eq. (3.38); $x_{\text{norm}}$ for a line source and $r_{\text{norm}}$ for a point source

$$x_{\text{norm}} = \frac{x}{\lambda_{\text{Rayleigh}}} \qquad r_{\text{norm}} = \frac{r}{\lambda_{\text{Rayleigh}}} \tag{3.38}$$

where $\lambda_{\text{Rayleigh}}$ is the wavelength of the Rayleigh waves.

### 3.2.1 Results for an infinite line source

The factors $M_X^{\text{Line}}$ and $M_Z^{\text{Line}}$, which allow to quantify the near field, depend a priori on the mechanical properties of the ground (Young's modulus $E$, density $\rho$, Poisson's ratio $\nu$, damping of P-waves $D_P$ and damping of S-waves $D_S$) and on the source (force amplitude $Q$ and excitation's angular frequency $\omega$). With regard to the load $Q$, both the Rayleigh wave expressions Eqs. (3.15) and (3.16) and the exact ones Eqs. (3.1) and (3.2) depend linearly on $Q$. Therefore this variable does not affect factors $M_X^{\text{Line}}$ and $M_Z^{\text{Line}}$.

The use of the adimensional distance $x_{\text{norm}}$ eliminates the dependence of factors $M_X^{\text{Line}}$ and $M_Z^{\text{Line}}$ with respect to frequency, Young's modulus and density, as is exemplified in Figs. 3.1 and 3.2 for the case of Young's modulus. The plots of the factors $M_X^{\text{Line}}$ and $M_Z^{\text{Line}}$ as a function of the adimensional distance and the frequency or the density are omitted since they are practically equal to these.

Figs. 3.1 and 3.2 are obtained using mechanical properties of a quaternary ground type of the Table 3.1 and ranging the Young's modulus between 10 and 5000 MPa. In this case the near field adimensional distances are 5.71 and 0.27, for the horizontal and vertical displacement respectively, for any Young's modulus in this range and for $M_{\text{nfd}} = 2$ dB.

On the other hand, there does exist a dependence of factors $M_X^{\text{Line}}(x_{\text{norm}})$ and $M_Z^{\text{Line}}(x_{\text{norm}})$ with respect to the other variables: $\nu$, $D_P$, $D_S$. Figs. 3.3 and 3.4 show how they modify factors $M_X^{\text{Line}}$ and $M_Z^{\text{Line}}$, estimated at $x_{\text{norm}} = 1$ and $x_{\text{norm}} = 1.5$, with respect to damping $D_P$ and $D_S$ and for different $\nu$ values. These distances $x_{\text{norm}}$ are chosen for the calculation of these planes because they coincide approximately with the first relative maximum, in the case of vertical displacement, and with the first relative minimum, in the case of horizontal displacement, of the functions $M_X^{\text{Line}}(x_{\text{norm}})$ and $M_Z^{\text{Line}}(x_{\text{norm}})$.

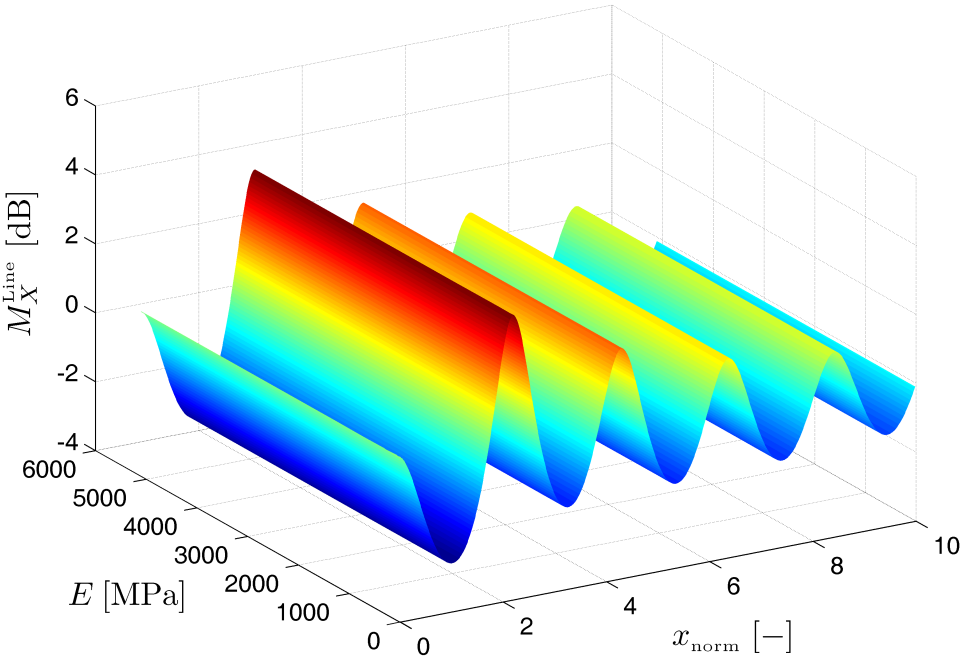


FIGURE 3.1: Variation of factor $M_X^{\text{Line}}$ with respect to adimensional distance $x_{\text{norm}}$ and Young's modulus.

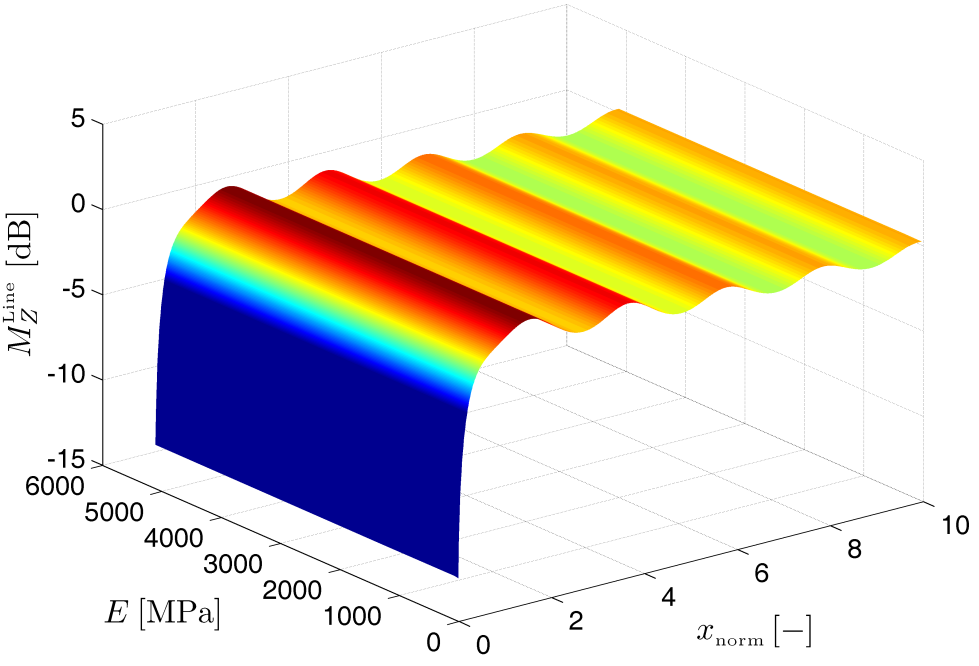


FIGURE 3.2: Variation of factor $M_Z^{\text{Line}}$ with respect to adimensional distance $x_{\text{norm}}$ and Young's modulus.

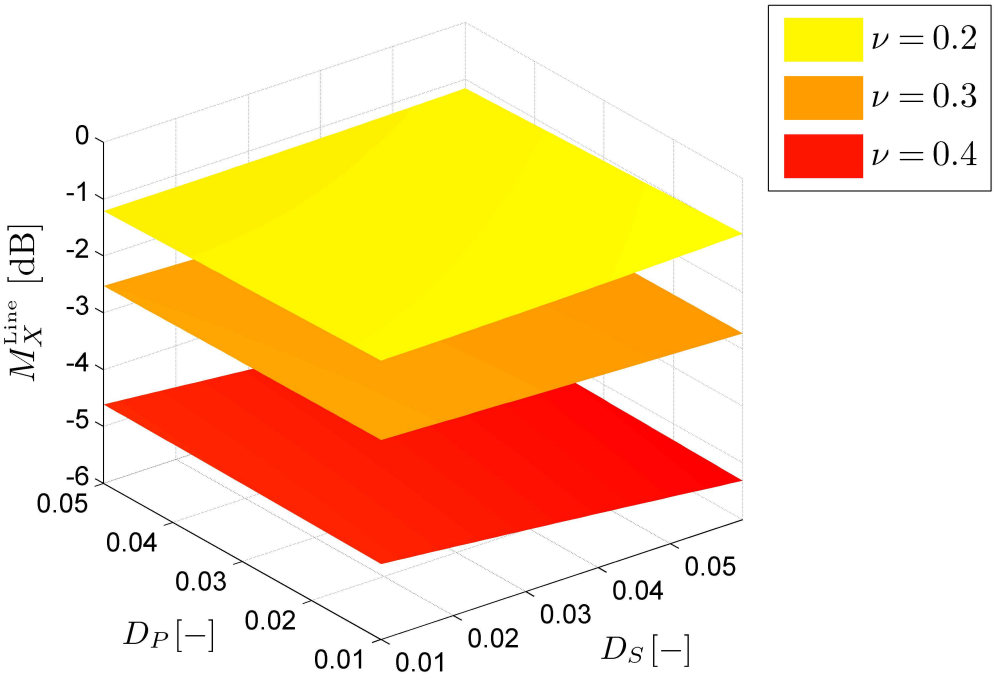


FIGURE 3.3: Variation of factor $M_X^{\text{Line}}$, estimated at $x_{\text{norm}} = 1$, with respect to the dampings $D_P$ and $D_S$ and for different Poisson's ratios.

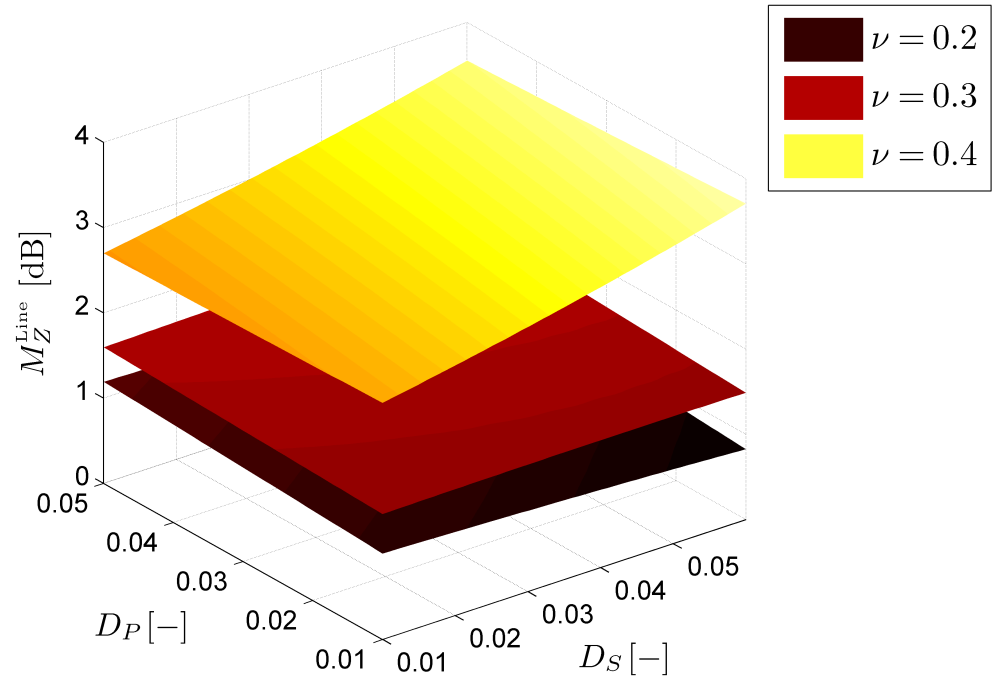


FIGURE 3.4: Variation of factor $M_Z^{\text{Line}}$, estimated at $x_{\text{norm}} = 1.5$, with respect to the dampings $D_P$ and $D_S$ and for different Poisson's ratios.

Figs. 3.3 and 3.4 are also obtained using mechanical properties of a quaternary ground type of the Table 3.1, ranging dampings $D_P$ and $D_S$ between 0.01 and 0.05, and between 0.01 and 0.06 respectively, and for three different Poisson's ratios: 0.2, 0.3 and 0.4. In these cases the near field adimensional distances range, in general, between 0-7.76 and 0.22-5.3 for the horizontal and vertical displacement respectively and for $M_{\text{nfd}} = 2$ dB. However, for some particular $D_P$ and $D_S$ combinations, factors $M_X^{\text{Line}}$ and $M_Z^{\text{Line}}$ do not clearly decrease with the adimensional distance. So, it is mandatory to calculate any particular case.

As can be seen in Figs. 3.3 and 3.4, for the same Poisson's ratio the dependence of factors $M_X^{\text{Line}}$ and $M_Z^{\text{Line}}$ with respect to the damping can be represented approximately, for both displacements, with very horizontal planes, which tilt slightly as the Poisson's ratio increases. When carrying out this procedure for other adimensionals $x_{\text{norm}}$ distances, qualitatively similar results are obtained. Therefore it is deduced that, in general, the effect of damping is not very significant.

With regard to the Poisson's ratio, a much higher incidence of this variable on factors $M_X^{\text{Line}}$ and $M_Z^{\text{Line}}$ is observed. Specifically it is seen that the increase of the value of this property causes an increment of these factors and this means that the near field distance increases significantly.

### 3.2.2 Results for a point source

Following the same procedure as in the previous section, it is also demonstrated that the use of an adimensional distance, in this case $r_{\text{norm}}$, entails the non-dependence on the results with respect to Young's modulus, density and frequency. This is exemplified in Fig. 3.5 for the specific case of frequency, radial displacement and point source.

The Fig. 3.5 is obtained using mechanical properties of a quaternary ground type of the Table 3.1 and ranging the frequency between 10 Hz and 100 Hz. In this case the near field adimensional distances are 4.14 and 0.33, for the horizontal and vertical displacement respectively and for $M_{\text{nfd}} = 2$ dB. As can be inferred from Eq. (3.38), the near field distance have a linear dependence with frequency for a specific ground kind.

In reference to the effect of the Poisson's ratio and the two dampings, Fig. 3.6 shows how the tendency is approximately the same as observed with an infinite line source. The variable with the most significant incidence is once again the Poisson's ratio.

The Fig. 3.6 is also obtained using mechanical properties of a quaternary ground type of the Table 3.1, ranging dampings $D_P$ and $D_S$ between 0.01 and 0.05, and between 0.01 and 0.06 respectively, and for three different Poisson's ratios: 0.2, 0.3 and 0.4. In

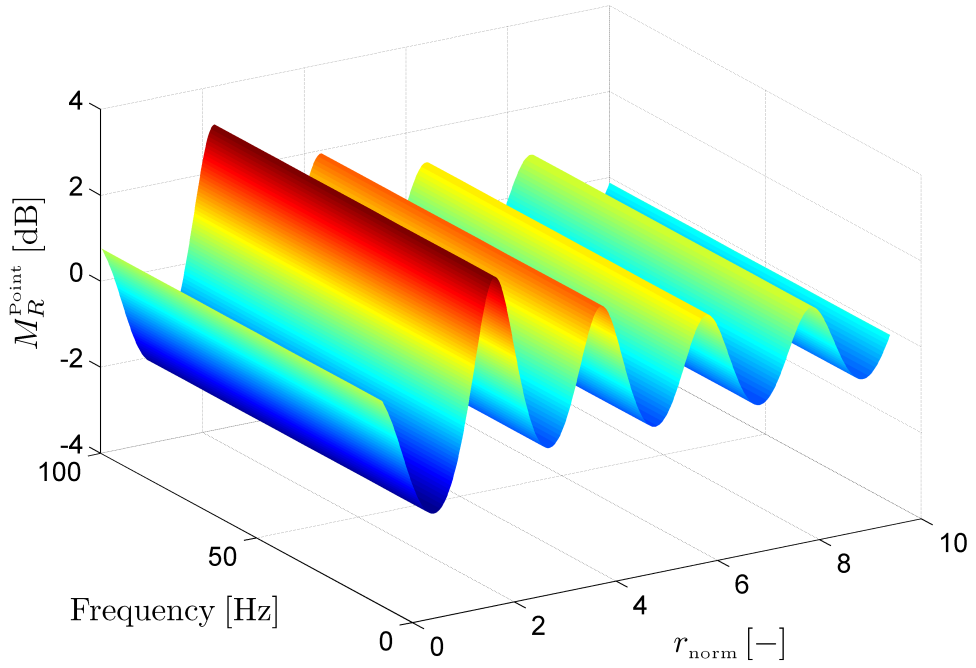


FIGURE 3.5: Variation of factor $M_R^{\text{Point}}$ with respect to the adimensional distance $r_{\text{norm}}$ and frequency.

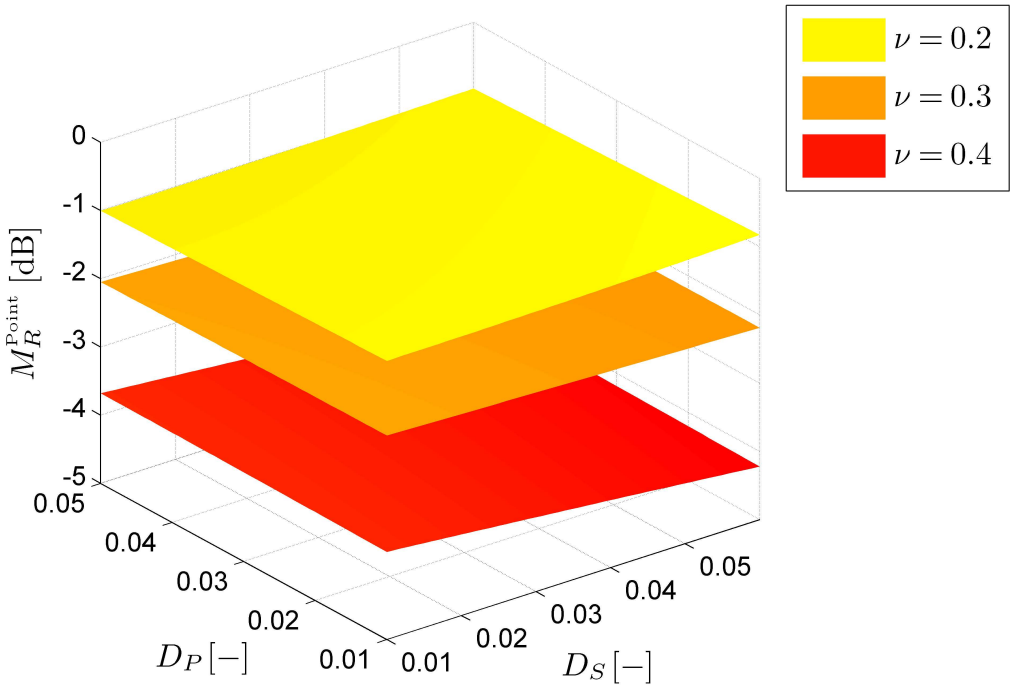


FIGURE 3.6: Variation of factor $M_R^{\text{Point}}$, estimated at $r_{\text{norm}} = 1$, with respect to the dampings $D_P$ and $D_S$ and for different Poisson's ratios.

these cases the near field adimensional distances range, in general, between 0-6.26 and 0.28-3.81, for the horizontal and vertical displacement respectively and for $M_{\text{nfd}} = 2$ dB.

If the factors $M_R^{\text{Point}}$ and $M_Z^{\text{Point}}$ are calculated with the approximate expressions of Rayleigh waves (Eqs. (3.23) and (3.24)) for different coefficients of significant ground properties ($\nu$, $D_P$, $D_S$), practically identical results are obtained for $r_{\text{norm}} > 1$. This fact is shown in Fig. 3.7, where only the case of radial displacement is shown, since it is better to observe the differences between the two solutions. Therefore, the differences between the complete solution and the exact Rayleigh wave solution decrease much more slowly than the differences between the approximate solution and the exact one for these waves. So, the near field distance is not affected in general (values of $M_{\text{nfd}} \leq 2$ dB) by the use of either the exact or the approximate solutions.

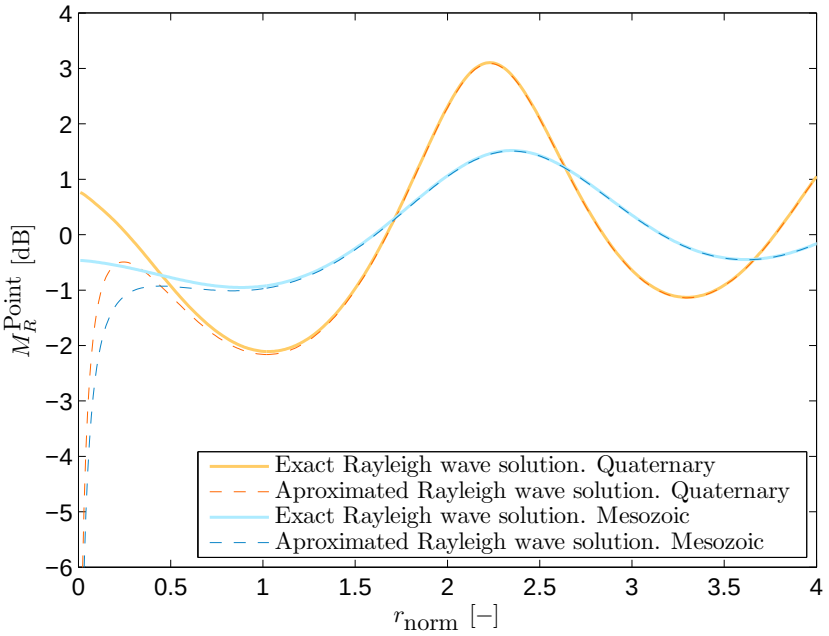


FIGURE 3.7: Variation of factor $M_R^{\text{Point}}$, from the exact and approximated Rayleigh wave solution for quaternary and mesozoic ground types (see Table 3.1).

### 3.2.3 Calculation example on real grounds

The method for calculating the near field distance is applied to five significantly different ground types, typical of the Barcelona (Spain) metropolitan area. The properties of these ground types can be found in Table 3.1. They have been determined by geotechnical tests carried out by GISA (Department of public works of Generalitat de Catalunya).

The results obtained, in the form of factors $M_X^{\text{Line}}(x_{\text{norm}})$, $M_Z^{\text{Line}}(x_{\text{norm}})$, $M_R^{\text{Point}}(r_{\text{norm}})$ and $M_Z^{\text{Point}}(r_{\text{norm}})$, are shown in Figs. 3.8, 3.9, 3.10 and 3.11. They show the small

| Ground | $\rho\,[\mathrm{kg/m^3}]$ | $E$[MPa] | $\nu[-]$ | $D_P[-]$ | $D_S[-]$ |
|---|---|---|---|---|---|
| Quaternary | 1950 | 20 | 0.3 | 0.04 | 0.03 |
| Tertiary | 2100 | 90 | 0.3 | 0.028 | 0.02 |
| Paleozoic | 2500 | 1500 | 0.2 | 0.017 | 0.01 |
| Mesozoic | 2500 | 350 | 0.3 | 0.025 | 0.015 |
| Igneous Rocks | 2500 | 4000 | 0.3 | 0.017 | 0.01 |

TABLE 3.1: Mechanical properties of five ground types in the Barcelona (Spain) metropolitan area. Source: GISA (Department of public works of Generalitat de Catalunya).

incidence of the variations in damping of P-waves or S-waves. They also show how the reduction in Poisson's ratio has a significant lowering effect in factors $M_X^{\mathrm{Line}}$, $M_Z^{\mathrm{Line}}$, $M_R^{\mathrm{Point}}$ and $M_Z^{\mathrm{Point}}$.

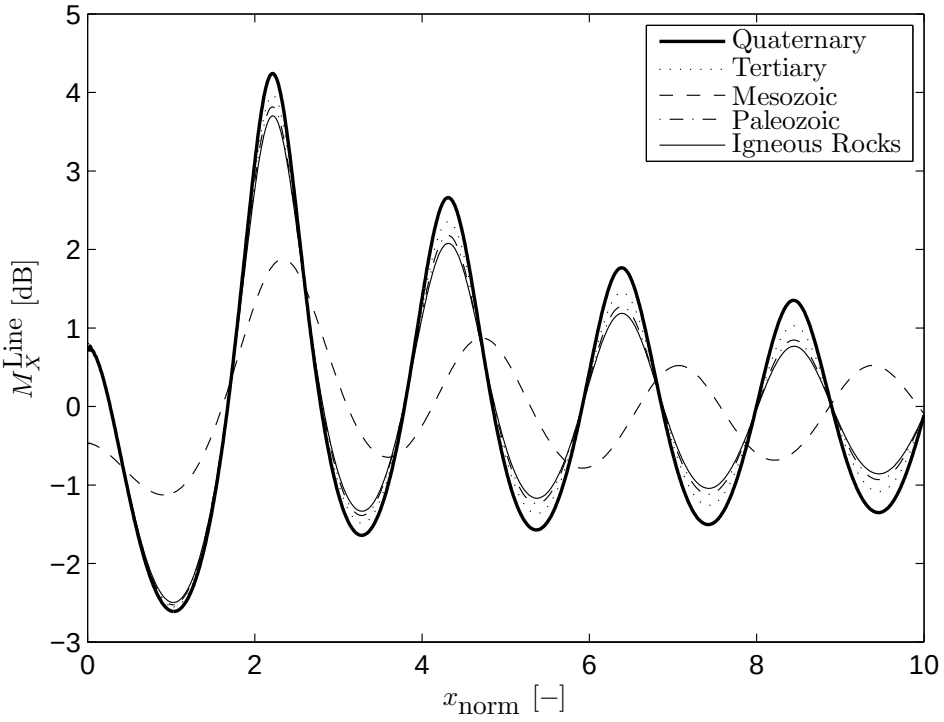


FIGURE 3.8: Variation in factor $M_X^{\mathrm{Line}}$ with respect to the adimensional distance $x_{\mathrm{norm}}$ for the different ground types. Line source case.

In order to calculate the near field distance for these five ground types a $M_{\mathrm{nfd}}$ factor of 2 dB is fixed. It is also assumed in all cases that the harmonic excitation load oscillates at a frequency of 30 Hz: many authors have found from large amount of experimental measurements, that the significant frequency range excited by train infrastructures is between 30 and 250 Hz [16, 25–32]. Therefore, if the near field distance is calculated at the minimum frequency of the range it ensures that this distance will always be above the one calculated at any other frequency within the range.

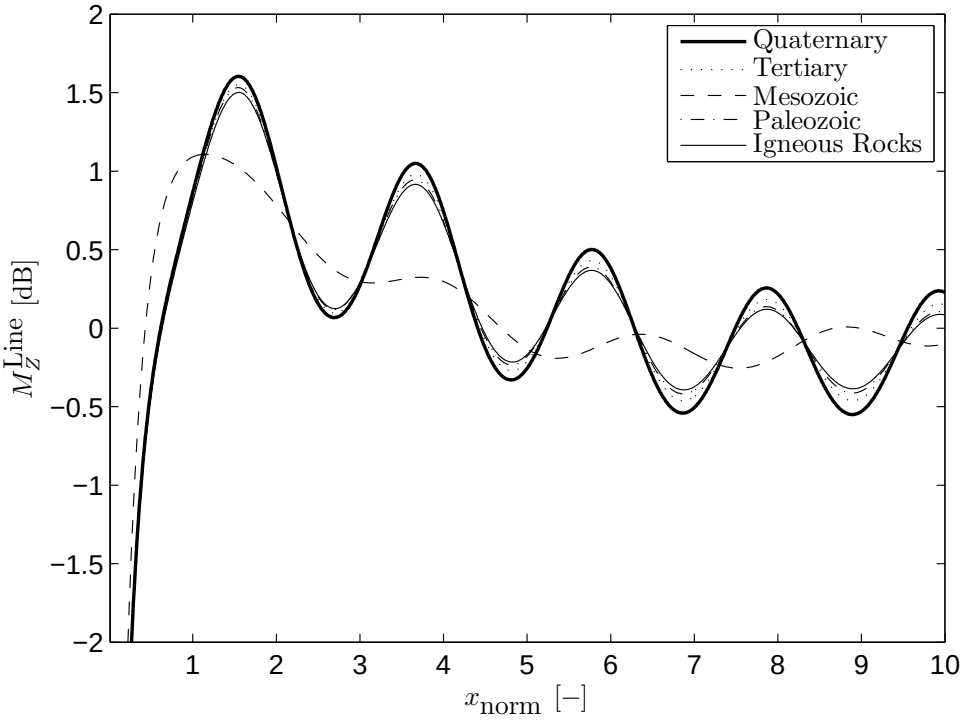


FIGURE 3.9: Variation in factor $M_Z^{\text{Line}}$ with respect to the adimensional distance $x_{\text{norm}}$ for the different ground types. Line source case.

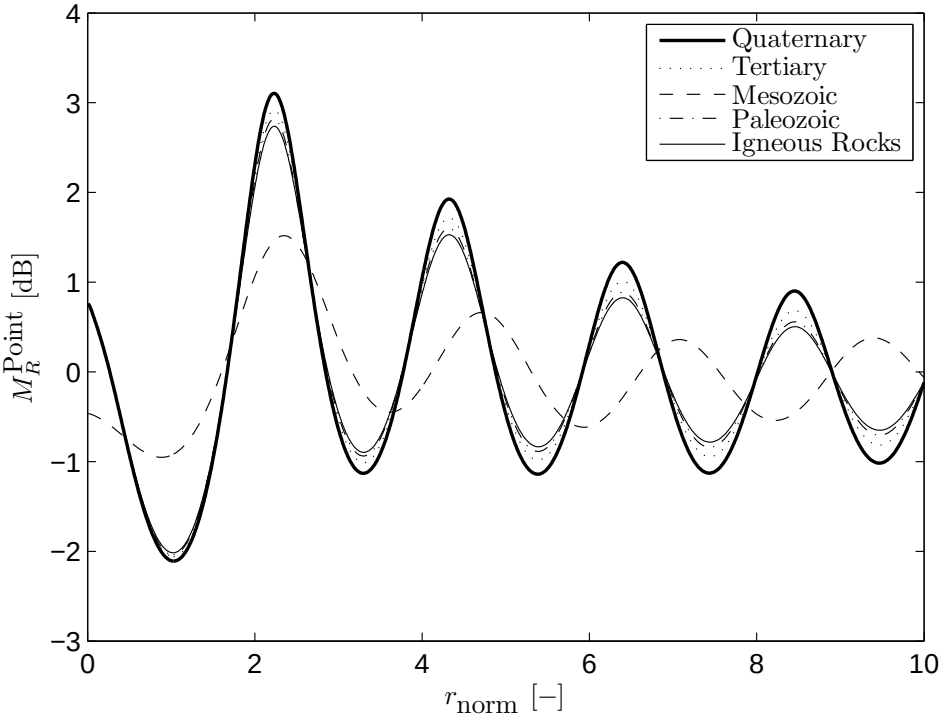


FIGURE 3.10: Variation in factor $M_R^{\text{Point}}$ with respect to the adimensional distance $x_{\text{norm}}$ for the different ground types. Point source case.

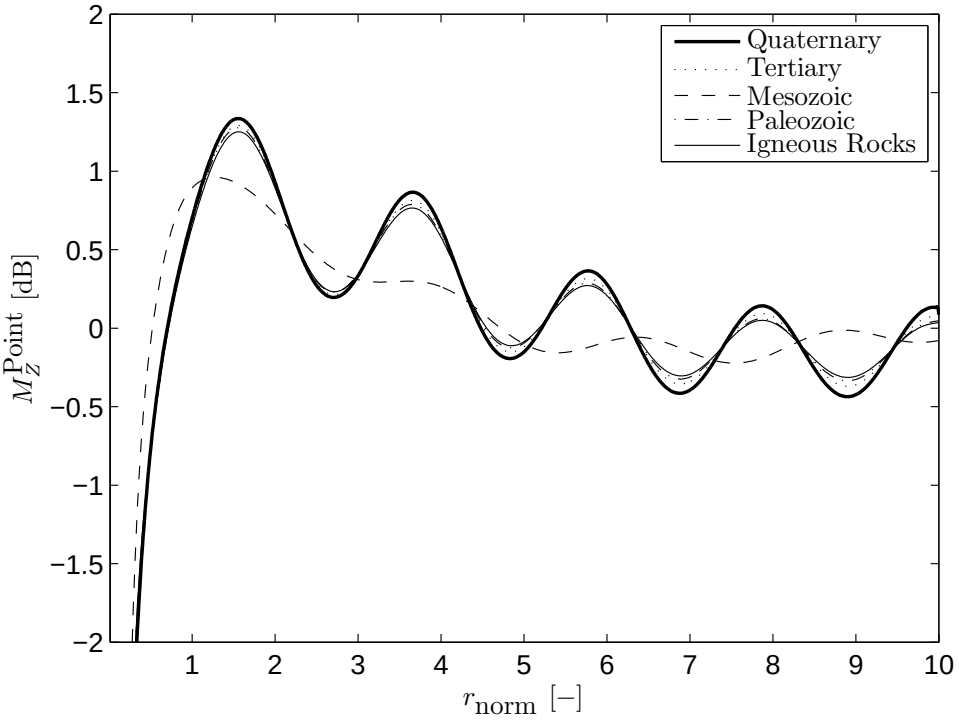


FIGURE 3.11: Variation in factor $M_Z^{\text{Point}}$ with respect to the adimensional distance $x_{\text{norm}}$ for the different ground types. Point source case.

The results of near field distances for the grounds in Table 3.1 are shown in Tables 3.2 and 3.3. These results are calculated by upper-bounding the relative maximums of the factors $\left|M_X^{\text{Line}}\right|$, $\left|M_Z^{\text{Line}}\right|$, $\left|M_R^{\text{Point}}\right|$ and $\left|M_Z^{\text{Point}}\right|$ with exponential curves.

| Near field distance [m] | | |
|---|---|---|
| Ground | Respect to $X_{g0}$ | Respect to $Z_{g0}$ |
| Quaternary | 11.1 | 0.52 |
| Tertiary | 19.8 | 1.07 |
| Mesozoic | 29.7 | 3.4 |
| Paleozoic | 33.2 | 1.94 |
| Igneous Rocks | 107.9 | 6.58 |

TABLE 3.2: Near field distances for the five ground types and for the line source case.

It can be observed how the horizontal component is the most restrictive with respect to near field distance, for a line source as well as for a point source. It can also be observed that when the soils under study are harder and/or have higher Poisson's ratios this distance increase as well. In fact there is a proportional relation between the wavelength of the Rayleigh waves and factors $M_X^{\text{Line}}$ and $M_Z^{\text{Line}}$ or $M_R^{\text{Point}}$ and $M_Z^{\text{Point}}$, as has been previously demonstrated.

| Near field distance [m] | | |
|---|---|---|
| Ground | Respect to $R_{g0}$ | Respect to $Z_{g0}$ |
| Quaternary | 8.05 | 0.65 |
| Tertiary | 14.6 | 1.31 |
| Mesozoic | 22.8 | 4.21 |
| Paleozoic | 24.9 | 2.29 |
| Igneous Rocks | 80.8 | 7.69 |

TABLE 3.3: Near field distances for the five ground types and for the point source case.

The comparison of results between line source and point source leads to assert that the similarities between them are more than noteworthy. Figs. 3.8, 3.9, 3.10 and 3.11 show an absolute similarity between the results of the two source types, since the wavelengths are exactly the same for a specific ground. The differences are only in the amplitudes of the oscillations, which vary slightly from one case to another due to the different values of geometric attenuation of the waves for the two source types. A infinite line source always has a higher near field distance than a point source,

In order to estimate the near field distance for a train source, it is proposed to use the results of an infinite line source and point source calculated according to the methodology explained in this study and taking the worst case, i.e., the maximum distance. As can be seen in Tables 3.2 and 3.3, the near field distance linked to the horizontal displacement and to the infinite line source is this maximum distance. Only the choice of very small $M_{\text{nfd}}$ factors can distort this trend.

In view of the results obtained, it is feasible to take measurements of Rayleigh waves that are not significantly polluted by volumetric waves when the ground under study is soft enough. The near field distance obtained in this case is close enough the source to ensure significant wave amplitude with respect to the background noise. Therefore, far field propagation models based on Rayleigh wave propagation have a great applicability in soft grounds.

On the other hand, for grounds with high stiffness and/or with high Poisson's ratios great dimensions of the near field region are expected. Thus, for this kind of grounds, it is necessary to take into account the volumetric waves in the ground-borne model.

## 3.3 Conclusions

The methodology presented in this chapter allows for the determination of the dimensions of the interference region between surface waves and volumetric waves; the so-called near field region. This is calculated for a point source as well as an infinite line source. It

is proposed to use these results for the determination of the near field distance of a train source. The ground has been modelled as an homogeneous and viscoelastic half-space.

The results show that the near field distance grows basically with the wavelength of the Rayleigh waves and with the Poisson's ratio, with the effect of other ground parameters not being very significant. Therefore, for grounds that are not excessively consolidated or grounds with low Poisson's ratios, the near field distances are small, a fact that makes viable the use an amplitude of reference not contaminated by volumetric waves with the objective to feed semi-analytical propagation models. For example, for 30 Hz and for the specific quaternary and tertiary grounds taken in this study, the near field distances do not exceed 20 m, taking the solution as the worst case between line and point sources. Otherwise, for very stiff grounds the near field distances can exceed 100 m, forcing to take into account the volumetric waves in any propagation model.

This work is summarised in a recently published article in Soil Dynamics and Earthquake Engineering journal [189].

# Chapter 4

# Superstructure model

This chapter presents a model of railway superstructure coupled with its subgrade and with the rolling stock, assuming the track to be a 2-layer continuous support model, the subgrade as a viscoelastic and homogeneous half-space and the rolling stock as a 1DOF model. As in the previous chapter, the homogeneous ground model is selected in order to reduce the time/economical costs of the model application. This vehicle/superstructure/subgrade model allows for the determination of the wheel/rail dynamical contact force, which is the first step in a complete generation/propagation model for preliminary assessment studies. Using this model, the effects of the subgrade on the response of the superstructure and on the dynamics of the wheel/rail contact during the passage of one wheel are investigated with the aim of simplifying the model if this influence is not significant. Specifically, the effects of the subgrade are observed on track receptances, on the wheel/rail contact force and on the vertical accelerations of the wheel and the rail. The model focuses in at-grade mid-speed trains (metropolitan and regional rail network) and for a ballasted superstructure, but it may be used in other cases by introducing small modifications.

## 4.1 Superstructure model definition

The superstructure is modelled as a 2-layer continuous support model, with the following hypothesis:

- Throughout superstructure system, with the exception of the subgrade, only vertical motion is considered.
- The rail is modelled as a Bernoulli-Euler beam, since this is a good model for frequencies below 500 Hz [20]. As can be seen in Section 2.1.1, with regard to the evaluation of vibrations generated by a train pass-by a significant frequency range can be 20 to 80 Hz. Therefore, this beam model of the rail is adequate in this case.
- The dynamic coupling between rails through the sleepers is not considered, as proposed by Thompson [38, 39].
- The normal stress between sleepers and the ground is considered as a continuous function along the rail longitudinal direction and as a rectangular step function along the rail transverse direction [49].
- Shear stresses between sleepers and the ground are not considered, as was demonstrated by Metrikine and Dieterman [50].
- Stiffnesses, viscous dampings and sleeper mass are uniformly distributed parameters along the track.

In Fig. 4.1 a representation of the adopted superstructure model can be observed, where $z_r$, $z_s$, $z_{g0}^{(0)}$ represent the rail, sleepers and subgrade surface vertical displacements (at $y = 0$ and $z = 0$: see Fig. 4.3) respectively. On the other hand $k_F$, $k_B$, $c_F$, $c_B$, are fasteners and ballast stiffnesses and viscous dampings, respectively. Given the complexity of ballast and fasteners dampings, it has been decided to include in the model both structural damping and viscous damping, in order to allow for better system modeling.

As can be seen, for example, in [78], the expression that governs the rail vertical displacement $z_r$, for this adopted model, due to the propagation of bending waves on it is

$$EI\frac{\partial^4 z_r}{\partial x^4} + \rho S\frac{\partial^2 z_r}{\partial t^2} + f(x,t) = q(x,t) \tag{4.1}$$

where $E$ is the Young's modulus of the rail, $I$ is the second moment of area, $\rho$ is the rail density and $S$ is the cross-sectional area. As can be seen in Fig. 4.2, $f(x,t)$ represents

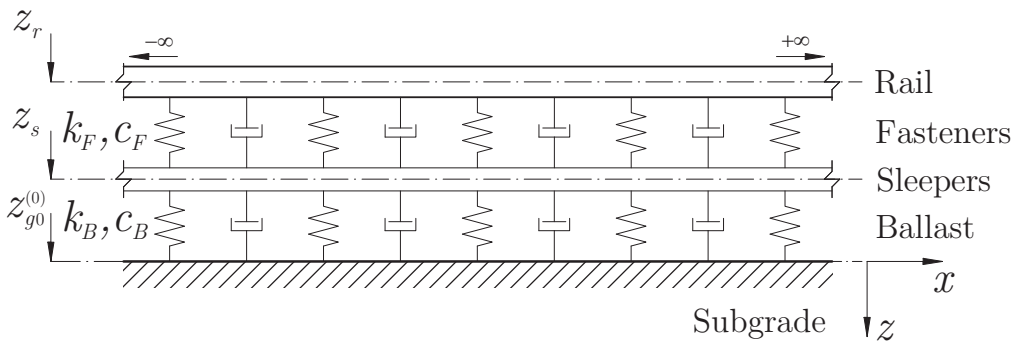


FIGURE 4.1: Adopted track model: 2-layer continuous support model with subgrade coupling.

the distributed force due to sleepers and $q(x,t)$ represents the distributed force due to wheel/rail contact dynamic excitation.

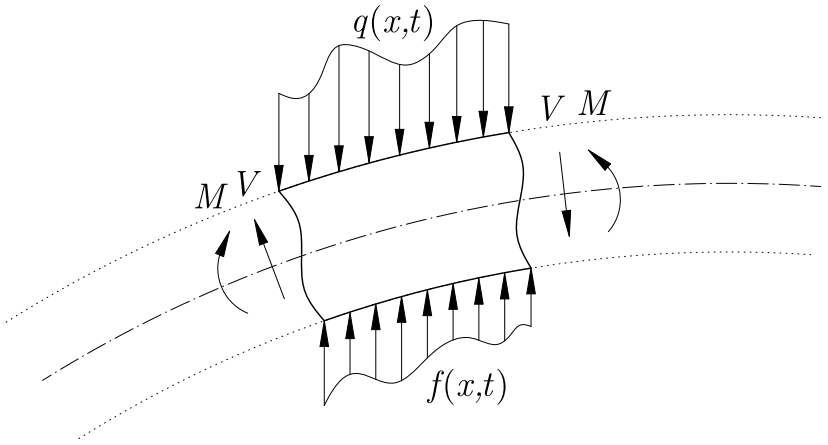


FIGURE 4.2: Free body diagram of a beam slice, in which no body force has been considered.

As can be inferred from Fig. 4.1, the distributed force due to sleepers is

$$f(x,t) = k_F(z_r - z_s) + c_F(\dot{z}_r - \dot{z}_s) \tag{4.2}$$

The equation of the motion of sleepers is

$$k_F(z_r - z_s) + c_F(\dot{z}_r - \dot{z}_s) - k_B(z_s - z_{g0}^{(0)}) - c_B(\dot{z}_s - \dot{z}_{g0}^{(0)}) = m_s\ddot{z}_s \tag{4.3}$$

where $m_s$ is the sleepers mass. They exert a force on the ground, called the superstructure/subgrade coupling force, given by

$$f_g(x,t) = k_B(z_s - z_{g0}^{(0)}) + c_B(\dot{z}_s - \dot{z}_{g0}^{(0)}) \tag{4.4}$$

The structural damping is defined with the loss coefficients $\eta_r$, $\eta_F$ and $\eta_B$, which are linked to the rail, the fasteners, and the ballast respectively. This is introduced into the previous governing equations (Eqs. (4.1), (4.2), (4.3) and (4.4)) by the expressions

$$E = \tilde{E}(1 + \mathrm{i}\eta_r); \quad k_F = \tilde{k}_F(1 + \mathrm{i}\eta_F); \quad k_B = \tilde{k}_B(1 + \mathrm{i}\eta_B); \tag{4.5}$$

where $\tilde{E}$, $\tilde{k}_F$ and $\tilde{k}_B$ are real parameters, without structural damping.

In order to derive the Green function of the system, a harmonic, unitary and vertical point load is applied at $x = \zeta$ on the running surface of the rail. The Eq. (4.1) becomes

$$EI\frac{\partial^4 z_r}{\partial x^4} + \rho S\frac{\partial^2 z_r}{\partial t^2} + f(x,t) = \delta(x-\zeta)\mathrm{e}^{\mathrm{i}\omega t} \tag{4.6}$$

where $\omega$ is the angular frequency of the excitation. The displacements induced by this excitation are also harmonic, and they have the form $z = Z\mathrm{e}^{\mathrm{i}\omega t}$. Applying this solution to Eqs. (4.2), (4.3), (4.4) and (4.6), changing the unitary force by the wheel/rail dynamic contact force $F_{w/r}(\omega)$ and operating gives

$$F(x,\omega) = Q(\omega)Z_r - G(\omega)Z_{g0}^{(0)} \tag{4.7}$$

$$F_g(x,\omega) = Q'(\omega)Z_r - G'(\omega)Z_{g0}^{(0)} \tag{4.8}$$

$$EI\frac{\partial^4 Z_r}{\partial x^4} - \rho S\omega^2 Z_r + F(x,\omega) = F_{w/r}(\omega)\,\delta(x-\zeta) \tag{4.9}$$

where

$$Q(\omega) = (k_F + \mathrm{i}\omega c_F)\left(1 - \frac{k_F + \mathrm{i}\omega c_F}{k_F + \mathrm{i}\omega c_F + k_B + \mathrm{i}\omega c_B - m_s\omega^2}\right) \tag{4.10}$$

$$G(\omega) = Q'(\omega) = \frac{(k_F + \mathrm{i}\omega c_F)(k_B + \mathrm{i}\omega c_B)}{k_F + \mathrm{i}\omega c_F + k_B + \mathrm{i}\omega c_B - m_s\omega^2} \tag{4.11}$$

$$G'(\omega) = (k_B + \mathrm{i}\omega c_B)\left(\frac{k_B + \mathrm{i}\omega c_B}{k_F + \mathrm{i}\omega c_F + k_B + \mathrm{i}\omega c_B - m_s\omega^2} - 1\right) \tag{4.12}$$

### 4.1.1 Subgrade model

The subgrade is modelled as a viscoelastic and homogeneous half-space, which is defined by the following properties: Lamé's constants $\lambda$ and $\mu$, density $\rho$, damping of P-waves $D_P$ and damping of S-waves $D_S$. Following the same procedure as in Chap. 3, the viscoelasticity of the medium is modelled according to the correspondence principle [114, 115]. Therefore Lamé's constants have become complex by using Eqs. (3.17) and (3.18). As Metrikine and Dieterman showed [50], the expression that governs displacements of this half-space, when these are assumed to be harmonic, in the wavenumber-frequency domain is

$$\bar{X}_g = -\mathrm{i}k_x A\mathrm{e}^{-\upsilon_{xy}z} - \frac{k_x k_y}{\upsilon'_{xy}} B\mathrm{e}^{-\upsilon'_{xy}z} - \frac{k_\beta^2 - {k_x}^2}{\upsilon'_{xy}} C\mathrm{e}^{-\upsilon'_{xy}z} \tag{4.13}$$

$$\bar{Y}_g = -\mathrm{i}k_y A\mathrm{e}^{-\upsilon_{xy}z} + \frac{k_\beta^2 - {k_y}^2}{\upsilon'_{xy}} B\mathrm{e}^{-\upsilon'_{xy}z} + \frac{k_x k_y}{\upsilon'_{xy}} C\mathrm{e}^{-\upsilon'_{xy}z} \tag{4.14}$$

$$\bar{Z}_g = -\upsilon_{xy} A\mathrm{e}^{-\upsilon_{xy}z} + \mathrm{i}k_y B\mathrm{e}^{-\upsilon'_{xy}z} - \mathrm{i}k_x C\mathrm{e}^{-\upsilon'_{xy}z} \tag{4.15}$$

for the coordinate system that appears in Fig. 4.3, where $A$, $B$ and $C$ are integration constants which can be calculated from boundary conditions imposed by the superstructure excitation and $k_x$ and $k_y$ are wavenumbers in $x$ and $y$ directions respectively. The parameters $\upsilon_{xy}$ and $\upsilon'_{xy}$ are

$$\upsilon_{xy} = \sqrt{{k_x}^2 + {k_y}^2 - {k_\alpha}^2} \qquad \upsilon'_{xy} = \sqrt{{k_x}^2 + {k_y}^2 - {k_\beta}^2} \tag{4.16}$$

and $k_\alpha$ and $k_\beta$ are already defined in Chap. 3 (Eq. (3.4)).

The boundary conditions to evaluate the integration constants $A$, $B$ and $C$ follow from the stresses at the free surface. Expressions of these stresses, which can be found in [87], are

$$\tau_{xz}|_{z=0} = \mu\left(\frac{\partial z_g}{\partial x} + \frac{\partial x_g}{\partial z}\right)\Bigg|_{z=0} \tag{4.17}$$

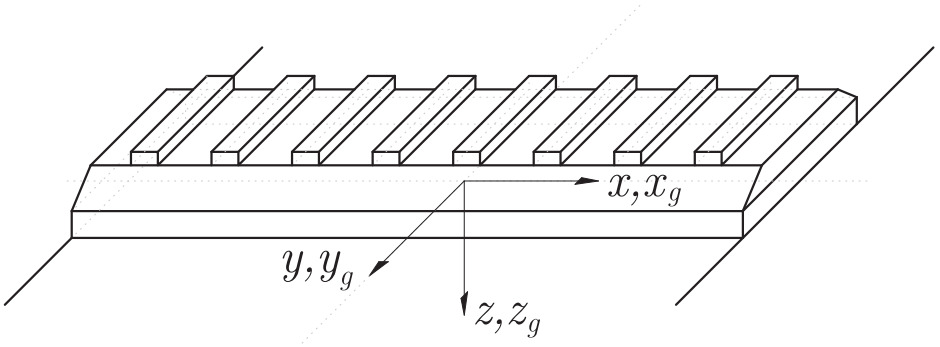


FIGURE 4.3: Coordinate system ($x$, $y$, $z$) and subgrade displacements ($x_g$, $y_g$, $z_g$).

$$\tau_{yz}|_{z=0} = \mu \left( \frac{\partial y_g}{\partial z} + \frac{\partial z_g}{\partial y} \right) \Bigg|_{z=0} \tag{4.18}$$

$$\tau_{zz}|_{z=0} = \lambda \left( \frac{\partial x_g}{\partial x} + \frac{\partial y_g}{\partial y} + \frac{\partial z_g}{\partial z} \right) + 2\mu \frac{\partial z_g}{\partial z} \Bigg|_{z=0} \tag{4.19}$$

The transformation of these expressions to the frequency domain is direct: only the displacements $x_g$, $y_g$ and $z_g$ are time-dependant and, therefore, they become $X_g$, $Y_g$ and $Z_g$. As Eqs. (4.13), (4.14) and (4.15) are obtained from the spatial domain by using the Fourier transform of the form

$$\bar{Z}(k_x, k_y, z) = \int_{-\infty}^{+\infty} \int_{-\infty}^{+\infty} Z(x, y, z) \mathrm{e}^{\mathrm{i}(k_x x + k_y y)} \mathrm{d}x \mathrm{d}y \tag{4.20}$$

it is necessary to use this expression to transform Eqs. (4.17), (4.18) and (4.19) to the wavenumber domain, thus obtaining

$$\bar{\tau}_{xz}|_{z=0} = \mu \left( -\mathrm{i}k_x \bar{Z}_g + \frac{\partial \bar{X}_g}{\partial z} \right) \Bigg|_{z=0} \tag{4.21}$$

$$\bar{\tau}_{yz}|_{z=0} = \mu \left( -\mathrm{i}k_y \bar{Z}_g + \frac{\partial \bar{Y}_g}{\partial z} \right) \Bigg|_{z=0} \tag{4.22}$$

$$\bar{\tau}_{zz}|_{z=0} = \left[ (\lambda + 2\mu) \frac{\bar{Z}_g}{z} - \mathrm{i}\lambda (k_x \bar{X}_g + k_y \bar{Y}_g) \right] \Bigg|_{z=0} \tag{4.23}$$

Having considered the superstructure excitation acting only in the vertical direction, the boundary conditions are [49]

$$\tau_{xz}|_{z=0} = \tau_{yz}|_{z=0} = 0 \tag{4.24}$$

$$\tau_{zz}|_{z=0} = \frac{f_g(x,t)}{2c} H(c - |y|) \tag{4.25}$$

where $H(.)$ is the Heaviside step function and $c$ is half the width of the superstructure/subgrade contact area ($2c$ is called superstructure width throughout this thesis). Transforming these boundary conditions to the wavenumber-frequency domain by following the same procedure as before and equating the resulting expressions with Eqs. (4.21), (4.22) and (4.23) gives

$$\bar{\tau}_{xz}|_{z=0} = \mu \left( -\mathrm{i}k_x \bar{Z}_g + \frac{\partial \bar{X}_g}{\partial z} \right) \Bigg|_{z=0} = 0 \tag{4.26}$$

$$\bar{\tau}_{yz}|_{z=0} = \mu \left( -\mathrm{i}k_y \bar{Z}_g + \frac{\partial \bar{Y}_g}{\partial z} \right) \Bigg|_{z=0} = 0 \tag{4.27}$$

$$\bar{\tau}_{zz}|_{z=0} = \left[ (\lambda + 2\mu) \frac{\partial \bar{Z}_g}{\partial z} - \mathrm{i}\lambda (k_x \bar{X}_g + k_y \bar{Y}_g) \right] \Bigg|_{z=0} = \bar{F}_g(k_x, \omega) \frac{\sin(ck_y)}{ck_y} \tag{4.28}$$

Substituting Eqs. (4.13), (4.14) and (4.15) into the boundary conditions yields

$$A = \bar{F}_g(k_x, \omega) \frac{\sin(ck_y)}{\mu c k_y} \left[ \frac{2(k_x^2 + k_y^2) - k_\beta^2}{F_R(k_x, k_y)} \right] \tag{4.29}$$

$$B = -\bar{F}_g(k_x, \omega) \frac{\sin(ck_y)}{\mu c k_y} \left[ \frac{2\mathrm{i}\upsilon_{xy} k_y}{F_R(k_x, k_y)} \right] \tag{4.30}$$

$$C = \bar{F}_g(k_x, \omega) \frac{\sin(ck_y)}{\mu c k_y} \left[ \frac{2\mathrm{i}\upsilon_{xy} k_x}{F_R(k_x, k_y)} \right] \tag{4.31}$$

where

$$F_R(k_x, k_y) = \left[ 2(k_x^2 + k_y^2) - k_\beta^2 \right]^2 - 4\upsilon_{xy}\upsilon'_{xy}(k_x^2 + k_y^2) \tag{4.32}$$

Substituting the integration constants $A$, $B$, and $C$ defined by Eqs. (4.29), (4.30) and (4.31) into Eqs. (4.13), (4.14) and (4.15) and evaluating resulting expressions at the surface of the half-space gives

$$\bar{X}_g|_{z=0} = \frac{\bar{F}_g(k_x,\omega)\sin(ck_y)}{\mu c k_y}\frac{\mathrm{i}k_x}{F_R(k_x,k_y)}\left(2\upsilon_{xy}\upsilon'_{xy} - {\upsilon'_{xy}}^2 - {k_x}^2 - {k_y}^2\right) \tag{4.33}$$

$$\bar{Y}_g|_{z=0} = \frac{\bar{F}_g(k_x,\omega)\sin(ck_y)}{\mu c k_y}\frac{\mathrm{i}k_y}{F_R(k_x,k_y)}\left(2\upsilon_{xy}\upsilon'_{xy} - {\upsilon'_{xy}}^2 - {k_x}^2 - {k_y}^2\right) \tag{4.34}$$

$$\bar{Z}_g|_{z=0} = \frac{\bar{F}_g(k_x,\omega)\sin(ck_y)}{\mu c k_y}\left[\frac{\upsilon_{xy}k_\beta^2}{F_R(k_x,k_y)}\right] \tag{4.35}$$

which are the expressions that represent the motion of the subgrade surface.

### 4.1.2 Superstructure/subgrade coupling

General subgrade displacements ($\bar{X}_g$, $\bar{Y}_g$ and $\bar{Z}_g$) are related to subgrade surface displacements under the superstructure ($\bar{X}_{g0}^{(0)}$, $\bar{Y}_{g0}^{(0)}$ and $\bar{Z}_{g0}^{(0)}$) according to

$$(\bar{X}_{g0}^{(0)}, \bar{Y}_{g0}^{(0)}, \bar{Z}_{g0}^{(0)}) = (\bar{X}_g, \bar{Y}_g, \bar{Z}_g)|_{y=0,z=0} \tag{4.36}$$

Therefore, the vertical subgrade surface displacement under the superstructure can be calculated from Eq. (4.35) by using Eq. (4.36), obtaining:

$$\bar{Z}_{g0}^{(0)} = \bar{F}_g(k_x,\omega)\left[\frac{1}{2\pi}\int_{-\infty}^{+\infty}\frac{\sin(ck_y)}{\mu c k_y}\frac{\upsilon_{xy}k_\beta^2}{F_R(k_x,k_y)}\mathrm{e}^{-\mathrm{i}k_y y}\mathrm{d}k_y\right]\Bigg|_{y=0} \tag{4.37}$$

where the Fourier antitransform used is in accordance to the Fourier transform defined in Eq. (4.20). Operating the $y = 0$ evaluation into the integral yields

$$\bar{Z}_{g0}^{(0)} = \bar{F}_g(k_x,\omega)\left[\frac{1}{2\pi}\int_{-\infty}^{+\infty}\frac{\sin(ck_y)}{\mu c k_y}\frac{\upsilon_{xy}k_\beta^2}{F_R(k_x,k_y)}\mathrm{d}k_y\right] \tag{4.38}$$

To couple the superstructure with its subgrade is required to operate at same domain: in this work the wavenumber-frequency domain has been chosen to achieve this coupling. Transforming Eqs. (4.7), (4.8) and (4.9) to the wavenumber-frequency domain by using a 1D Fourier transform (Eq. (B.7), as reduction of Eq. (4.20)) and inserting $\bar{F}(k_x,\omega)$ into the transformed Bernoulli-Euler beam equation gives

$$\bar{F}_g(k_x,\omega) = Q'(\omega)\bar{Z}_r - G'(\omega)\bar{Z}_{g0}^{(0)} \tag{4.39}$$

$$EIk_x^4\bar{Z}_r - \rho S\omega^2\bar{Z}_r + Q(\omega)\bar{Z}_r - G(\omega)\bar{Z}_{g0}^{(0)} = F_{w/r}(\omega)\,\mathrm{e}^{\mathrm{i}k_x\zeta} \tag{4.40}$$

Combining Eqs. (4.38) and (4.39) yields

$$\bar{Z}_{g0}^{(0)} = \frac{Q'(\omega)I_{k_y}(k_x,\omega)}{G'(\omega)I_{k_y}(k_x,\omega)+1}\bar{Z}_r \tag{4.41}$$

where

$$I_{k_y}(k_x,\omega) = \frac{1}{2\pi}\int_{-\infty}^{+\infty}\frac{\sin(ck_y)}{\mu ck_y}\frac{\upsilon_{xy}k_\beta^2}{F_R(k_x,k_y)}\mathrm{d}k_y \tag{4.42}$$

The integrand of the integral defined in Eq. (4.42) is symmetric with respect to $k_y = 0$ because

$$\frac{\sin(ck_y)}{k_y} = \frac{\sin(-ck_y)}{-k_y} \qquad \text{and} \qquad k_y^2 = (-k_y)^2$$

Therefore, Eq. (4.42) becomes

$$I_{k_y}(k_x,\omega) = \frac{1}{\pi}\int_{0}^{\infty}\frac{\sin(ck_y)}{\mu ck_y}\frac{\upsilon_{xy}k_\beta^2}{F_R(k_x,k_y)}\mathrm{d}k_y \tag{4.43}$$

Inserting Eq. (4.41) in Eq. (4.40) results in

$$\bar{Z}_r = \frac{F_{w/r}(\omega)\,\mathrm{e}^{\mathrm{i}k_x\zeta}}{EIk_x^4 - \omega^2\rho S + Q(\omega) - \frac{G(\omega)Q'(\omega)I_{k_y}(k_x,\omega)}{G'(\omega)I_{k_y}(k_x,\omega)+1}} \tag{4.44}$$

and, finally, the application of the Fourier antitransform on Eq. (4.44) gives the receptance of the system

$$\frac{Z_r}{F_{w/r}} = \frac{1}{2\pi}\int_{-\infty}^{+\infty}\frac{\mathrm{e}^{\mathrm{i}k_x\zeta}\;\mathrm{e}^{-\mathrm{i}k_x x}}{EIk_x^4 - \omega^2\rho S + Q(\omega) - \frac{G(\omega)Q'(\omega)I_{k_y}(k_x,\omega)}{G'(\omega)I_{k_y}(k_x,\omega)+1}}\mathrm{d}k_x \tag{4.45}$$

### 4.1.3 Numerical solution

In order to compute the integral represented by Eq. (4.45) a numerical integration is performed. The algorithm used to do it is the `quadgk` routine provided by MATLAB,

which is also used in the previous chapter. Again, this algorithm is chosen because it provides good accuracy but it is not the best solution with respect to computational efficiency: faster integration methods must be used when this model is implemented in a real computational algorithm (a review of these methods can be seen in Section 2.2.7). First, it is necessary to compute the integral defined by the Eq. (4.43) for any integration point, which are the values of $k_x$ used in the evaluation of the Eq. (4.45).

The examination of the Eq. (4.43) integrand, which is called $\tilde{I}_{k_y}(k_x, k_y, \omega)$, shows that there are no problems with the integration along the required integration path, which is the positive side of the real axis. In more detail:

- The first part of $\tilde{I}_{k_y}(k_x, k_y, \omega)$, the fraction $\frac{\sin(ck_y)}{\mu c k_y}$, has one pole at the origin. This singularity resides in the left limit of the integration interval. As Shampine has shown [128], `quadgk` routine can handle singularities at the endpoints. Therefore, there are no numerical problems with this part.
- The second part of $\tilde{I}_{k_y}(k_x, k_y, \omega)$, the fraction $\frac{\upsilon_{xy} k_\beta^2}{F_R(k_x, k_y)}$, is very similar to the Eq. (3.2) integrand. As shown in Section 3.1.3, when the half-space is modelled as a viscoelastic medium, its poles and branch cuts do not affect an integration along the real axis, since they are located in other regions of the complex plane [126].

Continuing with the examination of this integrand, it is observed that it has also an important oscillatory behaviour, like the integrals presented in Chapter 3. In this case this behaviour appears only with respect to the $k_y$ wavenumber because it is produced by the term $\sin(ck_y)$. Following the approach presented in Appendix A as well as in the previous chapter, Eq. (4.43) can be transformed to avoid problems in the calculation time due to the oscillatory behaviour:

$$\begin{aligned} I_{k_y}(k_x, \omega) = \frac{\alpha^2}{4\pi\mu(\beta^2 - \alpha^2)} \left[ \frac{\pi}{c|k_x|} - 2 \int_{|k_x|}^{\infty} \frac{\mathrm{e}^{-ck'_y}}{ck'_y \sqrt{k'^2_y - k_x^2}} \mathrm{d}k'_y \right] \\ + \frac{1}{\pi} \int_0^{+k_{lim}} \left[ \frac{\upsilon_{xy} k_\beta^2}{F_R(k_x, k_y)} - \frac{\alpha^2}{2\sqrt{k_x^2 + k_y^2}\,(\beta^2 - \alpha^2)} \right] \frac{\sin(ck_y)}{\mu c k_y} \mathrm{d}k_y \end{aligned} \tag{4.46}$$

The new integrand, which is called $\tilde{I}'_{k_y}(k_x, k_y, \omega)$, has an extremely reduced oscillatory behaviour with respect to the original integrand $\tilde{I}_{k_y}(k_x, k_y, \omega)$. This fact can be observed in Figs. 4.4, 4.5, 4.6 and 4.7.

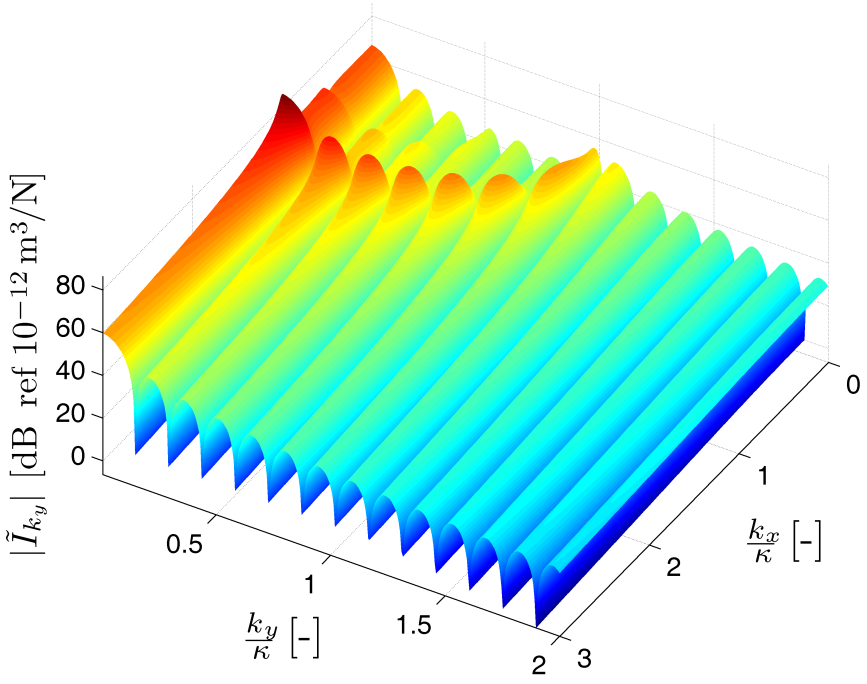


FIGURE 4.4: Module of $\tilde{I}_{k_y}(k_x, k_y, \omega)$ for quaternary ground type (see Table 3.1).

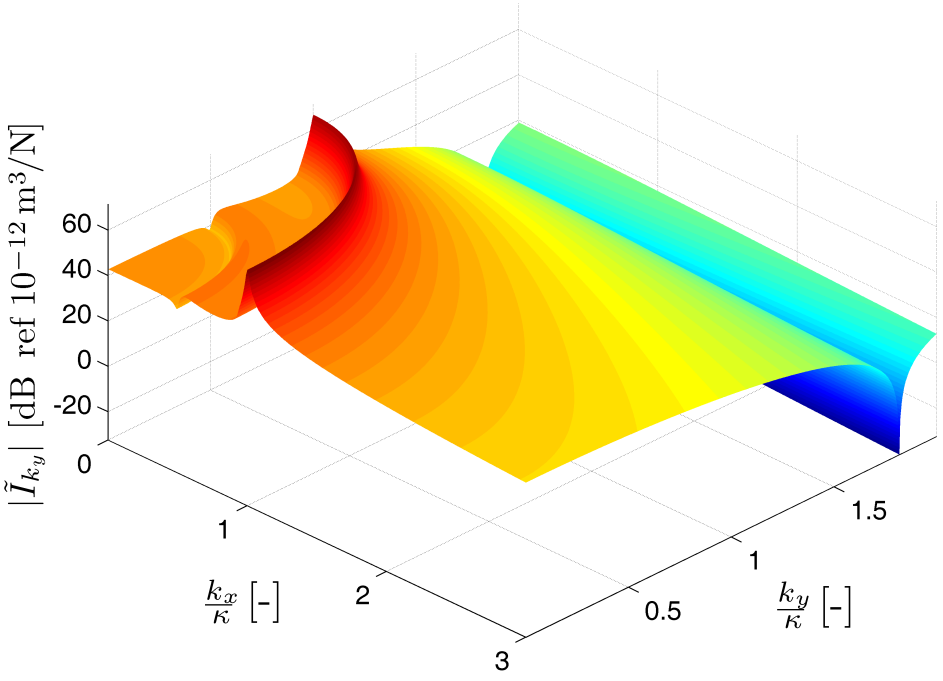


FIGURE 4.5: Module of $\tilde{I}_{k_y}(k_x, k_y, \omega)$ for igneous rocks ground type (see Table 3.1).

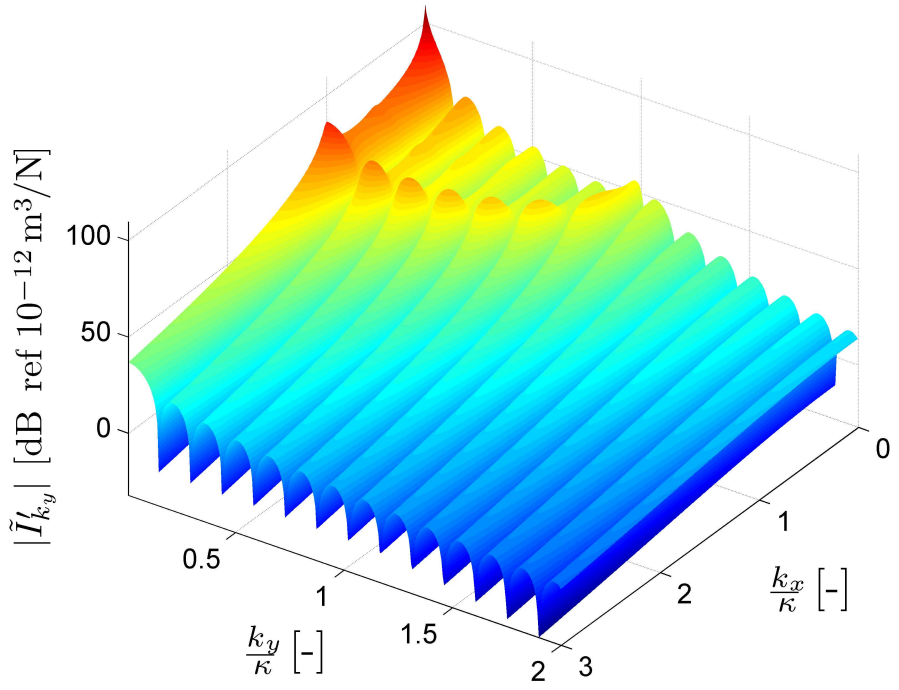


FIGURE 4.6: Module of $\tilde{I}'_{k_y}(k_x, k_y, \omega)$ for quaternary ground type (see Table 3.1).

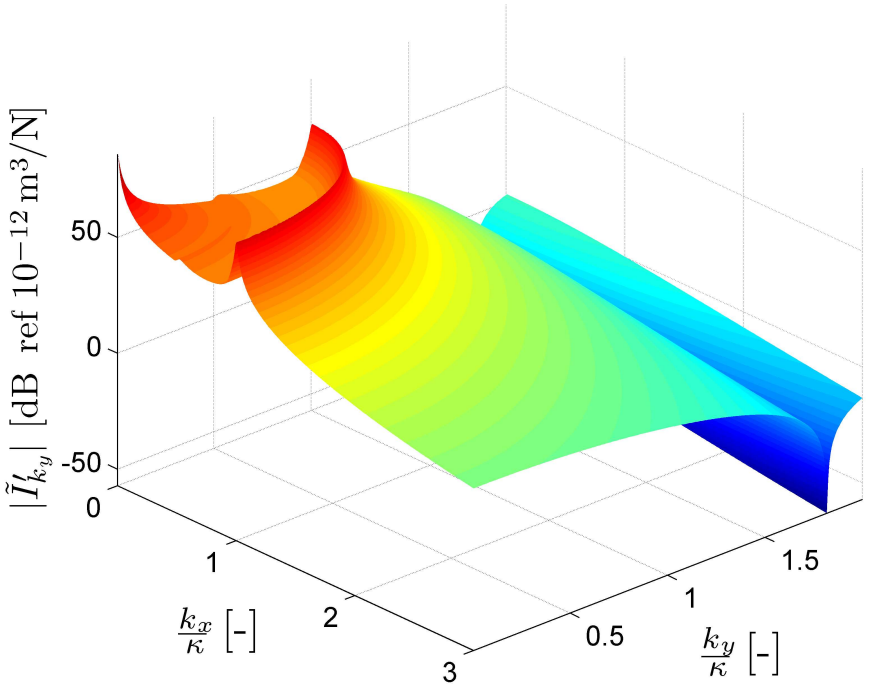


FIGURE 4.7: Module of $\tilde{I}'_{k_y}(k_x, k_y, \omega)$ for igneous rocks ground type (see Table 3.1).

In these figures one can also note that the oscillations of the integrands are more dense (in the adimensional wavenumber domain $\frac{k_y}{\kappa}$) in soft grounds than in hard grounds. Dense oscillations in integrands imply a higher computational cost of their numerical integration because too many integration points are required. Therefore, the application of a technique to lower the oscillatory behaviour of the integrand, such as that presented here, is much more important for soft grounds than for hard grounds.

The final integral, with respect to $k_x$, presented in Eq. (4.45) does not present problems with singularities. The poles generated by the denominator are not located at the real axis, because

$$\frac{-\omega^2\rho S + Q(\omega) - \frac{G(\omega)Q'(\omega)I_{k_y}(k_x,\omega)}{G'(\omega)I_{k_y}(k_x,\omega)+1}}{EI}$$

is complex-valued. Moreover, there is no oscillatory behaviour in the integrand, since $\tilde{I}_{k_y}(k_x, k_y, \omega)$ does not contain oscillations with respect to $k_x$ (see Figs. 4.4 and 4.5), and the other terms do not either, as long as the rail receptance is calculated at $x = \zeta$.

## 4.2 Influence of the subgrade parameters on the track receptance

In this section, the analytical solution of track receptance presented in the previous section is applied for different subgrade mechanical parameters. The receptance is always calculated at the load application point, therefore at $x = \zeta$. The numerical integration is always performed by setting the relative tolerance to $10^{-4}$. The parameters of the track used are shown in Tables 4.1, 4.2 and 4.3. As can be seen in these tables, four sets of superstructure parameters are studied: two with structural damping and two with viscous damping. These four sets of superstructure parameters have been taken from the following sources:

- **Case 1**: Otero [1].
- **Case 2**: Sheng et al. [190].
- **Case 3**: Grassie et al. [55], taking the set of parameters with low stiffnesses.
- **Case 4**: Grassie et al. [55], taking the set of parameters with high stiffnesses.

| **Rail mechanical parameters** | | | | | |
|---|---|---|---|---|---|
| Parameters | | Case 1 | Case 2 | Case 3 | Case 4 |
| $S$ | [m$^2$] | $6.93 \cdot 10^{-3}$ | $7.69 \cdot 10^{-3}$ | $7.13 \cdot 10^{-3}$ | $7.13 \cdot 10^{-3}$ |
| $I$ | [m$^4$] | $23.5 \cdot 10^{-6}$ | $30.55 \cdot 10^{-6}$ | $23.48 \cdot 10^{-6}$ | $23.48 \cdot 10^{-6}$ |
| $E$ | [GPa] | 207 | 210 | 207 | 207 |
| $\rho$ | [kg/m$^3$] | 7850 | 7850 | 7850 | 7850 |
| $\eta_r$ | [–] | 0.02 | 0.01 | – | – |

TABLE 4.1: Mechanical properties of a ballasted railway track. Rail mechanical parameters.

| **Fasteners and sleepers mechanical parameters** | | | | | |
|---|---|---|---|---|---|
| Parameters | | Case 1 | Case 2 | Case 3 | Case 4 |
| $k_F$ | [(N/m)/m] | $192 \cdot 10^6$ | $583.3 \cdot 10^6$ | $322.3 \cdot 10^6$ | $401.1 \cdot 10^6$ |
| $\eta_F$ | [–] | 0.196 | 0.25 | – | – |
| $c_F$ | [(Ns/m)/m] | – | – | $40.11 \cdot 10^3$ | $98.26 \cdot 10^3$ |
| $m_s$ | [kg/m] | 120 | 270 | 157.6 | 157.6 |

TABLE 4.2: Mechanical properties of a ballasted railway track. Fasteners and sleepers mechanical parameters.

| **Ballast mechanical parameters** | | | | | |
|---|---|---|---|---|---|
| Parameters | | Case 1 | Case 2 | Case 3 | Case 4 |
| $k_B$ | [(N/m)/m] | $22.89 \cdot 10^6$ | $83.3 \cdot 10^6$ | $100.3 \cdot 10^6$ | $257.9 \cdot 10^6$ |
| $\eta_B$ | [–] | 0.204 | 1 | – | – |
| $c_B$ | [(Ns/m)/m] | – | – | 42.98 | 206 |

TABLE 4.3: Mechanical properties of a ballasted railway track. Ballast mechanical parameters.

With regard to superstructure width, for single railways this parameter ranges between 2.5 m and 4.5 m, as is demonstrated in Appendix D. An average value, 3.5 m, is taken as a typical solution.

Using these superstructure parameters combined with subgrade properties given in Table 3.1 and with a superstructure width of 3.5 m ($c = 1.75$ m), different track receptances are obtained, which are shown in the Figs. 4.8, 4.9, 4.10, 4.11, 4.12, 4.13, 4.14 and 4.15.

The receptance of the track without subgrade coupling shown in these figures is obtained from the analytical solution presented in Appendix B. In these cases the resonant frequency for the case of no subgrade coupling are 57.26 Hz, 76.69 Hz, 105.09 Hz, 158.19 Hz for the four sets of parameters in Tables 4.1, 4.2 and 4.3 respectively. As can be seen in all figures mentioned (Figs. 4.8, 4.9, 4.10, 4.11, 4.12, 4.13, 4.14 and 4.15), for high

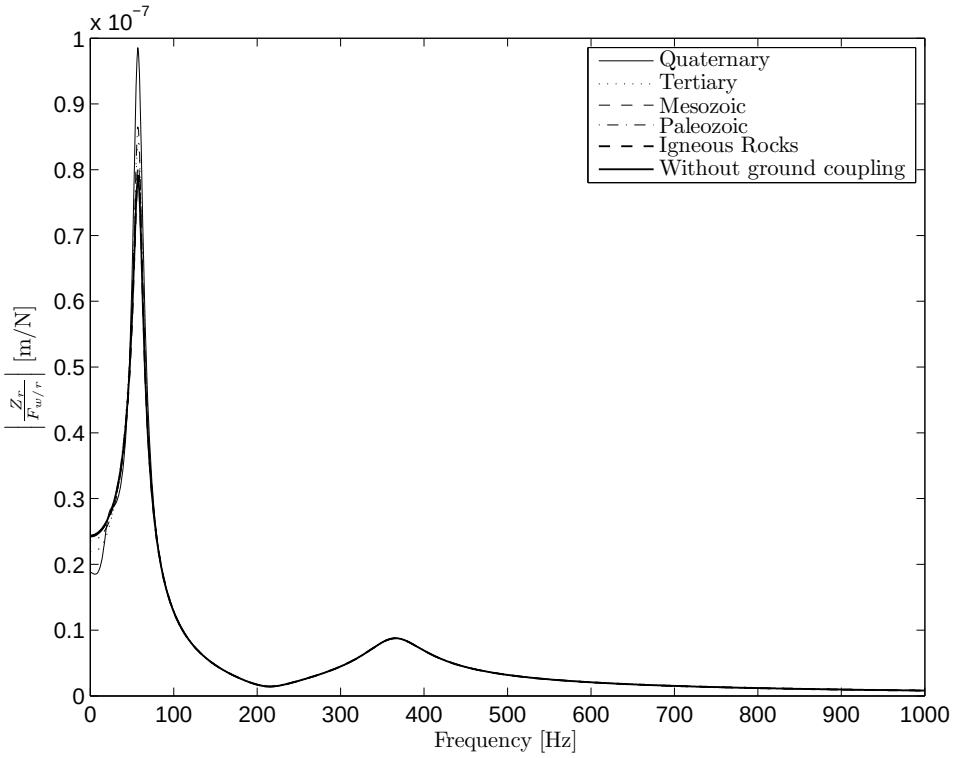


FIGURE 4.8: Module of the rail receptance for superstructure parameters in Case 1 (see Tables 4.1, 4.2 and 4.3) and for five different subgrade parameters of the Table 3.1.

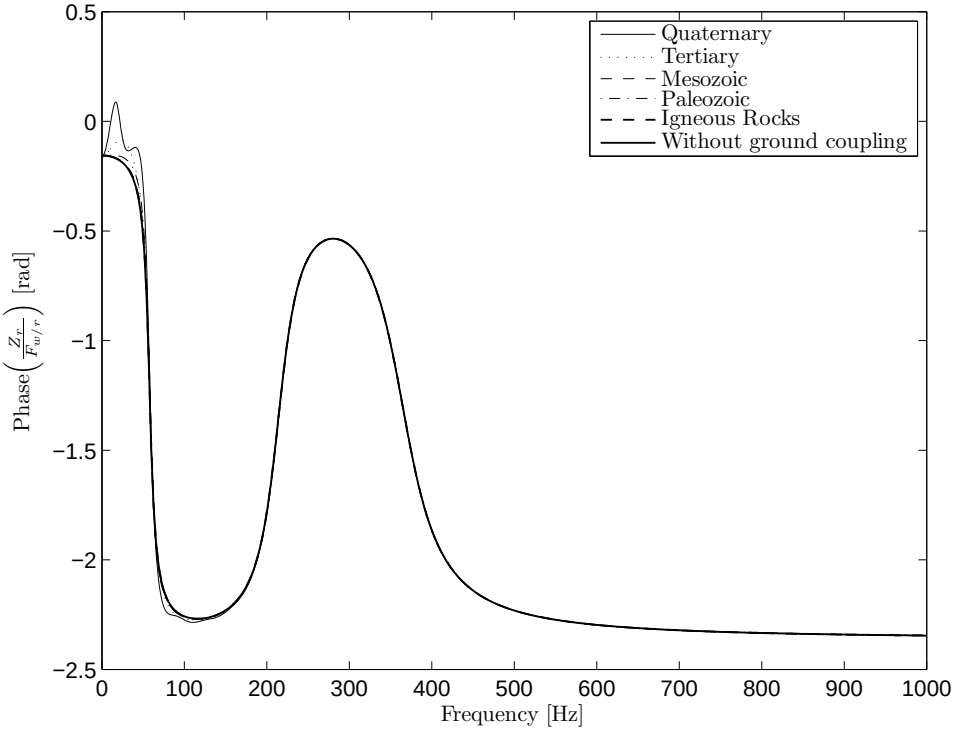


FIGURE 4.9: Phase of the rail receptance for superstructure parameters in Case 1 (see Tables 4.1, 4.2 and 4.3) and for five different subgrade parameters of the Table 3.1.

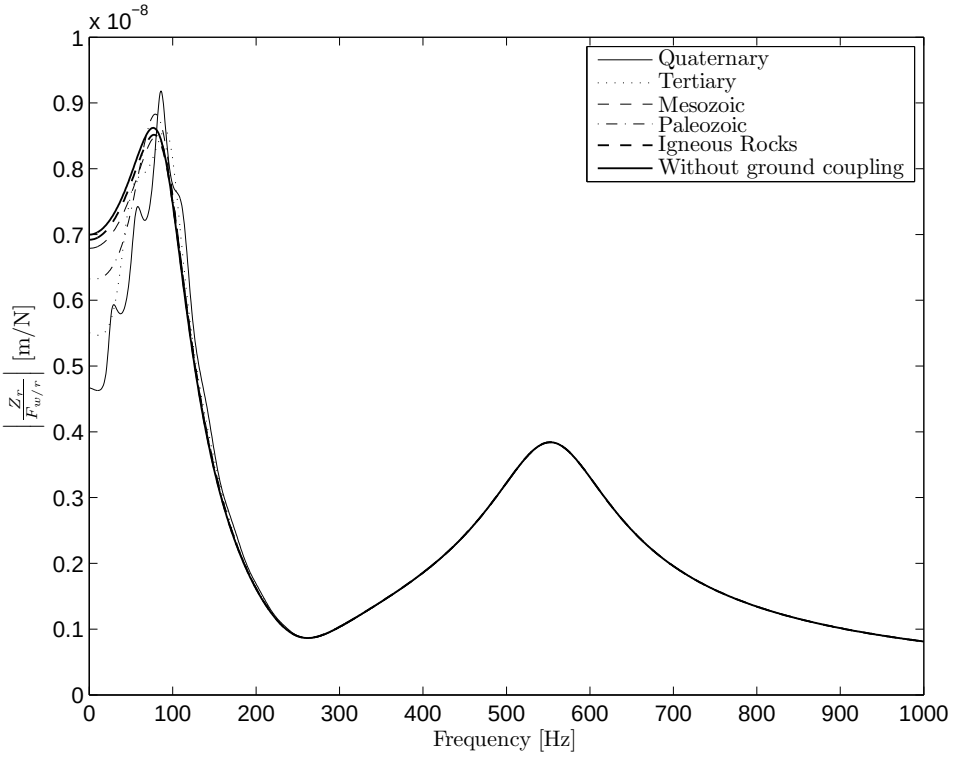


FIGURE 4.10: Module of the rail receptance for superstructure parameters in Case 2 (see Tables 4.1, 4.2 and 4.3) and for five different subgrade parameters of the Table 3.1.

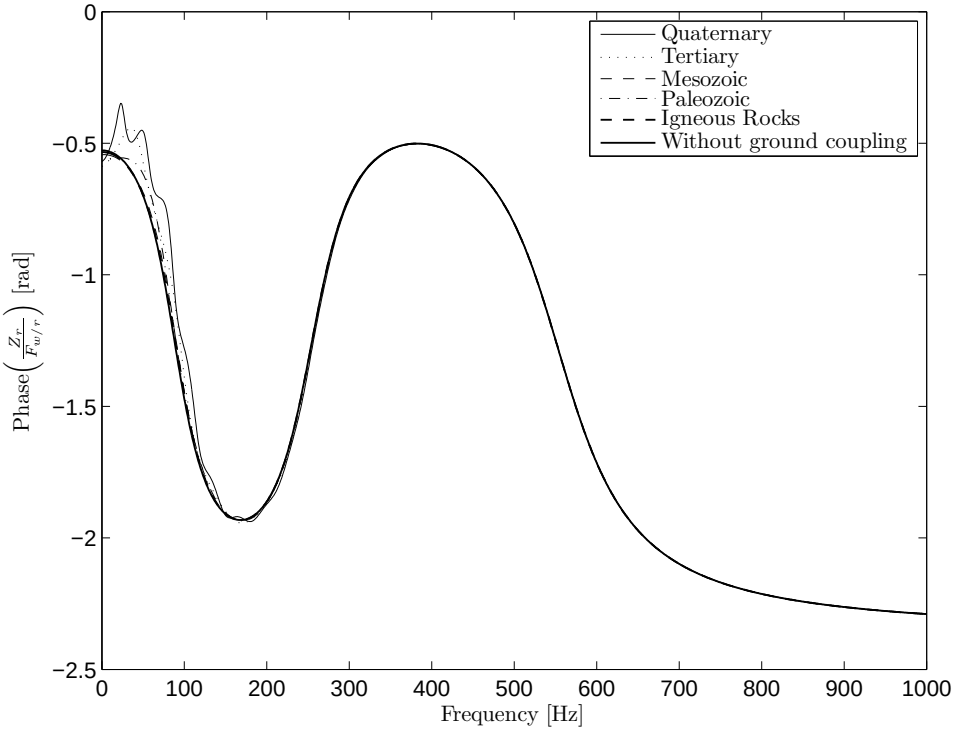


FIGURE 4.11: Phase of the rail receptance for superstructure parameters in Case 2 (see Tables 4.1, 4.2 and 4.3) and for five different subgrade parameters of the Table 3.1.

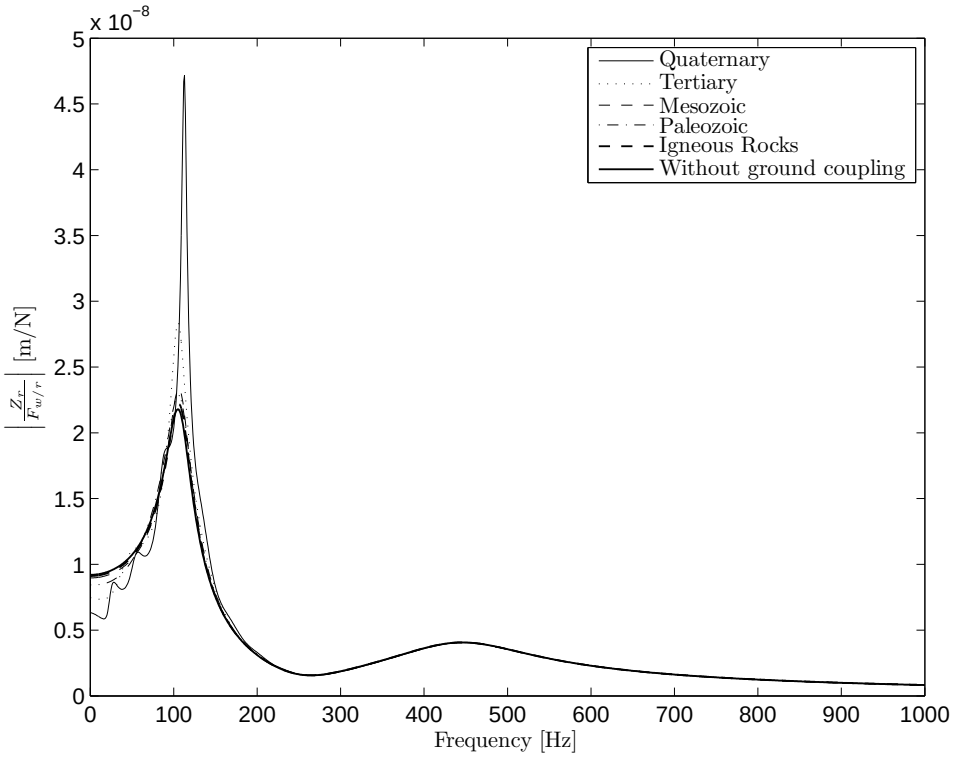


FIGURE 4.12: Module of the rail receptance for superstructure parameters in Case 3 (see Tables 4.1, 4.2 and 4.3) and for five different subgrade parameters of the Table 3.1.

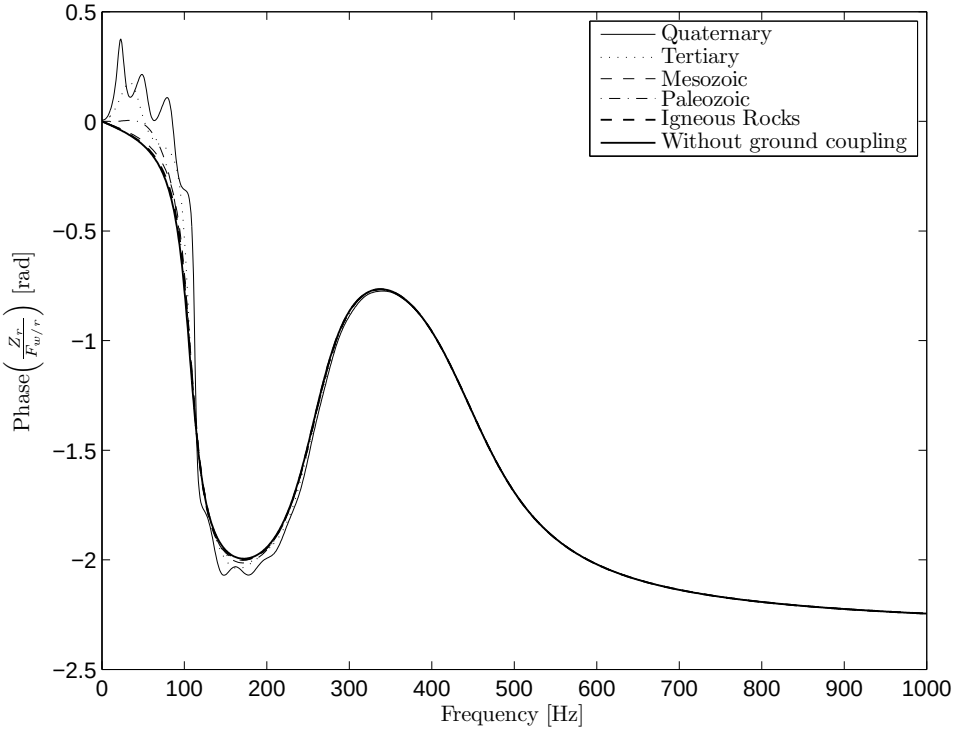


FIGURE 4.13: Phase of the rail receptance for superstructure parameters in Case 3 (see Tables 4.1, 4.2 and 4.3) and for five different subgrade parameters of the Table 3.1.

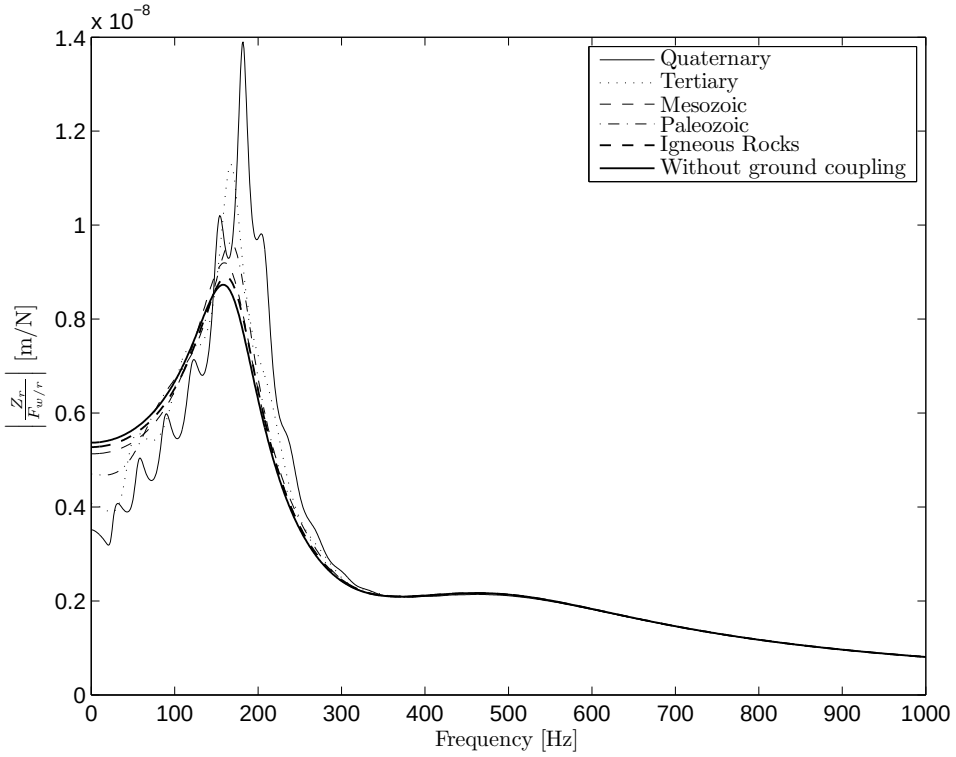


FIGURE 4.14: Module of the rail receptance for superstructure parameters in Case 4 (see Tables 4.1, 4.2 and 4.3) and for five different subgrade parameters of the Table 3.1.

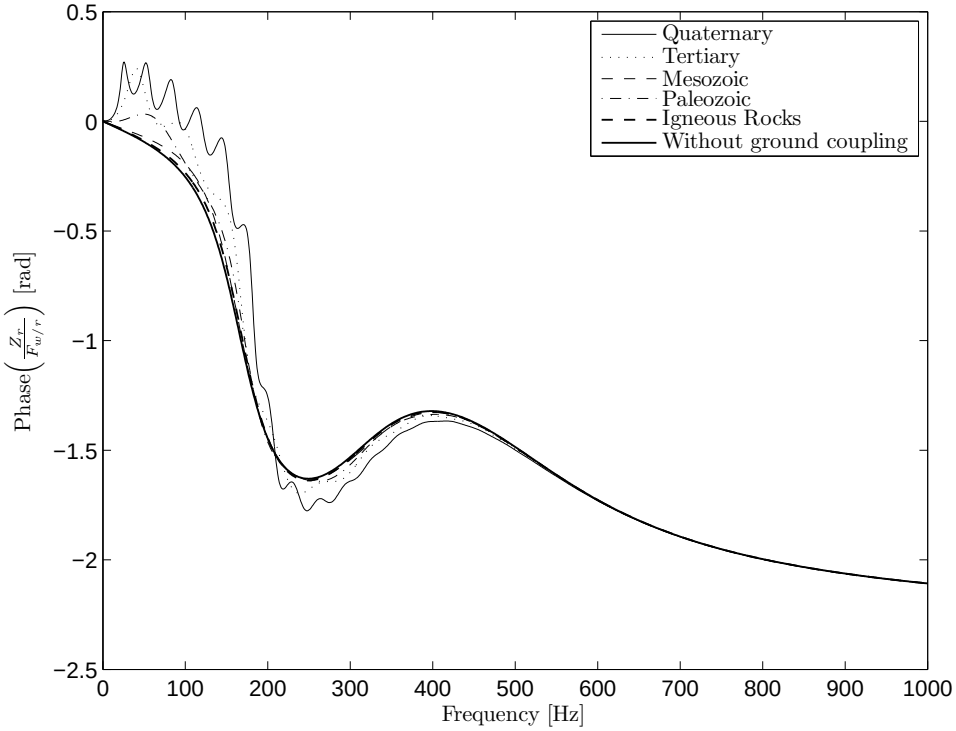


FIGURE 4.15: Phase of the rail receptance for superstructure parameters in Case 4 (see Tables 4.1, 4.2 and 4.3) and for five different subgrade parameters of the Table 3.1.

frequencies the receptance of the non-coupled case is a good approximation of the receptance of the coupled case. The limit frequency above which this simplification can be applied is directly proportional to the stiffness of the track or its first resonant frequency. Section 4.2.5 shows that this assumption can be extended to other superstructure widths.

From these figures, it is clear that the effect of superstructure/subgrade coupling on rail receptance is low but significant in the frequency range of interest (it ranges, as previously mentioned in Section 2.1.1, between 20 Hz and 80 Hz), above all when the superstructure has a high global stiffness, and, therefore, at high natural frequencies of the in-phase mode of the superstructure. These figures are presented in a non-dimensional form in Section C.1.1.

In subsequent sections the effect of any subgrade parameter is investigated in order to find what parameters are significant on the superstructure response. This research will also be useful to show the possible values that the resonant frequency of the in-phase mode of the receptance can take. For oscillatory receptances the resonant peak of the in-phase mode of the track is also taken as maximum value near the natural frequency of this mode. Variations of quaternary ground type are used to perform this investigation (see Table 3.1) since this is the kind of ground that most modifies track receptance with respect to the case which does not include superstructure/subgrade coupling. For the same reason, the parameters of Case 4 (see Tables 4.1, 4.2 and 4.3) are used.

The prime nomenclature is used throughout Section 4.2, in Section 4.3, in Appendix B and in Section C.1 of Appendix C to indicate that the vertical displacements of the rail and the sleepers ($z'_r$ and $z'_s$) and the natural frequencies of the track ($\bar{\omega}'_n$) are related to the non-coupled case. In contrast, the prime nomenclature used on stiffnesses, viscous/structural dampings and masses in Sections 4.4, 4.5 and C.2 denotes that these parameters are from the 2DOF equivalent model.

### 4.2.1 Effects of the dampings $D_P$ and $D_S$

Figs. 4.16 and 4.17 represent the module and the phase of the adimensional receptance with various realistic combinations of dampings. Complete results for the four Cases of study are presented in Section C.1.2.

For these different combinations, the results show that the resonant frequency of the in-phase mode ranges between 181.66 Hz and 181.73 Hz and the resonant amplitude ranges between $1.391 \cdot 10^{-8}$ m/N and $1.665 \cdot 10^{-8}$ m/N. Complete results about the resonance are shown in Table 4.4, where $\bar{f}_{1r}$ and $\bar{f}'_{1r}$ are the resonant frequencies of the in-phase mode for the case with and without subgrade coupling, respectively, and $\max|Z_r|$ and

$\max|Z'_r|$ are the resonant amplitude of the same mode, also for the case with and without subgrade coupling, respectively.

| Dampings | | $\bar{f}_{1r}$ [Hz] | $\frac{\bar{f}_{1r}}{\bar{f}'_{1r}}$ [-] | $\max\|Z_r\|$ [m/N] | $\frac{\max\|Z_r\|}{\max\|Z'_r\|}$ [-] |
|---|---|---|---|---|---|
| $D_P$ [-] | $D_S$ [-] | | | | |
| 0.04 | 0.03 | 181.73 | 1.149 | $1.391 \cdot 10^{-8}$ | 1.593 |
| 0.035 | 0.025 | 181.69 | 1.149 | $1.432 \cdot 10^{-8}$ | 1.64 |
| 0.028 | 0.02 | 181.68 | 1.149 | $1.487 \cdot 10^{-8}$ | 1.703 |
| 0.025 | 0.015 | 181.66 | 1.148 | $1.56 \cdot 10^{-8}$ | 1.787 |
| 0.017 | 0.01 | 181.68 | 1.149 | $1.665 \cdot 10^{-8}$ | 1.907 |

TABLE 4.4: Results of the resonant frequency and amplitude of track receptance obtained with different combination of subgrade dampings.

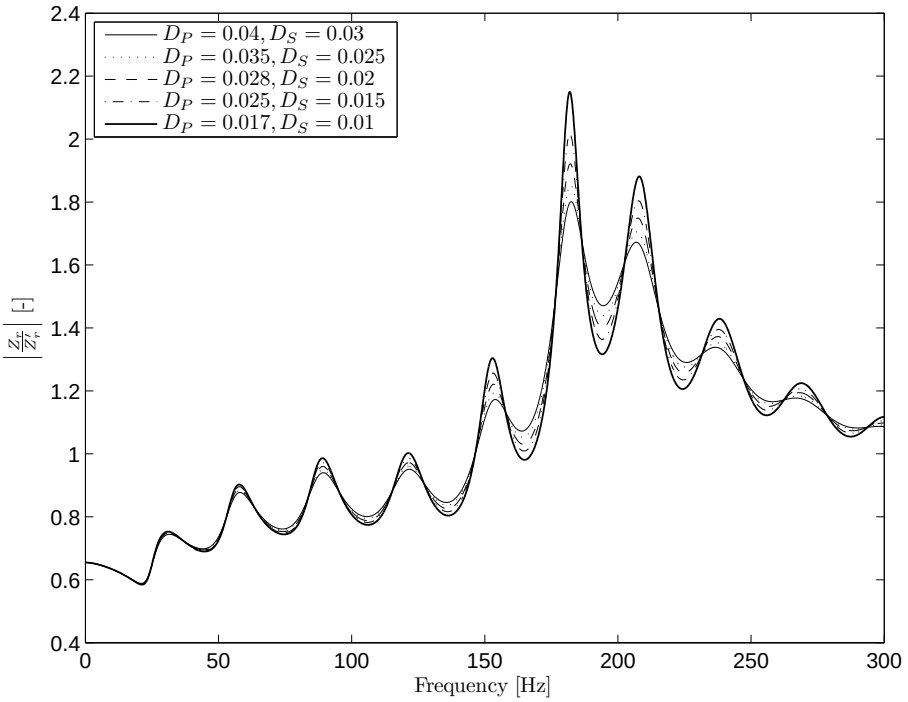


FIGURE 4.16: Adimensional module of the rail receptance for five different combinations of subgrade damping coefficients $D_P$ and $D_S$ and for the superstructure parameters in Case 4 (see Tables 4.1, 4.2 and 4.3). The other mechanical parameters of the subgrade are equal to the Quaternary ground type (see Table 3.1).

In this case, these results are obtained by setting the other mechanical parameters of the subgrade (Young's modulus $E$, Poisson's ratio $\nu$ and the density $\rho$) equal to the quaternary ground type. It is assumed to have a superstructure width of 3.5 m ($c = 1.75$ m). The observation of these results leads to the assumption that $D_S$ and $D_P$ do not affect the receptance significantly in the frequency range of interest.

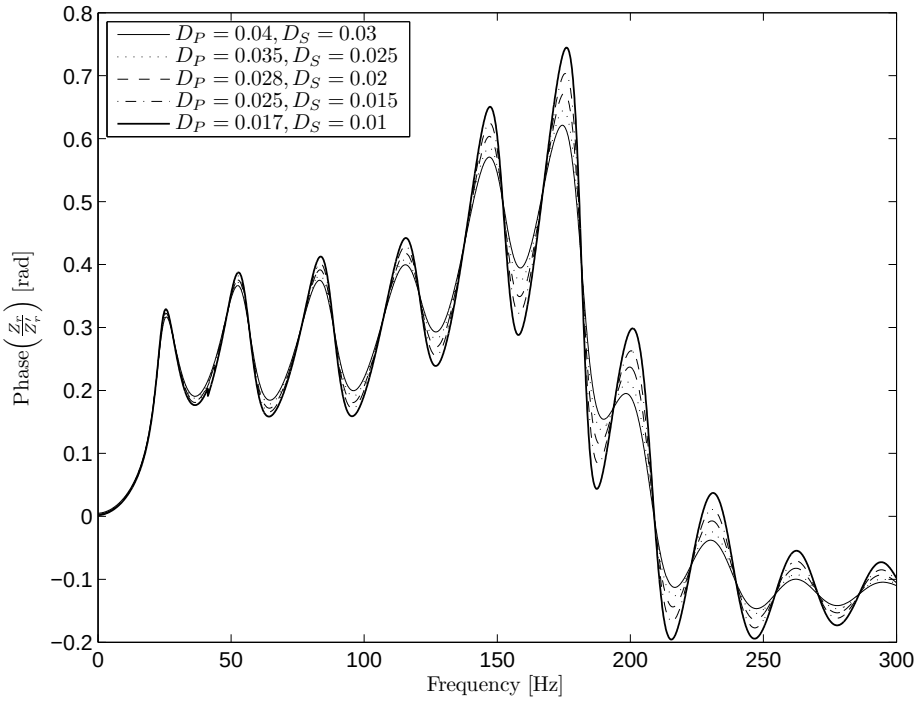


FIGURE 4.17: Adimensional phase of the rail receptance for five different combinations of subgrade damping coefficients $D_P$ and $D_S$ and for the superstructure parameters in Case 4 (see Tables 4.1, 4.2 and 4.3). The other mechanical parameters of the subgrade are equal to the Quaternary ground type (see Table 3.1).

### 4.2.2 Effects of the density

With respect to the density of the subgrade, Figs. 4.18 and 4.19 represent the module and the phase of receptance with various realistic values for it. Complete results for the four Cases of study are presented in Section C.1.3.

For these different values, the results show that the resonant frequency of the in-phase mode ranges between 171.8 Hz and 189.3 Hz and the resonant amplitude ranges between $1.228 \cdot 10^{-8}$ m/N and $1.417 \cdot 10^{-8}$ m/N. Complete results for the resonance are shown in Table 4.5.

| $\rho$ [kg/m$^3$] | $\bar{f}_{1r}$ [Hz] | $\frac{\bar{f}_{1r}}{f'_{1r}}$ [-] | max$\lvert Z_r \rvert$ [m/N] | $\frac{\max\lvert Z_r \rvert}{\max\lvert Z'_r \rvert}$ [-] |
|---|---|---|---|---|
| 1800 | 187.2 | 1.184 | $1.417 \cdot 10^{-8}$ | 1.622 |
| 1950 | 181.7 | 1.149 | $1.391 \cdot 10^{-8}$ | 1.593 |
| 2100 | 176.6 | 1.116 | $1.329 \cdot 10^{-8}$ | 1.521 |
| 2250 | 171.8 | 1.086 | $1.254 \cdot 10^{-8}$ | 1.436 |
| 2400 | 189.3 | 1.197 | $1.228 \cdot 10^{-8}$ | 1.407 |

TABLE 4.5: Results of the resonant frequency and amplitude of track receptance obtained with different subgrade densities.

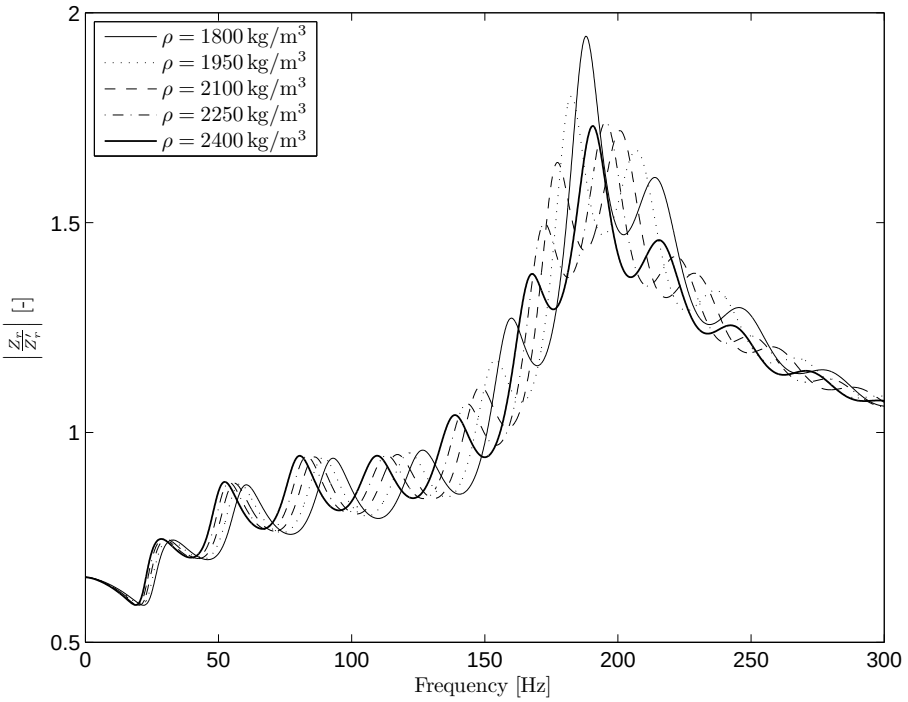


FIGURE 4.18: Adimensional module of the rail receptance for five different subgrade densities and for the superstructure parameters in Case 4 (see Tables 4.1, 4.2 and 4.3). The other mechanical parameters of the subgrade are equal to the Quaternary ground type (see Table 3.1).

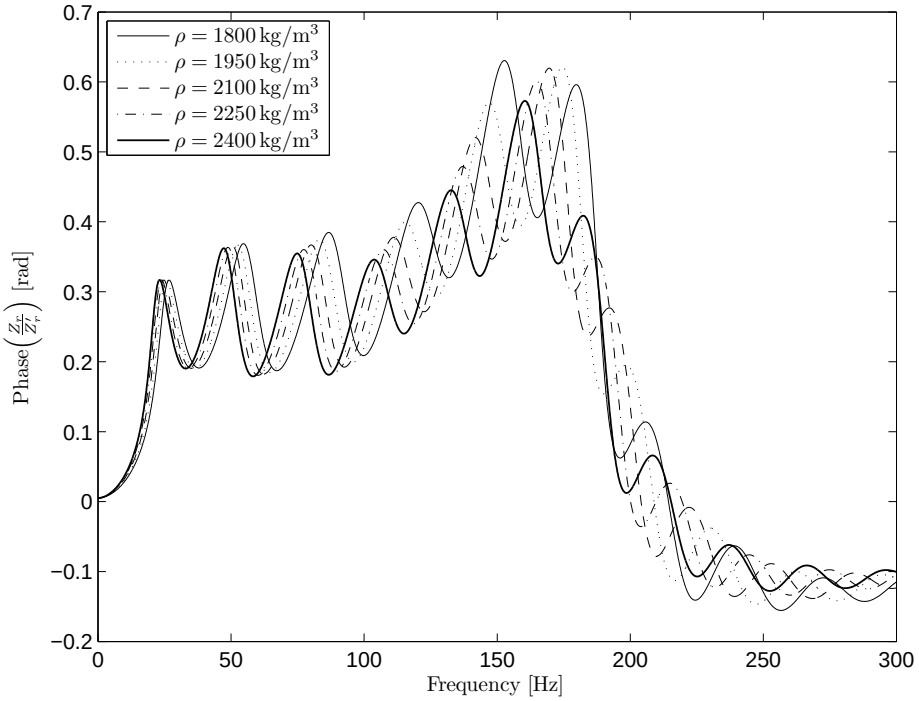


FIGURE 4.19: Adimensional phase of the rail receptance for five different subgrade densities and for the superstructure parameters in Case 4 (see Tables 4.1, 4.2 and 4.3). The other mechanical parameters of the subgrade are equal to the Quaternary ground type (see Table 3.1).

In this case, these results are obtained by setting the other mechanical parameters of the subgrade (Young's modulus $E$, Poisson's ratio $\nu$ and the dampings $D_P$ and $D_S$) equal to the quarternary ground type. It is assumed to have a superstructure width of 3.5 m ($c = 1.75$ m). They show that the density of the subgrade only modifies the phase of the receptance oscillations, therefore it can be assumed to be a low significant parameter.

### 4.2.3 Effects of the Poisson's ratio

With regard to the Poisson's ratio of the subgrade, Figs. 4.20 and 4.21 represent the module and the phase of receptance with various realistic values for it. Complete results for the four Cases of study are presented in Section C.1.4.

For these different values, the results show that the resonant frequency of the in-phase mode ranges between 176.86 Hz and 185.2 Hz and the resonant amplitude ranges between $1.263 \cdot 10^{-8}$ m/N and $1.515 \cdot 10^{-8}$ m/N. Complete results about the resonance are shown in Table 4.6.

| $\nu$ [-] | $\bar{f}_{1r}$ [Hz] | $\frac{\bar{f}_{1r}}{\bar{f}'_{1r}}$ [-] | max$\lvert Z_r \rvert$ [m/N] | $\frac{\max\lvert Z_r \rvert}{\max\lvert Z'_r \rvert}$ [-] |
|---|---|---|---|---|
| 0.2 | 185.2 | 1.17 | $1.515 \cdot 10^{-8}$ | 1.735 |
| 0.25 | 183.5 | 1.16 | $1.465 \cdot 10^{-8}$ | 1.678 |
| 0.3 | 181.7 | 1.149 | $1.391 \cdot 10^{-8}$ | 1.592 |
| 0.35 | 179.5 | 1.135 | $1.307 \cdot 10^{-8}$ | 1.497 |
| 0.4 | 176.86 | 1.118 | $1.263 \cdot 10^{-8}$ | 1.447 |

TABLE 4.6: Results of the resonant frequency and amplitude of track receptance obtained with different subgrade Poisson's ratios.

In this case, these results are obtained by setting the other mechanical parameters of the subgrade (the Young's modulus $E$, the density $\rho$ and the dampings $D_P$ and $D_S$) equal to the quarternary ground type. It is assumed to have a superstructure width of 3.5 m ($c = 1.75$ m). They show that the Poisson's ratio of the subgrade is not a very significant parameter with regard to track receptance in this frequency range in comparison to the other subgrade parameters.

### 4.2.4 Effects of the Young's modulus

Figs. 4.22 and 4.23 represent the module and the phase of the receptance with various realistic values of Young's modulus. Complete results for the four Cases of study are presented in Section C.1.5.

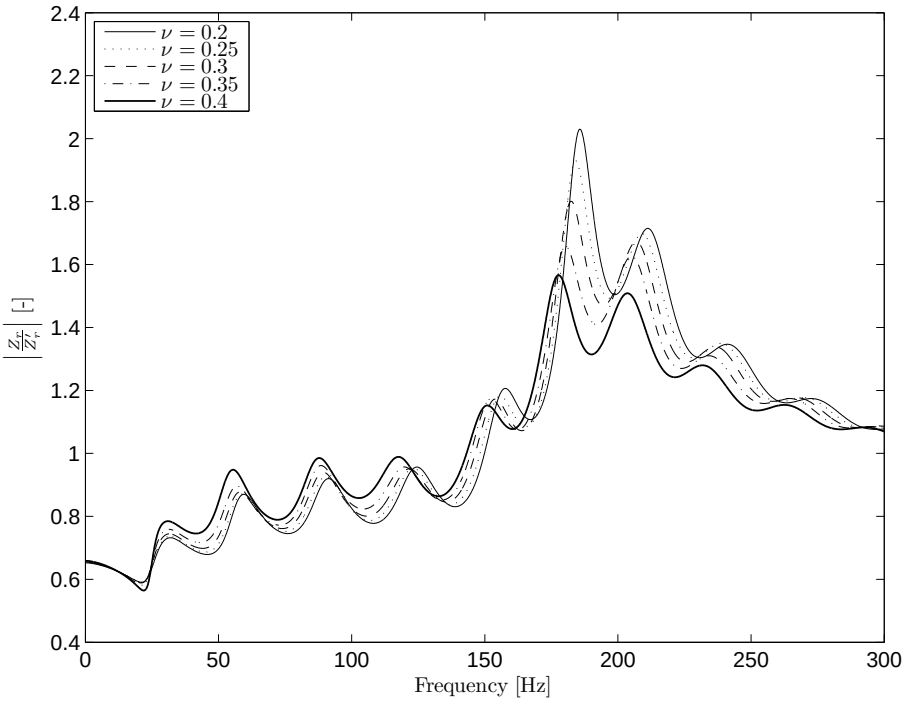


FIGURE 4.20: Adimensional module of the rail receptance for five different Poisson's ratios of the subgrade and for the superstructure parameters in Case 4 (see Tables 4.1, 4.2 and 4.3). The other mechanical parameters of the subgrade are equal to the Quaternary ground type (see Table 3.1).

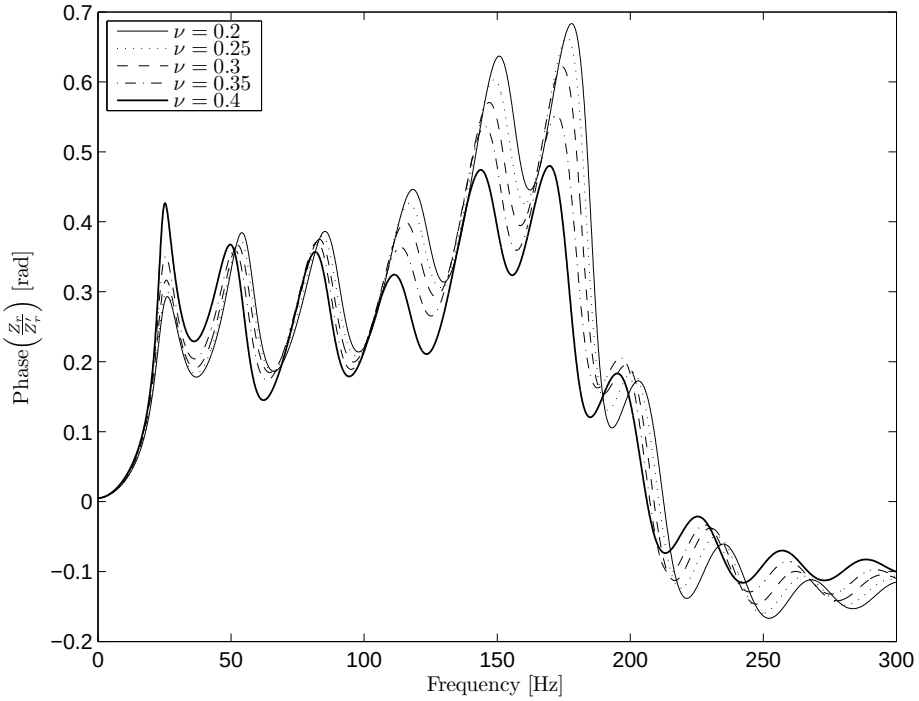


FIGURE 4.21: Adimensional phase of the rail receptance for five different Poisson's ratios of the subgrade and for the superstructure parameters in Case 4 (see Tables 4.1, 4.2 and 4.3). The other mechanical parameters of the subgrade are equal to the Quaternary ground type (see Table 3.1).

For these different values, the results show that the resonant frequency of the in-phase mode ranges between 161 Hz and 181.73 Hz and the resonant amplitude ranges between $8.863 \cdot 10^{-9}$ m/N and $1.593 \cdot 10^{-8}$ m/N. Complete results are shown in Table 4.7.

| $E$ [MPa] | $\bar{f}_{1r}$ [Hz] | $\frac{\bar{f}_{1r}}{\bar{f}'_{1r}}$ [-] | max$\lvert Z_r \rvert$ [m/N] | $\frac{\max\lvert Z_r \rvert}{\max\lvert Z'_r \rvert}$ [-] |
|---|---|---|---|---|
| 20 | 181.73 | 1.159 | $1.391 \cdot 10^{-8}$ | 1.593 |
| 90 | 170.84 | 1.08 | $1.126 \cdot 10^{-8}$ | 1.29 |
| 300 | 169.61 | 1.072 | $9.695 \cdot 10^{-9}$ | 1.11 |
| 1500 | 161 | 1.018 | $9.253 \cdot 10^{-9}$ | 1.06 |
| 4000 | 161.83 | 1.023 | $8.863 \cdot 10^{-9}$ | 1.015 |

TABLE 4.7: Results of the resonant frequency and amplitude of the track receptance obtained with different subgrade Young's modulus.

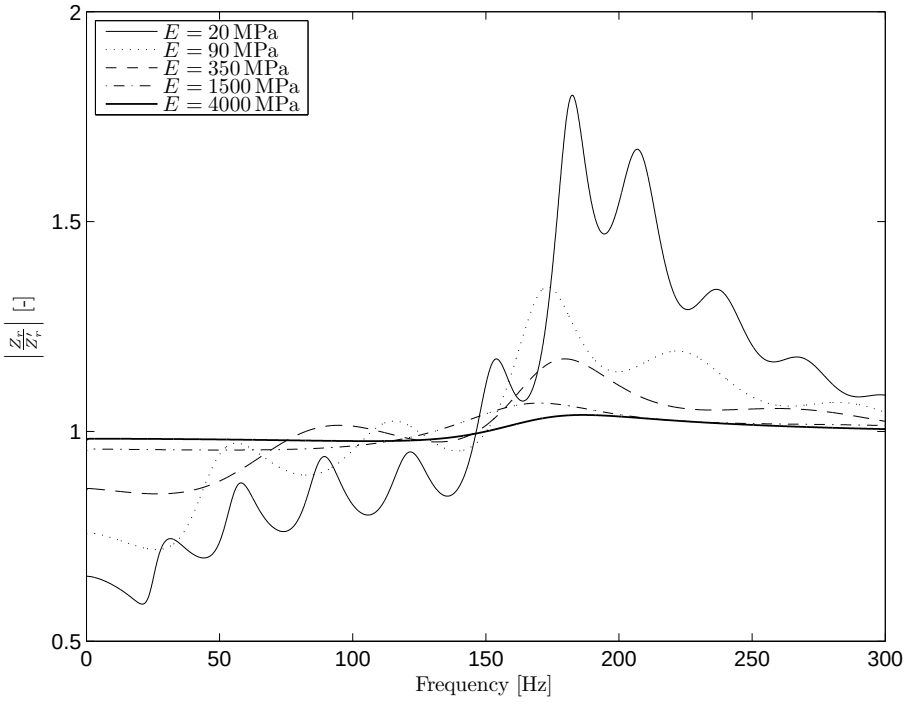


FIGURE 4.22: Adimensional module of the rail receptance for five different Young's modulus of the subgrade and for the superstructure parameters in Case 4 (see Tables 4.1, 4.2 and 4.3). The other mechanical parameters of the subgrade are equal to the Quaternary ground type (see Table 3.1).

In this case, these results are obtained by setting the other mechanical parameters of the subgrade (the Poisson's ratio $\nu$, the density $\rho$ and the dampings $D_P$ and $D_S$) equal to the quaternary ground type. It is assumed to have a superstructure width of 3.5 m ($c = 1.75$ m). They show that the Young's modulus of the subgrade is a significant subgrade mechanical parameter with regard to track receptance. In fact, this is the most significant parameter in view of the results of the other parameters, as can be seen in Sections 4.2.1, 4.2.2, 4.2.3, 4.2.4 and 4.2.5.

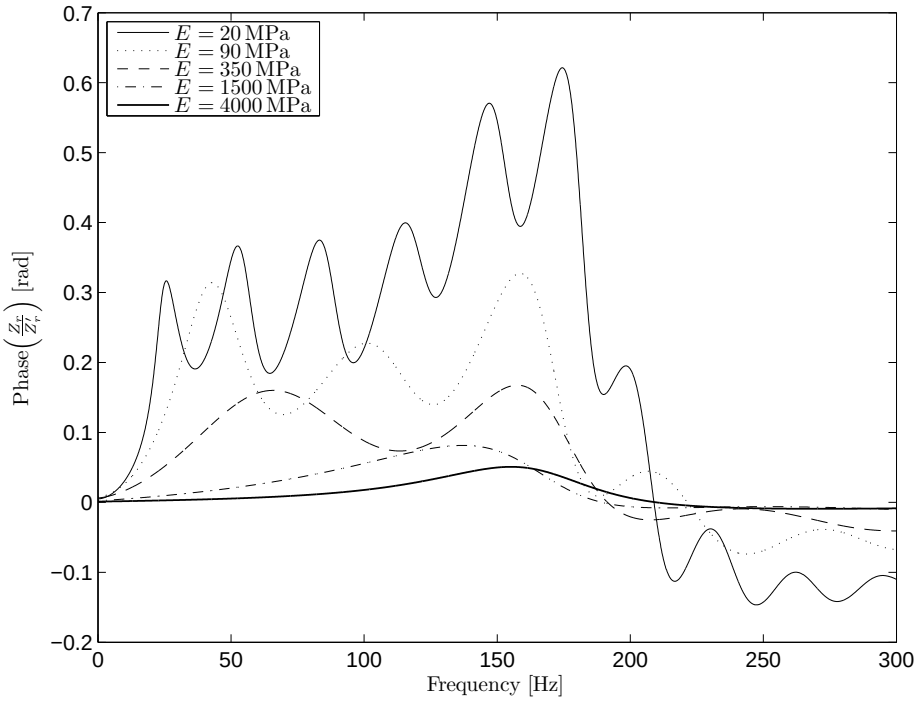


FIGURE 4.23: Adimensional phase of the rail receptance for five different Young's modulus of the subgrade and for the superstructure parameters in Case 4 (see Tables 4.1, 4.2 and 4.3). The other mechanical parameters of the subgrade are equal to the Quaternary ground type (see Table 3.1).

### 4.2.5 Effects of superstructure width

Finally, Figs. 4.24 and 4.25 represent the module and the phase of receptance with various values for superstructure width. Complete results for the four studied Cases are presented in Section C.1.6.

For these different values, the results show that the resonant frequency of the in-phase mode ranges between 168.83 Hz and 200.67 Hz and the resonant amplitude ranges between $1.343 \cdot 10^{-8}$ m/N and $2.048 \cdot 10^{-8}$ m/N. Complete results are shown in Table 4.8.

| $2c$ [m] | $\bar{f}_{1r}$ [Hz] | $\frac{\bar{f}_{1r}}{\bar{f}'_{1r}}$ [-] | $\max\|Z_r\|$ [m/N] | $\frac{\max\|Z_r\|}{\max\|Z'_r\|}$ [-] |
|---|---|---|---|---|
| 2.5 | 200.67 | 1.264 | $1.788 \cdot 10^{-8}$ | 2.048 |
| 3 | 176.1 | 1.113 | $1.491 \cdot 10^{-8}$ | 1.707 |
| 3.5 | 181.73 | 1.149 | $1.391 \cdot 10^{-8}$ | 1.593 |
| 4 | 185.22 | 1.171 | $1.259 \cdot 10^{-8}$ | 1.442 |
| 4.5 | 168.83 | 1.067 | $1.172 \cdot 10^{-8}$ | 1.343 |

TABLE 4.8: Results of the resonant frequency and amplitude of track receptance obtained with different superstructure widths.

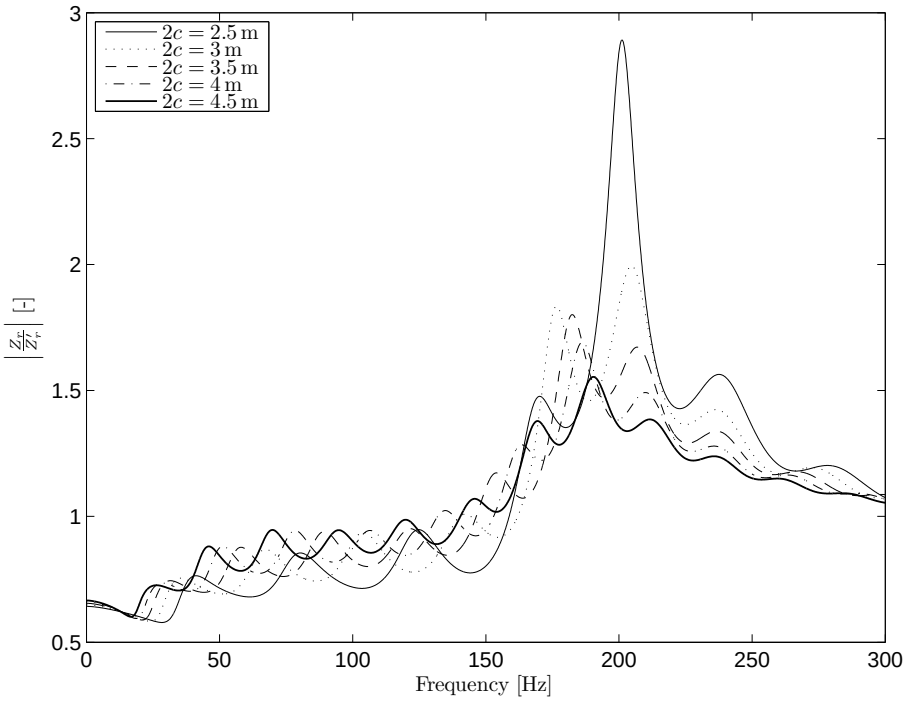


FIGURE 4.24: Adimensional module of the rail receptance for five different widths of the contact area between the superstructure and the subgrade and for the superstructure parameters in Case 4 (see Tables 4.1, 4.2 and 4.3). The other mechanical parameters of the subgrade are equal to the Quaternary ground type (see Table 3.1).

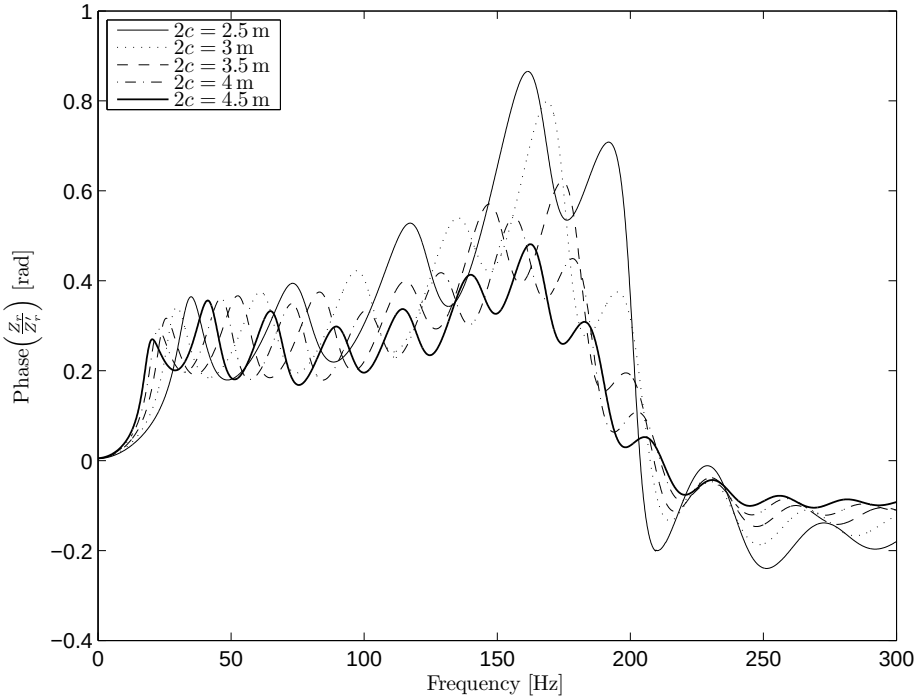


FIGURE 4.25: Adimensional phase of the rail receptance for five different widths of the contact area between the superstructure and the subgrade and for the superstructure parameters in Case 4 (see Tables 4.1, 4.2 and 4.3). The other mechanical parameters of the subgrade are equal to the Quaternary ground type (see Table 3.1).

These results are obtained by setting the mechanical parameters of the subgrade equal to the quaternary ground type. They show that the superstructure width is also a significant parameter with regard to track receptance, but not as much as the effect of Young's modulus.

## 4.3 Fast method to obtain track receptance in the case of subgrade coupling

All the receptances presented in the previous section are calculated using a methodology to reduce the computational effort in the numerical integration, as presented in Section 4.1.3. But the calculation time for these receptances can be reduced further by taking advantage of three particularities, which can be observed in the results: figures and tables presented in Section 4.2:

- The resonant frequency of any case with subgrade coupling does not differ significantly, in general, from the non-coupled case. This advantage is more pronounced when the stiffnesses of the superstructure are low, but for high stiffnesses it is also a good approximation. Furthermore, since the superstructure does not demonstrate very strong viscous damping behaviour, the resonant frequency can be assumed to be similar to the natural frequency of the non-coupled case $\bar{f}_1'$, which is defined in Eq. (B.24). However, some models of superstructure are designed with viscous damping, in Cases 3 and 4 (see Tables 4.2 and 4.3) and as shown by other references [2, 30, 56, 71, 191]. In these cases it is better to use the resonant frequency of the uncoupled case, instead of the natural frequency.
- The receptance solutions are smooth functions of frequency.
- For frequencies above 1.5 times the resonant frequency, the receptance of the non-coupled case can be taken as a good approximation of the receptance of the coupled case.

With these advantages, the exact frequency and amplitude of resonance can be easily evaluated with low computational cost: calculating the receptance at frequencies near the natural frequency of the non-coupled case. These parameters can be calculated with high accuracy by evaluating very few points and by using interpolation methods, as receptance is always a smooth function. The author suggests the use of a cubic spline interpolation in order to achieve more accurate results.

The same method can be used in the evaluation of complete receptance, setting that the most significant frequencies (zero and the resonant frequencies of the in-phase and anti-phase modes) are within the vector calculation points, and considering the maximum of this vector at 1.5 times the natural frequency of the non-coupled case. Above this maximum, the non-coupled solution can be used.

Only for cases with highly stiff superstructures and, at the same time, with soft grounds, the receptance solution differs very significantly from the non-coupled case. In these cases, a more dense vector of calculation points is mandatory to achieve accurate results.

## 4.4 Superstructure equivalent model

As seen in the previous section, the track model coupled with the subgrade have basically two modes which are closely related to the in-phase and anti-phase modes of the non-coupled track model (see Appendix B). Following a non-linear least squares modal analysis method [192] modified to obtain the spatial model instead of the modal model, one can obtain an equivalent 2DOF model, represented in Fig. 4.26, with equivalent masses ($m'_r$ and $m'_s$), stiffnesses ($k'_F$ and $k'_B$) and viscous and/or structural dampings ($c'_F$, $c'_B$ and/or $h'_F$, $h'_B$), by matching the receptances of the two models.

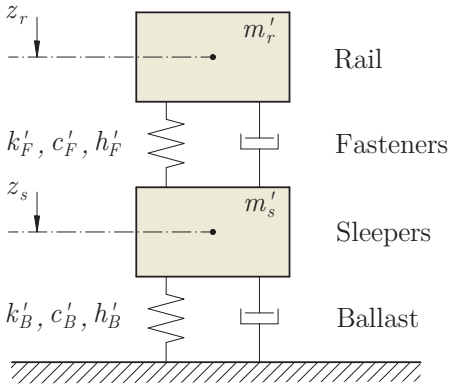


FIGURE 4.26: Equivalent 2DOF model.

### 4.4.1 Superstructure equivalent model with constant parameters

The simplest form of this model assumes that the parameters are constant with respect to the frequency and real-valued. In this case a very accurate adjustment is usually unapproachable. For example, for the parameters in Case 1 (see Tables 4.1, 4.2 and 4.3), the parameters of a quaternary ground (see Table 3.1) and using a least squares curve fitting approach [192], an adjustment is obtained as shown in Figs. 4.27 and 4.28.

The least squares curve fitting approach is implemented using a non-linear least squares algorithm provided by MATLAB, which is called `lsqnonlin`. In this example, only viscous damping is used. Structural damping can be used instead or besides of viscous damping, but no more accurate results are obtained.

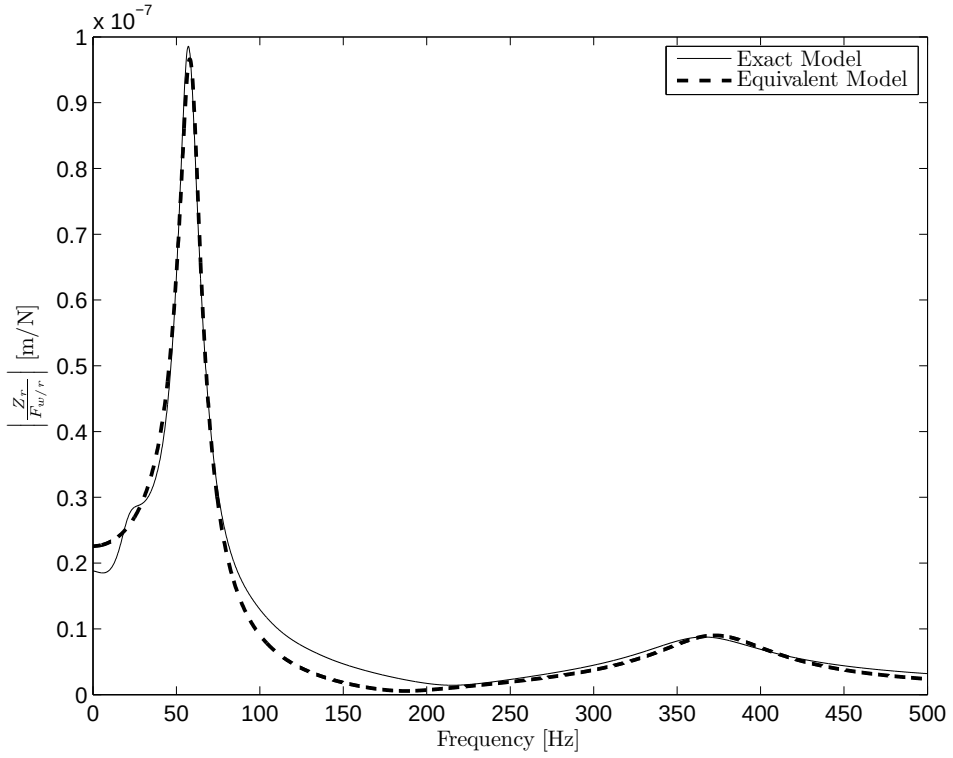


FIGURE 4.27: Exact and adjusted receptances for Case 1 (see Tables 4.1, 4.2 and 4.3) and for a quaternary subgrade (see Table 3.1). Constant parameters. Module.

The parameters of the equivalent model obtained for this case are

| **Equivalent model parameters** | |
|---|---|
| $m'_r$ [kg] | 80.45 |
| $m'_s$ [kg] | 288.57 |
| $k'_F$ [N/m] | $3.447 \cdot 10^8$ |
| $k'_B$ [N/m] | $5.081 \cdot 10^7$ |
| $c'_F$ [N s/m] | $2.716 \cdot 10^4$ |
| $c'_B$ [N s/m] | $3.012 \cdot 10^4$ |

TABLE 4.9: Equivalent model parameters obtained for Case 1 (see Tables 4.1, 4.2 and 4.3) and for a quaternary subgrade (see Table 3.1). Constant parameters.

In Section C.2.1, the results of this fitting for the four cases of superstructure parameters (see Tables 4.1, 4.2 and 4.3) are presented by showing the parameters $m'_r$, $m'_s$, $k'_F$, $k'_B$,

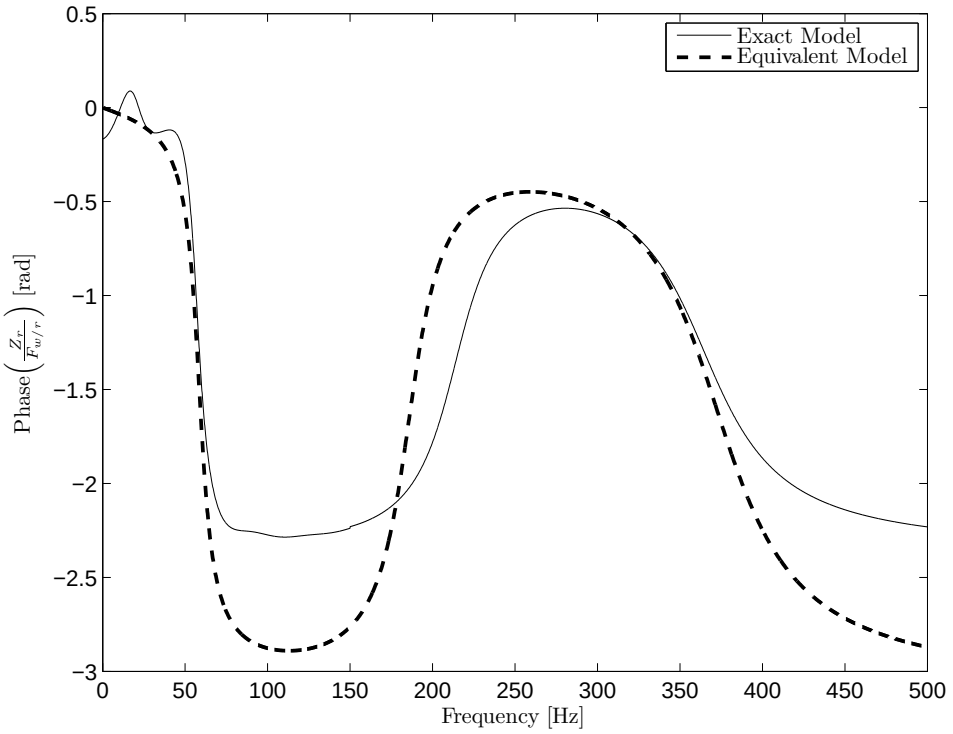


FIGURE 4.28: Exact and adjusted receptances for Case 1 (see Tables 4.1, 4.2 and 4.3) and for a quaternary subgrade (see Table 3.1). Constant parameters. Phase.

$c'_F$ and $c'_B$, only for the case of the quaternary ground type (see Table 3.1).

### 4.4.2 Superstructure equivalent model with frequency dependant parameters

A more sophisticated equivalent model could be that which incorporates a frequency dependant stiffnesses and dampings. Viscous damping models do not allow the achievement of precise adjustments at very low frequencies, because the phase of their response at zero frequency is always null. Therefore, structural damping is used instead. Taking into account these improvements, the fitting can be done with high accuracy.

To achieve this adjustment an algorithm which calculates the equivalent parameters for each frequency is designed. This algorithm calculates analytically these equivalent parameters at zero frequency and uses the `lsqnonlin` algorithm to fit the other frequencies, using the parameters obtained for the previous frequency as starting point values needed by this least squares algorithm. An example of this precise fitting is presented in Figs. 4.29 and 4.30. These equivalent frequency dependant parameters are presented in Figs. 4.31 and 4.32. The masses used in this equivalent model are those obtained for the case of frequency non-dependant parameters (see Table C.1).

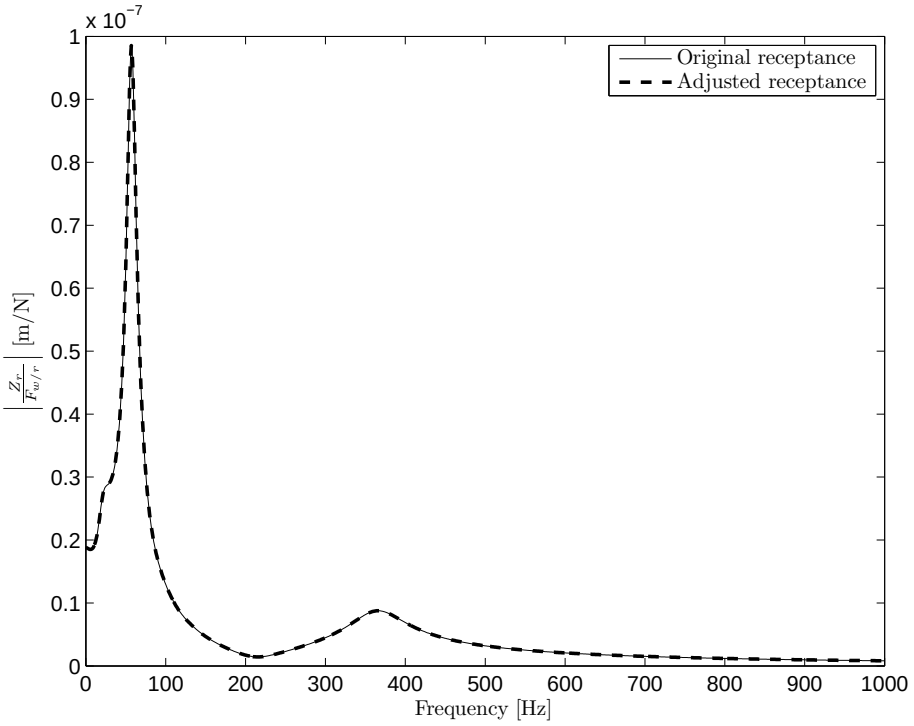


FIGURE 4.29: Exact and adjusted receptances for Case 1 (see Tables 4.1, 4.2 and 4.3) and for a different subgrade parameters (see Table 3.1). Frequency dependant parameters. Module.

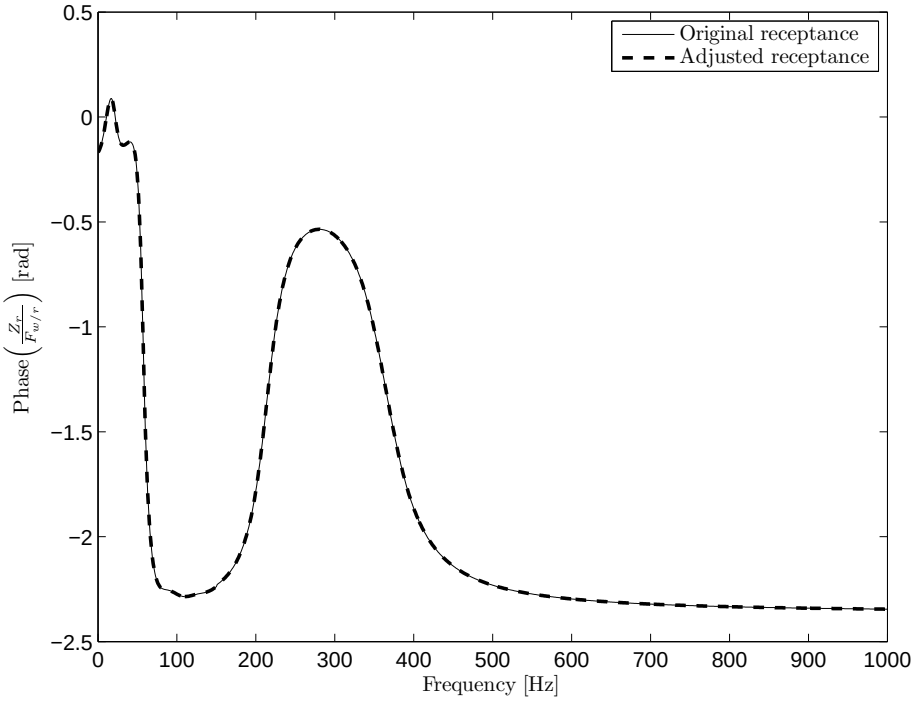


FIGURE 4.30: Exact and adjusted receptances for Case 1 (see Tables 4.1, 4.2 and 4.3) and for a quaternary subgrade (see Table 3.1). Frequency dependant parameters. Phase.

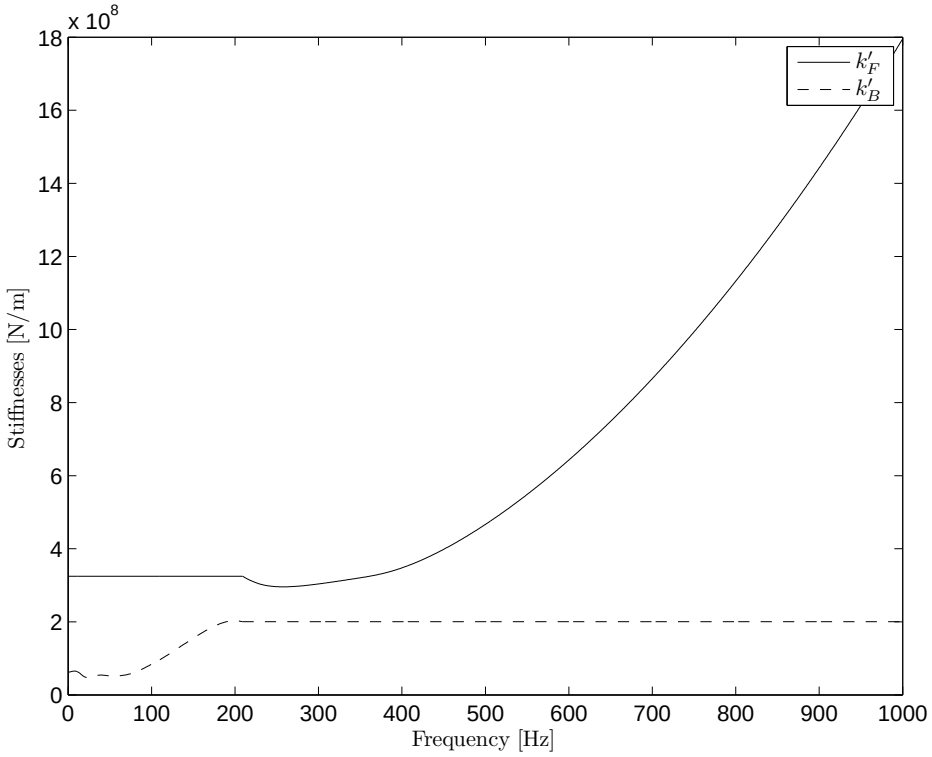


FIGURE 4.31: Fasteners equivalent stiffness as a function of the frequency for Case 1 (see Tables 4.1, 4.2 and 4.3) and for a quaternary subgrade (see Table 3.1).

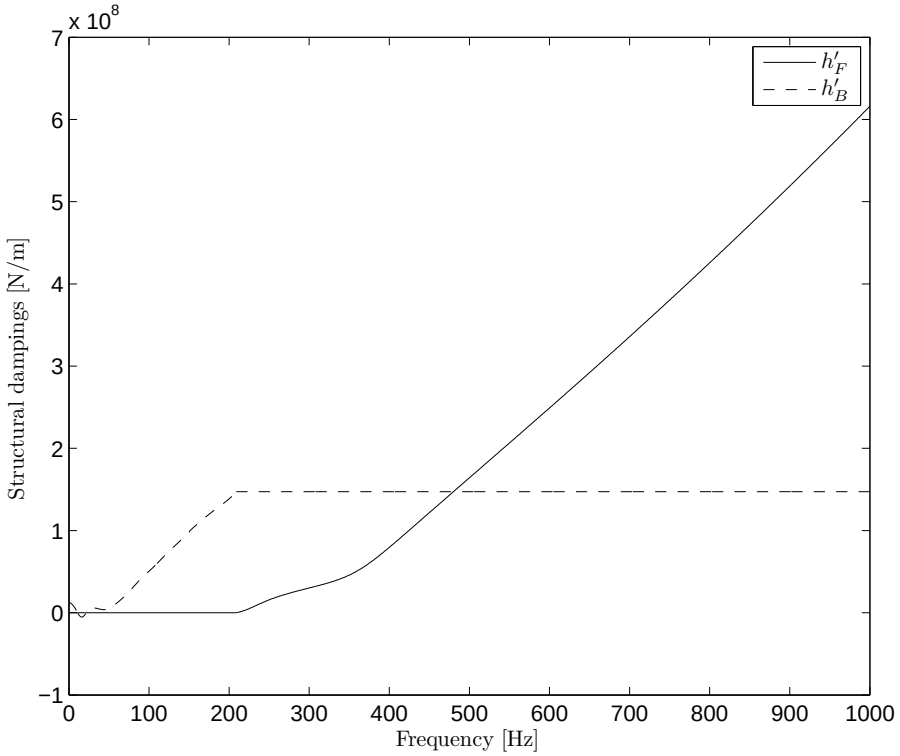


FIGURE 4.32: Fasteners equivalent structural damping as a function of the frequency for Case 1 (see Tables 4.1, 4.2 and 4.3) and for a quaternary subgrade (see Table 3.1).

In Section C.2.2, inside the Appendix C, the results of this fitting for any combination of superstructure and subgrade parameters are presented by showing the parameters $k'_F$, $k'_B$, $h'_F$ and $h'_B$ as a function of the frequency in each case.

## 4.5 Coupling between superstructure and rolling stock

To obtain the wheel/rail dynamic contact force the superstructure model must be coupled with a rolling stock model. A contact force model must be also defined in order to relate the deformation of the solids with the force generated in the contact.

### 4.5.1 Rolling stock model

With regard to the rolling stock, it is modelled as a single DOF model, where the oscillating mass is the unsprung mass. This is linked to the sprung mass with the primary suspension. The sprung mass $m_{\text{sprung}}$ is considered as a non-oscillating body, since its natural frequencies are far below the excitation frequencies generated by the dynamic phenomena of the wheel/rail contact [20]. The sprung mass considered in this model $m_{\text{sprung}}$ is an eighth of the total sprung mass, since it is the mass associated to one wheel. The secondary suspension is not taken into account because primary suspension isolates it for frequencies above 20 Hz [20, 32, 44].

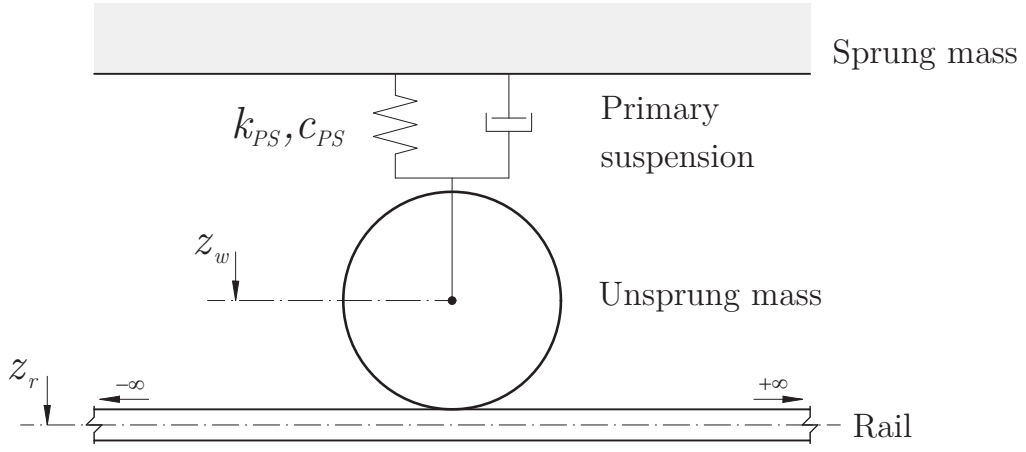


FIGURE 4.33: Rolling stock model

The equation of motion of the wheel is

$$m_w \ddot{z}_w + c_{PS}\dot{z}_w + k_{PS} z_w = -f_{w/r}(t) \tag{4.47}$$

where $m_w$ is the unsprung mass associated to a single wheel, $z_w$ is the vertical displacement of this unsprung mass, $f_{w/r}(t)$ is the wheel/rail dynamic contact force and $k_{PS}$ and $c_{PS}$ are the primary suspension stiffness and viscous damping respectively.

### 4.5.2 Contact force model

The contact between the wheel and the rail is modelled, taking into account only the normal contact between the wheel and the rail, as an elliptical Hertz contact [62], for which the dynamic contact force, based on the non-lineal Hertz contact theory, is

$$f_{w/r}(t) = k_{\text{Hertz}}\, h(t)^{3/2} - (m_w + m_{\text{sprung}})\text{g} \tag{4.48}$$

where $(m_w + m_{\text{sprung}})$g is the static contact force and $m_{\text{sprung}}$ is the sprung mass, both associated only with a single wheel, and where $k_{\text{Hertz}}$ is the non-lineal elasticity constant and $h(t)$ is the joint deformation of the solids in contact; the wheel and the rail in this case. $k_{\text{Hertz}}$ can be calculated from the geometric characteristics of the contact and from the static contact force [1].

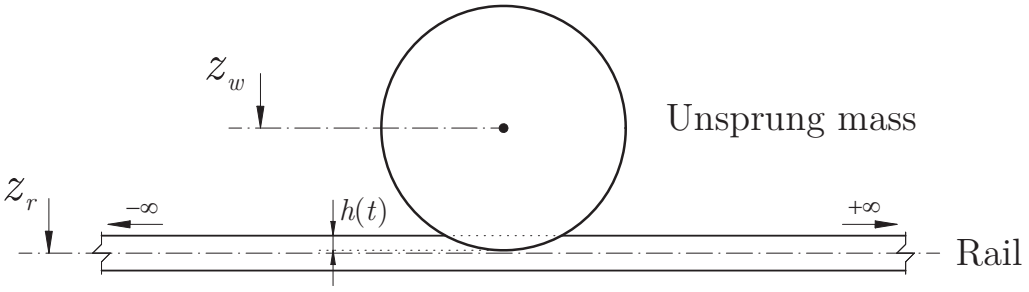


FIGURE 4.34: Joint deformation of the wheel and the rail

Observing the Fig. 4.34 it can be deduced that the Hertz dynamic contact force can be defined as a function of the wheel and rail vertical displacements as follows

$$f_{w/r}(t) = k_{\text{Hertz}}\, \left[z_w - z_r + \epsilon(t) + h_0\right]^{3/2} - (m_w + m_{\text{sprung}})\text{g} \tag{4.49}$$

where $\epsilon(t)$ is the sum of wheel and rail irregularities (whenever they are considered positive when they generate solid dimensions enlargements) $\epsilon(t) = \epsilon_w(t) + \epsilon_r(t)$, and where $h_0$ is the static deformation defined by

$$h_0 = \left[\frac{(m_w + m_{\text{sprung}})\text{g}}{k_{\text{Hertz}}}\right]^{2/3} \tag{4.50}$$

Eq. (4.49) is valid only when $h(t) > 0$; in the opposite case the bodies would be separated and, therefore, the contact force would be null.

As is demonstrated by Otero [1], the contact force model can be assumed to only contemplate one wheel, since the effect of the other wheel of the bogie on the contact point of the first is not excessively significant.

A simpler model is that which considers dynamic contact force as a linear function of deformation. As this model is linear, it can be solved in the frequency domain instead of the non-lineal model, which must be solved in the time domain. For this linear model

$$f_{w/r}(t) = k_{\text{Hertz}}^{\text{lin}} \ [z_w - z_r + \epsilon(t)] \tag{4.51}$$

where

$$k_{\text{Hertz}}^{\text{lin}} = \left.\frac{\mathrm{d}f_{w/r}}{\mathrm{d}h}\right|_{h=h_0} = \frac{3}{2} k_{\text{Hertz}} \sqrt{h_0} \tag{4.52}$$

As Otero [1] has demonstrated, the linearised model do not works properly for important singularities of the rail or the wheel, as for example wheel flats or rail transverse fissures. But, as demonstrated in the next section, this model gives good results when the irregularities of the rail and the wheel are smooth and stationary.

With regard to the equivalent models presented in Section 4.4, the first one (constant parameters) can be used with both contact force models presented. The model with frequency dependant parameters can also be used with both contact models but, as the non-linear model must be solved in the time domain, the frequency dependance of the stiffnesses and structural damping entails some difficulties. Some approaches have been developed to solve this problems, allowing to work with frequency dependant parameters in the time domain [193–195]. Obviously, the implementation of these methods means more computational time used for the contact force evaluation procedure.

### 4.5.3 Wheel/rail contact force evaluation

Once the rolling stock model and the contact force model have been defined, a complete model can be constructed by coupling them with one of the 2DOF equivalent models of the superstructure presented in Section 4.4. Fig. 4.35 represents this complete model.

For the case of the non-linear contact force model, the governing equations of the complete model can be written in a compacted form as

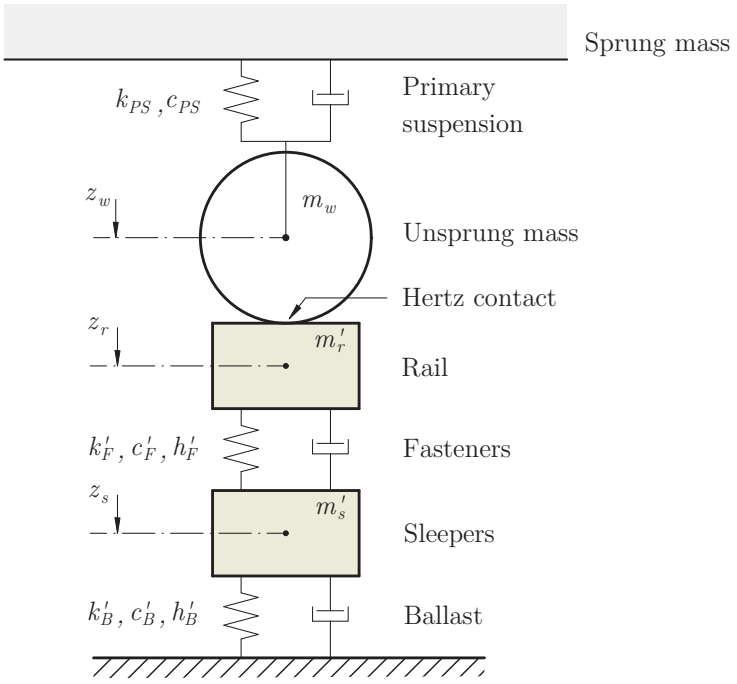


FIGURE 4.35: Complete model: Rolling stock model + Contact force model + 2DOF superstructure equivalent model

$$\begin{bmatrix} m_w & & \\ & m'_r & \\ & & m'_s \end{bmatrix} \begin{Bmatrix} \ddot{z}_w \\ \ddot{z}_r \\ \ddot{z}_s \end{Bmatrix} + \begin{bmatrix} c_{PS} & & \\ & c'_F & -c'_F \\ & -c'_F & c'_F + c'_B \end{bmatrix} \begin{Bmatrix} \dot{z}_w \\ \dot{z}_r \\ \dot{z}_s \end{Bmatrix} + \\ + \begin{bmatrix} k_{PS} & & \\ & k'_F & -k'_F \\ & -k'_F & k'_F + k'_B \end{bmatrix} \begin{Bmatrix} z_w \\ z_r \\ z_s \end{Bmatrix} = \begin{Bmatrix} -f_{w/t} \\ f_{w/t} \\ 0 \end{Bmatrix} \quad (4.53)$$

Introducing Eq. (4.48) in Eq. (4.53) results in a system consisting of three ordinary differential equations. To solve this system an algorithm provided by MATLAB is used (`ode23`) which is the implementation of an explicit Runge-Kutta formulae.

On the other hand, the governing differential equations of the linearised model can be written as

$$\begin{bmatrix} m_w & & \\ & m'_r & \\ & & m'_s \end{bmatrix} \begin{Bmatrix} \ddot{z}_w \\ \ddot{z}_r \\ \ddot{z}_s \end{Bmatrix} + \begin{bmatrix} c_{PS} & & \\ & c'_F & -c'_F \\ & -c'_F & c'_F + c'_B \end{bmatrix} \begin{Bmatrix} \dot{z}_w \\ \dot{z}_r \\ \dot{z}_s \end{Bmatrix} + \\ + \begin{bmatrix} k_{PS} + k^{\text{lin}}_{\text{Hertz}} & -k^{\text{lin}}_{\text{Hertz}} & \\ -k^{\text{lin}}_{\text{Hertz}} & k'_F + k^{\text{lin}}_{\text{Hertz}} & -k'_F \\ & -k'_F & k'_F + k'_B \end{bmatrix} \begin{Bmatrix} z_w \\ z_r \\ z_s \end{Bmatrix} = \begin{Bmatrix} k^{\text{lin}}_{\text{Hertz}} \epsilon(t) \\ -k^{\text{lin}}_{\text{Hertz}} \epsilon(t) \\ 0 \end{Bmatrix} \tag{4.54}$$

Transforming to the frequency domain and performing trivial operations one can obtain the following transfer functions:

$$\frac{Z_r}{\epsilon(\omega)} = \frac{k^{\text{lin}}_{\text{Hertz}} - T(\omega)}{k^{\text{lin}}_{\text{Hertz}} + k'_F + \mathrm{i}\omega c_{PS} - \omega^2 m_w} \tag{4.55}$$

$$\frac{Z_w}{\epsilon(\omega)} = \frac{T(\omega)}{k^{\text{lin}}_{\text{Hertz}}} \left[ \frac{Z_r}{\epsilon(\omega)} - 1 \right] \tag{4.56}$$

$$\frac{Z_s}{\epsilon(\omega)} = \frac{Q(\omega)}{k'_F + \mathrm{i}\omega c'_F} \frac{Z_r}{\epsilon(\omega)} \tag{4.57}$$

where

$$T(\omega) = \frac{{k^{\text{lin}}_{\text{Hertz}}}^2}{k^{\text{lin}}_{\text{Hertz}} + k_{PS} + \mathrm{i}\omega c_{PS} - \omega^2 m_w} \tag{4.58}$$

and where $Q(\omega)$ must be calculated, in this case, substituting the equivalent 2DOF model parameters ($k'_F$, $h'_F$, $c'_F$, $m'_s$, $k'_B$, $h'_B$, $c'_B$) into Eq. (4.10).

Finally, using Eq. (4.51), the transfer function between the wheel/rail dynamic contact force and the roughness excitation is

$$\frac{F_{w/r}}{\epsilon(\omega)} = k^{\text{lin}}_{\text{Hertz}} \left[ \frac{Z_w}{\epsilon(\omega)} + \frac{Z_r}{\epsilon(\omega)} + 1 \right] \tag{4.59}$$

For this linearised model, the response of the system can be easily and quickly evaluated by applying Fourier transform (on the excitation: $TF\left[\epsilon(t)\right] = \epsilon(\omega)$) and anti-transforms (on the responses: $TF^{-1}\left[\frac{Z_w}{\epsilon(\omega)}\epsilon(\omega), \frac{Z_r}{\epsilon(\omega)}\epsilon(\omega), \frac{F_{w/r}}{\epsilon(\omega)}\epsilon(\omega)\right] = z_w, z_r, f_{w/r}$) using a Fast Fourier Transform algorithm. If the structural dampings $h'_F$ or $h'_B$ are no set null, the transfer functions $\frac{Z_w}{\epsilon(\omega)}$, $\frac{Z_r}{\epsilon(\omega)}$ and $\frac{F_{w/r}}{\epsilon(\omega)}$ are complex at $\omega = 0$. Thus, the responses in

the time domain will be also complex. The imaginary part of these responses must be removed to obtain a physical time signal [194].

Having defined their formulation, a comparison between these non-linear and linear contact force models is performed. The roughness profiles of the wheel and the rail used to obtain these results are presented in Fig. 4.36. These profiles are taken from measurements done in different placements of the Catalonia rail network, in the frame of the CATdBTren project (www.catdbtren.cat). These measurements are performed using a rough meter developed and constructed by Ødegaard & Danneskiold-Samsøe (Rail recording frame type TRM 02 and wheel recording frame type RRM 02) based on the standards [69, 70]. The contact filter proposed by Remington [196] is used to treat these roughness signals adequately.

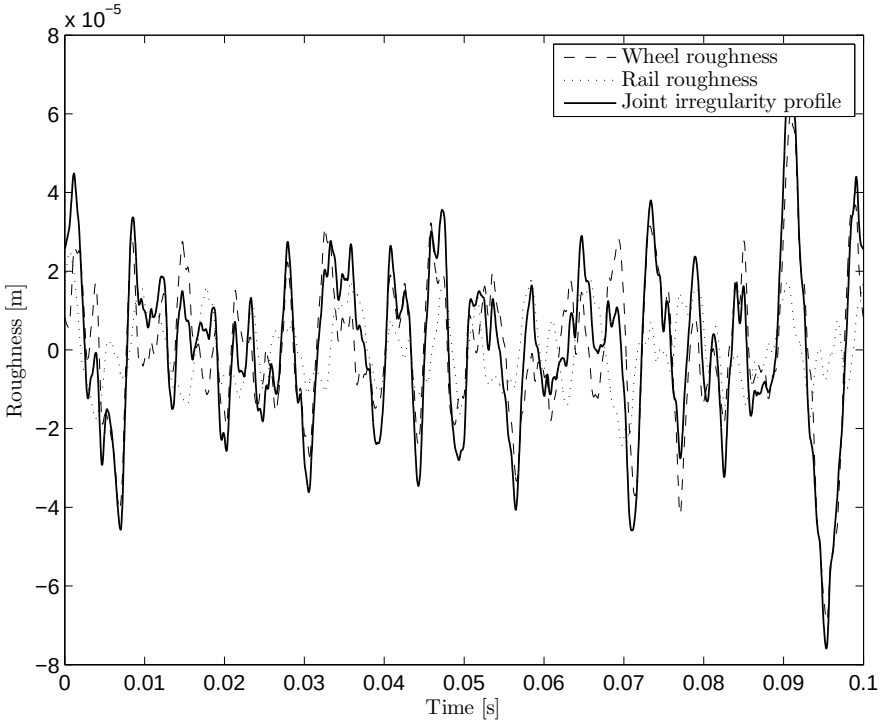


FIGURE 4.36: Roughness profiles used in the comparison of the non-linear and linear contact models.

To transform the roughness spatial profile into a time history, a train velocity of 25 m/s is assumed. The other rolling stock parameters used in this calculation are shown in Table 4.10. Using the 2DOF equivalent model of the superstructure with constant parameters for Case 1 and for a quaternary ground (see Table 4.9) the responses to its excitation are obtained for both procedures. The results are shown in Figs. 4.37, 4.38 and 4.39, where it is observed that the differences between the two models are negligible for times when the transient initial behaviour of the Runge-Kutta numerical integration procedure have already vanished. This has been checked for any combination of superstructure and subgrade parameters, and for other roughness excitations. Therefore, the linearised

contact force model are adopted since it gives sufficiently accurate results and involves very low computational time.

| **Rolling stock parameters** | | |
|---|---|---|
| $m_{\text{sprung}}$ | [kg] | 6000 |
| $m_w$ | [kg] | 500 |
| $k_{\text{Hertz}}$ | [N/m$^{3/2}$] | $8.937 \cdot 10^{10}$ |
| $k_{PS}$ | [N/m] | $2.2 \cdot 10^{7}$ |
| $c_{PS}$ | [N s/m] | $4.9 \cdot 10^{3}$ |

TABLE 4.10: Rolling stock parameters. Source: [1] and [2] for the viscous damping. These are typical bibliography values.

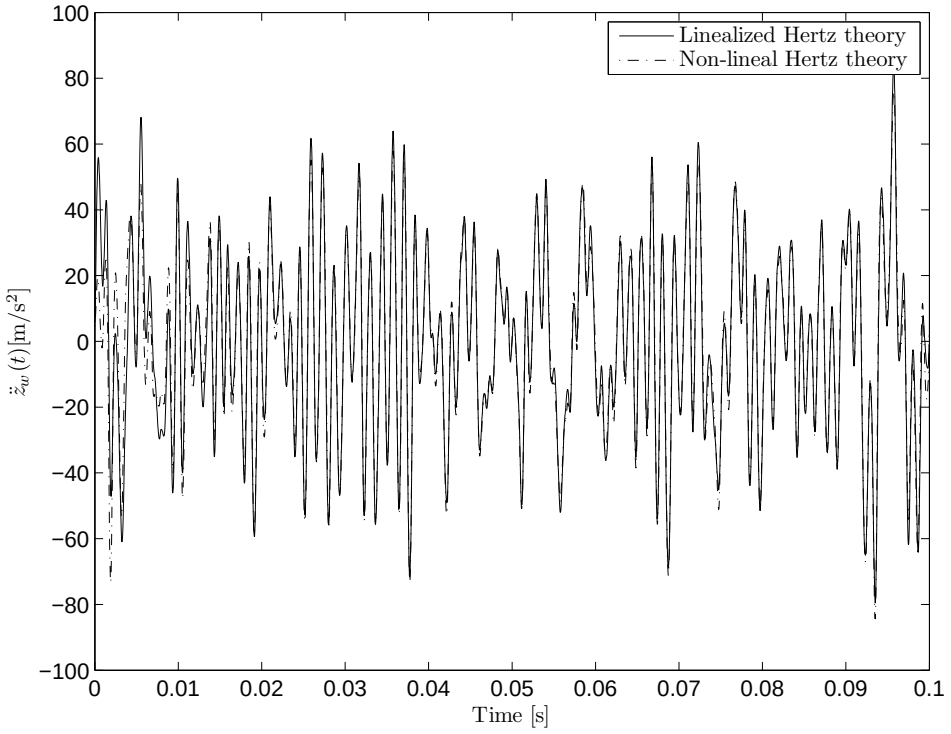


FIGURE 4.37: Comparison between the non-linear and linearised contact models. Wheel vertical accelerations.

### 4.5.4 Indirect evaluation of the roughness time histories

The rail or wheel roughness are random stationary ergodic processes [64–67]. They can be described in the wavenumber or wavelength domain by the module of their Power Spectral Density (PSD) or by standard octave bands [61]. These descriptions do not take into account the phase information of the transform, making an exact inversion process impossible. However, Lu Sun [68] and other authors [16, 45] propose a method

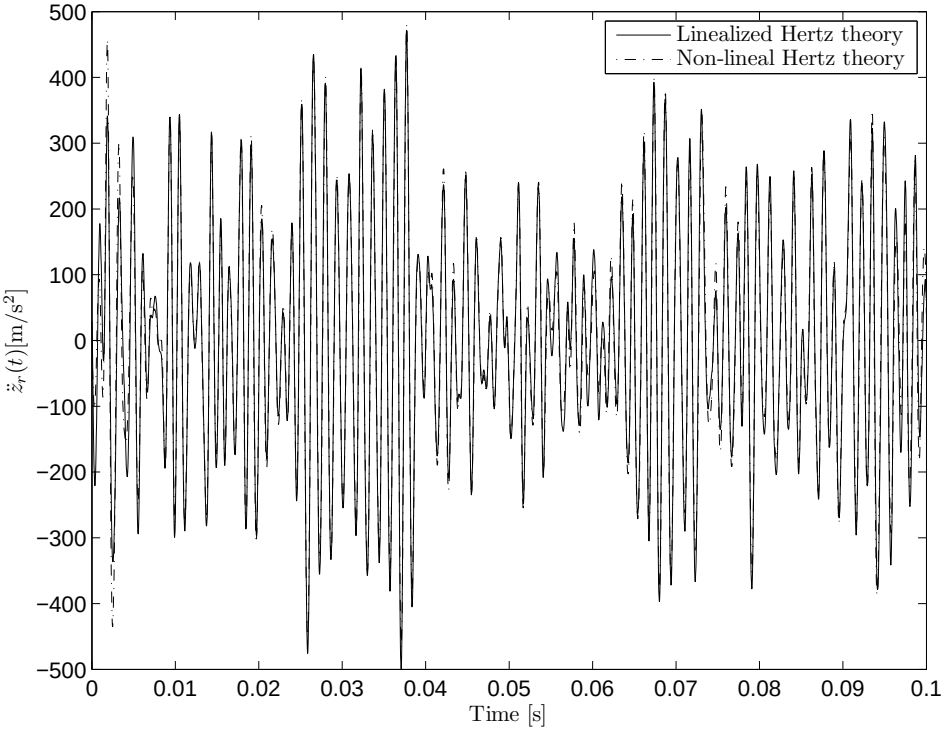


FIGURE 4.38: Comparison between the non-linear and linearised contact models. Rail vertical accelerations.

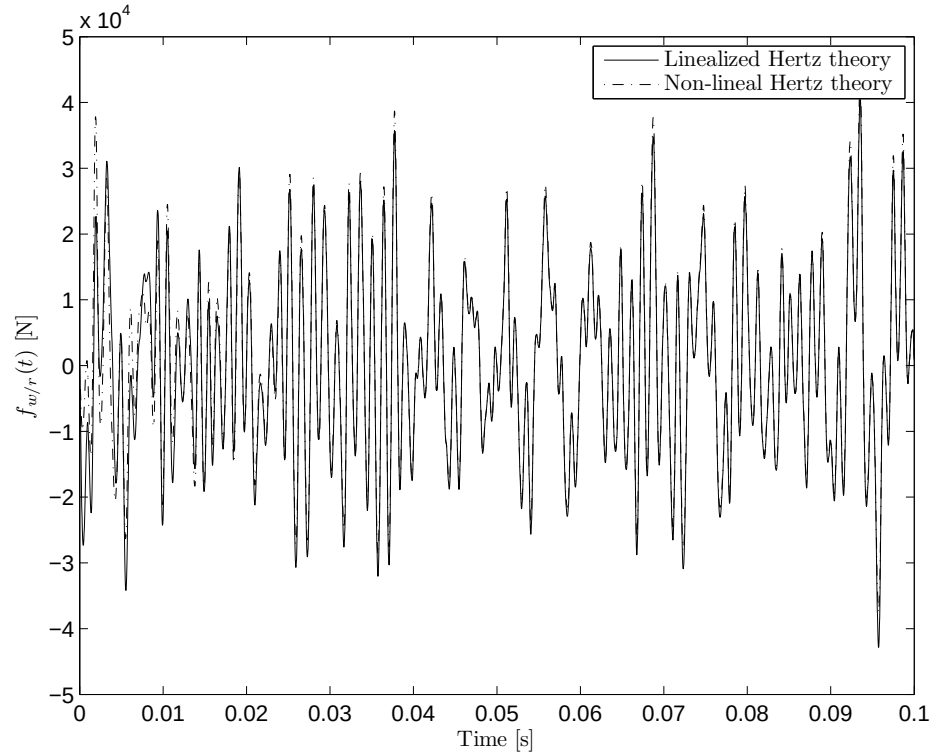


FIGURE 4.39: Comparison between the non-linear and linearised contact models. Wheel/rail dynamic contact force.

to obtain roughness random time histories which are described by the same PSD for example, based on the use a combination of triangular series [73]. The principal concept involved in this procedure is to represent a stochastic process in terms of the sum of a certain number of cosine functions with uniform distribution random phase.

To obtain an approximation of the aleatory roughness spatial histories of any spatial period, the original roughness PSD can be randomly interpolated and rescaled, imposing that the total energy of the signal has to remain unchanged. This procedure can also be used when the roughness spectral information has been defined as the form of one-third octave bands.

This approach is developed using some random parameters. Therefore, the resulting simulated process is not a unique solution. In fact, there are infinite possible simulated processes which satisfy the original PSD distribution.

## 4.6 Influence of the subgrade parameters on the wheel/rail contact force

Finally, the effects of the subgrade on the wheel/rail dynamic contact force are presented in this section. Figs. 4.40, 4.41, 4.42, 4.43, 4.44, 4.45, 4.46 and 4.47 display the transfer function between the wheel/rail dynamic contact force and the roughness excitation (Eq. (4.59)) for the four cases of superstructure parameters (see Tables 4.1, 4.2 and 4.3) and for five different subgrade parameters of the Table 3.1. The superstructure equivalent model with frequency dependant parameters 4.4.2 is used to obtain these transfer functions. In Sections C.3.2 and C.3.1, the responses of the wheel and the rail due to the roughness excitation are also presented.

As can be seen in these figures, the influence of the subgrade parameters on wheel/rail dynamic contact force is more intense when for high stiffness tracks combined with low stiffness grounds. As shown in Section 4.2, the influence of the subgrade parameters on the track receptance behaves in the same manner.

As can also be observed, the effects of the subgrade parameters on the wheel/rail dynamic contact force are significant solely near the resonance of the in-phase mode of the complete model. Note that this resonance is always below the resonance of the in-phase mode shown in the results of the track receptance (Section 4.2) since the unsprung mass incorporated by the rolling stock model reduces the natural frequencies of the system.

Finally, a evaluation example of wheel/rail dynamic contact force is presented here. The module of the joint roughness PSD used to do this calculation is shown in Fig. 4.48. The

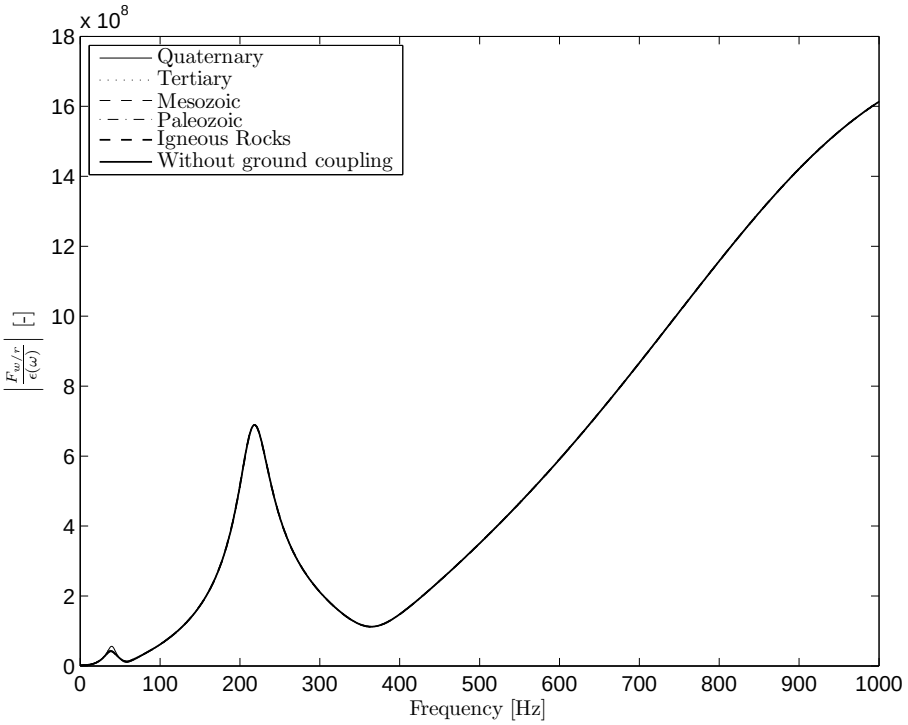


FIGURE 4.40: Module of the transfer function between the wheel/rail dynamic contact force and the roughness excitation for Case 1 (see Tables 4.1, 4.2 and 4.3) and for five different subgrade parameters in Table 3.1.

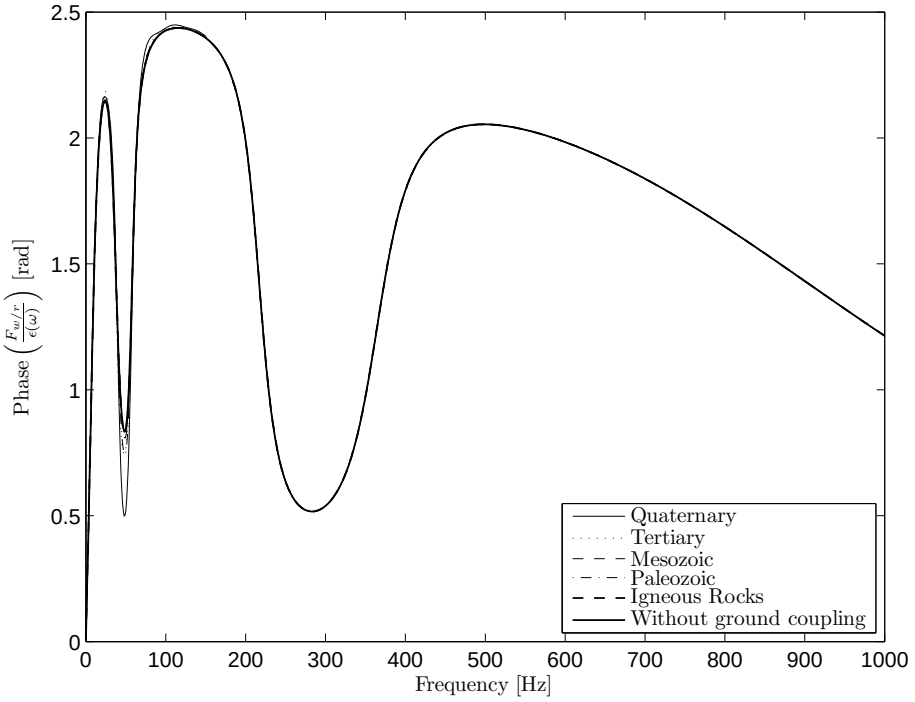


FIGURE 4.41: Phase of the transfer function between the wheel/rail dynamic contact force and the roughness excitation for Case 1 (see Tables 4.1, 4.2 and 4.3) and for five different subgrade parameters in Table 3.1.

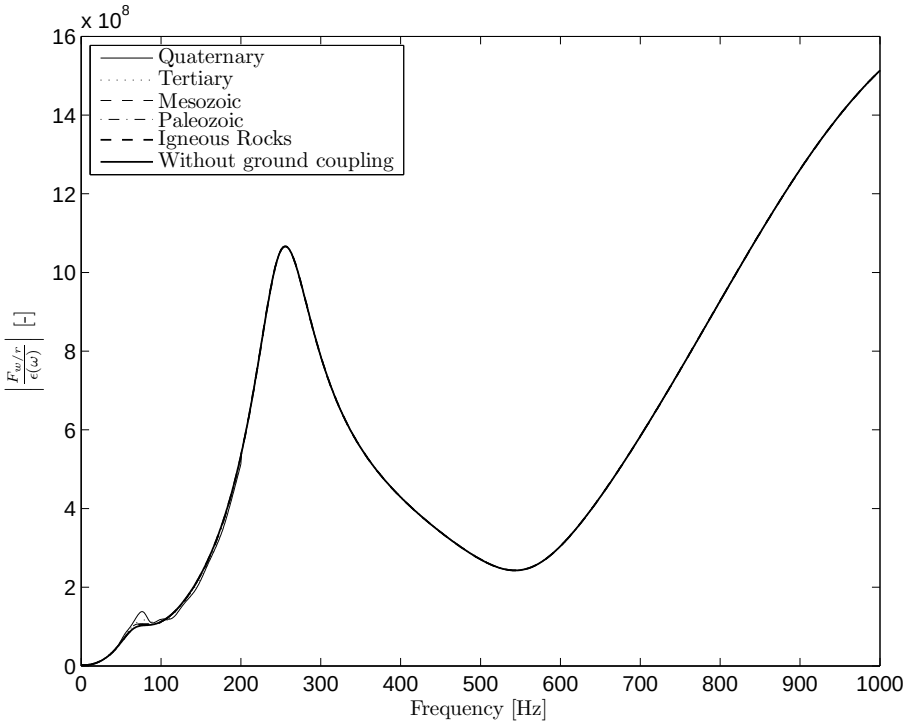


FIGURE 4.42: Module of the transfer function between the wheel/rail dynamic contact force and the roughness excitation for Case 2 (see Tables 4.1, 4.2 and 4.3) and for five different subgrade parameters in Table 3.1.

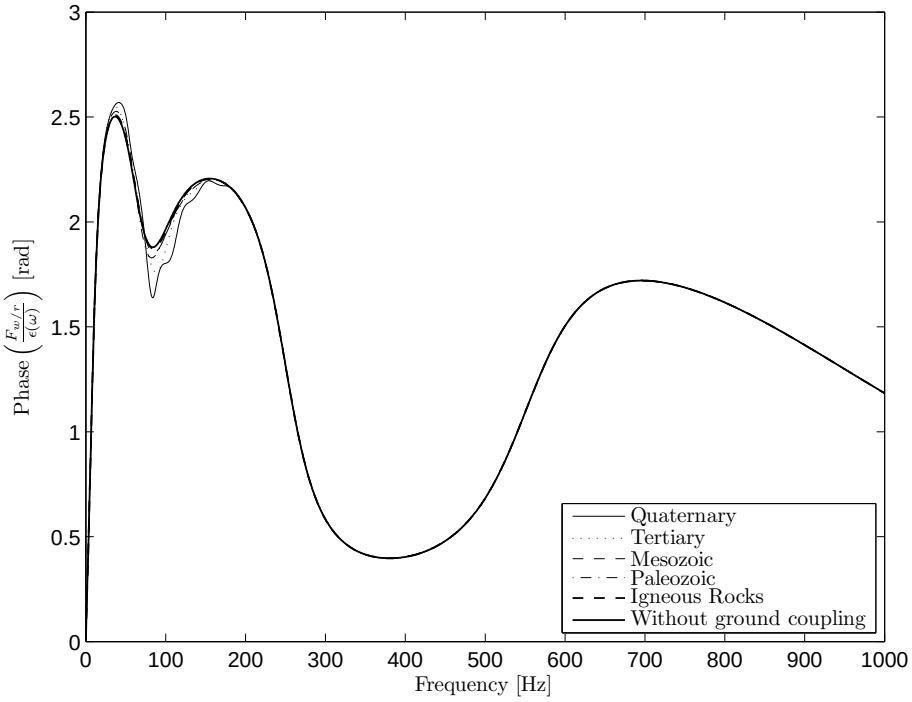


FIGURE 4.43: Phase of the transfer function between the wheel/rail dynamic contact force and the roughness excitation for Case 2 (see Tables 4.1, 4.2 and 4.3) and for five different subgrade parameters in Table 3.1.

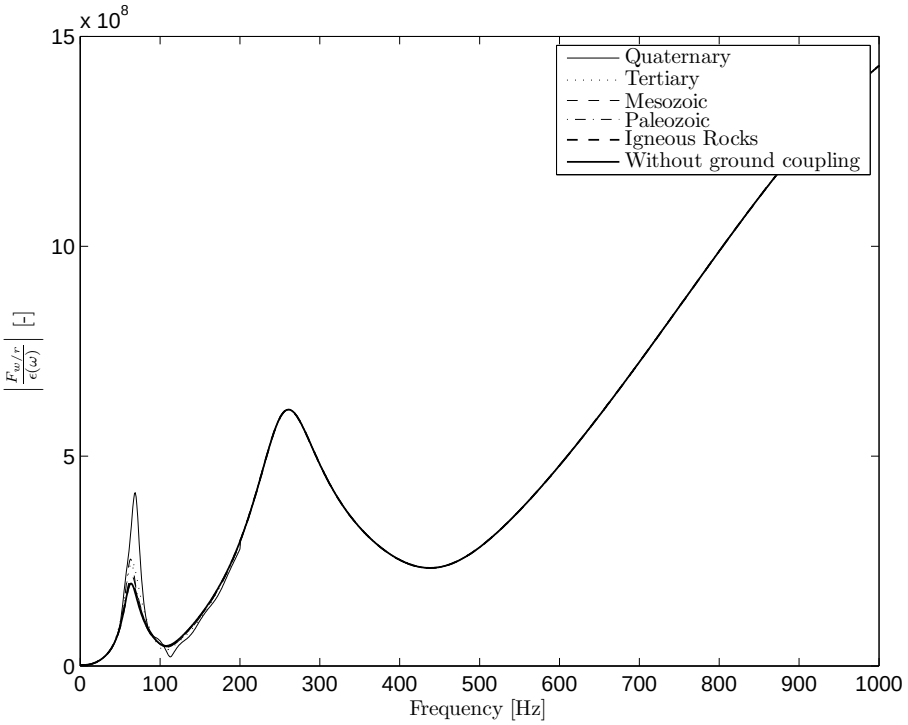


FIGURE 4.44: Module of the transfer function between the wheel/rail dynamic contact force and the roughness excitation for Case 3 (see Tables 4.1, 4.2 and 4.3) and for five different subgrade parameters in Table 3.1.

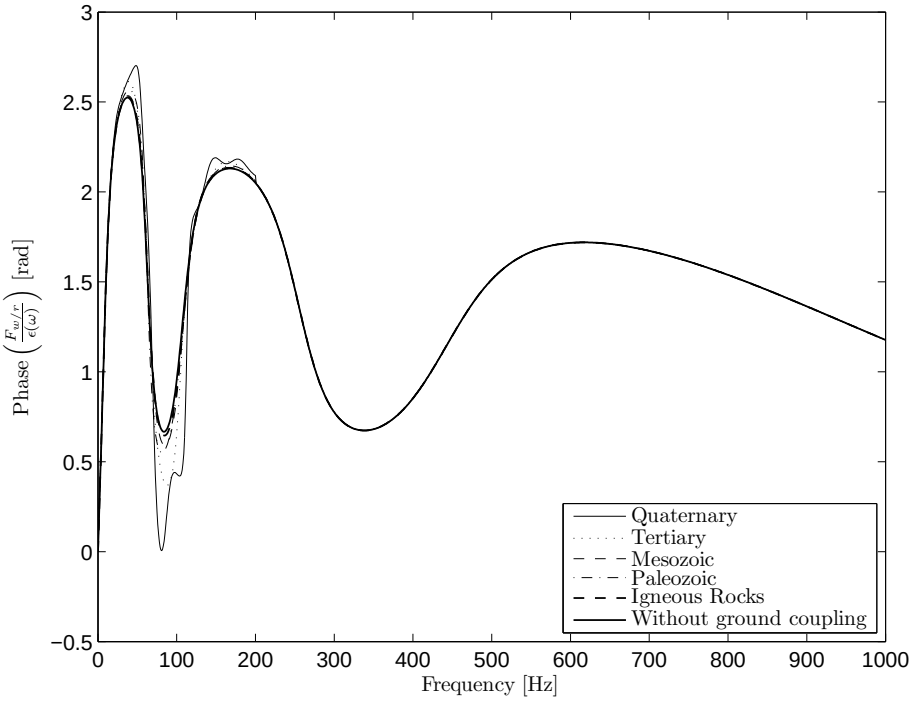


FIGURE 4.45: Phase of the transfer function between the wheel/rail dynamic contact force and the roughness excitation for Case 3 (see Tables 4.1, 4.2 and 4.3) and for five different subgrade parameters in Table 3.1.

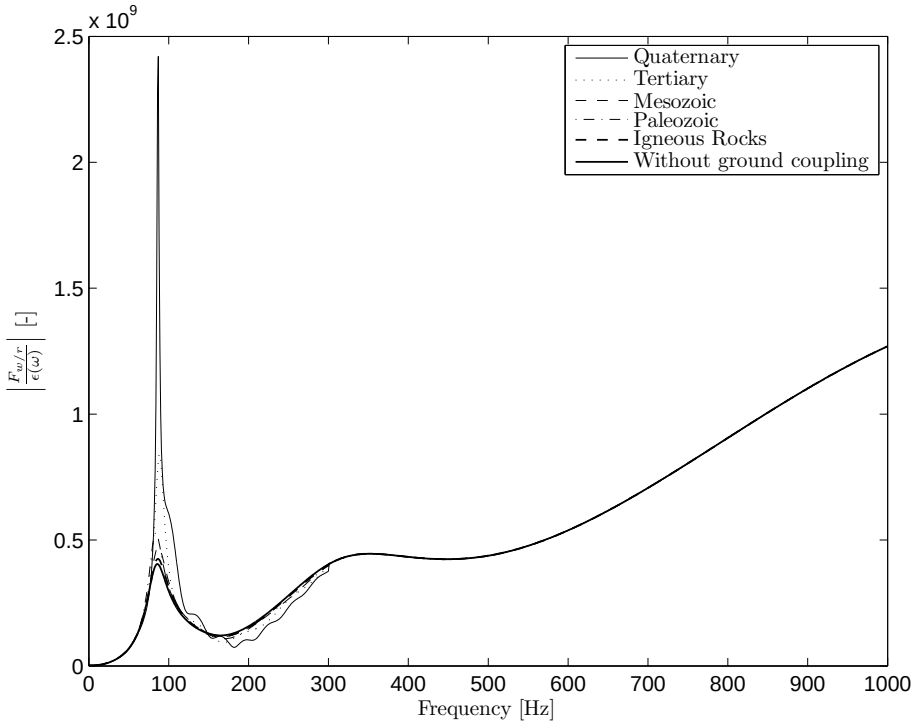


FIGURE 4.46: Module of the transfer function between the wheel/rail dynamic contact force and the roughness excitation for Case 4 (see Tables 4.1, 4.2 and 4.3) and for five different subgrade parameters in Table 3.1.

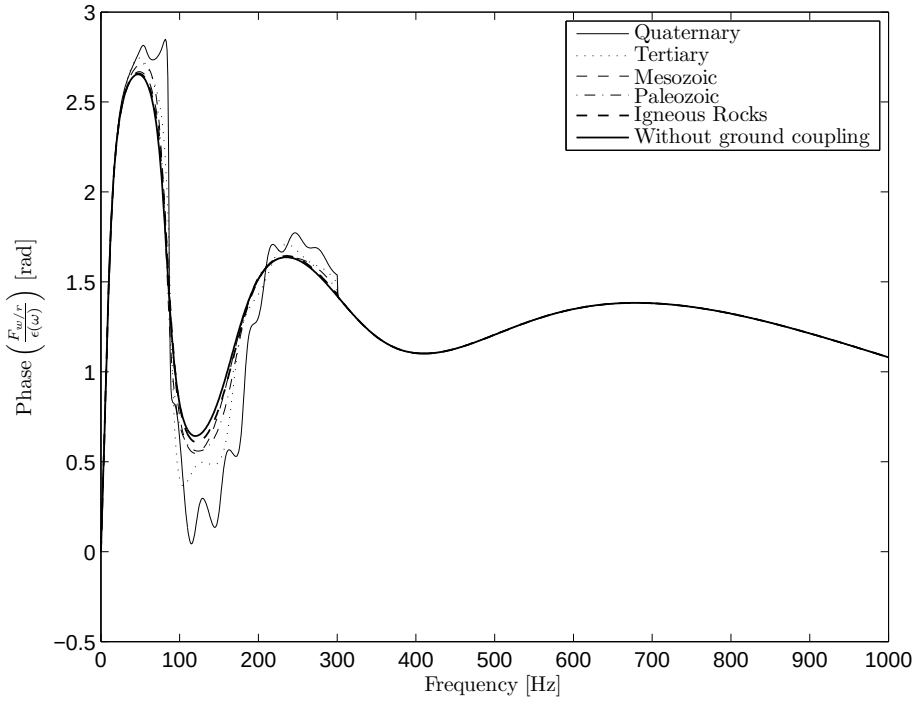


FIGURE 4.47: Phase of the transfer function between the wheel/rail dynamic contact force and the roughness excitation for Case 4 (see Tables 4.1, 4.2 and 4.3) and for five different subgrade parameters in Table 3.1.

contact filter proposed by Remington [196] is used again to treat this roughness data. From this spectral information, one hundred different spatial histories are simulated using the method presented in Section 4.5.4. The evaluation is performed by assuming:

- Train velocities tested: 15, 25 and 35 m/s.
- Rolling stock parameters of the Table 4.10.
- Superstructure parameters: Case 1, 2, 3 and 4 (see Tables 4.1, 4.2 and 4.3).
- Subgrade parameters: all five study cases (see 3.1).
- Frequency ranges tested: Complete range (all the significant frequency range of the wheel/rail contact force) and the frequency range between 1 and 80 Hz (as defined by standards [33, 34]).

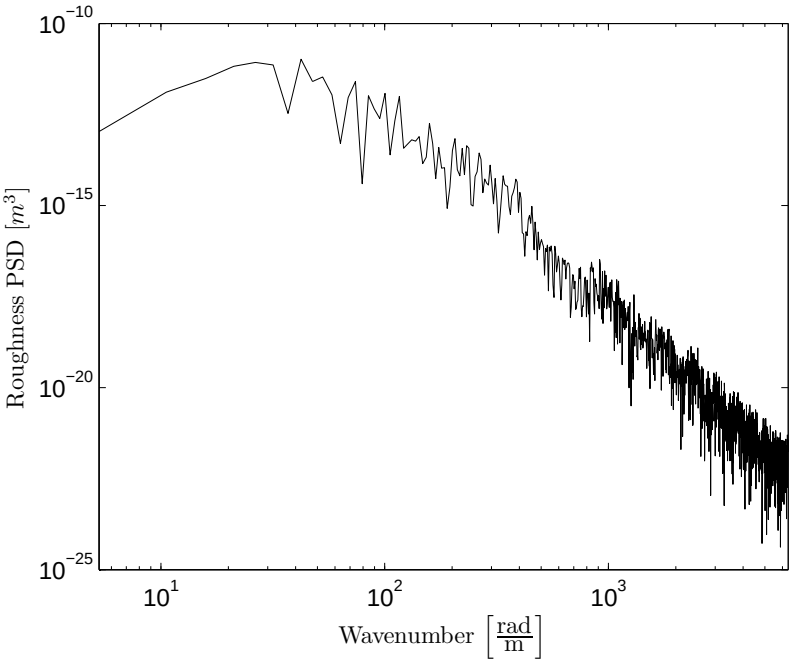


FIGURE 4.48: Joint roughness power spectral density (PSD) of the wheel and the rail.

For the complete frequency range, the results of the wheel/rail dynamic contact force are presented in Tables 4.11, 4.12, 4.13 and 4.14. The results calculated considering only the frequency range between 1 and 80 Hz are presented in Tables 4.16, 4.17, 4.18 and 4.19. To calculate the wheel/rail dynamic contact force in this reduced frequency range (1-80 Hz), a 8-order Butterworth filter is used, setting the cutoff frequency to 100 Hz. This kind of filter is selected to ensure very low passband ripple. In Tables 4.15 and 4.20 the ratio between the mean value of the standard deviation induced by subgrade influence

| **RMS value [N] of the wheel/rail dynamic contact force** | | | |
|---|---|---|---|
| | Train velocity | | |
| Grounds | 15 m/s | 25 m/s | 35 m/s |
| Quaternary | $3692.59 \pm 181.67$ | $6047.67 \pm 277.66$ | $8243.92 \pm 329.93$ |
| Tertiary | $3691.59 \pm 181.74$ | $6048.08 \pm 277.65$ | $8244.15 \pm 329.92$ |
| Mesozoic | $3691.87 \pm 181.73$ | $6048.46 \pm 277.63$ | $8244.48 \pm 329.91$ |
| Paleozoic | $3692.13 \pm 181.71$ | $6048.38 \pm 277.63$ | $8244.35 \pm 329.91$ |
| Igneous Rocks | $3691.77 \pm 181.74$ | $6048.47 \pm 277.63$ | $8244.47 \pm 329.91$ |
| No subgrade coupling | $3691.87 \pm 181.73$ | $6048.59 \pm 277.62$ | $8244.55 \pm 329.91$ |

TABLE 4.11: RMS value of the wheel/rail dynamic contact force for Case 1 (see Tables 4.1, 4.2 and 4.3), for the five different grounds (see Table 3.1) and for 15, 25 and 35 m/s of train velocity. 95% of confidence intervals. Complete frequency range.

| **RMS value [N] of the wheel/rail dynamic contact force** | | | |
|---|---|---|---|
| | Train velocity | | |
| Grounds | 15 m/s | 25 m/s | 35 m/s |
| Quaternary | $5947.6 \pm 320.1$ | $8442.02 \pm 321$ | $12494.99 \pm 655.44$ |
| Tertiary | $5933.07 \pm 320.44$ | $8475.38 \pm 322.12$ | $12518.66 \pm 654.86$ |
| Mesozoic | $5934.98 \pm 320.45$ | $8500.3 \pm 322.77$ | $12534.8 \pm 654.55$ |
| Paleozoic | $5935.19 \pm 320.33$ | $8489.09 \pm 322.47$ | $12528.48 \pm 654.65$ |
| Igneous Rocks | $5934.12 \pm 320.49$ | $8503.02 \pm 322.83$ | $12536.87 \pm 654.47$ |
| No subgrade coupling | $5933.78 \pm 320.57$ | $8507.51 \pm 322.99$ | $12540 \pm 654.45$ |

TABLE 4.12: RMS value of the wheel/rail dynamic contact force for Case 2 (see Tables 4.1, 4.2 and 4.3), for the five different grounds (see Table 3.1) and for 15, 25 and 35 m/s of train velocity. 95% of confidence intervals. Complete frequency range.

| **RMS value [N] of the wheel/rail dynamic contact force** | | | |
|---|---|---|---|
| | Train velocity | | |
| Grounds | 15 m/s | 25 m/s | 35 m/s |
| Quaternary | $4856.87 \pm 366.69$ | $5615.41 \pm 200.62$ | $8090.93 \pm 325.91$ |
| Tertiary | $4169.14 \pm 231.04$ | $5477.04 \pm 186.19$ | $8071.44 \pm 327.02$ |
| Mesozoic | $4002.07 \pm 207.02$ | $5457.22 \pm 185.16$ | $8075.54 \pm 327.12$ |
| Paleozoic | $4105.73 \pm 224.96$ | $5462.01 \pm 185.7$ | $8073.57 \pm 327.12$ |
| Igneous Rocks | $3955.75 \pm 200.81$ | $5448.57 \pm 184.76$ | $8074.11 \pm 327.19$ |
| No subgrade coupling | $3933.8 \pm 198.19$ | $5447.18 \pm 184.79$ | $8075.86 \pm 327.22$ |

TABLE 4.13: RMS value of the wheel/rail dynamic contact force for Case 3 (see Tables 4.1, 4.2 and 4.3), for the five different grounds (see Table 3.1) and for 15, 25 and 35 m/s of train velocity. 95% of confidence intervals. Complete frequency range.

| **RMS value [N] of the wheel/rail dynamic contact force** | | | |
|---|---|---|---|
| | Train velocity | | |
| Grounds | 15 m/s | 25 m/s | 35 m/s |
| Quaternary | $8018.68 \pm 800.39$ | $10186.11 \pm 1501.64$ | $8278.61 \pm 496.51$ |
| Tertiary | $5954.32 \pm 447.18$ | $7175.14 \pm 521.89$ | $7191.07 \pm 197.22$ |
| Mesozoic | $5058.15 \pm 332.44$ | $6142.23 \pm 277.75$ | $6932.66 \pm 166.73$ |
| Paleozoic | $5229.3 \pm 346.22$ | $6249.76 \pm 290.16$ | $6939.64 \pm 166.6$ |
| Igneous Rocks | $4878.73 \pm 310.27$ | $5993.25 \pm 248.73$ | $6905.21 \pm 166.07$ |
| No subgrade coupling | $4758.51 \pm 294.81$ | $5901.15 \pm 232.59$ | $6887.09 \pm 165.88$ |

TABLE 4.14: RMS value of the wheel/rail dynamic contact force for Case 4 (see Tables 4.1, 4.2 and 4.3), for the five different grounds (see Table 3.1) and for 15, 25 and 35 m/s of train velocity. 95% of confidence intervals. Complete frequency range.

| **Standard deviations ratio: Subgrade influence / Random behaviour** | | | |
|---|---|---|---|
| | Train velocity | | |
| Superstructure parameters | 15 m/s | 25 m/s | 35 m/s |
| Case 1 | $4.313 \cdot 10^{-3}$ | $2.446 \cdot 10^{-3}$ | $1.447 \cdot 10^{-3}$ |
| Case 2 | $3.549 \cdot 10^{-2}$ | $1.507 \cdot 10^{-1}$ | $5.083 \cdot 10^{-2}$ |
| Case 3 | 2.892 | $6.848 \cdot 10^{-1}$ | $4.383 \cdot 10^{-2}$ |
| Case 4 | 5.791 | 6.387 | 4.763 |

TABLE 4.15: Ratio of the standard deviations induced by the subgrade influence and by the aleatory behaviour of the roughness for Cases 1, 2, 3 and 4 (see Tables 4.1, 4.2 and 4.3), for the five different grounds (see Table 3.1) and for 15, 25 and 35 m/s of train velocity. Complete frequency range.

| **RMS value [N] of the wheel/rail dynamic contact force** | | | |
|---|---|---|---|
| | Train velocity | | |
| Grounds | 15 m/s | 25 m/s | 35 m/s |
| Quaternary | $495.39 \pm 42.53$ | $383.1 \pm 58.39$ | $278.11 \pm 152.59$ |
| Tertiary | $480.31 \pm 41.57$ | $380.82 \pm 58.72$ | $277.08 \pm 152.98$ |
| Mesozoic | $479.49 \pm 41.66$ | $382.22 \pm 58.64$ | $277.88 \pm 152.73$ |
| Paleozoic | $482.78 \pm 41.63$ | $383.25 \pm 58.55$ | $278.32 \pm 152.56$ |
| Igneous Rocks | $478.54 \pm 41.62$ | $382.3 \pm 58.65$ | $277.93 \pm 152.72$ |
| No subgrade coupling | $478.16 \pm 41.6$ | $382.63 \pm 58.65$ | $278.1 \pm 152.66$ |

TABLE 4.16: RMS value of the wheel/rail dynamic contact force for Case 1 (see Tables 4.1, 4.2 and 4.3), for the five different grounds (see Table 3.1) and for 15, 25 and 35 m/s of train velocity. 95% of confidence intervals. Frequency range: 1-80 Hz.

| **RMS value [N] of the wheel/rail dynamic contact force** | | | |
|---|---|---|---|
| | Train velocity | | |
| Grounds | 15 m/s | 25 m/s | 35 m/s |
| Quaternary | $1544.47 \pm 148.37$ | $1093.76 \pm 104.07$ | $695.85 \pm 192.7$ |
| Tertiary | $1409.99 \pm 130.7$ | $1015.47 \pm 100.99$ | $655.45 \pm 200.98$ |
| Mesozoic | $1341.26 \pm 122.65$ | $969.43 \pm 97.94$ | $633.16 \pm 206.33$ |
| Paleozoic | $1366.01 \pm 126.39$ | $971.5 \pm 97.58$ | $634.4 \pm 206.19$ |
| Igneous Rocks | $1323.69 \pm 120.31$ | $958.98 \pm 97.44$ | $628.07 \pm 207.49$ |
| No subgrade coupling | $1311.17 \pm 119$ | $948.82 \pm 97$ | $622.97 \pm 208.84$ |

TABLE 4.17: RMS value of the wheel/rail dynamic contact force for Case 2 (see Tables 4.1, 4.2 and 4.3), for the five different grounds (see Table 3.1) and for 15, 25 and 35 m/s of train velocity. 95% of confidence intervals. Frequency rang: 1-80 Hz.

| **RMS value [N] of the wheel/rail dynamic contact force** | | | |
|---|---|---|---|
| | Train velocity | | |
| Grounds | 15 m/s | 25 m/s | 35 m/s |
| Quaternary | $3513.76 \pm 476.54$ | $1958.25 \pm 254.95$ | $1140.91 \pm 154.15$ |
| Tertiary | $2468.55 \pm 297.64$ | $1387.27 \pm 147.28$ | $815.6 \pm 103.71$ |
| Mesozoic | $2151.41 \pm 256.18$ | $1216.97 \pm 124.84$ | $720.02 \pm 96.51$ |
| Paleozoic | $2345.19 \pm 294.44$ | $1275.86 \pm 138.49$ | $756.06 \pm 102.71$ |
| Igneous Rocks | $2060.17 \pm 241.14$ | $1168.95 \pm 116.94$ | $692 \pm 94.17$ |
| No subgrade coupling | $2012.81 \pm 234.41$ | $1137.89 \pm 113.1$ | $675.78 \pm 93.55$ |

TABLE 4.18: RMS value of the wheel/rail dynamic contact force for Case 3 (see Tables 4.1, 4.2 and 4.3), for the five different grounds (see Table 3.1) and for 15, 25 and 35 m/s of train velocity. 95% of confidence intervals. Frequency range: 1-80 Hz.

| **RMS value [N] of the wheel/rail dynamic contact force** | | | |
|---|---|---|---|
| | Train velocity | | |
| Grounds | 15 m/s | 25 m/s | 35 m/s |
| Quaternary | $5638.41 \pm 727.99$ | $7445.5 \pm 1641.11$ | $4233.86 \pm 771.73$ |
| Tertiary | $4226.38 \pm 339.3$ | $4426.67 \pm 592.38$ | $2531.23 \pm 284.53$ |
| Mesozoic | $3385.31 \pm 296.78$ | $3079.51 \pm 341.94$ | $1773.53 \pm 167.77$ |
| Paleozoic | $3721.2 \pm 355.2$ | $3353.14 \pm 376.27$ | $1921.64 \pm 184.73$ |
| Igneous Rocks | $3230.39 \pm 286.11$ | $2865.9 \pm 308.58$ | $1651.9 \pm 152.19$ |
| No subgrade coupling | $3163.24 \pm 284.71$ | $2765.18 \pm 293.54$ | $1592 \pm 145.16$ |

TABLE 4.19: RMS value of the wheel/rail dynamic contact force for Case 4 (see Tables 4.1, 4.2 and 4.3), for the five different grounds (see Table 3.1) and for 15, 25 and 35 m/s of train velocity. 95% of confidence intervals. Frequency range: 1-80 Hz.

| **Standard deviations ratio: Subgrade influence / Random behaviour** | | | |
|---|---|---|---|
| | Train velocity | | |
| Superstructure parameters | 15 m/s | 25 m/s | 35 m/s |
| Case 1 | $6.031 \cdot 10^{-1}$ | $3.339 \cdot 10^{-2}$ | $6.738 \cdot 10^{-3}$ |
| Case 2 | 1.34 | 1.085 | $2.654 \cdot 10^{-1}$ |
| Case 3 | 3.697 | 4.072 | 3.207 |
| Case 4 | 4.814 | 5.998 | 7.05 |

TABLE 4.20: Ratio of the standard deviations induced by the subgrade influence and by the aleatory behaviour of the roughness for Cases 1, 2, 3 and 4 (see Tables 4.1, 4.2 and 4.3), for the five different grounds (see Table 3.1) and for 15, 25 and 35 m/s of train velocity. Frequency range: 1-80 Hz.

and the mean value of the standard deviation induced by the aleatory behaviour of the roughness is shown, for both frequency ranges.

As can be seen in Tables 4.11, 4.12, 4.13 and 4.14, the effect of the subgrade is totally negligible for Cases 1 and 2, since the variability induced by the aleatory behaviour of the roughness is more important. In contrast, for Cases 3 and 4 the variability induced by the subgrade kind is, in general, more important than the variability induced by the roughness. This is an expected result, since the receptance of the track (Section 4.2) and the transfer functions $F_{w/r}/\epsilon(\omega)$ (Figs. 4.40, 4.41, 4.42, 4.43, 4.44, 4.45, 4.46 and 4.47) behave in the same manner. Therefore, combinations of low stiffness grounds with high stiffness superstructures induce important changes on the rail/wheel dynamic contact force with respect to the non-coupled case. As the effect of the subgrade is more significant at low frequencies, the results for the 1-80 Hz frequency range show a more important influence of the subgrade on the wheel-rail contact force. In this case the effect of the subgrade in Cases 1 and 2 is no longer clearly negligible.

With regard to train velocity, this parameter expands the roughness spectra in the frequency domain since $\omega = kv_{\text{train}}$, modifying the significant frequency range of the excitation. In consequence, the velocity modifies the response of the system. Specifically, from the transfer functions $F_{w/r}/\epsilon(\omega)$ presented before one can infer that, in general, the wheel/rail dynamic contact forces increases with the excitation frequency. Therefore, in the case of the complete frequency range, the wheel/rail dynamic contact force increases with train velocity. This tendency can be observed in the results presented in Tables 4.11, 4.12, 4.13 and 4.14. In contrast, an inverse behaviour can be observed for the case of the reduced frequency range (1 to 80 Hz) in Tables 4.16, 4.17, 4.18 and 4.19. As the excitation spectra is modified by the train velocity by the expression $\omega = kv_{\text{train}}$, the spectral energy contained in this frequency range and, thus, the dynamic wheel/rail contact force decrease as the train velocity increases.

## 4.7 Conclusions

The coupled superstructure model developed in this chapter allows to evaluate the dynamics of the wheel/rail contact, taking into account the subgrade, the superstructure and the vehicle. The relevance of the superstructure/subgrade coupling has been studied for a wide range of superstructure and subgrade parameters. It is shown that for combination of high stiffness subgrades and low stiffness superstructures, the effect of the subgrade is totally negligible with regard to the dynamics of the wheel/rail contact, significantly reducing the time consuming of this model. Only in the case of low stiffness subgrades and high stiffness superstructures the superstructure/subgrade interaction is really important. But, even in this extreme case, this interaction does not significantly affect at frequencies above to 200 Hz.

# Chapter 5

# Reference vibration amplitude determination

Finally, a methodology to calculate the vibration time history at any point on the surface of the ground induced by the passage of one wheel is presented. It follows from the analytical development showed in Chapter 4 and by using the wheel/rail contact force as a moving excitation load. This model is the second step and final step of a complete generation/propagation model in preliminary assessment studies.

## 5.1 Generalisation of the track response to a moving force arbitrarily varying in time

In the previous chapter, a methodology to evaluate the track receptance to a fixed concentrated harmonic load in the application point and the time history of the wheel/rail contact force has been presented. A modification of this development is presented here with the aim of calculating the vibration time history at any point on the ground surface induced by one wheelset travelling at a velocity $v_{\text{train}}$ along the track.

First, the Bernoulli-Euler differential equation (Eq. (4.6) for the case of fixed concentrated load) must be modified to take into account the motion of the source:

$$EI\frac{\partial^4 z_r}{\partial x^4} + \rho S\frac{\partial^2 z_r}{\partial t^2} + f(x,t) = f_{w/r}(t)\ \delta(x - v_{\text{train}}t) \tag{5.1}$$

Transforming to the wavenumber-time domain by using Eq. (B.7) gives

$$EIk_x^4\bar{z}_r + \rho S\frac{\partial^2 \bar{z}_r}{\partial t^2} + \bar{f}(k_x,t) = \bar{f}_{w/r}(t)\ \mathrm{e}^{\mathrm{i}k_x v_{\text{train}}t} \tag{5.2}$$

and now transforming to the wavenumber-frequency domain by using the Fourier transform of the form

$$\bar{Z}(k,\omega) = \int_{-\infty}^{+\infty} \bar{z}(k,t)\mathrm{e}^{-\mathrm{i}\omega t}\mathrm{d}t \tag{5.3}$$

finally results in

$$EIk_x^4\bar{Z}_r - \rho S\omega^2\bar{Z}_r + \bar{F}(k_x,t) = \int_{-\infty}^{+\infty} \bar{f}_{w/r}(t)\ \mathrm{e}^{-\mathrm{i}(\omega - k_x v_{\text{train}})t}\mathrm{d}t \tag{5.4}$$

A change of variables $\tilde{\omega} = \omega - k_x v_{\text{train}}$, as proposed by Lombaert and Degrande [16], gives the following expression

$$EI\left(\frac{\omega-\tilde{\omega}}{v_{\text{train}}}\right)^4\bar{Z}_r - \rho S\omega^2\bar{Z}_r + \bar{F}\left(\frac{\omega-\tilde{\omega}}{v_{\text{train}}},t\right) = \int_{-\infty}^{+\infty} \bar{f}_{w/r}(t)\ \mathrm{e}^{-\mathrm{i}\tilde{\omega}t}\mathrm{d}t \tag{5.5}$$

and, since the right term for the latter equation has the form of the Fourier transform shown in Eq. (5.3), Eq. (5.5) reduces to

$$EI\left(\frac{\omega-\tilde{\omega}}{v_{\text{train}}}\right)^4 \bar{Z}_r - \rho S\omega^2 \bar{z}_r + \bar{F}\left(\frac{\omega-\tilde{\omega}}{v_{\text{train}}}, t\right) = F_{w/r}(\tilde{\omega}) \tag{5.6}$$

In view of these expressions, it seems clear that the Doppler effect appears in this case [190, 197], where $\tilde{\omega}$ is the frequency emitted by the moving source and $\omega$ is the frequency observed at the receiver. Thus, from the point of view of a fixed receiver, the frequency content of the excitation is stretched: specifically it is expanded or contracted by a factor ranging between $[v_p^{\min}/(v_p^{\min}+v_{\text{train}}), v_p^{\min}/(v_p^{\min}-v_{\text{train}})]$, where $v_p^{\min}$ is the smallest phase velocity of interest. Supporting this hypothesis, Ditzel has identified the Doppler effect in field measurements of railway induced vibrations [187].

## 5.2 Ground response to a moving load arbitrarily varying in time

The response of the ground due to a strip load $\bar{F}_g(k_x,\omega)$ is described by the Eqs. (4.33), (4.34) and (4.35). This load can be written in terms of only the rail vertical displacement as

$$\bar{F}_g(k_x,\omega) = \left[\frac{Q'(\omega)}{G'(\omega)I_{k_y}(k_x,\omega)+1}\right]\bar{Z}_r \tag{5.7}$$

by the combination of Eqs. (4.39) and (4.41). Following a similar procedure that is used to obtain Eq. (4.44), Eq. (5.6) can be written as a function of only the rail vertical displacement:

$$\bar{Z}_r = \frac{F_{w/r}(\tilde{\omega})}{EI\left(\frac{\omega-\tilde{\omega}}{v_{\text{train}}}\right)^4 - \omega^2\rho S + Q(\omega) - \frac{G(\omega)Q'(\omega)I_{k_y}(\frac{\omega-\tilde{\omega}}{v_{\text{train}}},\omega)}{G'(\omega)I_{k_y}(\frac{\omega-\tilde{\omega}}{v_{\text{train}}},\omega)+1}} \tag{5.8}$$

Mixing Eqs. (5.7) and (5.8) gives the following expression of the distributed load applied by the superstructure to the subgrade:

$$\bar{F}_g(k_x,\omega) = \frac{Q'(\omega)}{G'(\omega)I_{k_y}(\frac{\omega-\tilde{\omega}}{v_{\text{train}}},\omega)+1}\cdot \cdot\frac{F_{w/r}(\tilde{\omega})}{EI\left(\frac{\omega-\tilde{\omega}}{v_{\text{train}}}\right)^4 - \omega^2\rho S + Q(\omega) - \frac{G(\omega)Q'(\omega)I_{k_y}(\frac{\omega-\tilde{\omega}}{v_{\text{train}}},\omega)}{G'(\omega)I_{k_y}(\frac{\omega-\tilde{\omega}}{v_{\text{train}}},\omega)+1}} \tag{5.9}$$

Finally, introducing this expression in Eqs. (4.33), (4.34) and (4.35) one can obtain the response of the ground in the wavenumber-frequency domain. To obtain the response of the ground in the spatial-time domain a Fourier antitransform of the form

$$(x_{g0}, y_{g0}, z_{g0}) = \frac{1}{8\pi^3} \int_{-\infty}^{\infty} \int_{-\infty}^{\infty} \int_{-\infty}^{\infty} (\bar{X}_{g0}, \bar{Y}_{g0}, \bar{Z}_{g0})\, \mathrm{e}^{\mathrm{i}(\omega t - k_x x - k_y y)} \mathrm{d}\omega \mathrm{d}k_x \mathrm{d}k_y \tag{5.10}$$

must be applied. It may be computed using a Fast Fourier Transform algorithm [172], for example `fftn` which is provided by MATLAB and allows to perform a N-D discrete Fourier transform. As shown before, a more powerful algorithm for the case of typical seismological oscillatory integrands is the Logarithmic Fast Fourier Transform [135, 136]. The previous evaluation of the $I_{k_y}$ term, performed in the track receptance calculation, can be used to lower the computational time of the Eq. (5.10). Other options, as explained in Section 2.2.7, are performing a numerical integration using the Filon's method [108, 124, 125, 172], the Nonuniform Fast Fourier Transform [137], or any other numerical integration approach that allows to deal with high oscillatory integrands, as for example the complex exponential window method [198]. The application of Apsel's technique (see Appendix A) will improve the speed of any numerical integration approach, whenever an analytical solution of the static integral can be obtained.

The wheel/rail contact force evaluation performed in the previous chapter gives only its dynamic part. To take into account also the quasi-static excitation, the wheel/rail static contact force ($(m_w + m_{\text{sprung}})$g) must be added to the wheel/rail dynamic contact force in order to obtain a time history of the complete contact force.

To obtain a solution in the time domain for a complete train passage a properly delayed summation of single wheel solutions must be carried out. With this resulting signal, one can obtain one-third octave band spectra at far-field evaluation point (see Chapter 3) and, finally, use a semi-analytical propagation law (as, for example, a multi-point source Barkan law) to obtain the vibration field at the infrastructure surroundings.

# Chapter 6

# Contributions and recommendations

This work is focused on the generation and propagation parts of the at-grade train induced vibrations problem in the frame of preliminary assessment projects. These preliminary studies must be faced in first stages of train infrastructure construction projects or before the construction of any residential complex near to an existing train infrastructure. The simplicity and efficiency of the model used, in terms of economic and time costs, are the most important aspects of these studies. The model presented in this thesis is developed by taking into account all these requirements. Its simple analytical formulation allows for the calculation of any particular case, with good computational efficiency and without too many input parameters. These input parameters are the mechanical properties of the viscoelastic and homogeneous ground model, the distributed mechanical parameters of the ballast, the sleepers, the fasteners and the rail for the 2-layer supporting model of the superstructure and the mechanical parameters of the vehicle modelled as a 1DOF system. The analytical behaviour of this model allows for the evaluation of the effect of these parameters on the response of the track and the surrounding ground, becoming a tool to obtain a first approximation for the evaluation of the required vibration mitigation measures. Additionally, the model can be easily adapted for the use of semi-analytical or empirical models in the propagation part, becoming a generation model that gives a reference vibration amplitude at a certain reference distance, which is a proper feeding of these semi-analytical or empirical propagation models.

## 6.1 Principal contributions of this work

As introduced before, the principal contribution of this work is the development of a complete generation/propagation model to be used in preliminary assessment studies. In the process of this development, other important contributions have emerged:

- **First approximation of the near field region dimensions.** The viscoelastic and homogeneous half-space model has been used to calculate an approximation to the near field region dimensions. This model is used because its low time/economical cost makes it the best option in preliminary assessment studies. The quantification of the near field region dimensions will delimit the applicability of semi-analytical propagation models based on Rayleigh wave spreading. The influence of the ground parameters on the near field distance (the dimension that defines the near field region) is studied. With the aim of make a wide calculation example, parameters of five very distinct real grounds are chosen to quantify numerically the near field distance.

- **Application of Apsel's technique to accelerate the superstructure/subgrade coupling evaluation.** Apsel's technique (Appendix A) was developed to deal with the oscillatory integrands which appear in seismic wave propagation problems. This technique has been applied successfully to the evaluation of the superstructure/subgrade coupling, thus improving the computational efficiency of this calculus.

- **Obtain an accurate equivalent 2DOF model of the superstructure using frequency dependent parameters**. The frequency dependency of the equivalent 2DOF model parameters allows for an exact representation of the receptance of the coupled system, accurately taking into account the distortions induced by the superstructure/subgrade coupling on the track response.

- **The influence of the subgrade on the track response has been characterised.** The track response, in terms of its static receptance and of the wheel/rail contact force, has been evaluated for different combinations of rolling stock, superstructure and subgrade parameters. This investigation concludes that this influence is generally only significant for high stiffness superstructures combined with soft soils and below 200 Hz. In the other cases, the non-coupled system can be used, significantly reducing the computational time involved in model calculation.

## 6.2 Recommendations for future research

Railway induced vibrations and, more specifically, the research lines within this main issue, such as vehicle/track dynamics, soil-structure interaction and surface wave propagation, are fascinating and challenging subjects where much remains to be investigated. In the case of this thesis, the ideas and investigations presented can be further expanded to improve the precision or computational efficiency of any part of the complete model presented. The research presented also opens the door to new research lines that the author considers interesting to better understand the complete phenomena. Here the most interesting further extensions and new research lines are outlined:

- As metioned in Chapter 3, there are some combinations of damping ratios ($D_P$ and $D_S$) that produce strange results on the $M_X$ and $M_Z$ factors. Specifically, it has been found that, in these strange cases, the Rayleigh amplitude decreases much more than the combined contribution of both the P-wave and S-wave. Since this is a contradiction with the amount of experimental data available to seismological science, one may assume that these damping ratio combinations are probably non-physical, and, therefore, it will be important to know what these combinations are.

- A quantification of the near field distance for more accurate models of the ground (layered, anisotropic, other models of damping...) and the source will quantify the error induced by the viscoelastic and homogeneous model and delimit its applicability.

- Obtain an approximation to the period of frequency dependent receptance oscillations to improve the computational efficiency and accuracy of the fast method to obtain the coupled receptance presented in Section 4.3.

- As the computational efficiency is the most important parameter in the case of this study, the numerical integration of the oscillatory integrands becomes a very interesting and necessary field of research.

- Develop an efficient and very accurate approach to obtain, experimentally, the parameters of the superstructure and the subgrade, with which to validate the model. Most authors have stated that the precision of this determination is much important than the model accuracy, therefore it is also an important line of research.

- The adaptation of this model for the case of underground railways may be very useful to make preliminary assessment studies of the impact of railway induced

vibrations in urban areas, ensuring that the principal advantages of this model (low time/economical costs) will remain unchanged.

# Appendix A

# Static integrands and integrals

As Apsel and Luco stated [105, 106, 126], the oscillatory behavior of the integrals used to calculate the displacement and stress fields of a point source buried in a viscoelastic half-space can be minimised using the following approach:

$$I(r,\omega) = I(r,0) + \int_0^{k_{lim}} \left[\tilde{I}(k,\omega) - \tilde{I}(k,0)\right] J_n(kr)\mathrm{d}k \tag{A.1}$$

where $I$ are integrals, $\tilde{I}$ are integrands, $k_{lim}$ is a truncated superior limit of integration and $J_n(.)$ is the nth-order Bessel function of the first kind. This technique can be generalized to integrals used for other sources or other ground models and thus, with other kinds of oscillatory kernels.

With regard to this thesis, some integrals used in Chapters 3 and 4 can be transformed using this technique in order to reduce the computational cost of the numerical integration. With respect to the excitation source, these integrals are:

- **Infinite line source**. Eqs. (3.1) and (3.2).
- **Point source**. Eqs. (3.19) and (3.20).
- **Infinite strip source** at $y = 0$. Eq. (4.43).

## A.1 Static integrands and integrals for infinite line source expressions

The original integrand of the Eq. (3.1) avoiding the kernel is

$$\tilde{I}_u(k,\omega) = \frac{k(2k^2 - k_\beta^2 - 2\upsilon\upsilon')}{(2k^2 - k_\beta^2)^2 - 4k^2\upsilon\upsilon'} \tag{A.2}$$

The evaluation of $\tilde{I}_u(x,0)$ is not obvious because the direct substitution of $\omega = 0$ gives an indeterminate form: $0/0$. Calculating the limit of $\tilde{I}_u(x,w)$ when $\omega$ tends to zero by the application of the l'Hôpital's rule results in

$$\tilde{I}_u(k,0) = \lim_{\omega\to 0}\left[\frac{k(2k^2 - k_\beta^2 - 2\upsilon\upsilon')}{(2k^2 - k_\beta^2)^2 - 4k^2\upsilon\upsilon'}\right] = \frac{\beta^2}{2k(\beta^2 - \alpha^2)} \tag{A.3}$$

Therefore, the expression (3.1) evaluated at $\omega = 0$ can be written as

$$I_u(x,0) = \frac{\mathrm{i}Q}{2\pi\mu}\,\frac{\beta^2}{2(\beta^2 - \alpha^2)}\,\mathcal{P}\int_{-\infty}^{+\infty}\frac{\mathrm{e}^{-\mathrm{i}kx}}{k}\mathrm{d}k \tag{A.4}$$

where $\mathcal{P}$ represents the Cauchy principal value, which is required because there is a pole at $k = 0$ and it resides inside the integration path along the real axis. This Cauchy principal value integral can be evaluated using contour integration around, for example, the integration path showed in Fig. A.1. This approach results in

$$\int_{-R}^{-\varepsilon} + \int_{C_\varepsilon} + \int_{\varepsilon}^{R} + \int_{C_R} = -2\pi\mathrm{i}\sum \mathrm{Res} \tag{A.5}$$

where $R$ tends to infinity and $\varepsilon$ tends to zero.

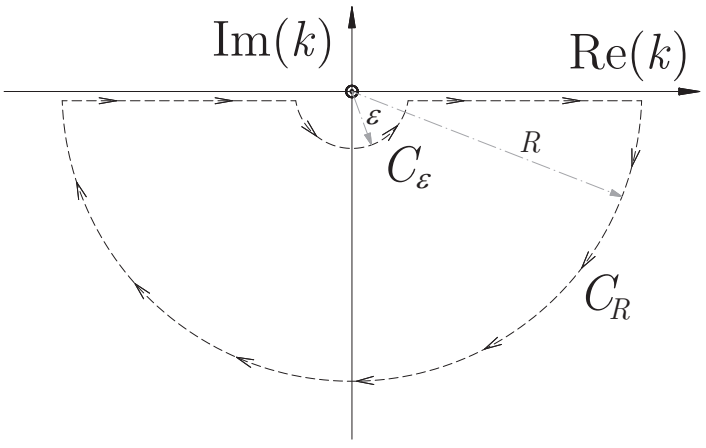


FIGURE A.1: Integration path used in the evaluation of the integral inside Eq. (A.4). Symbol ⊙ represents the pole.

In consequence, the integral inside Eq. (A.5) is equal to

$$\mathcal{P}\int_{-\infty}^{+\infty}\frac{\mathrm{e}^{-\mathrm{i}kx}}{k}\mathrm{d}k=-\int_{C_\varepsilon}-\int_{C_R}-2\pi\mathrm{i}\sum\mathrm{Res} \tag{A.6}$$

As can be seen in Fig. A.1, there are no poles inside the integration closed loop. Therefore, $\sum\mathrm{Res}=0$. On the other hand, as

$$\lim_{|k|\to\infty}\left[\frac{\mathrm{e}^{-\mathrm{i}kx}}{k}\right]=0 \quad \text{when} \quad 0\geq\arg(k)\geq-\pi \tag{A.7}$$

the integral along the loop $C_R$ is

$$\lim_{R\to\infty}\int_{C_R}\frac{\mathrm{e}^{-\mathrm{i}kx}}{k}\mathrm{d}k=0 \tag{A.8}$$

Finally, the integral along the loop $C_\varepsilon$ is

$$\int_{C_\varepsilon}=\pi\mathrm{i}\mathrm{Res}\left(\frac{\mathrm{e}^{-\mathrm{i}kx}}{k},0\right) \tag{A.9}$$

and by the application of Cauchy's integral formula, by which a residue for a simple pole located at $z=b$ of the function $f(z)$ is

$$\mathrm{Res}(f,b)=\lim_{z\to b}(z-b)f(z) \tag{A.10}$$

where $z$ is a complex variable, one can obtain

$$\int_{C_\varepsilon}=\pi\mathrm{i}\lim_{|k|\to0}\left[(k-0)\left(\frac{\mathrm{e}^{-\mathrm{i}kx}}{k}\right)\right]=\pi\mathrm{i} \tag{A.11}$$

Thus, Eq. (A.4) is reduced to

$$I_u(x,0)=\frac{Q\beta^2}{4\mu(\beta^2-\alpha^2)} \tag{A.12}$$

Following the same approach for the case of vertical displacement, the static integrand (also avoiding the kernel) and integral result in, respectively

$$\tilde{I}_w(k,0)=\lim_{\omega\to0}\left[\frac{k_\beta^2\upsilon}{(2k^2-k_\beta^2)^2-4k^2\upsilon\upsilon'}\right]=\frac{\alpha^2}{2k(\beta^2-\alpha^2)} \tag{A.13}$$

$$I_w(x,0) = \frac{\mathrm{i}Q\alpha^2}{4\mu(\beta^2-\alpha^2)} \tag{A.14}$$

## A.2 Static integrands and integrals for point source expressions

For the case of a vertical point source, the static integrands associated to the radial and vertical displacement expressions (Eqs. (3.19) and (3.20) respectively) can be evaluated also applying the l'Hôpital's rule:

$$\tilde{I}_q(k,0) = \lim_{\omega\to 0}\left[\frac{k^2(2k^2-k_\beta^2-2\upsilon\upsilon')}{(2k^2-k_\beta^2)^2-4k^2\upsilon\upsilon'}\right] = \frac{\beta^2}{2(\beta^2-\alpha^2)} \tag{A.15}$$

$$\tilde{I}_w(k,0) = \lim_{\omega\to 0}\left[\frac{kk_\beta^2\upsilon}{(2k^2-k_\beta^2)^2-4k^2\upsilon\upsilon'}\right] = \frac{\alpha^2}{2(\beta^2-\alpha^2)} \tag{A.16}$$

Now, using the well-known integral

$$\int_0^\infty J_n(kr)\mathrm{d}k = \frac{1}{r} \qquad n > -1 \tag{A.17}$$

the static integrals are

$$I_q(x,0) = -\frac{L\beta^2}{4\pi\mu r(\alpha^2-\beta^2)} \tag{A.18}$$

$$I_w(x,0) = \frac{L\alpha^2}{4\pi\mu r(\alpha^2-\beta^2)} \tag{A.19}$$

## A.3 Static integrands and integrals for infinite strip source expressions at its directrix

As can be seen in Chapter 4, Eq. (4.43) allows for a calculation of the vertical displacement of the ground surface due to an infinite strip source at its directrix ($y = 0$). For this case, the static integrand is

$$\tilde{I}_{k_y}(k_x,k_y,0) = \lim_{\omega\to 0}\left[\frac{\upsilon_{xy}k_\beta^2}{\left[2(k_x^2+k_y^2)-k_\beta^2\right]^2 - 4\upsilon_{xy}\upsilon'_{xy}(k_x^2+k_y^2)}\right] = \tag{A.20}$$

$$= \frac{\alpha^2}{2\sqrt{k_x^2+k_y^2}\,(\beta^2-\alpha^2)}$$

which is also calculated using l'Hôpital's rule. Therefore, Eq. (4.43) evaluated at $\omega = 0$ can be written as

$$I_{k_y}(k_x,0) = \frac{\alpha^2}{2\pi\mu(\beta^2-\alpha^2)}\int_0^\infty \frac{\sin(ck_y)}{ck_y}\frac{1}{\sqrt{k_x^2+k_y^2}}\mathrm{d}k_y \tag{A.21}$$

The contour integration approach is used, as in the previous sections, to solve the integral inside Eq. (A.21). In this case, the following function is assumed initially as the integrand to integrate:

$$\frac{\mathrm{e}^{\mathrm{i}ck_y}}{ck_y\sqrt{k_x^2+k_y^2}} \tag{A.22}$$

This integration can be performed using the integration path showed in Fig. A.2. As can be seen in this figure, a branch cut appears in the complex plane due to the square root contained in the denominator of the integrand.

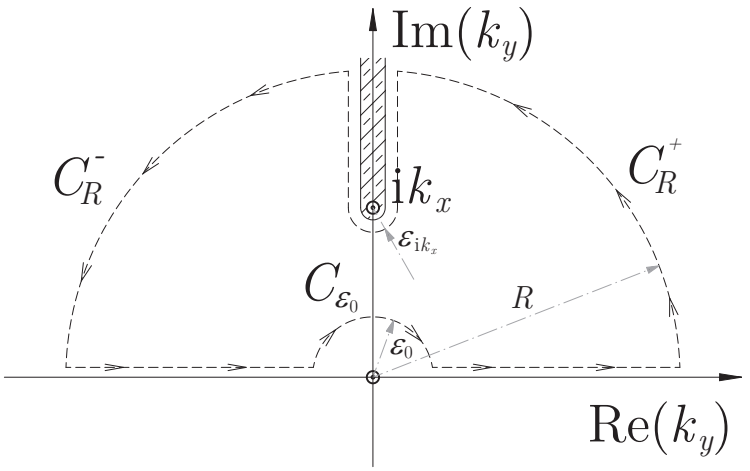


FIGURE A.2: Integration path used in the evaluation of the integral of the Eq. (A.22). Symbols ⊙ represent the poles and the strip line represents the branch cut.

The application of contour integration leads to

$$\int_{-R}^{-\varepsilon_0} + \int_{C_{\varepsilon_0}} + \int_{\varepsilon_0}^{R} + \int_{C_R^-} + \int_{C_{\varepsilon_{\mathrm{i}k_x}}} + \int_{C_R^+} = 2\pi\mathrm{i}\sum \mathrm{Res} \tag{A.23}$$

Letting $\varepsilon_0$ and $\varepsilon_{\mathrm{i}k_x}$ tend to zero and $R$ tends to infinity

$$\mathcal{P}\int_{-\infty}^{+\infty} = \int_{-R}^{-\varepsilon_0} + \int_{\varepsilon_0}^{R} = -\int_{C_{\varepsilon_0}} - \int_{C_R^-} - \int_{C_{\varepsilon_{\mathrm{i}k_x}}} - \int_{C_R^+} + 2\pi\mathrm{i}\sum \mathrm{Res} \tag{A.24}$$

As before, there are no poles inside the closed loop. Furthermore, the limit of the integrand when $|k_y|$ tends to infinity and $0 \leq \arg(k_y) \leq \pi$ is zero, and therefore the integral along the loops $C_R^-$ and $C_R^+$ is zero. Thus, Eq. (A.24) reduces to

$$\mathcal{P}\int_{-\infty}^{+\infty} = -\int_{C_{\varepsilon_0}} - \int_{C_{\varepsilon_{\mathrm{i}k_x}}} \tag{A.25}$$

On the one hand and in similar manner as in Eq. (A.11)

$$\int_{C_{\varepsilon_0}} = -\pi\mathrm{i}\lim_{k_y\to 0}\left[(k_y - 0)\left(\frac{\mathrm{e}^{-\mathrm{i}ck_y}}{ck_y\sqrt{k_x^2+k_y^2}}\right)\right] = -\frac{\pi\mathrm{i}}{c|k_x|} \tag{A.26}$$

On the other hand, the integral along the loop $C_{\varepsilon_{\mathrm{i}k_x}}$ can be written as

$$\begin{aligned}\int_{C_{\varepsilon_{\mathrm{i}k_x}}} &= \int_{\mathrm{i}\infty}^{\mathrm{i}k_x} \frac{\mathrm{e}^{\mathrm{i}ck_y}}{ck_y k_{xy}^+}\mathrm{d}k_y - \pi\mathrm{i}\lim_{k_y\to\mathrm{i}k_x}\left[(k_y - \mathrm{i})\frac{\mathrm{e}^{\mathrm{i}ck_y}}{ck_y(k_x^2+k_y^2)}\right] + \\ &+ \int_{\mathrm{i}k_x}^{\mathrm{i}\infty} \frac{\mathrm{e}^{\mathrm{i}ck_y}}{ck_y k_{xy}^-}\mathrm{d}k_y = 2\int_{\mathrm{i}k_x}^{\mathrm{i}\infty} \frac{\mathrm{e}^{\mathrm{i}ck_y}}{ck_y k_{xy}^-}\mathrm{d}k_y\end{aligned} \tag{A.27}$$

where

$$\begin{aligned} k_{xy}^+ &= \sqrt{k_x^2+k_y^2} \qquad \text{imposing that} \qquad \mathrm{Im}(k_{xy}^+) > 0 \\ k_{xy}^- &= \sqrt{k_x^2+k_y^2} \qquad \text{imposing that} \qquad \mathrm{Im}(k_{xy}^-) < 0 \end{aligned} \tag{A.28}$$

And if one adopts $k_y = -\mathrm{i}k_y'$ as a variable substitution, Eq. (A.28) becomes

$$\int_{C_{\varepsilon_{\mathrm{i}k_x}}} = 2\int_{k_x}^{\infty} \frac{\mathrm{e}^{-ck'_y}}{ck'_y\sqrt{k'^2_y - k_x^2}}\mathrm{i}\mathrm{d}k'_y \tag{A.29}$$

Finally, inserting Eqs. (A.26) and (A.29) in Eq. (A.25), taking advantage of the Eq. (A.22) symmetry and taking only the imaginary part (as the Euler's formula states that $\mathrm{e}^{\mathrm{i}\theta} = \cos\theta + \mathrm{i}\sin\theta$), Eq. (A.21) reduces to

$$I_{k_y}(k_x, 0) = \frac{\alpha^2}{4\pi\mu(\beta^2 - \alpha^2)}\left[\frac{\pi}{c|k_x|} - 2\int_{|k_x|}^{\infty} \frac{\mathrm{e}^{-ck'_y}}{ck'_y\sqrt{k'^2_y - k_x^2}}\mathrm{d}k'_y\right] \tag{A.30}$$

# Appendix B

# Superstructure model without subgrade coupling

In this appendix the analytical solution of the superstructure model presented in Section 4.1 in the assumption of no superstructure/subgrade coupling is presented. This simplified superstructure model is shown in Fig. B.1.

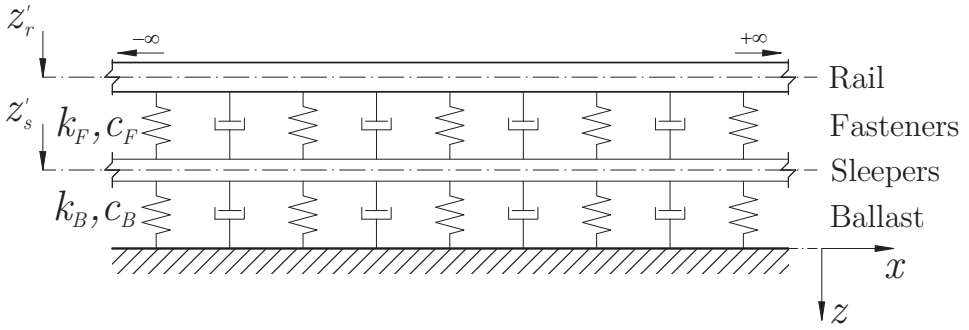


FIGURE B.1: 2-layer continuous support model without superstructure/subgrade coupling.

## B.1 Governing equations

Eqs. (4.6), (4.2) and (4.3) define the motion, induced by a unitary, vertical and harmonic point load applied on the head of the rail at $x = \zeta$, of the superstructure model with superstructure/subgrade coupling, which is presented in Chapter 4. Since the applied load is unitary, the specified problem is, of course, one of determining the Green's function for the system. Assuming the subgrade as a completely rigid body, Eqs. (4.6) and (4.2) remain unchanged and the equation of motion of the sleepers (Eq. (4.3)) becomes

$$k_F(z'_r - z'_s) + c_F(\dot{z}'_r - \dot{z}'_s) - k_B z'_s - c_B \dot{z}'_s = m_s \ddot{z}'_s \tag{B.1}$$

Considering a solution of the form

$$z = Z\mathrm{e}^{\mathrm{i}\omega t} \tag{B.2}$$

the governing equation of the sleepers reduces to

$$(k_F + \mathrm{i}\omega c_F)(Z'_r - Z'_s) - (k_B + \mathrm{i}\omega c_B)Z'_s = -m_s\omega^2 Z'_s \tag{B.3}$$

that is defined in the frequency domain. In this domain, the governing equation of the rail can be written as

$$EI\frac{\partial^4 Z'_r}{\partial x^4} - \rho S\omega^2 Z'_r + (k_F + \mathrm{i}\omega c_F)(Z'_r - Z'_s) = F_{w/r}(\omega)\,\delta(x - \zeta) \tag{B.4}$$

which is obtained mixing Eqs. (4.9) and (4.2) and considering displacement solutions of the form (B.2). From Eq. (B.3), the vertical motion of the distributed sleepers in the frequency domain can be expressed as

$$Z'_s = \frac{k_F + \mathrm{i}\omega c_F}{k_F + \mathrm{i}\omega c_F + k_B + \mathrm{i}\omega c_B - m_s\omega^2} Z'_r \tag{B.5}$$

Substituting Eq. (B.5) into (B.4) gives

$$EI\frac{\partial^4 Z'_r}{\partial x^4} - \rho S\omega^2 Z'_r + Q(\omega)Z'_r = F_{w/r}(\omega)\,\delta(x - \zeta) \tag{B.6}$$

where $Q(\omega)$ is defined by the expression (4.10). By the application of a Fourier transform of the form

$$\bar{Z}(k,\omega) = \int_{-\infty}^{+\infty} Z(x,\omega)\mathrm{e}^{\mathrm{i}kx}\mathrm{d}x \tag{B.7}$$

to Eq. (B.6) is possible to obtain the rail displacement solution in the wavenumber-frequency domain:

$$EIk^4\bar{Z}_r' - \rho S\omega^2\bar{Z}_r' + Q(\omega)\bar{Z}_r' = F_{w/r}\,\mathrm{e}^{\mathrm{i}k\zeta} \tag{B.8}$$

This expression can be also expressed as

$$k^4\bar{Z}_r' - k_0^4\bar{Z}_r' = \frac{F_{w/r}}{EI}\,\mathrm{e}^{\mathrm{i}k\zeta} \tag{B.9}$$

where

$$k_0 = \sqrt[4]{\frac{\omega^2\rho S - Q(\omega)}{EI}} \tag{B.10}$$

Therefore, the rail displacement in the wavenumber-frequency domain can be defined by

$$\bar{Z}_r' = \frac{F_{w/r}}{EI}\frac{\mathrm{e}^{\mathrm{i}k\zeta}}{k^4 - k_0^4} \tag{B.11}$$

Applying the Fourier antitranform associated to the transform defined by the Eq. (B.7), which have the form

$$Z(x,\omega) = \frac{1}{2\pi}\int_{-\infty}^{+\infty} \bar{Z}(k,\omega)\mathrm{e}^{-\mathrm{i}kx}\mathrm{d}k \tag{B.12}$$

one can obtain that the rail vertical receptance in the spatial-frequency domain is given by

$$\frac{Z_r'}{F_{w/r}} = \frac{1}{2\pi EI}\int_{-\infty}^{+\infty} \frac{\mathrm{e}^{-\mathrm{i}k(x-\zeta)}}{k^4 - k_0^4}\mathrm{d}k \tag{B.13}$$

## B.2 Analytical solution by contour integration

The denominator of the integrand of the Eq. (B.13) have four roots:

$$k = \pm k_0, \pm \mathrm{i} k_0 \tag{B.14}$$

If $k_0$ is a real number, two of these four roots are real and two imaginary. For this case, it can be found the development of contour integration and the solution of this problem in [78]. But when $k_0$ is a complex value any of the four roots are not pure real nor pure imaginary, as can be seen in Figs. B.2 and B.3.

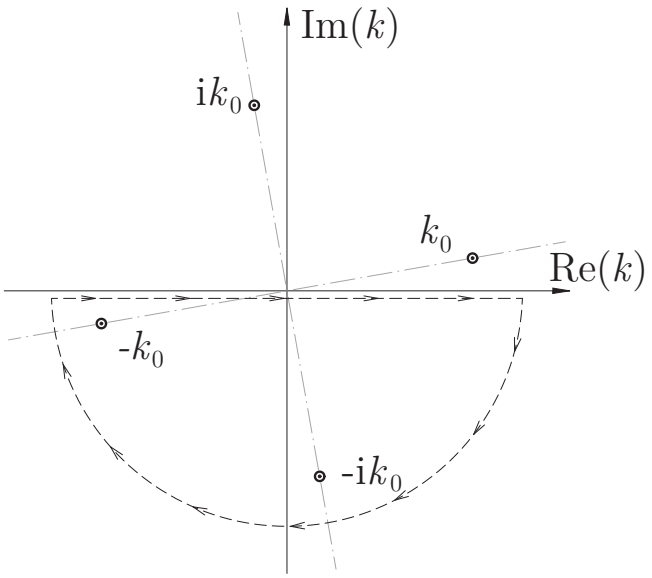


FIGURE B.2: Poles distribution for $k_0$ located in the first quadrant of the complex plane and integration path for $x > \zeta$. Symbols $\odot$ represent the poles.

In these figures it is also presented two different integration paths that allow for a evaluation, following the contour integration technique, of the integral in Eq. (B.13). Applying this approach to both paths gives the following expression

$$\int_{-\infty}^{+\infty} + \int_{SC} = \pm 2\pi \mathrm{i} \sum \mathrm{Res} \tag{B.15}$$

where $\int_{SC}$ is the integration along the semicircular portion of the path and $\sum \mathrm{Res}$ is the summation of the residues of the poles inside the integration contour. The sign of the term $\pm 2\pi \mathrm{i} \sum \mathrm{Res}$ is defined by the direction of rotation: positive for anticlockwise direction and negative for clockwise direction.

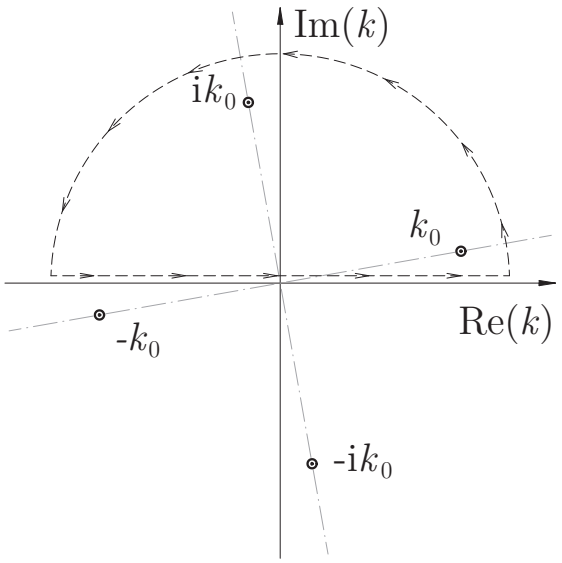


FIGURE B.3: Poles distribution for $k_0$ located in the first quadrant of the complex plane and integration path for $x < \zeta$. Symbols $\odot$ represent the poles.

On one hand, the first path (Fig. B.2) is used when $x > \zeta$ because, in this case, the integral along this semicircular path is equal to zero. On the other hand, the second path (Fig. B.3) is used when $x < \zeta$ for the same reason.

Therefore, the calculation of the integral reduces to the evaluation of the residues enclosed by the selected contour. Using Cauchy's integral formula, Eq. (A.10), to evaluate the residues in all possible cases (for the two different integration paths and for $k_0$ in each quadrant of the complex plane) gives the rail vertical displacement solution, that is defined, for $\mathrm{Re}(k_0) > 0$ and $\mathrm{Im}(k_0) > 0$ by

$$\begin{aligned} \frac{Z_r'}{F_{w/r}} &= \frac{1}{4k_0^3 EI}\left(-\mathrm{e}^{-k_0(x-\zeta)} + \mathrm{i}\mathrm{e}^{\mathrm{i}k_0(x-\zeta)}\right) \qquad \text{for } x > \zeta \\ \frac{Z_r'}{F_{w/r}} &= \frac{1}{4k_0^3 EI}\left(-\mathrm{e}^{k_0(x-\zeta)} + \mathrm{i}\mathrm{e}^{-\mathrm{i}k_0(x-\zeta)}\right) \qquad \text{for } x < \zeta \end{aligned} \tag{B.16}$$

for $\mathrm{Re}(k_0) < 0$ and $\mathrm{Im}(k_0) > 0$ by

$$\begin{aligned} \frac{Z_r'}{F_{w/r}} &= \frac{1}{4k_0^3 EI}\left(\mathrm{e}^{k_0(x-\zeta)} + \mathrm{i}\mathrm{e}^{\mathrm{i}k_0(x-\zeta)}\right) \qquad \text{for } x > \zeta \\ \frac{Z_r'}{F_{w/r}} &= \frac{1}{4k_0^3 EI}\left(\mathrm{e}^{-k_0(x-\zeta)} + \mathrm{i}\mathrm{e}^{-\mathrm{i}k_0(x-\zeta)}\right) \qquad \text{for } x < \zeta \end{aligned} \tag{B.17}$$

for $\mathrm{Re}(k_0) < 0$ and $\mathrm{Im}(k_0) < 0$ by

$$\begin{aligned}\frac{Z'_r}{F_{w/r}} &= \frac{1}{4k_0^3 EI}\left(\mathrm{e}^{k_0(x-\zeta)} - \mathrm{i}\mathrm{e}^{-\mathrm{i}k_0(x-\zeta)}\right) \qquad \text{for } x > \zeta \\ \frac{Z'_r}{F_{w/r}} &= \frac{1}{4k_0^3 EI}\left(\mathrm{e}^{-k_0(x-\zeta)} - \mathrm{i}\mathrm{e}^{\mathrm{i}k_0(x-\zeta)}\right) \qquad \text{for } x < \zeta\end{aligned} \tag{B.18}$$

and for $\mathrm{Re}(k_0) > 0$ and $\mathrm{Im}(k_0) < 0$ by

$$\begin{aligned}\frac{Z'_r}{F_{w/r}} &= \frac{1}{4k_0^3 EI}\left(-\mathrm{e}^{-k_0(x-\zeta)} - \mathrm{i}\mathrm{e}^{-\mathrm{i}k_0(x-\zeta)}\right) \qquad \text{for } x > \zeta \\ \frac{Z'_r}{F_{w/r}} &= \frac{1}{4k_0^3 EI}\left(-\mathrm{e}^{k_0(x-\zeta)} - \mathrm{i}\mathrm{e}^{\mathrm{i}k_0(x-\zeta)}\right) \qquad \text{for } x < \zeta\end{aligned} \tag{B.19}$$

This solution is the Green's function of the problem or the receptance of the rail to this kind of load (vertical and applied at $x = \zeta$ and at the rail head).

## B.3 Natural frequencies

This track model have two resonant frequencies, associated to the in-phase and anti-phase modes. In the case of the undamped system, this two modes are defined by two natural frequencies. The analytical expressions of these natural frequencies follow from Eq. (B.16) by assuming no viscous and structural dampings. In this case, $k_0$ can be expressed as

$$k_0 = \sqrt[4]{\frac{\omega^2 \rho S(k_F + k_B - m_s\omega^2) - k_F(k_B - m_s\omega^2)}{EI(k_F + k_B - m_s\omega^2)}} \tag{B.20}$$

To evaluate the natural frequencies $\bar{\omega}'_n$ Eq. (B.16) denominator must be equalled to zero. Therefore, natural frequencies are the positive solutions of the equation

$$-m_s\rho S\bar{\omega}'^4_n + (\rho S(k_F + k_B) + k_F m_s)\bar{\omega}'^2_n - k_F k_B = 0 \tag{B.21}$$

where $n$ is the number of the mode. Solving this fourth-degree equation gives 4 solutions

$$\begin{aligned}
\bar{\omega}_1'^- &= -\sqrt{\frac{\rho S(k_F+k_B)+k_F m_s - R}{2m_s\rho S}} \\
\bar{\omega}_1'^+ &= \sqrt{\frac{\rho S(k_F+k_B)+k_F m_s - R}{2m_s\rho S}} \\
\bar{\omega}_2'^- &= -\sqrt{\frac{\rho S(k_F+k_B)+k_F m_s + R}{2m_s\rho S}} \\
\bar{\omega}_2'^+ &= \sqrt{\frac{\rho S(k_F+k_B)+k_F m_s + R}{2m_s\rho S}}
\end{aligned} \tag{B.22}$$

where

$$R = \sqrt{S^2\rho^2(k_B+k_F)^2 + 2S\rho m_s k_F(k_F-k_B) + k_F^2 m_s^2} \tag{B.23}$$

As the term $\rho S(k_F+k_B)+k_F m_s$ is always higher than $R$, $\bar{\omega}_1'^+$ and $\bar{\omega}_2'^+$ are always real positive values and $\bar{\omega}_1'^-$ and $\bar{\omega}_2'^-$ are always real negative values. Ignoring these negative solutions, the natural frequencies of the in-phase and anti-phase modes are, respectively,

$$\bar{\omega}_1' = \sqrt{\frac{\rho S(k_F+k_B)+k_F m_s - R}{2m_s\rho S}} \tag{B.24}$$

$$\bar{\omega}_2' = \sqrt{\frac{\rho S(k_F+k_B)+k_F m_s + R}{2m_s\rho S}} \tag{B.25}$$

In contrast to an SDOF or MDOF typical vibration models, the natural frequency of this model is not exactly equal to the resonant frequency for the case of structural damping.

# Appendix C

# Complete results obtained by using the superstructure model

In this appendix, the results obtained for any combination of superstructure and subgrade parameters shown in Tables 4.1, 4.2, 4.3 and 3.1 are presented. This results are:

- Track receptances at the load application point: the effects of the subgrade parameters on them. Section C.1.
- The parameters of the equivalent model obtained by fitting the receptances. Section C.2.
- The effect of the subgrade parameters on the wheel/rail contact dynamics. Section C.3.

## C.1 Effects of the subgrade parameters on the track receptance

In this section the effects of the subgrade mechanical parameters, which are the Young's modulus, Poisson's ratio, density, and the dampings $D_P$ and $D_S$, on the track receptance at the load application point is presented in its non-dimensionless and dimensionless forms. It is also presented the effects of the superstructure width in this track receptance. This results are obtained following the approach presented in Sections 4.1 and 4.2 and complete the results presented there.

### C.1.1 Effects of the ground types

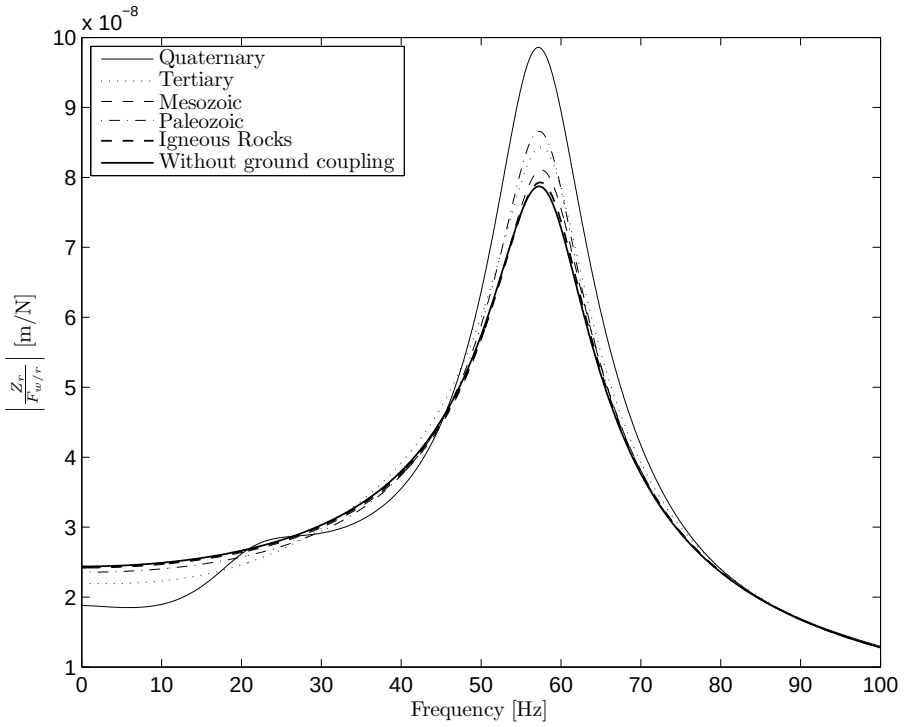


FIGURE C.1: Module of the rail receptance for five different subgrade parameters of the Table 3.1 and for the superstructure parameters in Case 1 (see Tables 4.1, 4.2 and 4.3).

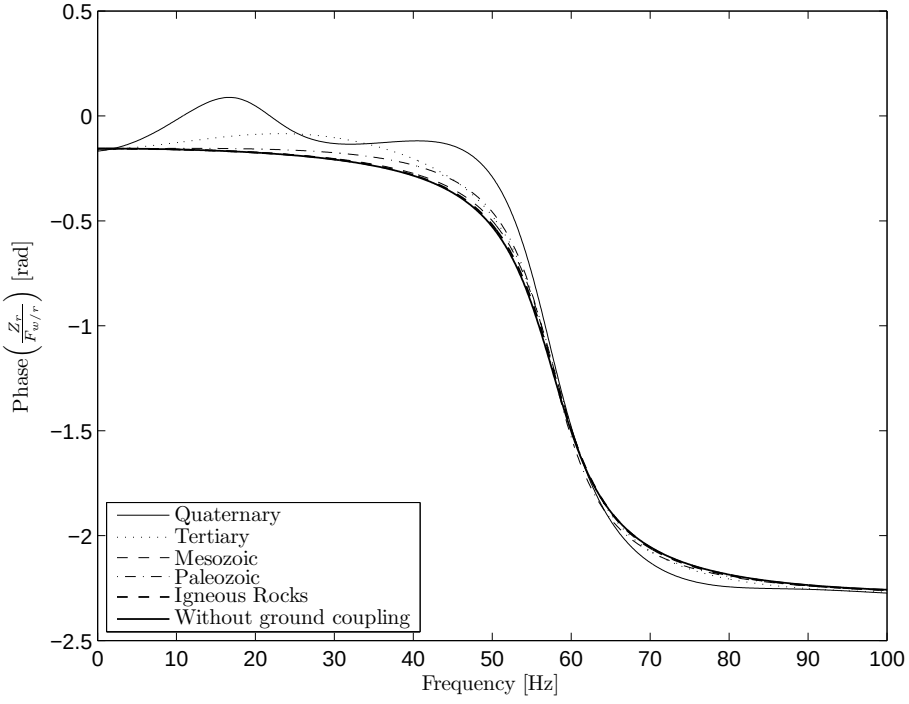


FIGURE C.2: Phase of the rail receptance for five different subgrade parameters of the Table 3.1 and for the superstructure parameters in Case 1 (see Tables 4.1, 4.2 and 4.3).

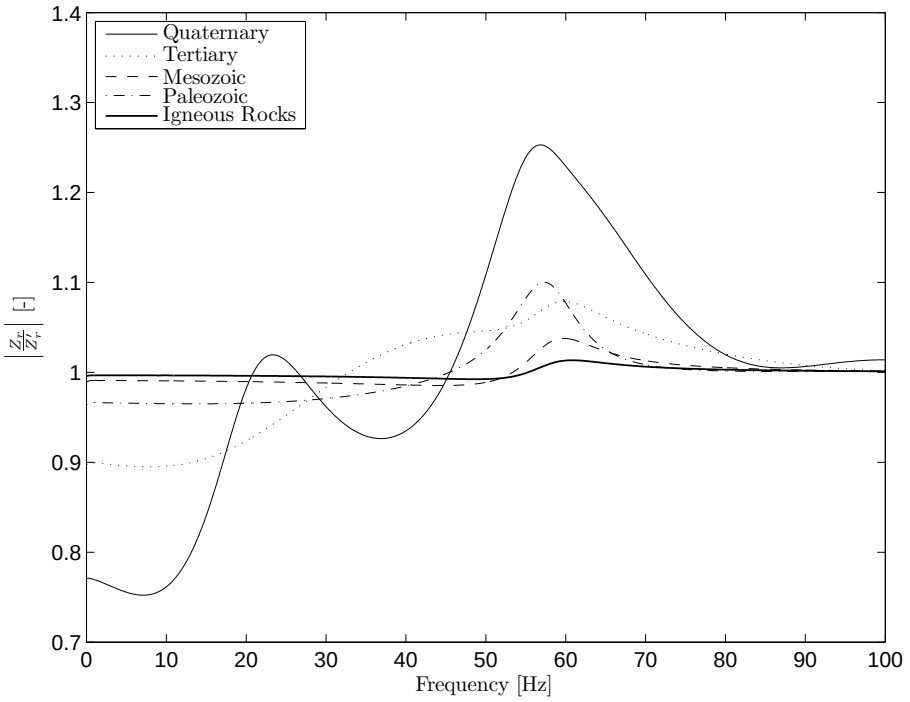


FIGURE C.3: Adimensional module of the rail receptance for five different subgrade parameters of the Table 3.1 and for the superstructure parameters in Case 1 (see Tables 4.1, 4.2 and 4.3).

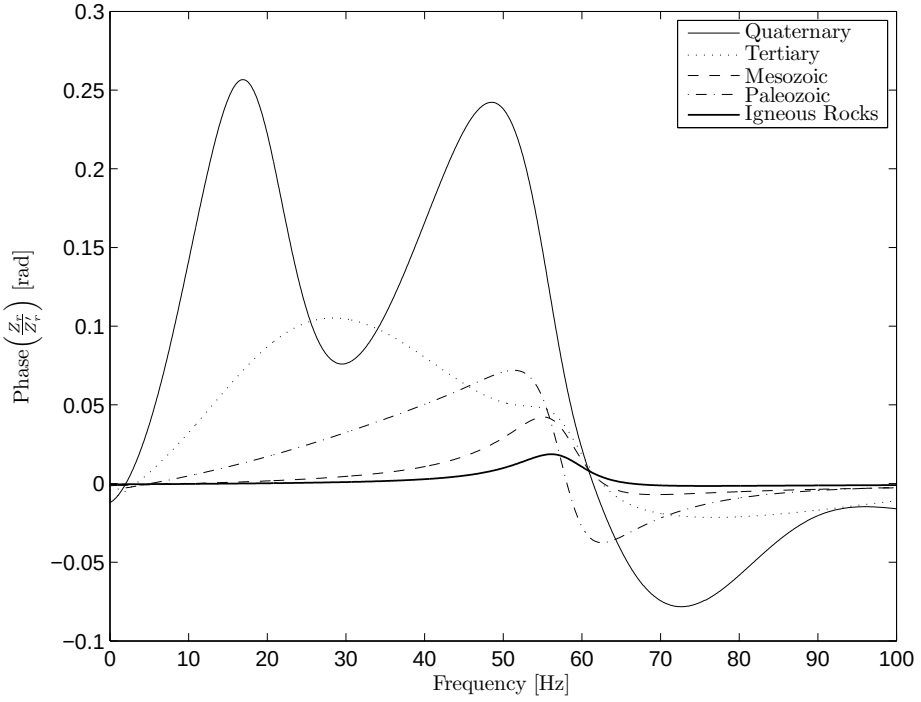


FIGURE C.4: Adimensional phase of the rail receptance for five different subgrade parameters of the Table 3.1 and for the superstructure parameters in Case 1 (see Tables 4.1, 4.2 and 4.3).

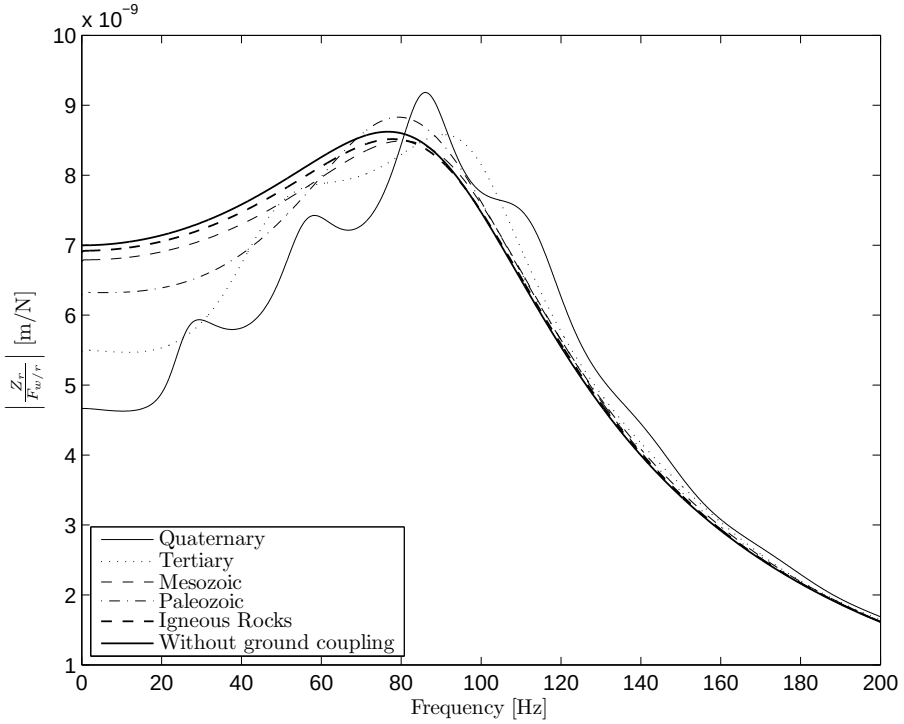


FIGURE C.5: Module of the rail receptance for five different subgrade parameters of the Table 3.1 and for the superstructure parameters in Case 2 (see Tables 4.1, 4.2 and 4.3).

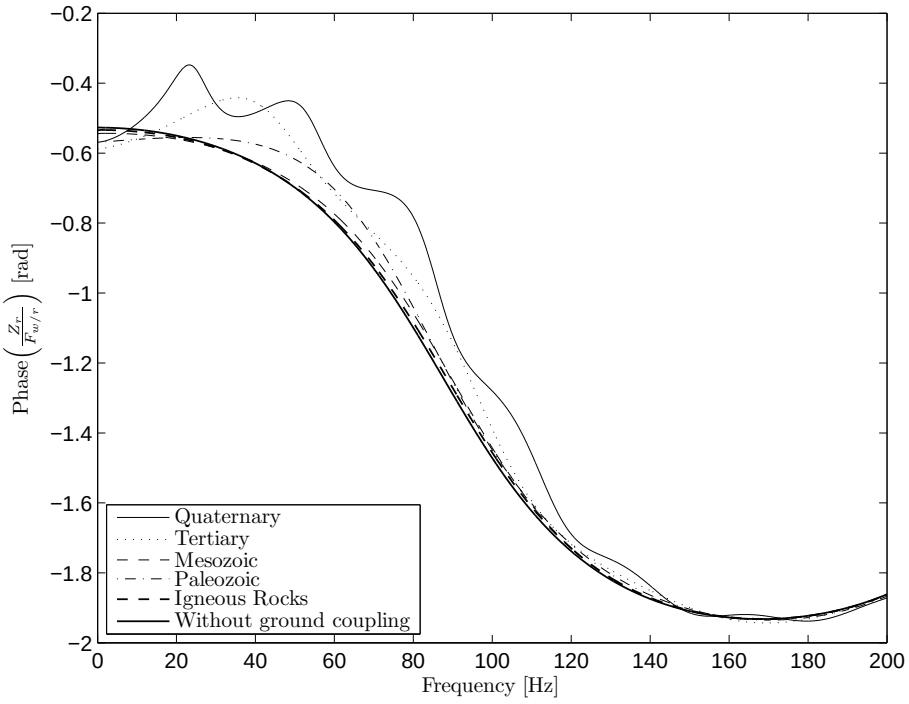


FIGURE C.6: Phase of the rail receptance for five different subgrade parameters of the Table 3.1 and for the superstructure parameters in Case 2 (see Tables 4.1, 4.2 and 4.3).

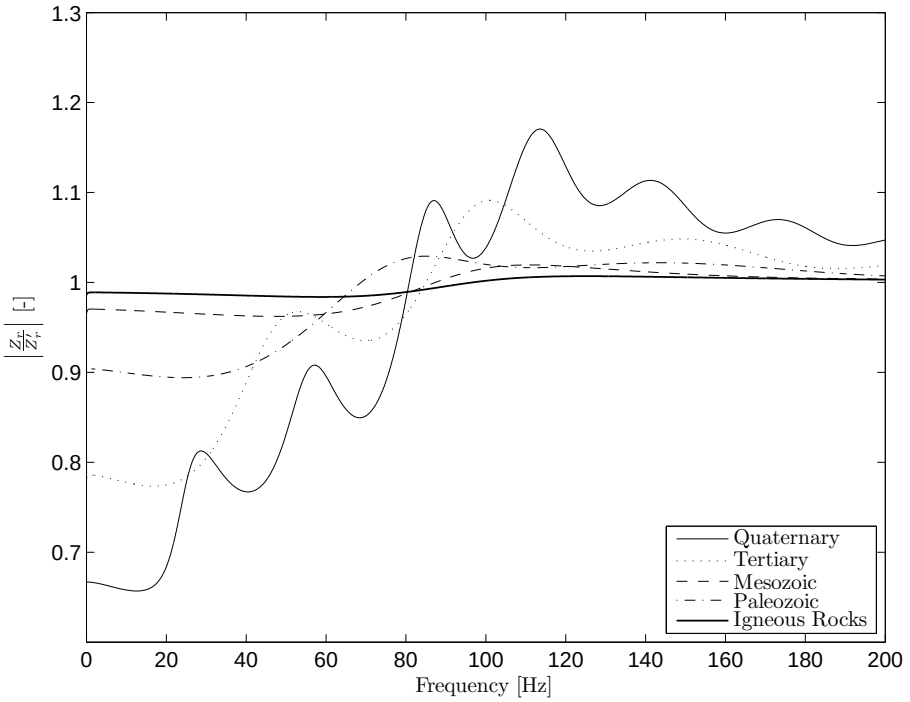


FIGURE C.7: Adimensional module of the rail receptance for five different subgrade parameters of the Table 3.1 and for the superstructure parameters in Case 2 (see Tables 4.1, 4.2 and 4.3).

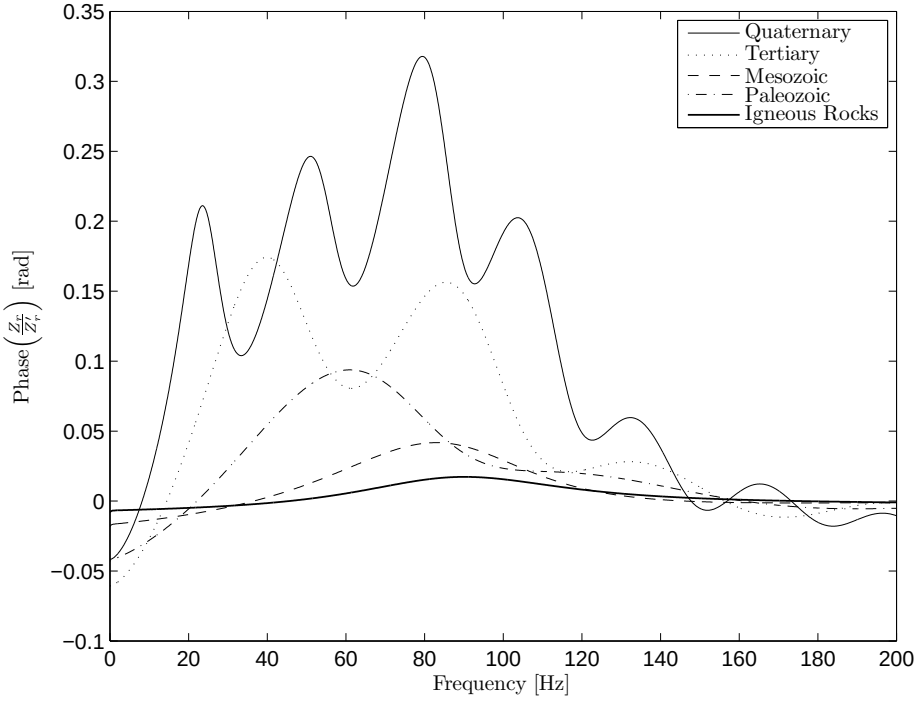


FIGURE C.8: Adimensional phase of the rail receptance for five different subgrade parameters of the Table 3.1 and for the superstructure parameters in Case 2 (see Tables 4.1, 4.2 and 4.3).

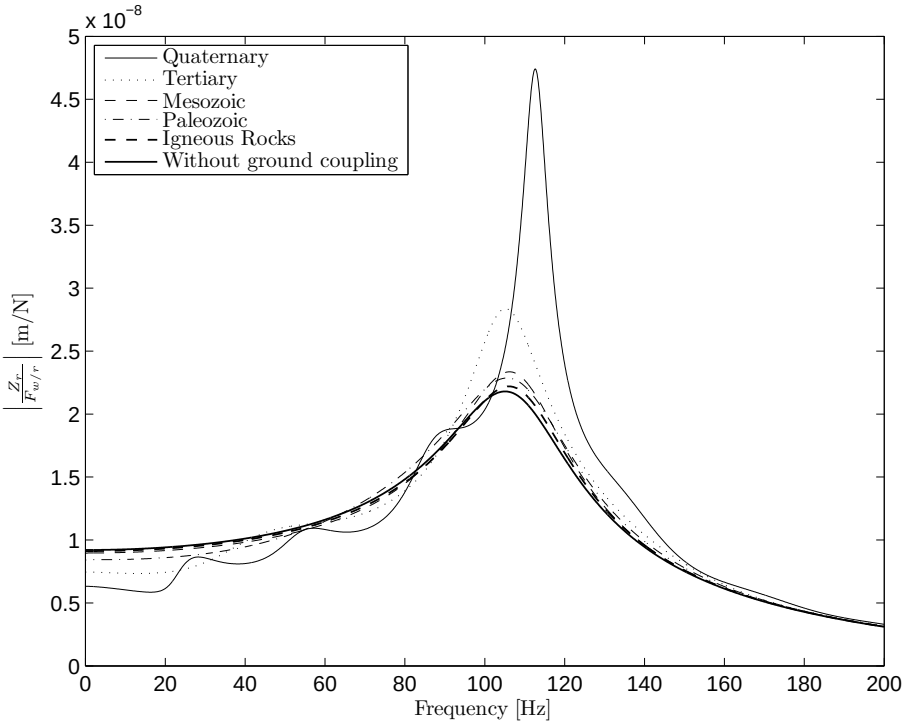


FIGURE C.9: Module of the rail receptance for five different subgrade parameters of the Table 3.1 and for the superstructure parameters in Case 3 (see Tables 4.1, 4.2 and 4.3).

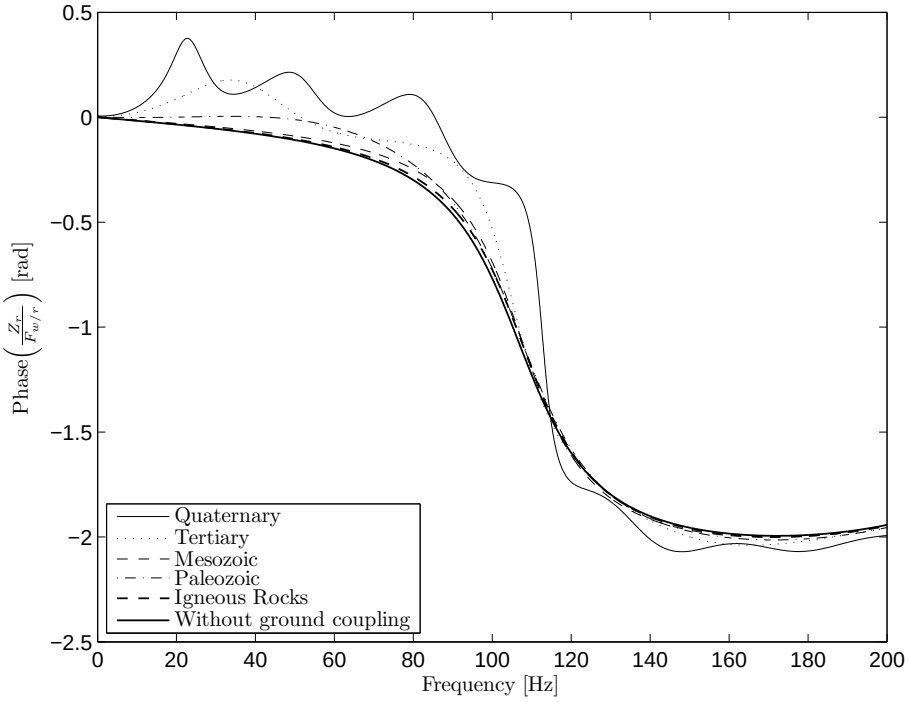


FIGURE C.10: Phase of the rail receptance for five different subgrade parameters of the Table 3.1 and for the superstructure parameters in Case 3 (see Tables 4.1, 4.2 and 4.3).

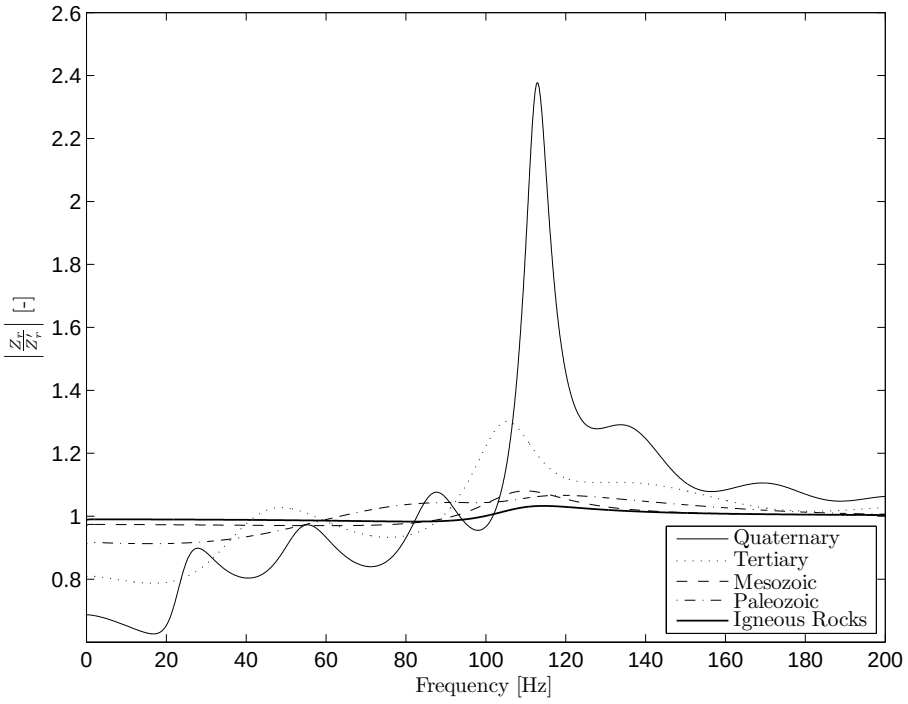


FIGURE C.11: Adimensional module of the rail receptance for five different subgrade parameters of the Table 3.1 and for the superstructure parameters in Case 3 (see Tables 4.1, 4.2 and 4.3).

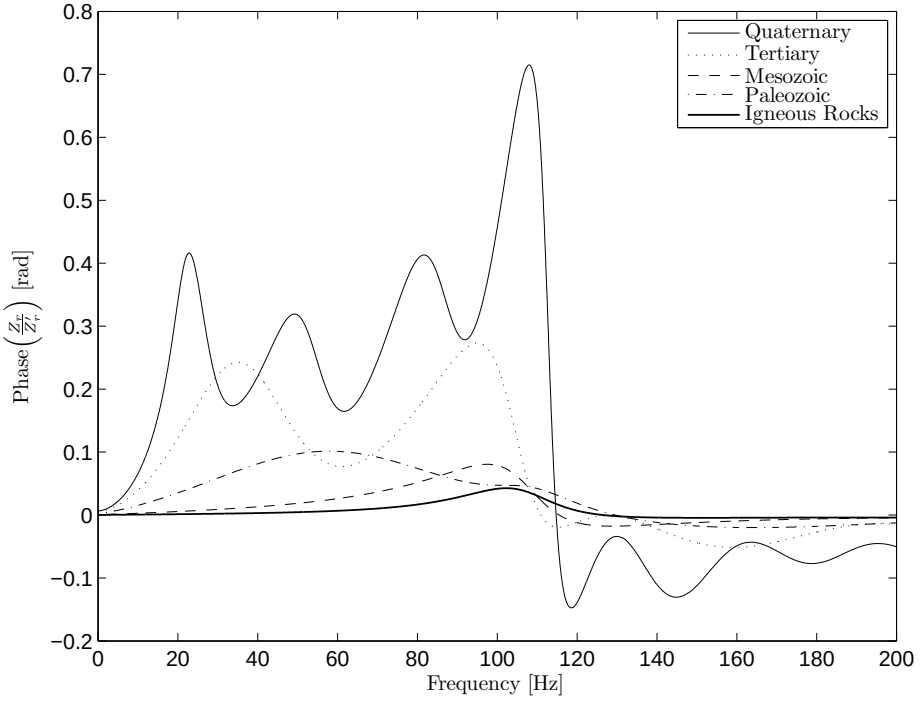


FIGURE C.12: Adimensional phase of the rail receptance for five different subgrade parameters of the Table 3.1 and for the superstructure parameters in Case 3 (see Tables 4.1, 4.2 and 4.3).

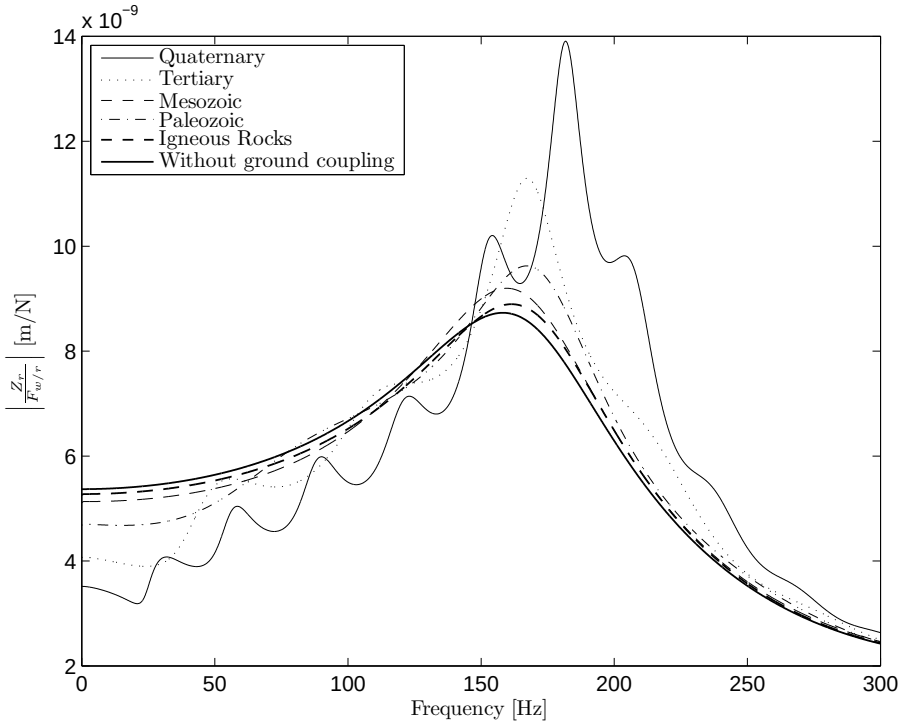


FIGURE C.13: Module of the rail receptance for five different subgrade parameters of the Table 3.1 and for the superstructure parameters in Case 4 (see Tables 4.1, 4.2 and 4.3).

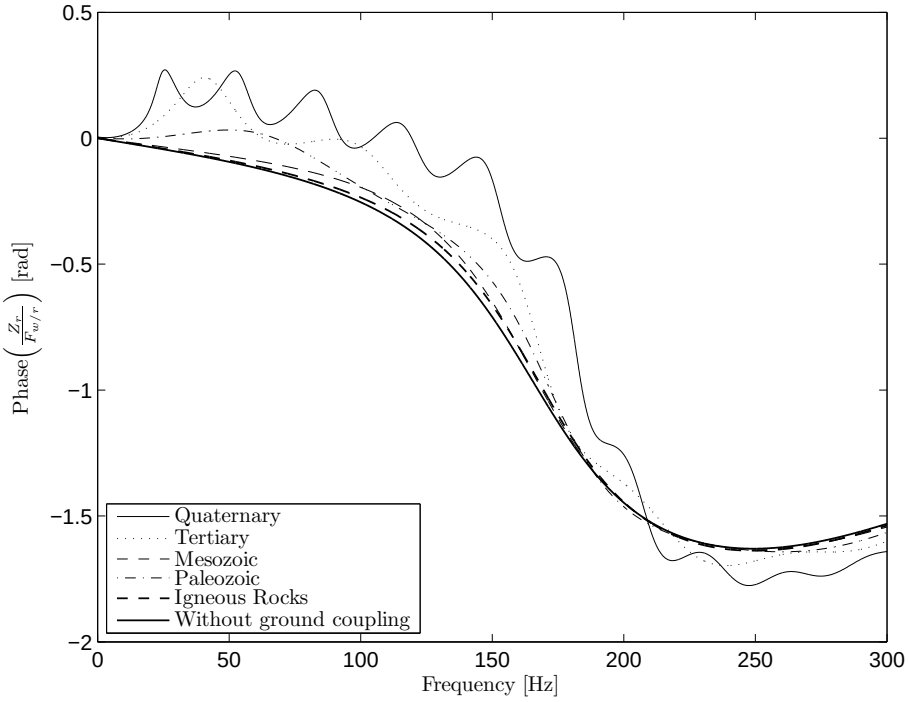


FIGURE C.14: Phase of the rail receptance for five different subgrade parameters of the Table 3.1 and for the superstructure parameters in Case 4 (see Tables 4.1, 4.2 and 4.3).

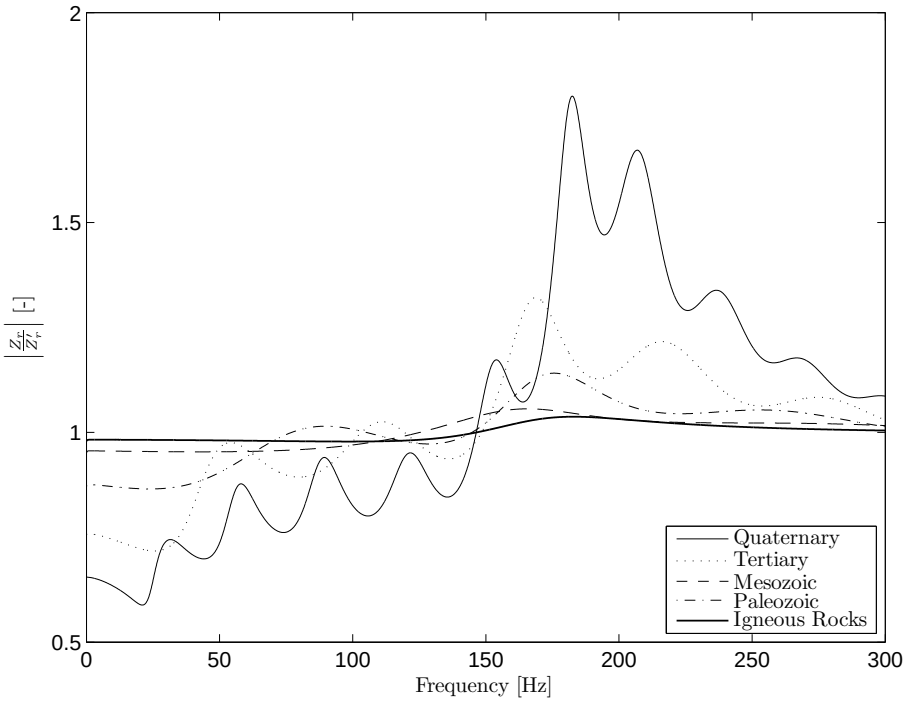


FIGURE C.15: Adimensional module of the rail receptance for five different subgrade parameters of the Table 3.1 and for the superstructure parameters in Case 4 (see Tables 4.1, 4.2 and 4.3).

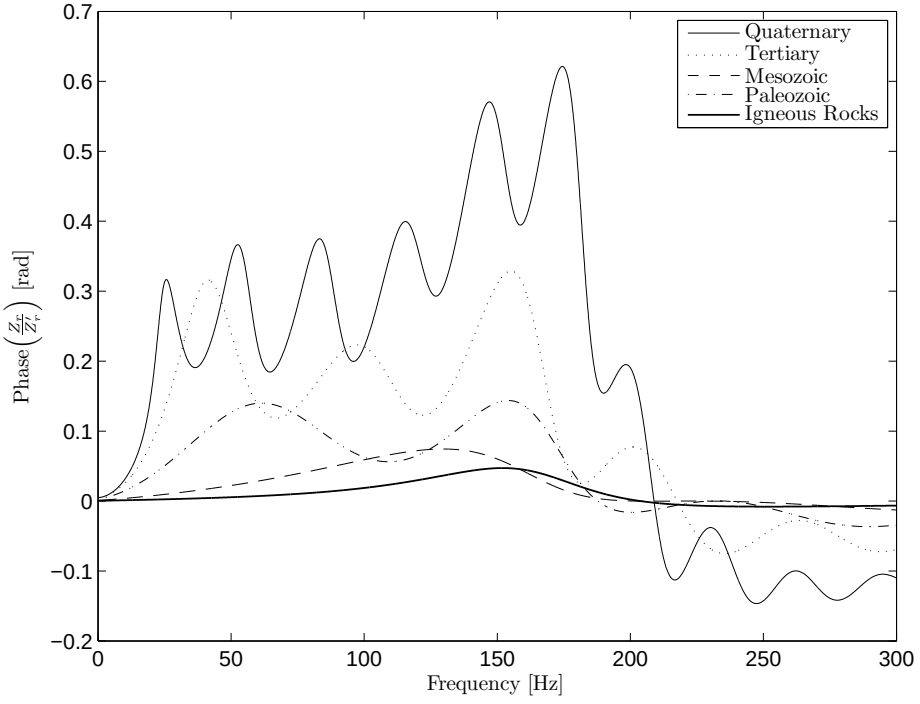


FIGURE C.16: Adimensional phase of the rail receptance for five different subgrade parameters of the Table 3.1 and for the superstructure parameters in Case 4 (see Tables 4.1, 4.2 and 4.3).

### C.1.2 Effects of the dampings $D_P$ and $D_S$

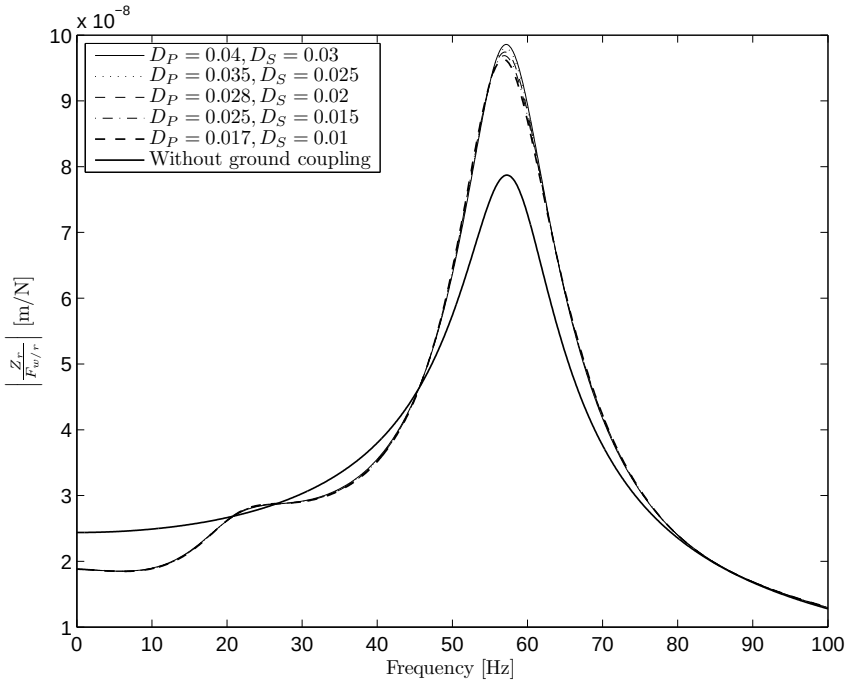


FIGURE C.17: Module of the rail receptance for five different combinations of subgrade damping coefficients $D_P$ and $D_S$ and for the superstructure parameters in Case 1 (see Tables 4.1, 4.2 and 4.3). The other mechanical parameters of the subgrade are equal to the Quaternary ground type (see Table 3.1).

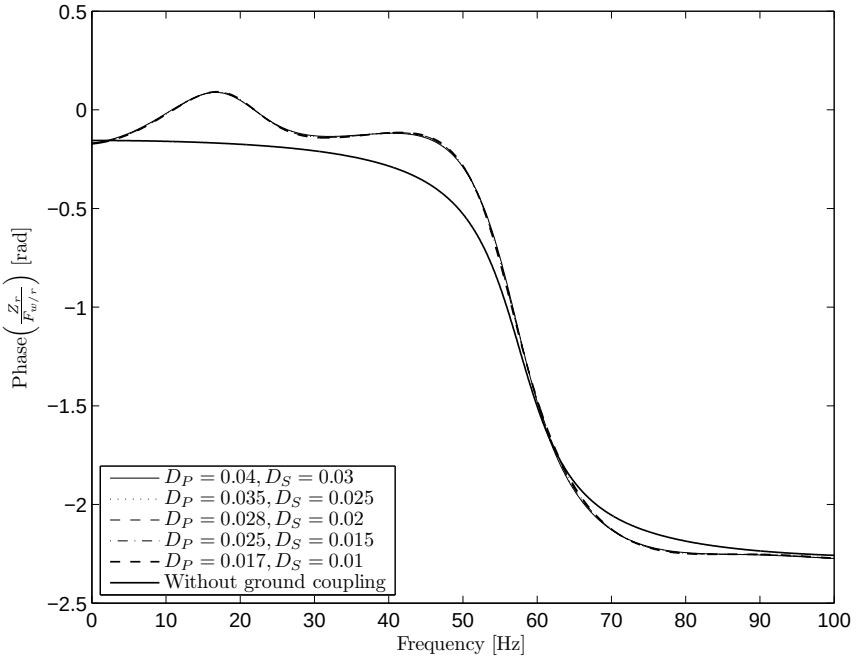


FIGURE C.18: Phase of the rail receptance for five different combinations of subgrade damping coefficients $D_P$ and $D_S$ and for the superstructure parameters in Case 1 (see Tables 4.1, 4.2 and 4.3). The other mechanical parameters of the subgrade are equal to the Quaternary ground type (see Table 3.1).

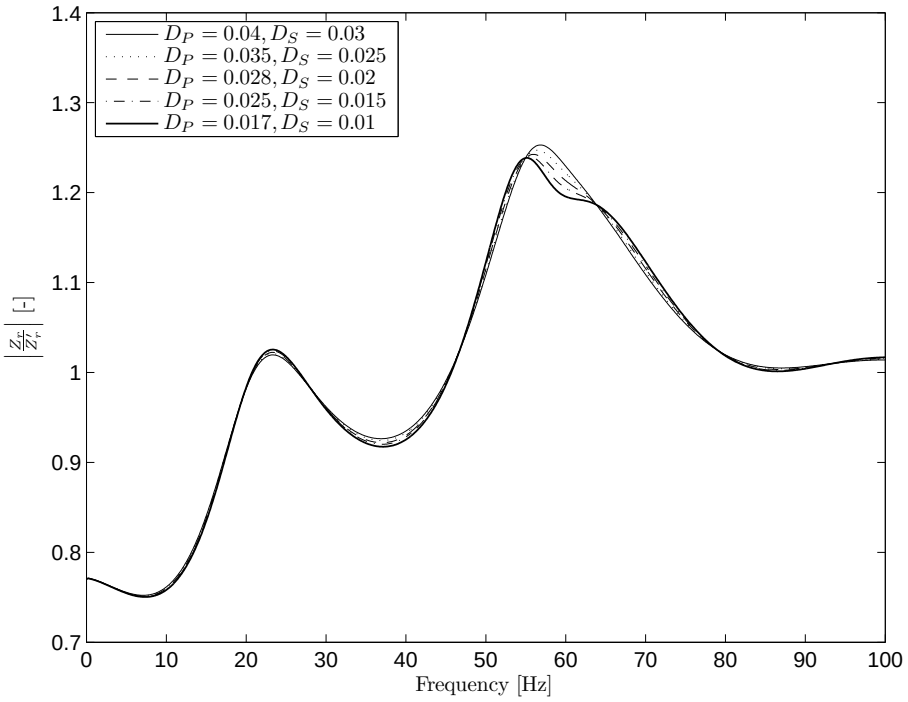


FIGURE C.19: Adimensional module of the rail receptance for five different combinations of subgrade damping coefficients $D_P$ and $D_S$ and for the superstructure parameters in Case 1 (see Tables 4.1, 4.2 and 4.3). The other mechanical parameters of the subgrade are equal to the Quaternary ground type (see Table 3.1).

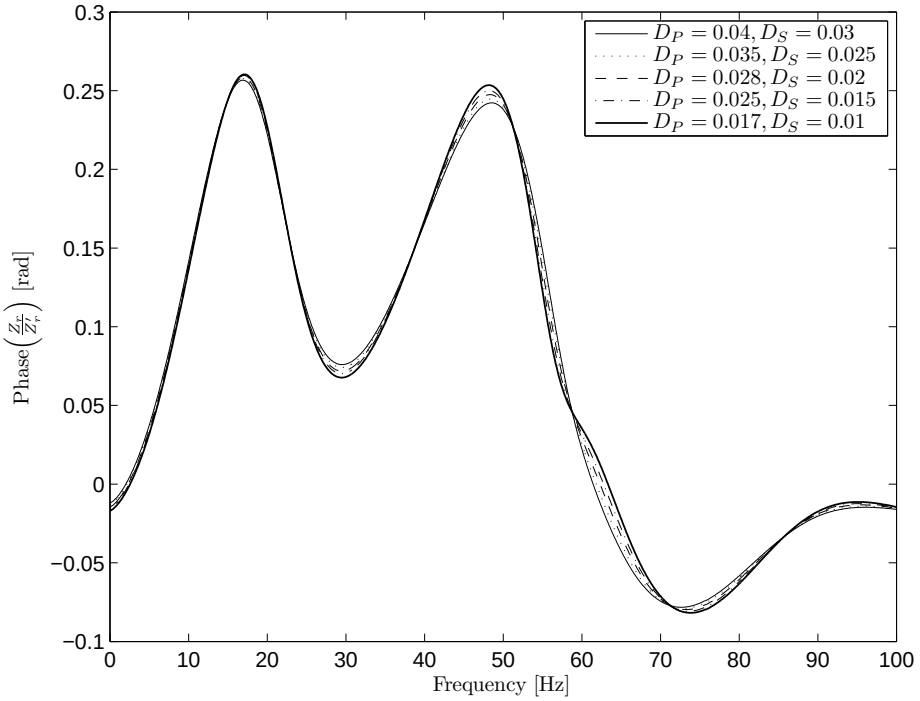


FIGURE C.20: Adimensional phase of the rail receptance for five different combinations of subgrade damping coefficients $D_P$ and $D_S$ and for the superstructure parameters in Case 1 (see Tables 4.1, 4.2 and 4.3). The other mechanical parameters of the subgrade are equal to the Quaternary ground type (see Table 3.1).

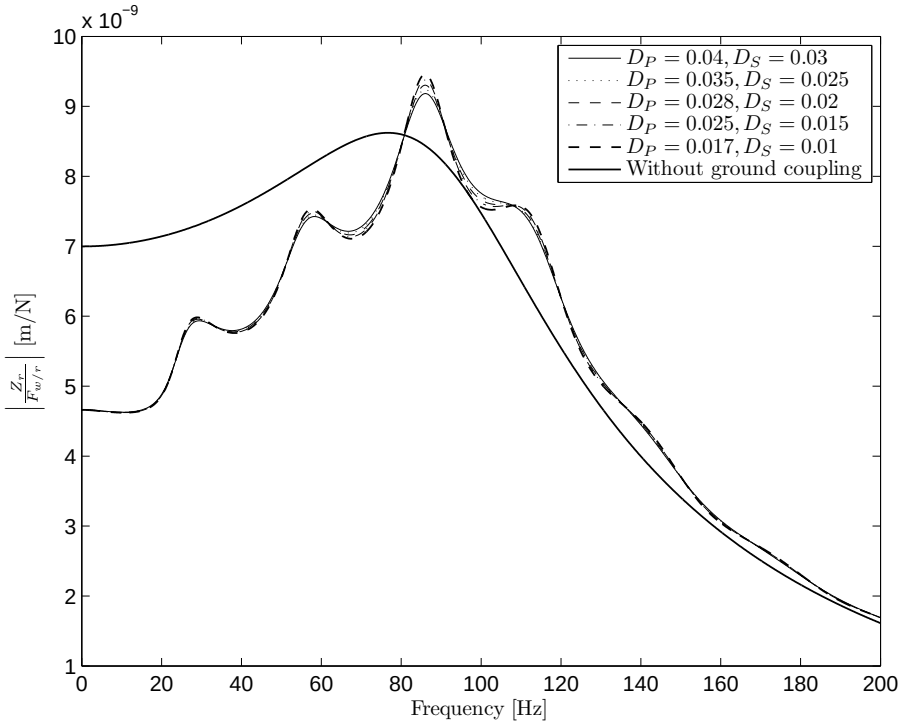


FIGURE C.21: Module of the rail receptance for five different combinations of subgrade damping coefficients $D_P$ and $D_S$ and for the superstructure parameters in Case 2 (see Tables 4.1, 4.2 and 4.3). The other mechanical parameters of the subgrade are equal to the Quaternary ground type (see Table 3.1).

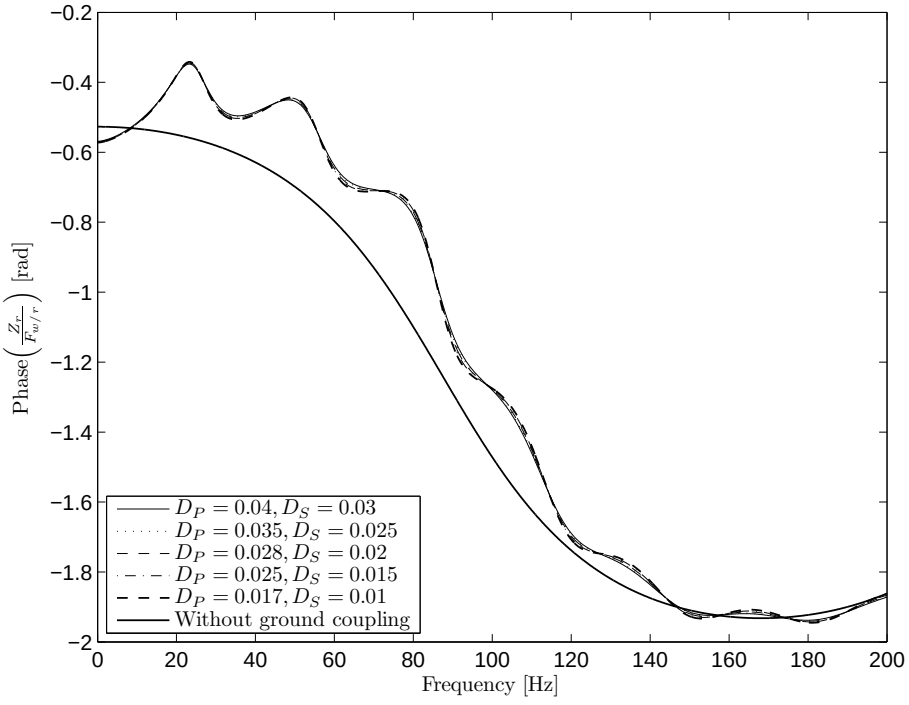


FIGURE C.22: Phase of the rail receptance for five different combinations of subgrade damping coefficients $D_P$ and $D_S$ and for the superstructure parameters in Case 2 (see Tables 4.1, 4.2 and 4.3). The other mechanical parameters of the subgrade are equal to the Quaternary ground type (see Table 3.1).

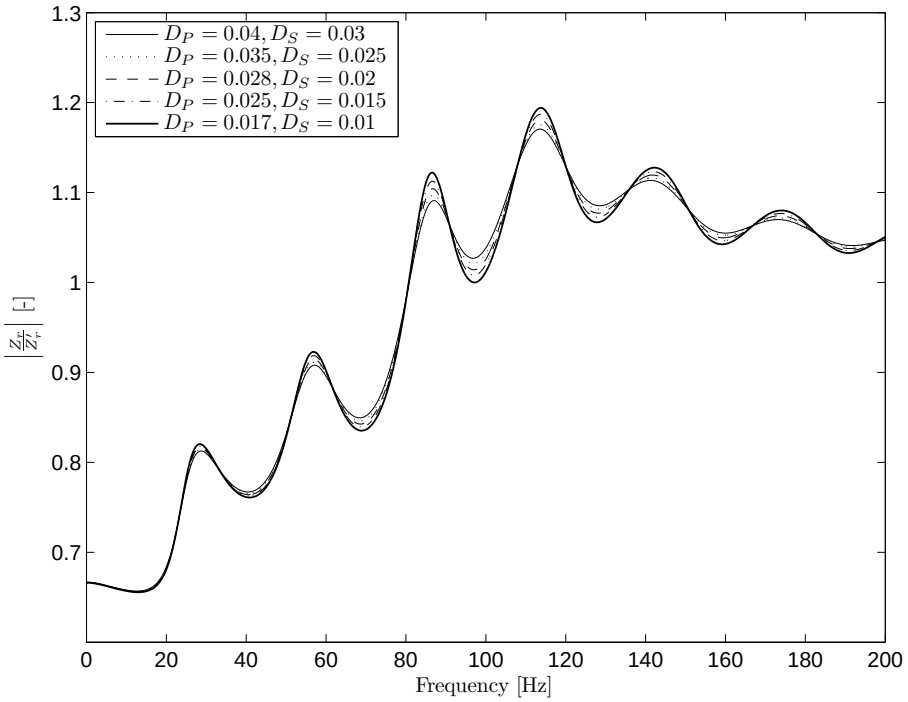


FIGURE C.23: Adimensional module of the rail receptance for five different combinations of subgrade damping coefficients $D_P$ and $D_S$ and for the superstructure parameters in Case 2 (see Tables 4.1, 4.2 and 4.3). The other mechanical parameters of the subgrade are equal to the Quaternary ground type (see Table 3.1).

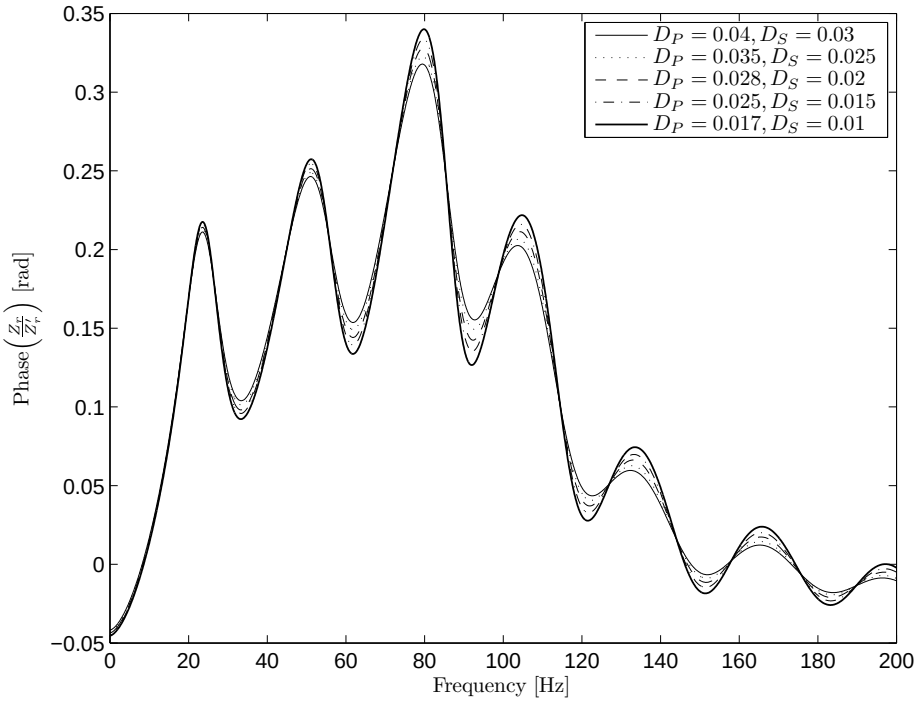


FIGURE C.24: Adimensional phase of the rail receptance for five different combinations of subgrade damping coefficients $D_P$ and $D_S$ and for the superstructure parameters in Case 2 (see Tables 4.1, 4.2 and 4.3). The other mechanical parameters of the subgrade are equal to the Quaternary ground type (see Table 3.1).

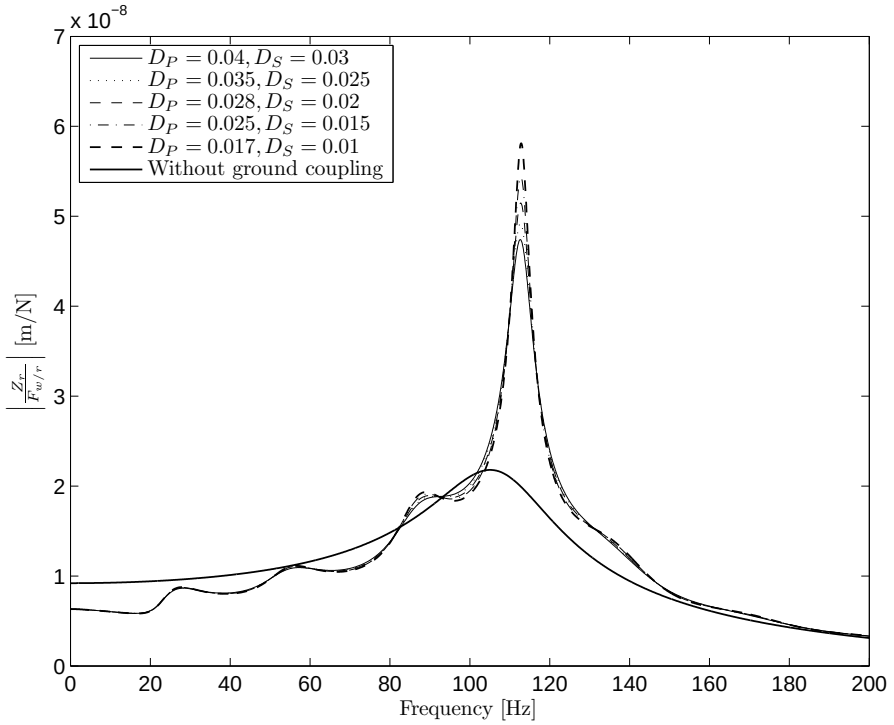


FIGURE C.25: Module of the rail receptance for five different combinations of subgrade damping coefficients $D_P$ and $D_S$ and for the superstructure parameters in Case 3 (see Tables 4.1, 4.2 and 4.3). The other mechanical parameters of the subgrade are equal to the Quaternary ground type (see Table 3.1).

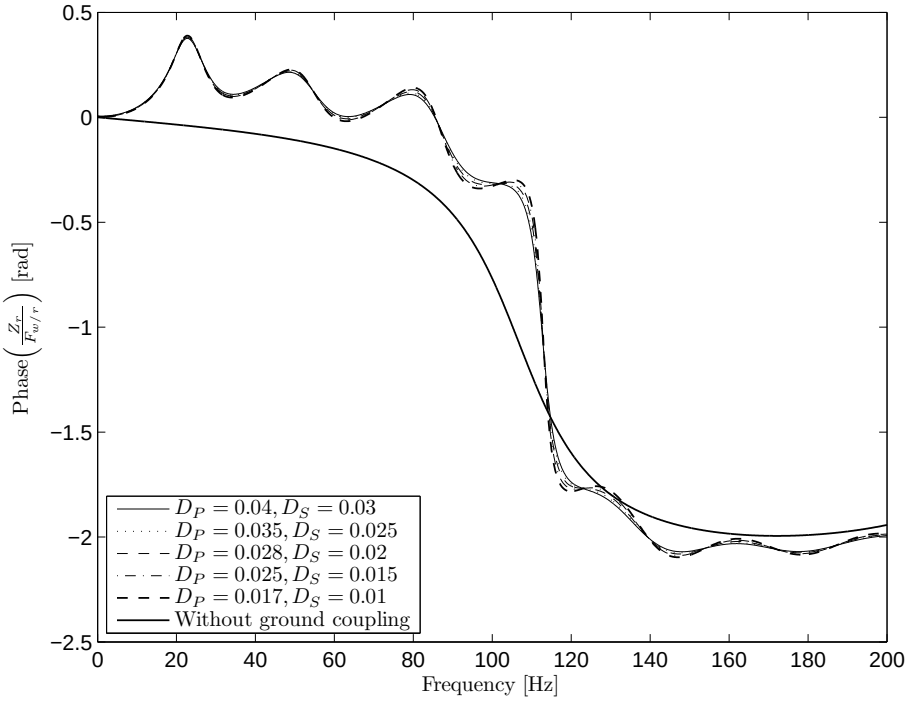


FIGURE C.26: Phase of the rail receptance for five different combinations of subgrade damping coefficients $D_P$ and $D_S$ and for the superstructure parameters in Case 3 (see Tables 4.1, 4.2 and 4.3). The other mechanical parameters of the subgrade are equal to the Quaternary ground type (see Table 3.1).

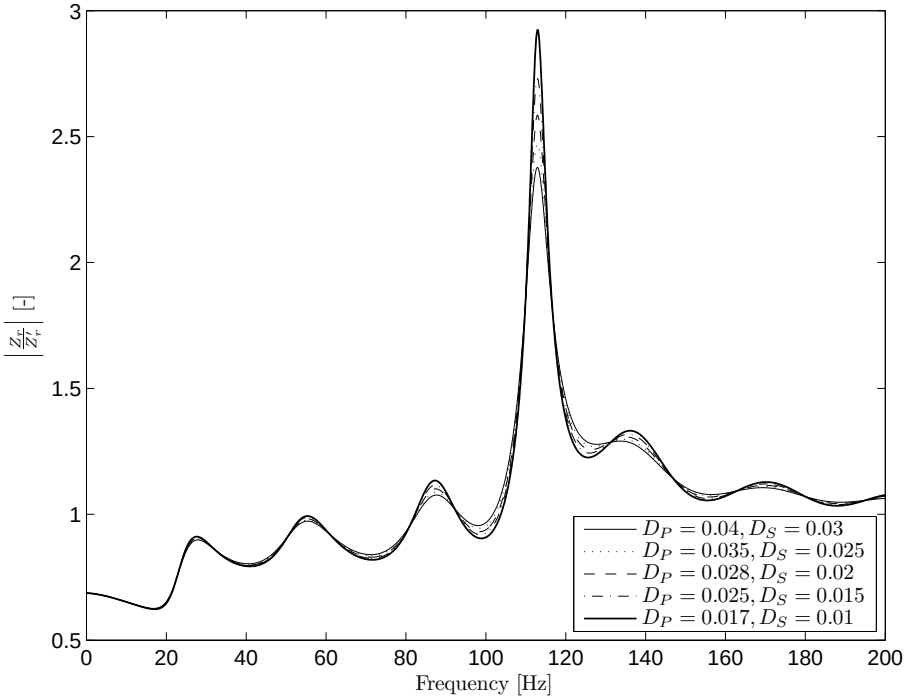


FIGURE C.27: Adimensional module of the rail receptance for five different combinations of subgrade damping coefficients $D_P$ and $D_S$ and for the superstructure parameters in Case 3 (see Tables 4.1, 4.2 and 4.3). The other mechanical parameters of the subgrade are equal to the Quaternary ground type (see Table 3.1).

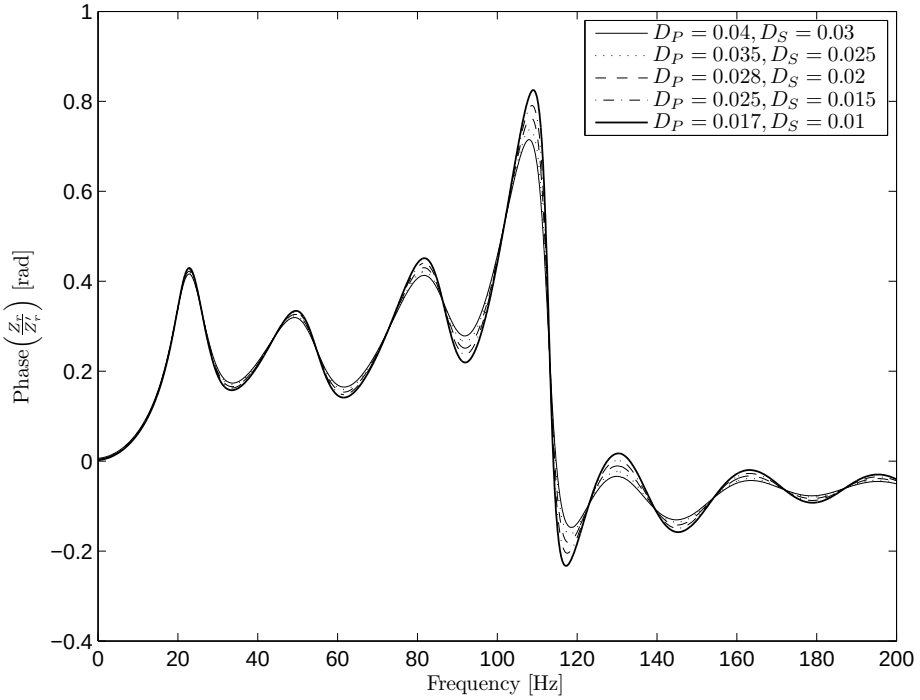


FIGURE C.28: Adimensional phase of the rail receptance for five different combinations of subgrade damping coefficients $D_P$ and $D_S$ and for the superstructure parameters in Case 3 (see Tables 4.1, 4.2 and 4.3). The other mechanical parameters of the subgrade are equal to the Quaternary ground type (see Table 3.1).

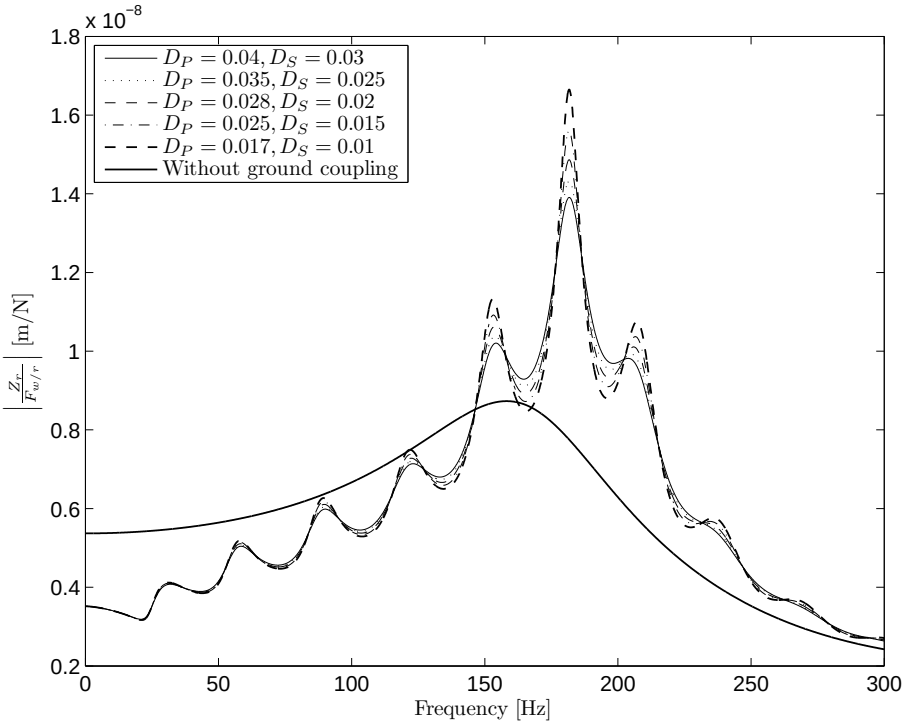


FIGURE C.29: Module of the rail receptance for five different combinations of subgrade damping coefficients $D_P$ and $D_S$ and for the superstructure parameters in Case 4 (see Tables 4.1, 4.2 and 4.3). The other mechanical parameters of the subgrade are equal to the Quaternary ground type (see Table 3.1).

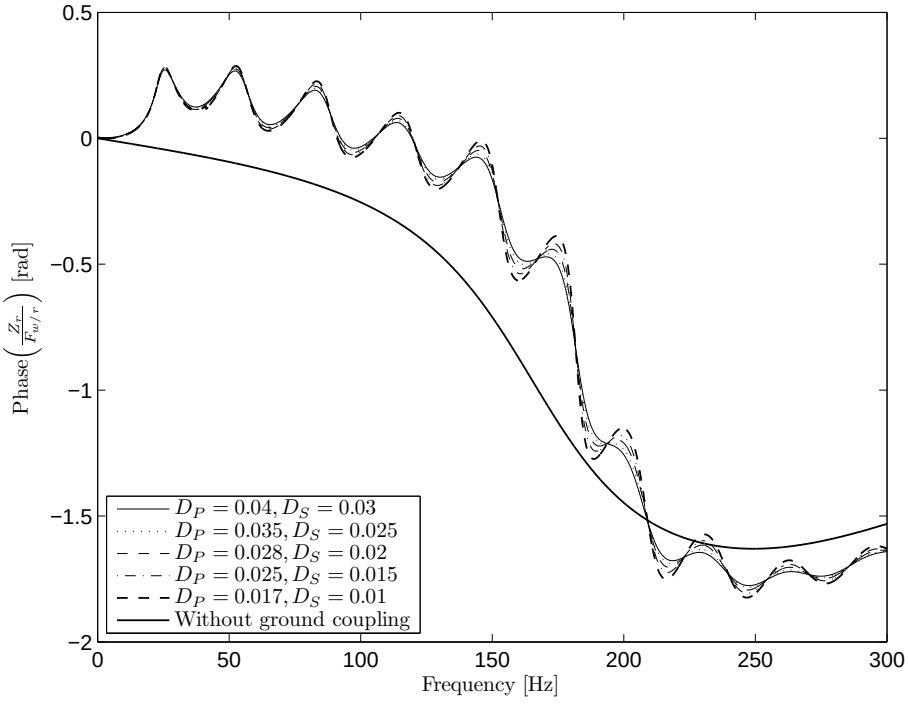


FIGURE C.30: Phase of the rail receptance for five different combinations of subgrade damping coefficients $D_P$ and $D_S$ and for the superstructure parameters in Case 4 (see Tables 4.1, 4.2 and 4.3). The other mechanical parameters of the subgrade are equal to the Quaternary ground type (see Table 3.1).

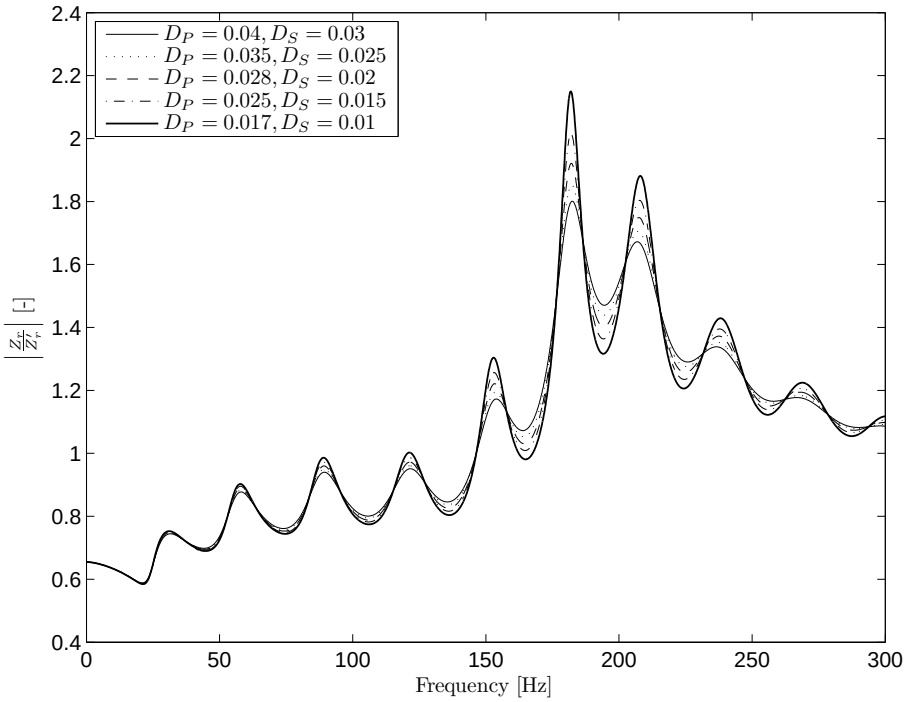


FIGURE C.31: Adimensional module of the rail receptance for five different combinations of subgrade damping coefficients $D_P$ and $D_S$ and for the superstructure parameters in Case 4 (see Tables 4.1, 4.2 and 4.3). The other mechanical parameters of the subgrade are equal to the Quaternary ground type (see Table 3.1).

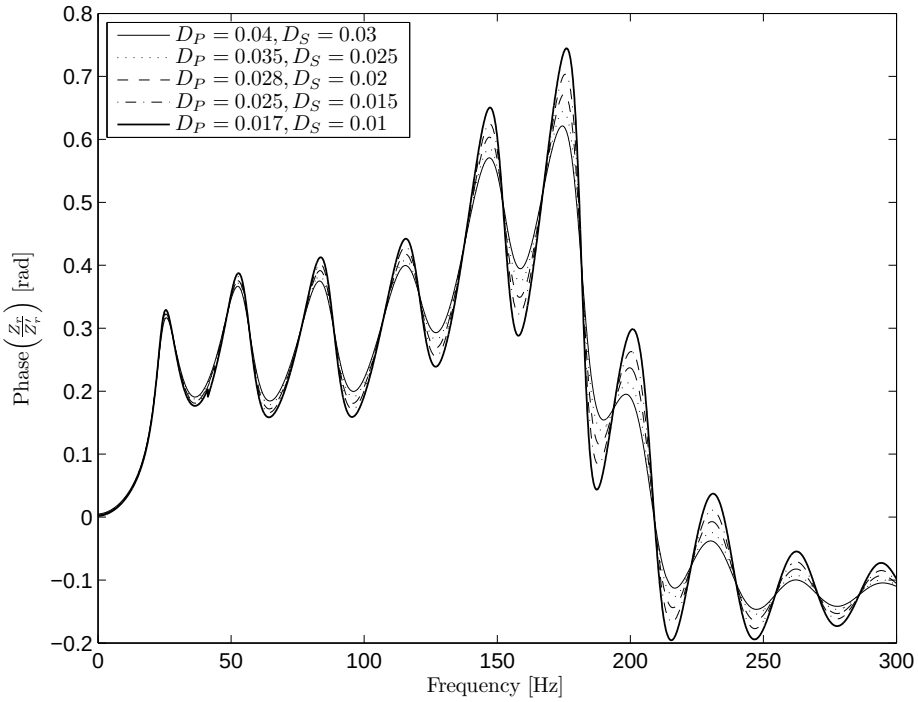


FIGURE C.32: Adimensional phase of the rail receptance for five different combinations of subgrade damping coefficients $D_P$ and $D_S$ and for the superstructure parameters in Case 4 (see Tables 4.1, 4.2 and 4.3). The other mechanical parameters of the subgrade are equal to the Quaternary ground type (see Table 3.1).

### C.1.3 Effects of the density

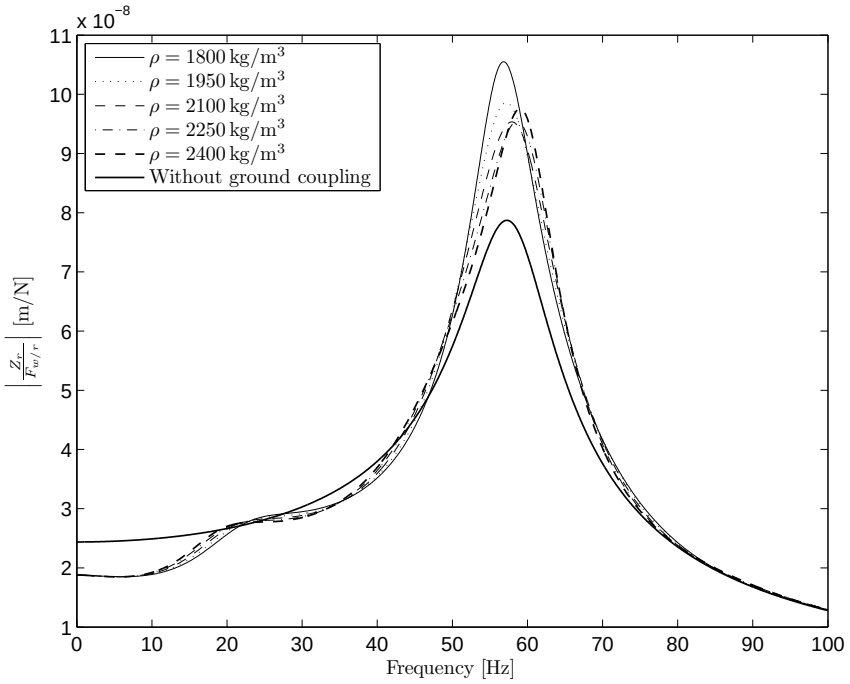


FIGURE C.33: Module of the rail receptance for five different subgrade densities and for the superstructure parameters in Case 1 (see Tables 4.1, 4.2 and 4.3). The other mechanical parameters of the subgrade are equal to the Quaternary ground type (see Table 3.1).

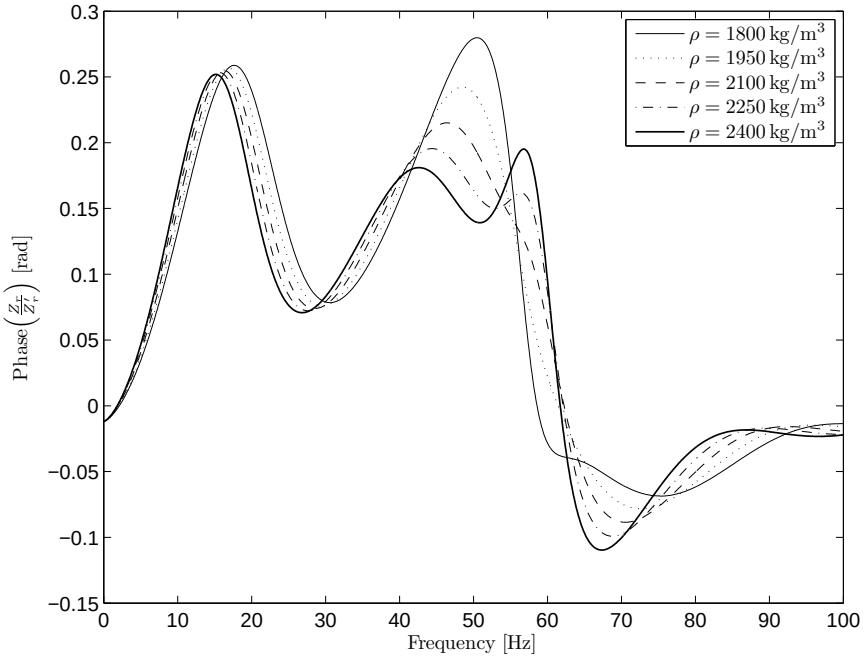


FIGURE C.34: Phase of the rail receptance for five different subgrade densities and for the superstructure parameters in Case 1 (see Tables 4.1, 4.2 and 4.3). The other mechanical parameters of the subgrade are equal to the Quaternary ground type (see Table 3.1).

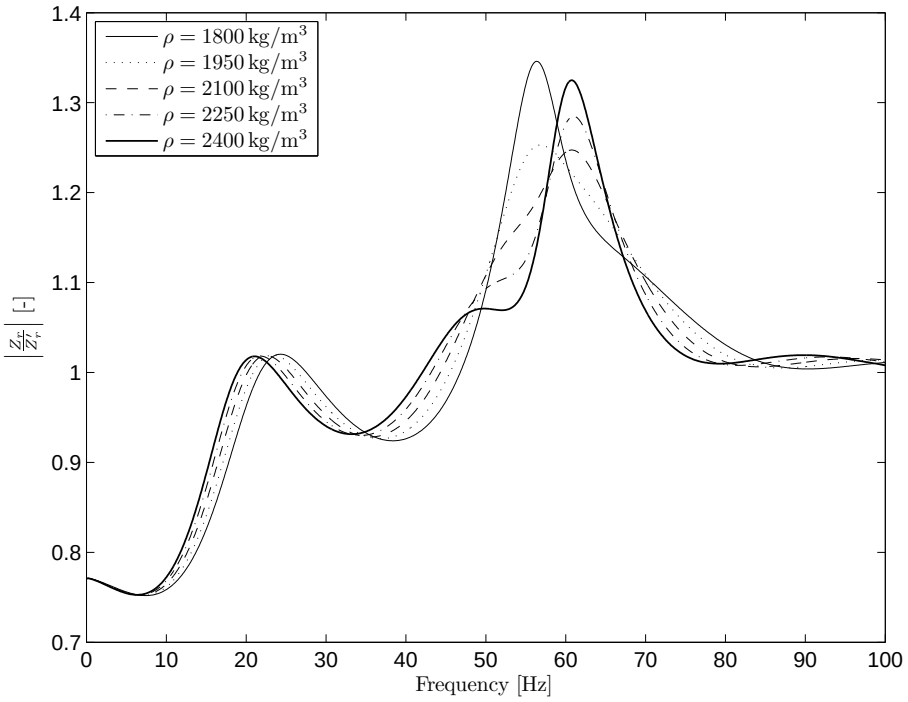


FIGURE C.35: Adimensional module of the rail receptance for five different subgrade densities and for the superstructure parameters in Case 1 (see Tables 4.1, 4.2 and 4.3). The other mechanical parameters of the subgrade are equal to the Quaternary ground type (see Table 3.1).

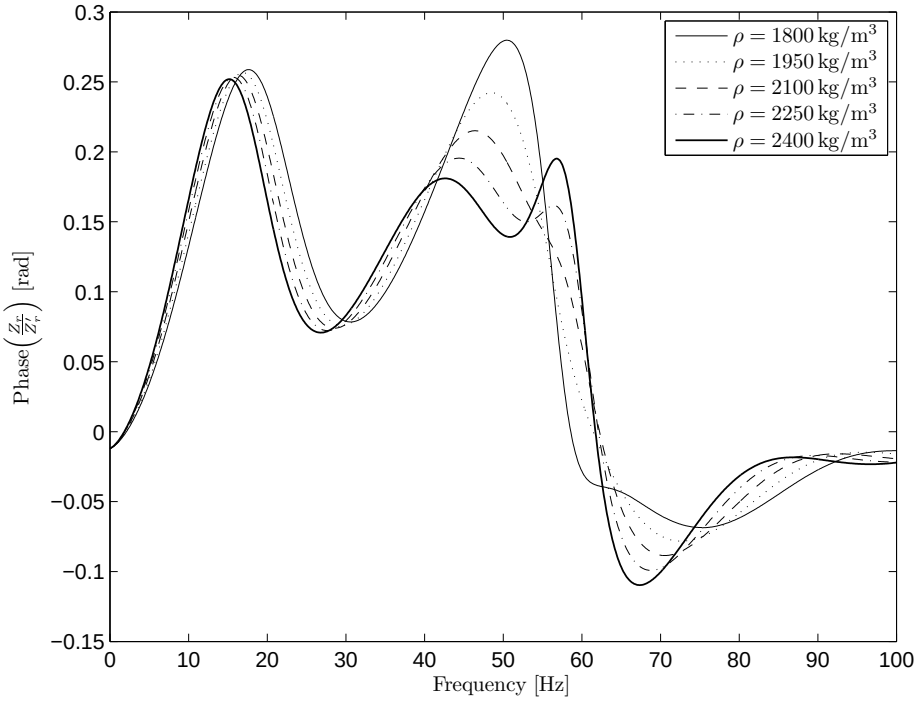


FIGURE C.36: Adimensional phase of the rail receptance for five different subgrade densities and for the superstructure parameters in Case 1 (see Tables 4.1, 4.2 and 4.3). The other mechanical parameters of the subgrade are equal to the Quaternary ground type (see Table 3.1).

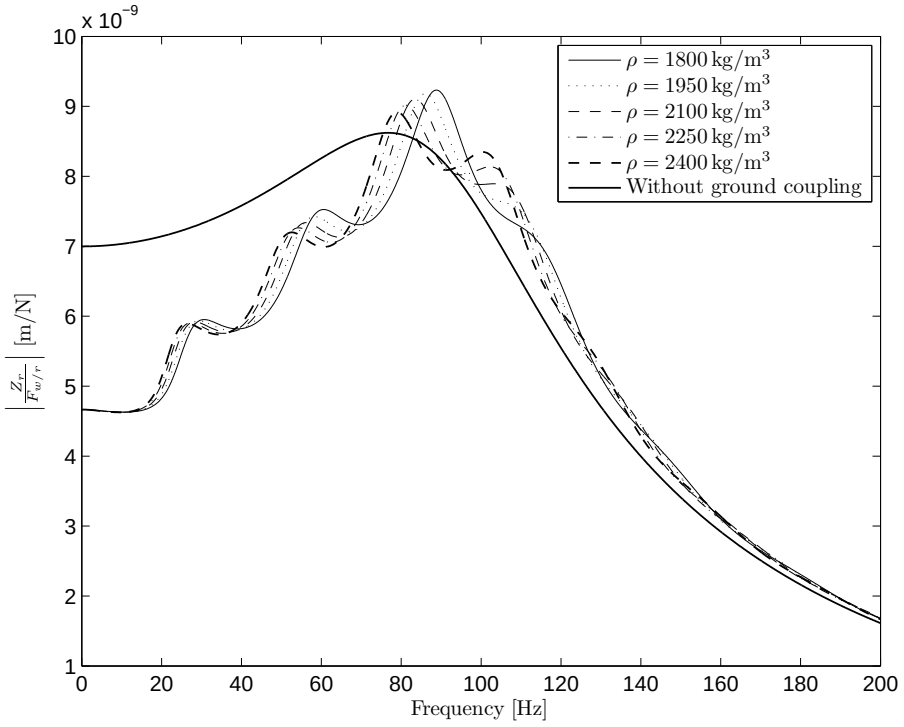


FIGURE C.37: Module of the rail receptance for five different subgrade densities and for the superstructure parameters in Case 2 (see Tables 4.1, 4.2 and 4.3). The other mechanical parameters of the subgrade are equal to the Quaternary ground type (see Table 3.1).

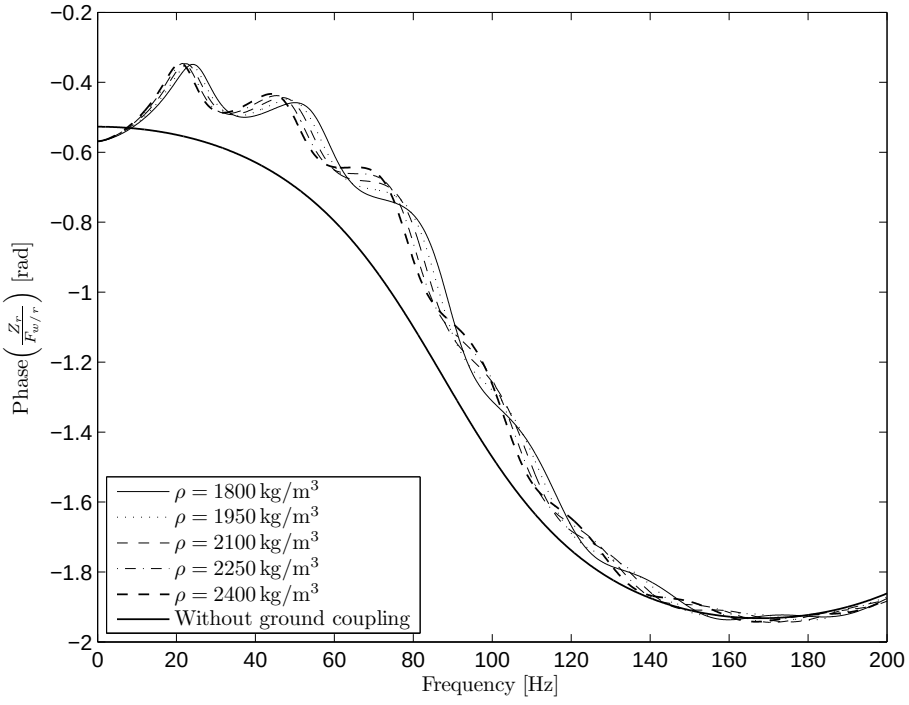


FIGURE C.38: Phase of the rail receptance for five different subgrade densities and for the superstructure parameters in Case 2 (see Tables 4.1, 4.2 and 4.3). The other mechanical parameters of the subgrade are equal to the Quaternary ground type (see Table 3.1).

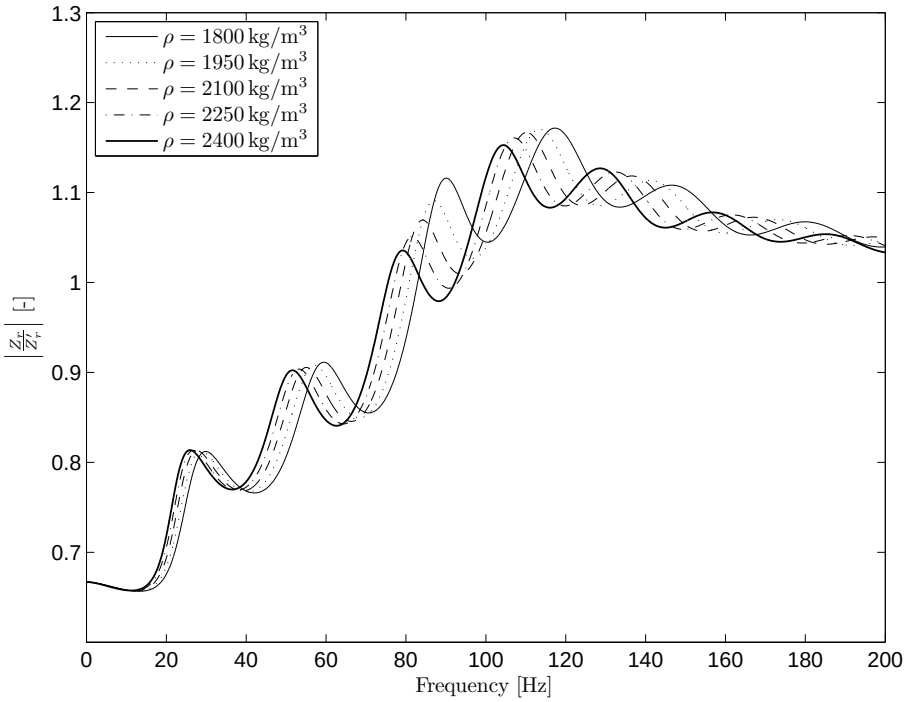


FIGURE C.39: Adimensional module of the rail receptance for five different subgrade densities and for the superstructure parameters in Case 2 (see Tables 4.1, 4.2 and 4.3). The other mechanical parameters of the subgrade are equal to the Quaternary ground type (see Table 3.1).

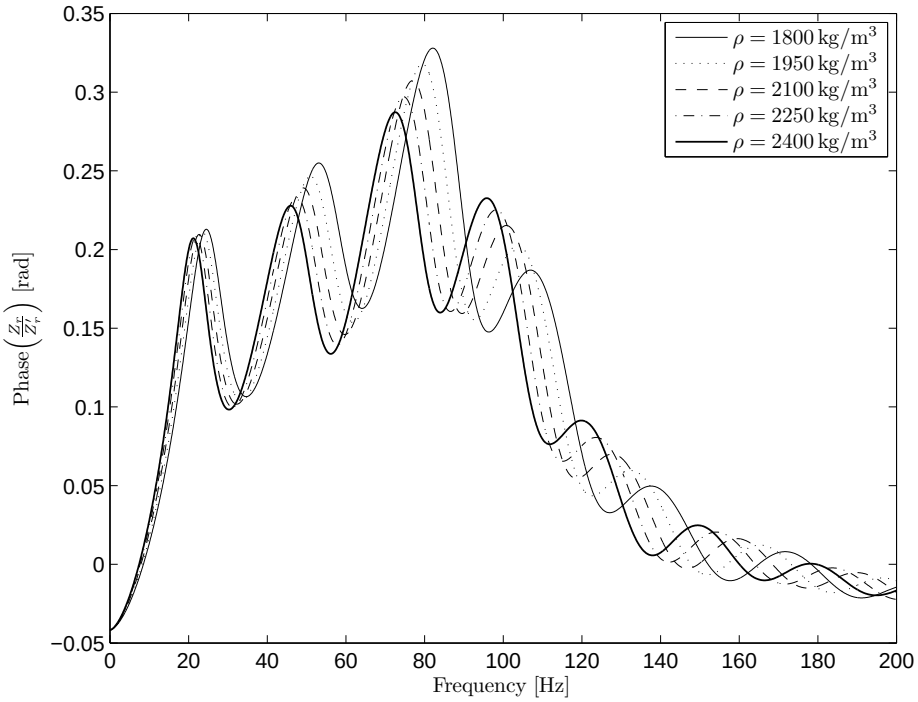


FIGURE C.40: Adimensional phase of the rail receptance for five different subgrade densities and for the superstructure parameters in Case 2 (see Tables 4.1, 4.2 and 4.3). The other mechanical parameters of the subgrade are equal to the Quaternary ground type (see Table 3.1).

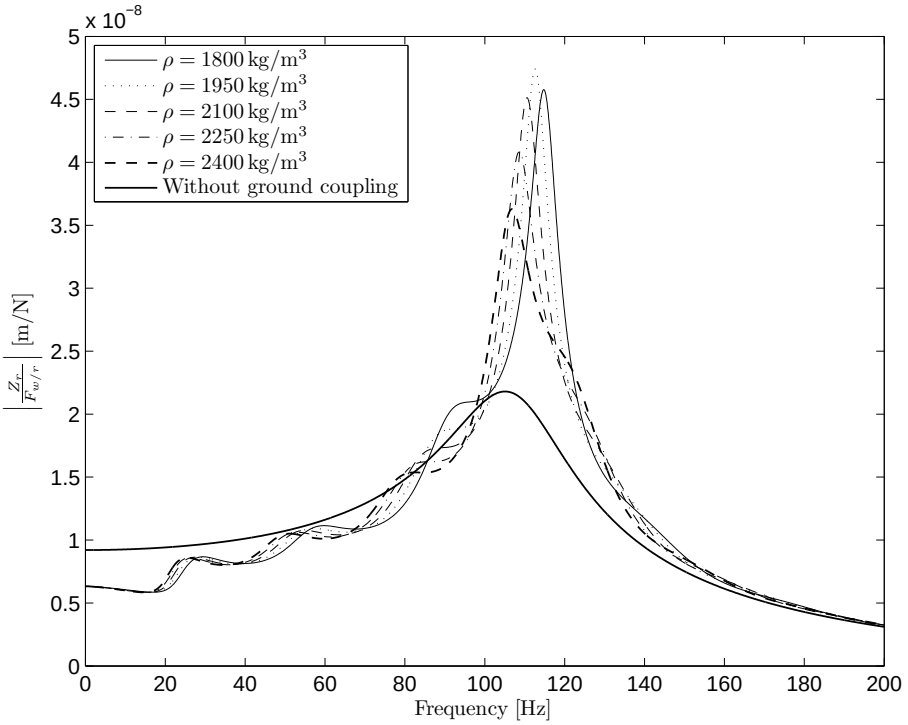


FIGURE C.41: Module of the rail receptance for five different subgrade densities and for the superstructure parameters in Case 3 (see Tables 4.1, 4.2 and 4.3). The other mechanical parameters of the subgrade are equal to the Quaternary ground type (see Table 3.1).

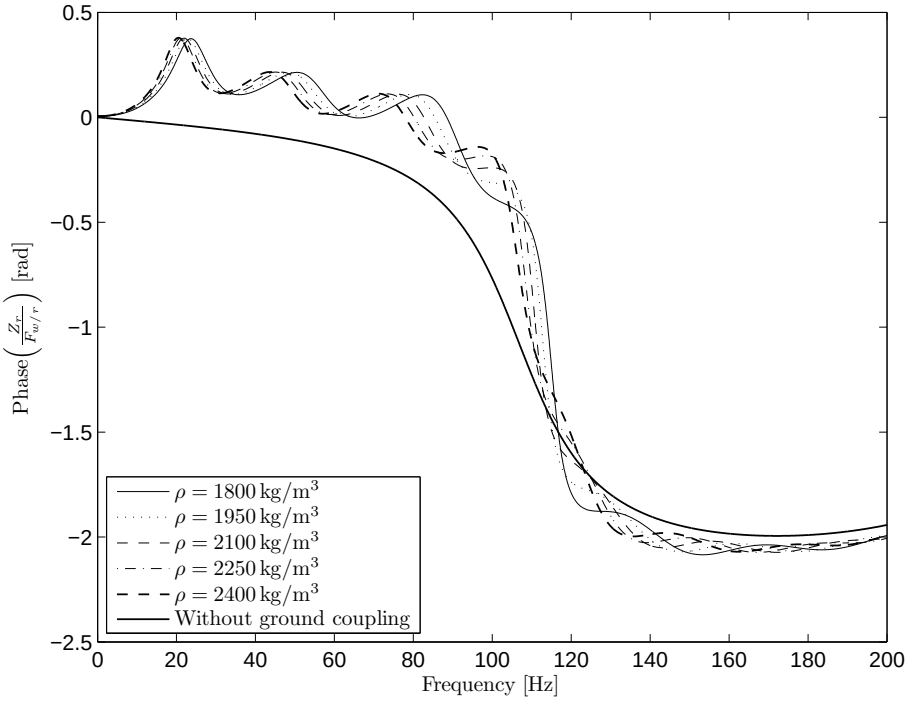


FIGURE C.42: Phase of the rail receptance for five different subgrade densities and for the superstructure parameters in Case 3 (see Tables 4.1, 4.2 and 4.3). The other mechanical parameters of the subgrade are equal to the Quaternary ground type (see Table 3.1).

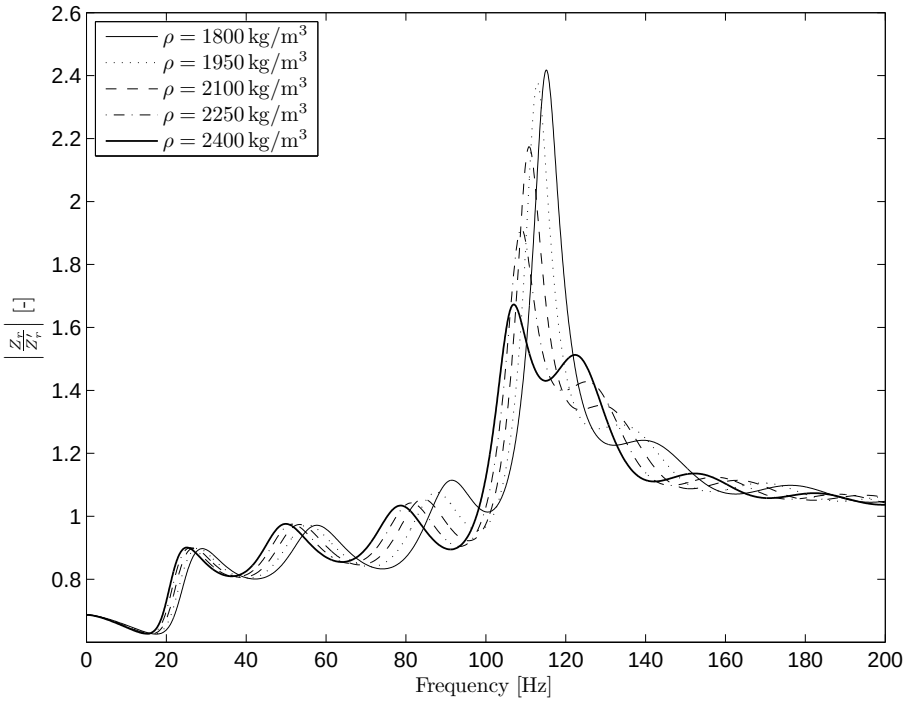


FIGURE C.43: Adimensional module of the rail receptance for five different subgrade densities and for the superstructure parameters in Case 3 (see Tables 4.1, 4.2 and 4.3). The other mechanical parameters of the subgrade are equal to the Quaternary ground type (see Table 3.1).

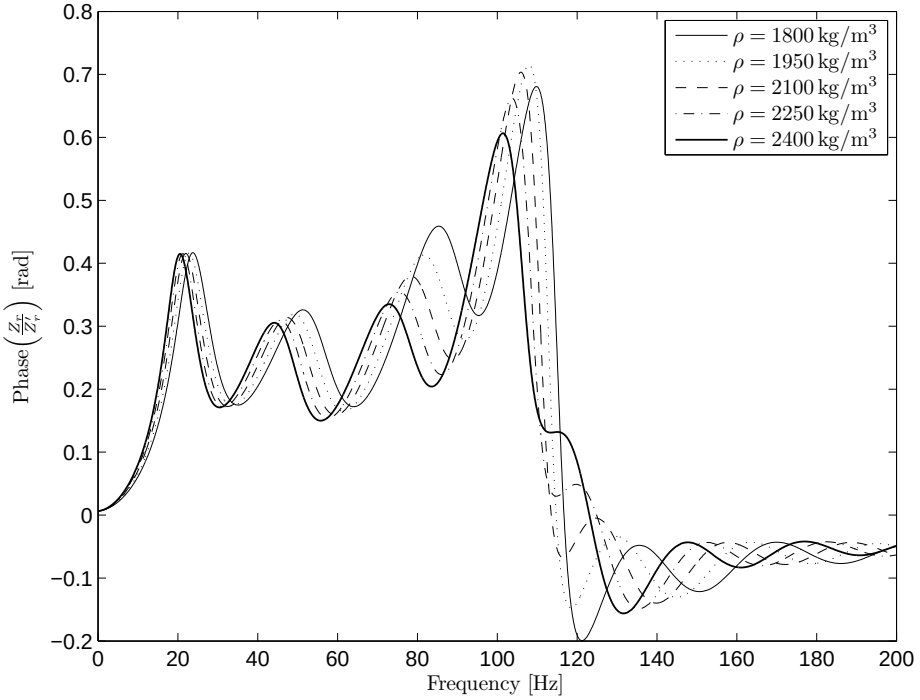


FIGURE C.44: Adimensional phase of the rail receptance for five different subgrade densities and for the superstructure parameters in Case 3 (see Tables 4.1, 4.2 and 4.3). The other mechanical parameters of the subgrade are equal to the Quaternary ground type (see Table 3.1).

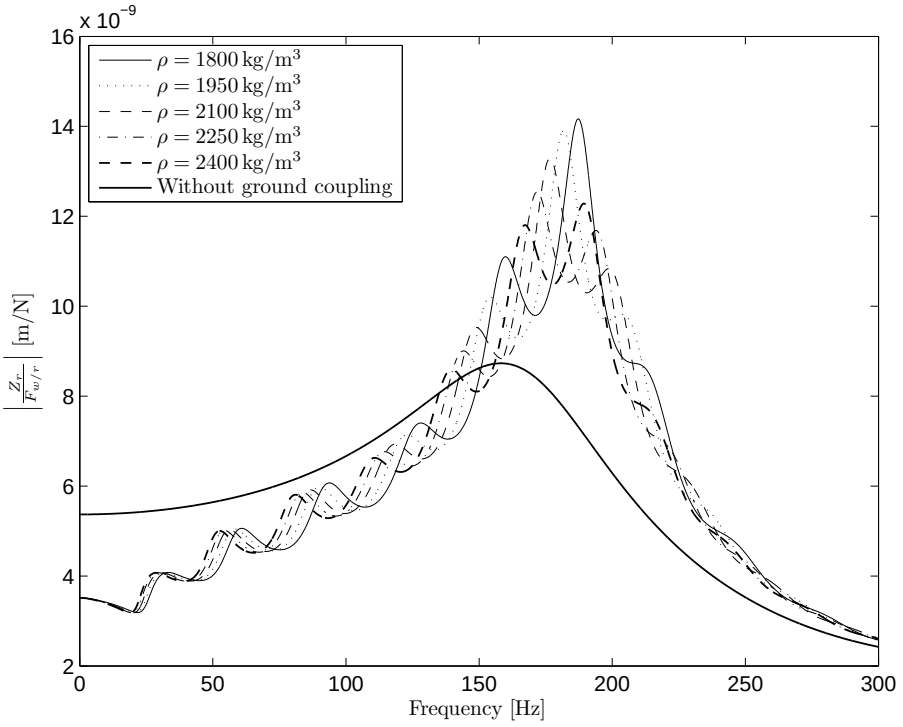


FIGURE C.45: Module of the rail receptance for five different subgrade densities and for the superstructure parameters in Case 4 (see Tables 4.1, 4.2 and 4.3). The other mechanical parameters of the subgrade are equal to the Quaternary ground type (see Table 3.1).

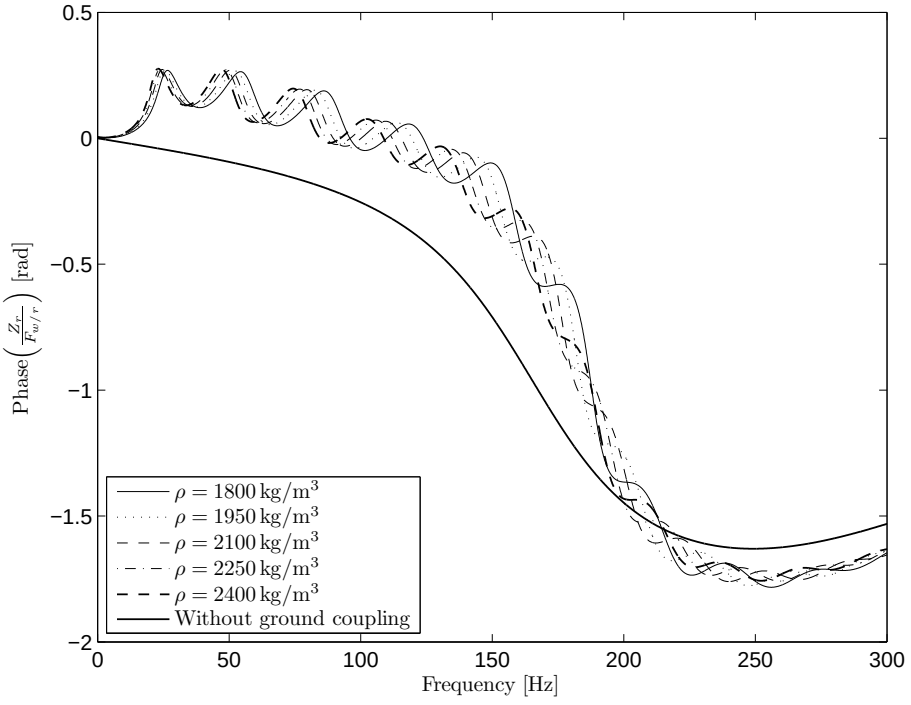


FIGURE C.46: Phase of the rail receptance for five different subgrade densities and for the superstructure parameters in Case 4 (see Tables 4.1, 4.2 and 4.3). The other mechanical parameters of the subgrade are equal to the Quaternary ground type (see Table 3.1).

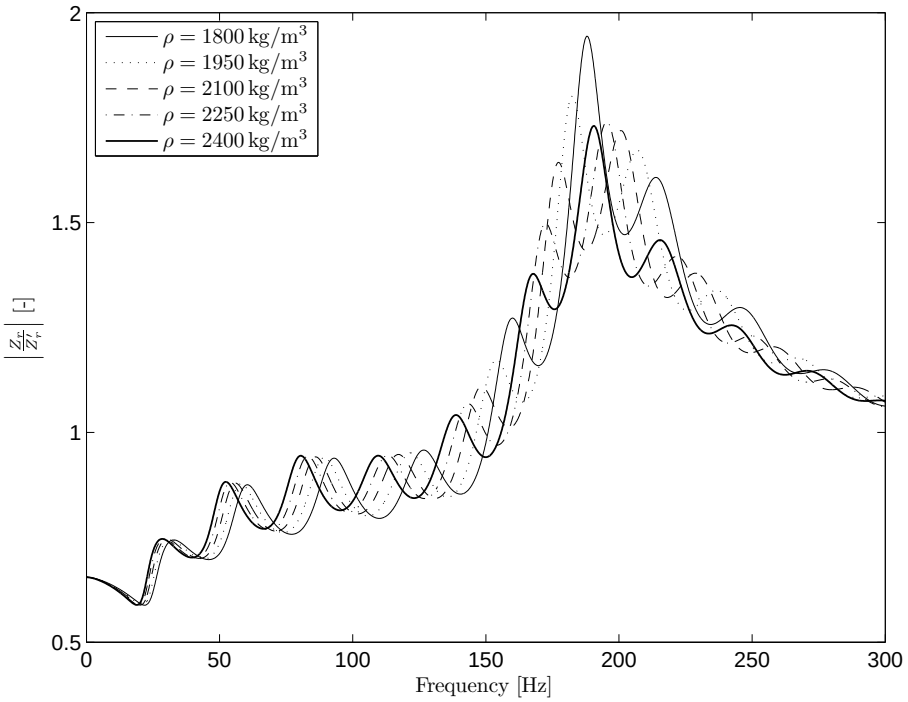


FIGURE C.47: Adimensional module of the rail receptance for five different subgrade densities and for the superstructure parameters in Case 4 (see Tables 4.1, 4.2 and 4.3). The other mechanical parameters of the subgrade are equal to the Quaternary ground type (see Table 3.1).

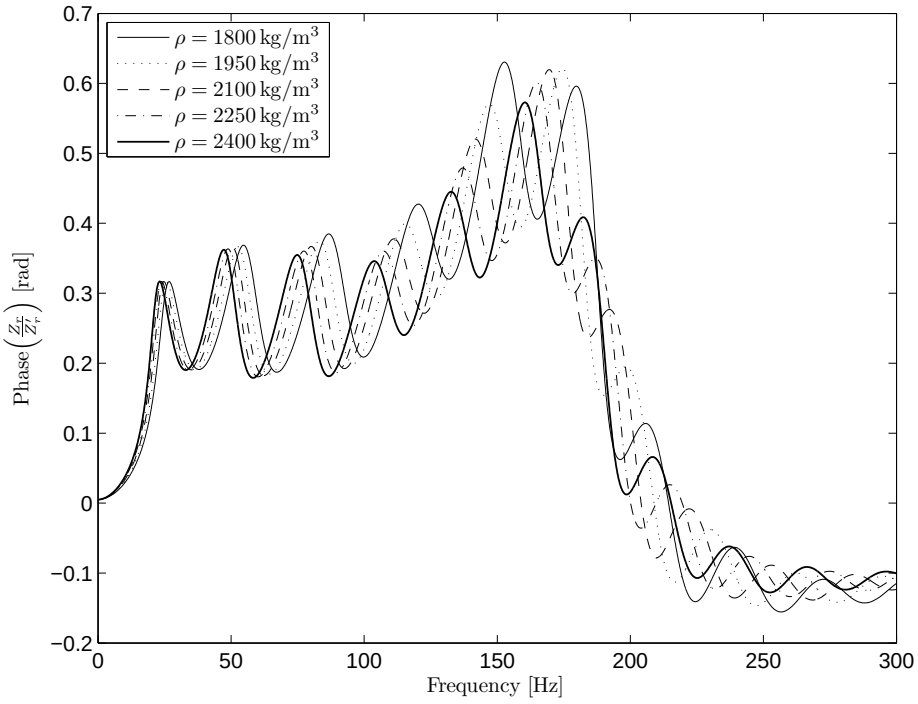


FIGURE C.48: Adimensional phase of the rail receptance for five different subgrade densities and for the superstructure parameters in Case 4 (see Tables 4.1, 4.2 and 4.3). The other mechanical parameters of the subgrade are equal to the Quaternary ground type (see Table 3.1).

### C.1.4 Effects of the Poisson's ratio

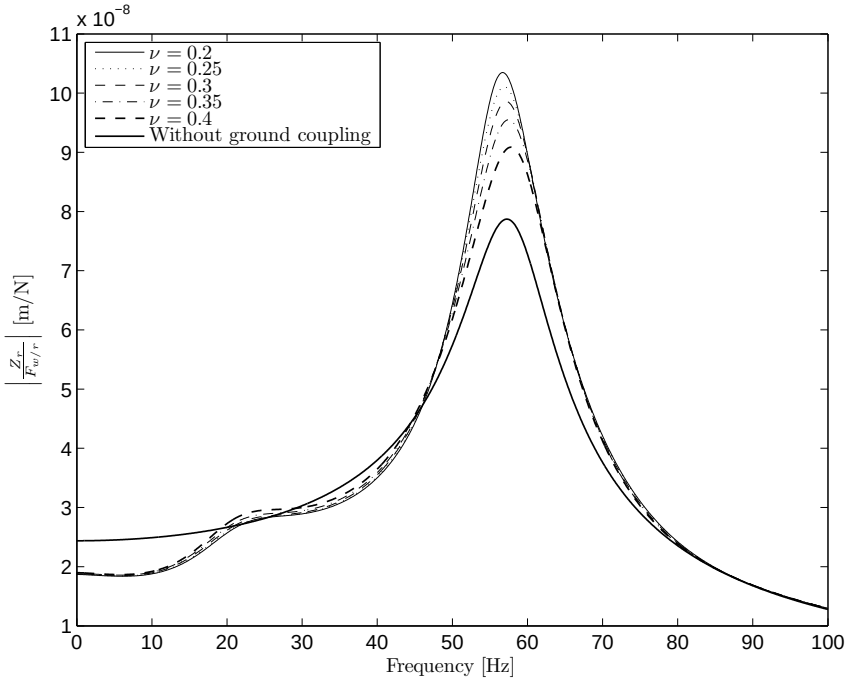


FIGURE C.49: Module of the rail receptance for five different Poisson's ratios of the subgrade and for the superstructure parameters in Case 1 (see Tables 4.1, 4.2 and 4.3). The other mechanical parameters of the subgrade are equal to the Quaternary ground type (see Table 3.1).

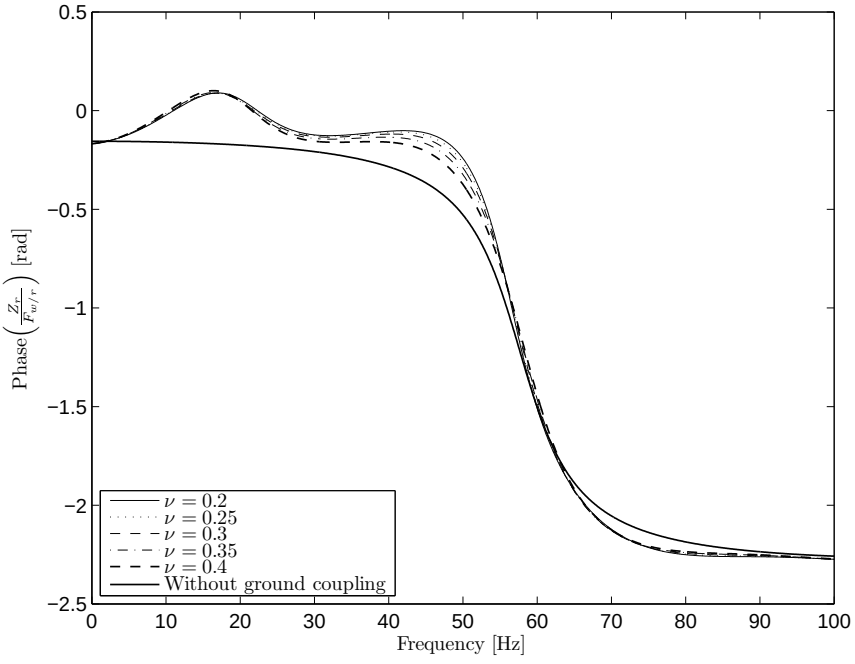


FIGURE C.50: Phase of the rail receptance for five different Poisson's ratios of the subgrade and for the superstructure parameters in Case 1 (see Tables 4.1, 4.2 and 4.3). The other mechanical parameters of the subgrade are equal to the Quaternary ground type (see Table 3.1).

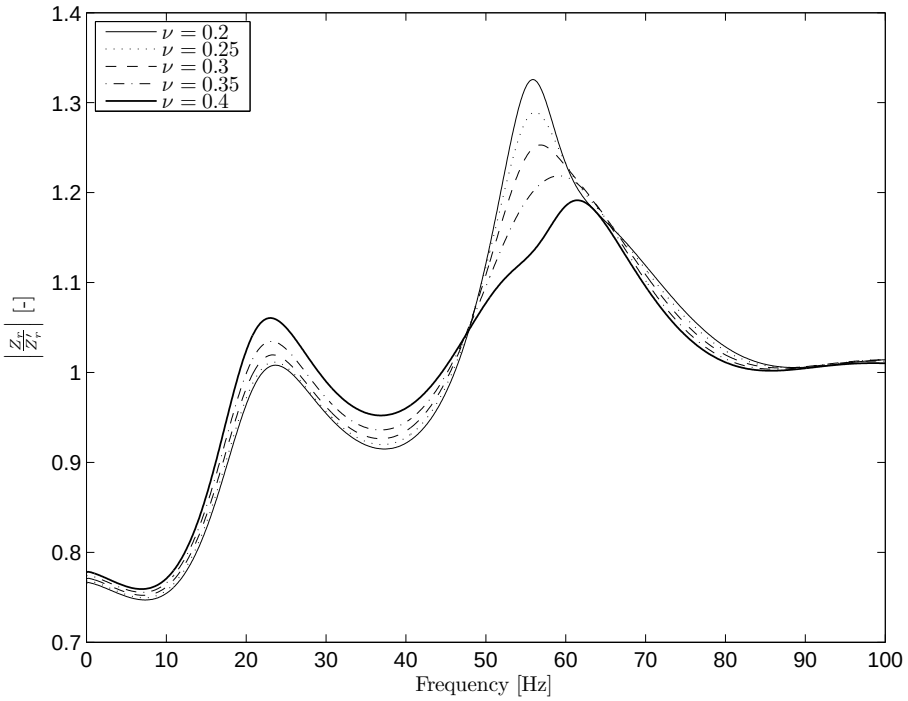


FIGURE C.51: Adimensional module of the rail receptance for five different Poisson's ratios of the subgrade and for the superstructure parameters in Case 1 (see Tables 4.1, 4.2 and 4.3). The other mechanical parameters of the subgrade are equal to the Quaternary ground type (see Table 3.1).

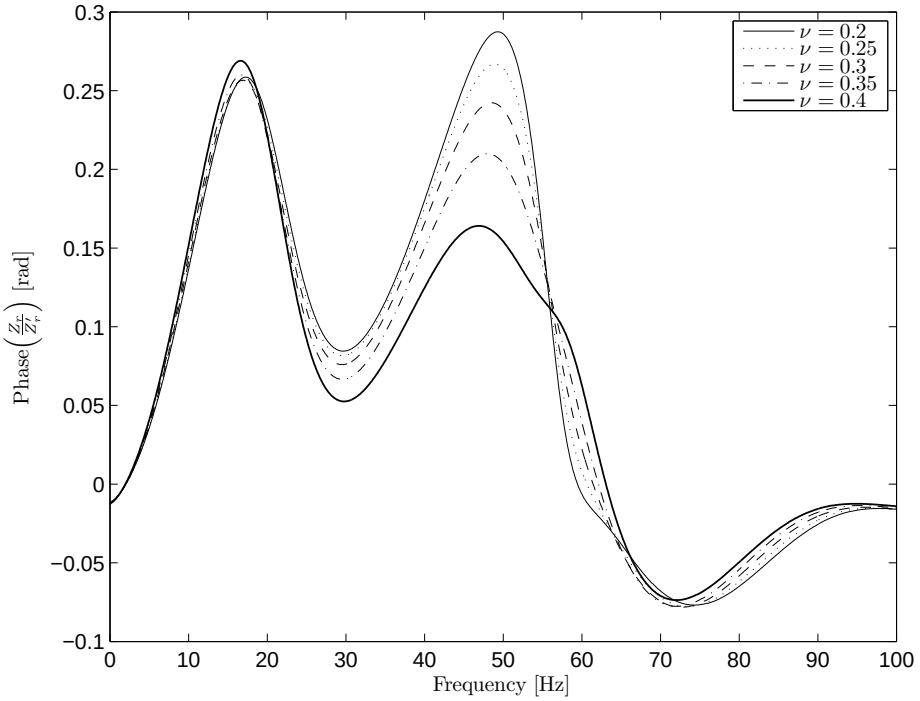


FIGURE C.52: Adimensional phase of the rail receptance for five different Poisson's ratios of the subgrade and for the superstructure parameters in Case 1 (see Tables 4.1, 4.2 and 4.3). The other mechanical parameters of the subgrade are equal to the Quaternary ground type (see Table 3.1).

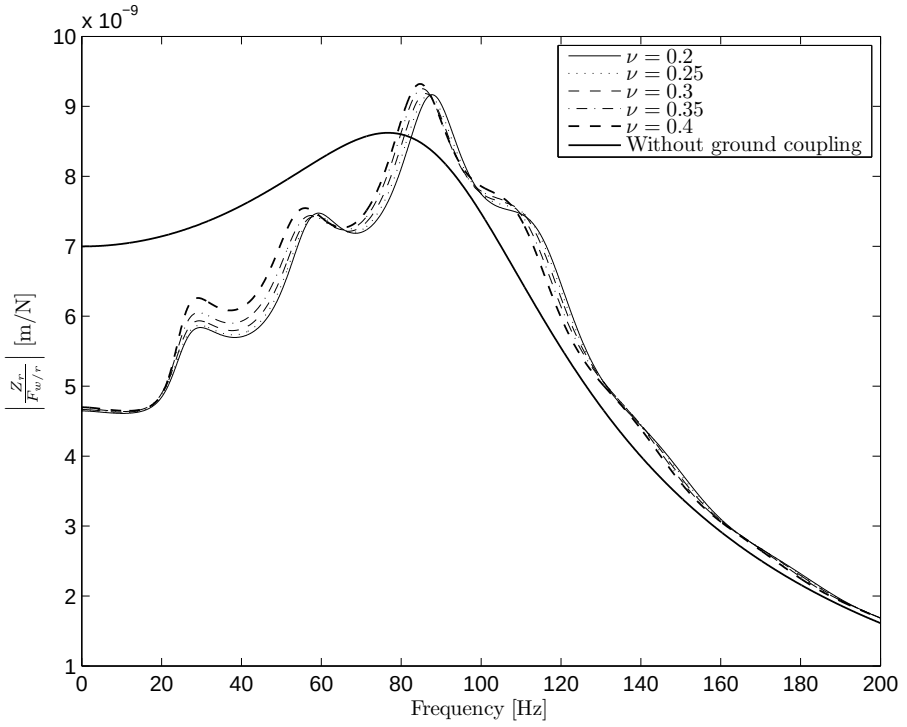


FIGURE C.53: Module of the rail receptance for five different Poisson's ratios of the subgrade and for the superstructure parameters in Case 2 (see Tables 4.1, 4.2 and 4.3). The other mechanical parameters of the subgrade are equal to the Quaternary ground type (see Table 3.1).

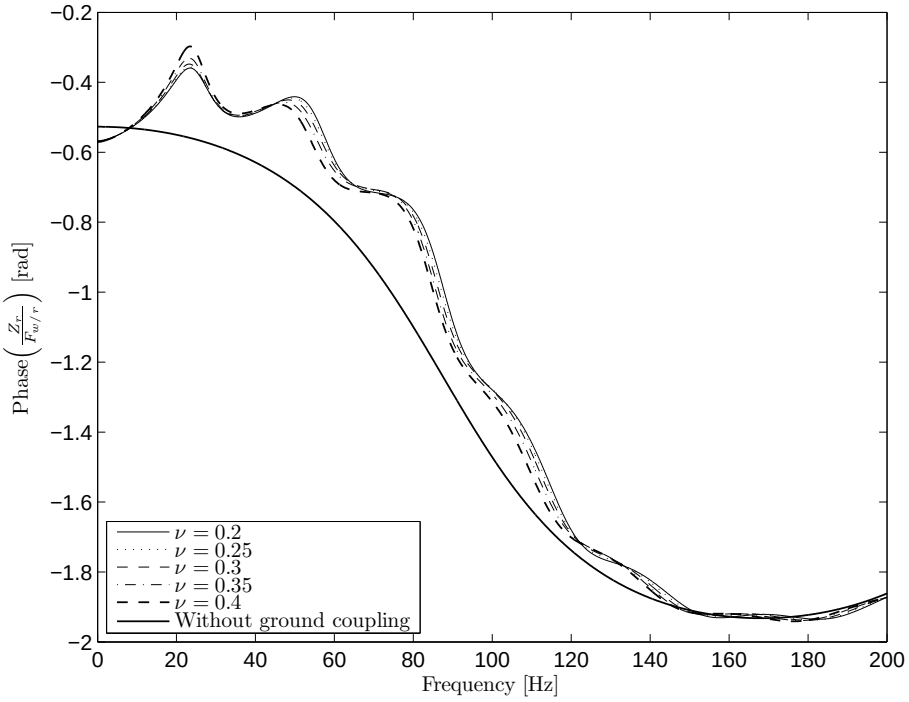


FIGURE C.54: Phase of the rail receptance for five different Poisson's ratios of the subgrade and for the superstructure parameters in Case 2 (see Tables 4.1, 4.2 and 4.3). The other mechanical parameters of the subgrade are equal to the Quaternary ground type (see Table 3.1).

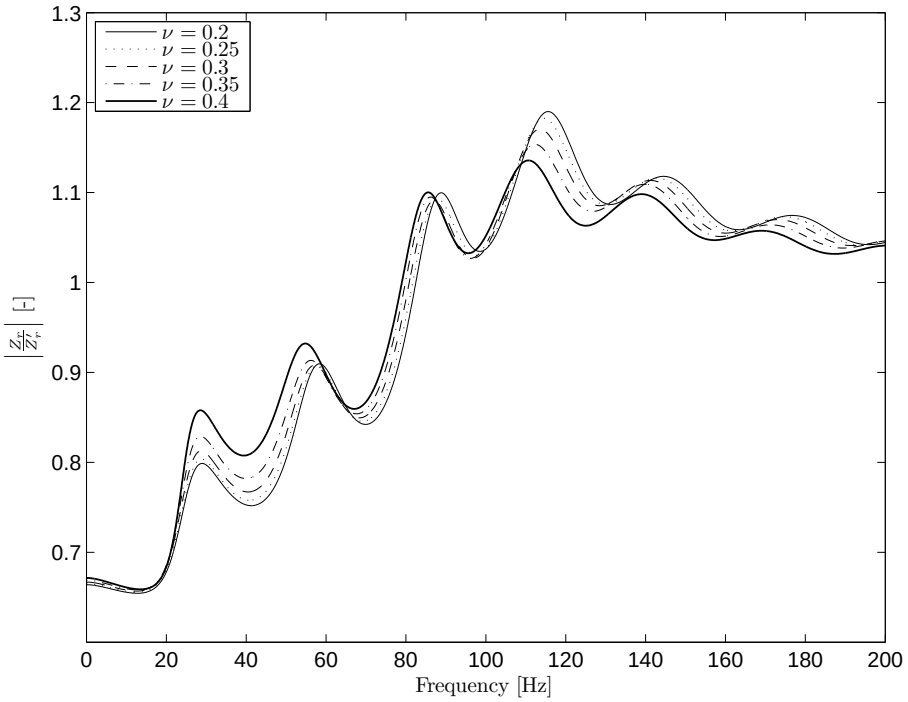


FIGURE C.55: Adimensional module of the rail receptance for five different Poisson's ratios of the subgrade and for the superstructure parameters in Case 2 (see Tables 4.1, 4.2 and 4.3). The other mechanical parameters of the subgrade are equal to the Quaternary ground type (see Table 3.1).

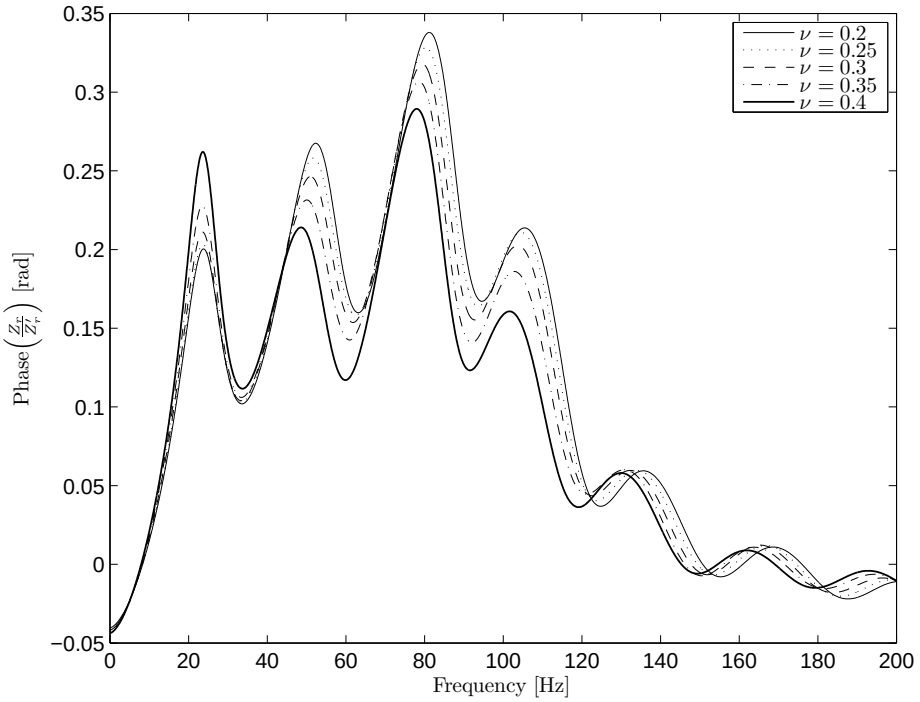


FIGURE C.56: Adimensional phase of the rail receptance for five different Poisson's ratios of the subgrade and for the superstructure parameters in Case 2 (see Tables 4.1, 4.2 and 4.3). The other mechanical parameters of the subgrade are equal to the Quaternary ground type (see Table 3.1).

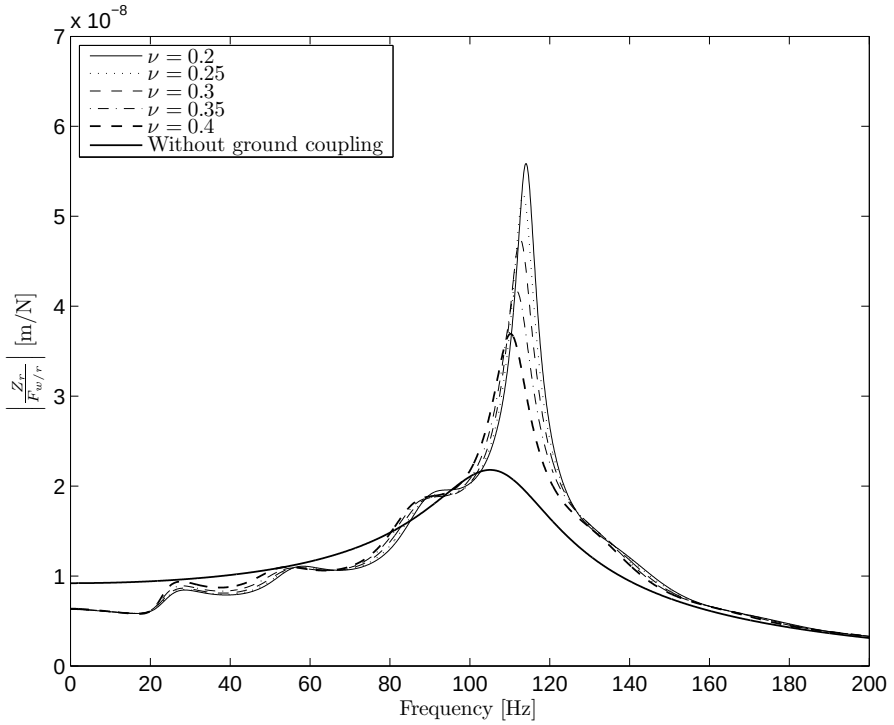


FIGURE C.57: Module of the rail receptance for five different Poisson's ratios of the subgrade and for the superstructure parameters in Case 3 (see Tables 4.1, 4.2 and 4.3). The other mechanical parameters of the subgrade are equal to the Quaternary ground type (see Table 3.1).

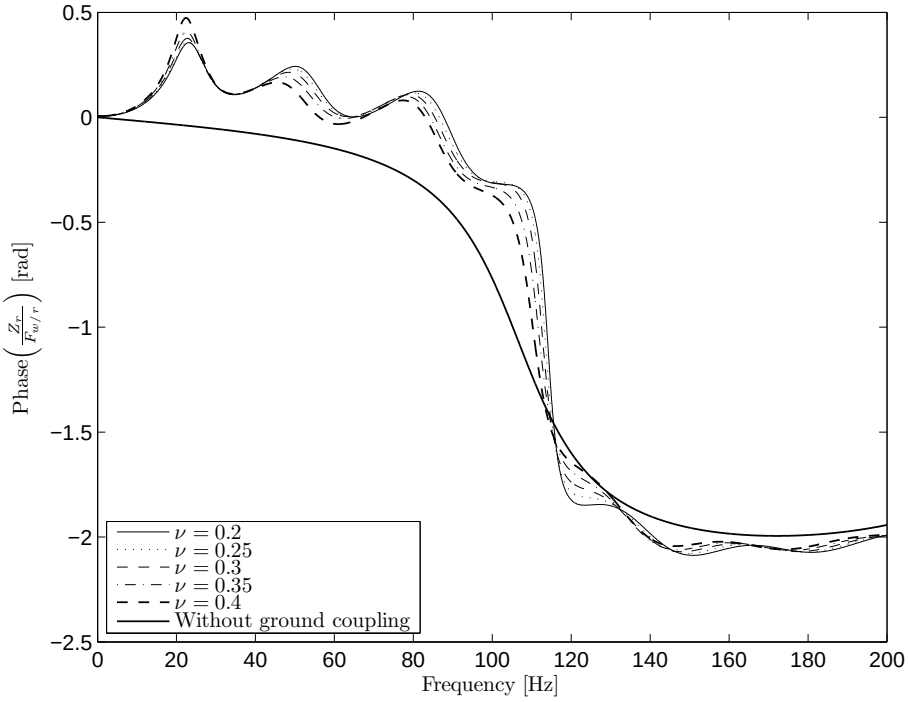


FIGURE C.58: Phase of the rail receptance for five different Poisson's ratios of the subgrade and for the superstructure parameters in Case 3 (see Tables 4.1, 4.2 and 4.3). The other mechanical parameters of the subgrade are equal to the Quaternary ground type (see Table 3.1).

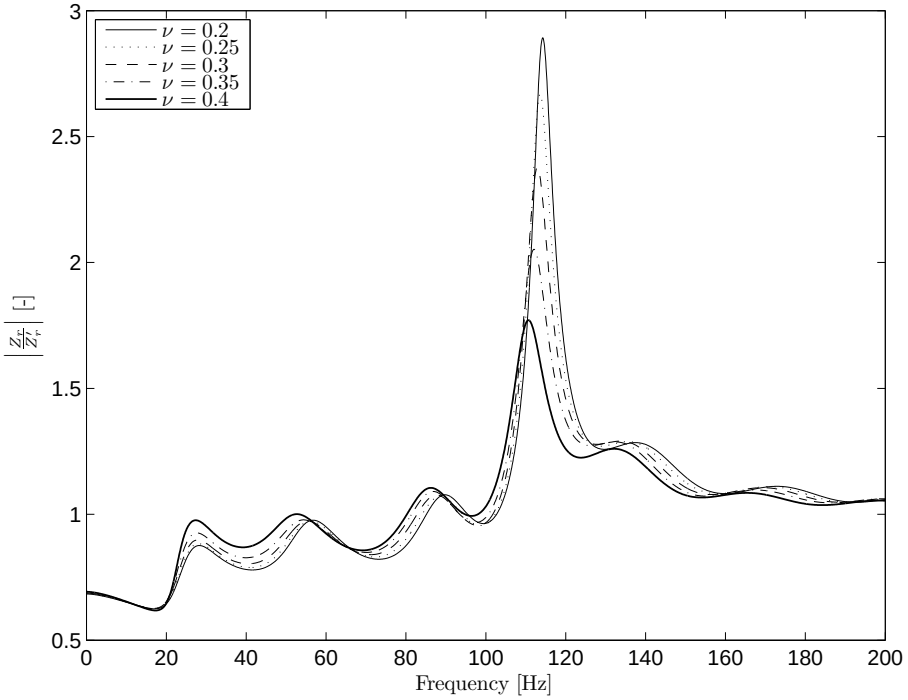


FIGURE C.59: Adimensional module of the rail receptance for five different Poisson's ratios of the subgrade and for the superstructure parameters in Case 3 (see Tables 4.1, 4.2 and 4.3). The other mechanical parameters of the subgrade are equal to the Quaternary ground type (see Table 3.1).

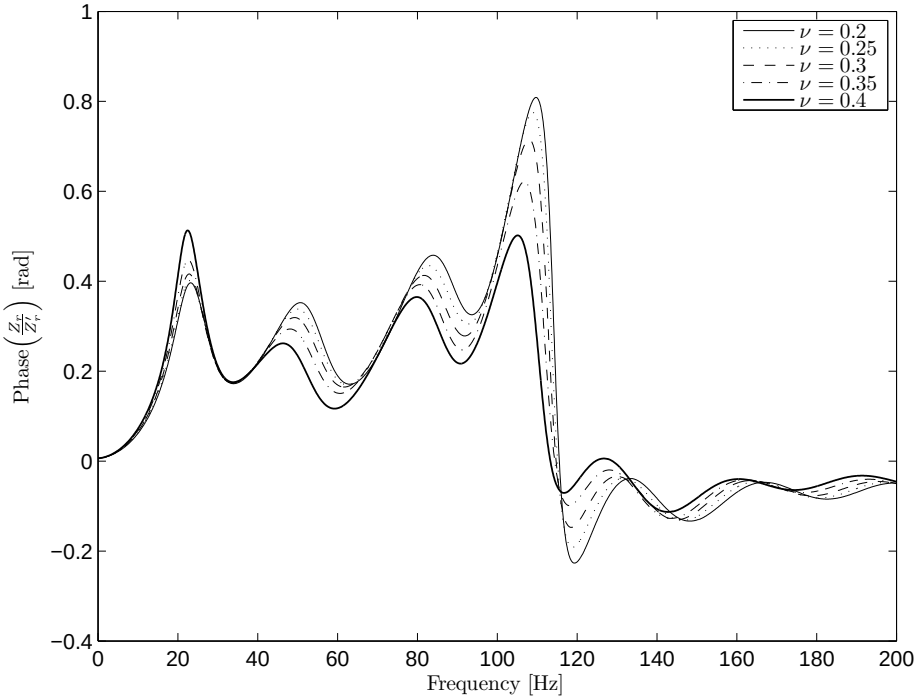


FIGURE C.60: Adimensional phase of the rail receptance for five different Poisson's ratios of the subgrade and for the superstructure parameters in Case 3 (see Tables 4.1, 4.2 and 4.3). The other mechanical parameters of the subgrade are equal to the Quaternary ground type (see Table 3.1).

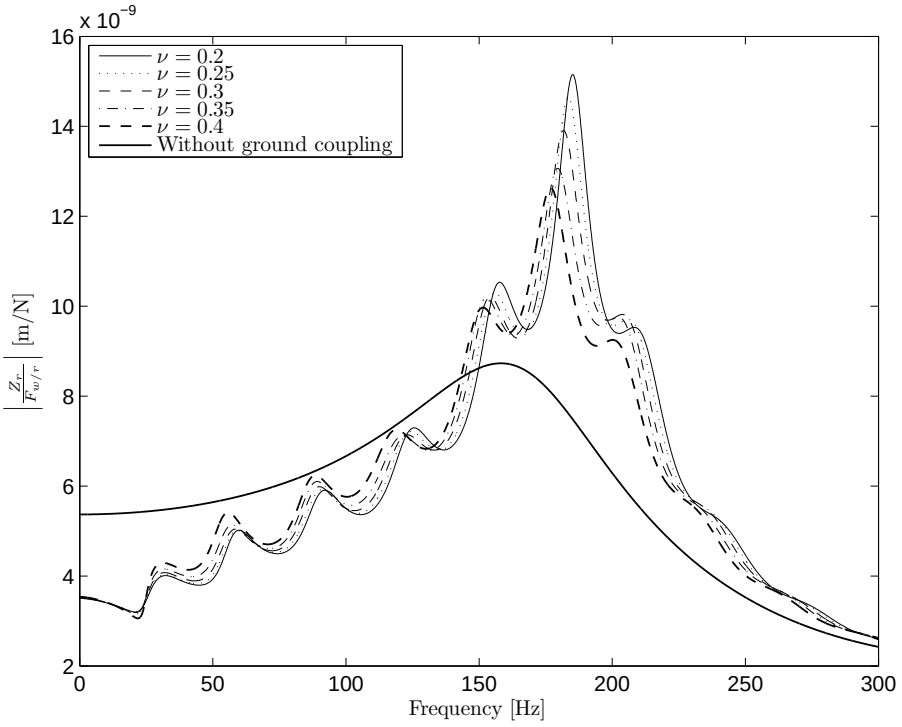


FIGURE C.61: Module of the rail receptance for five different Poisson's ratios of the subgrade and for the superstructure parameters in Case 4 (see Tables 4.1, 4.2 and 4.3). The other mechanical parameters of the subgrade are equal to the Quaternary ground type (see Table 3.1).

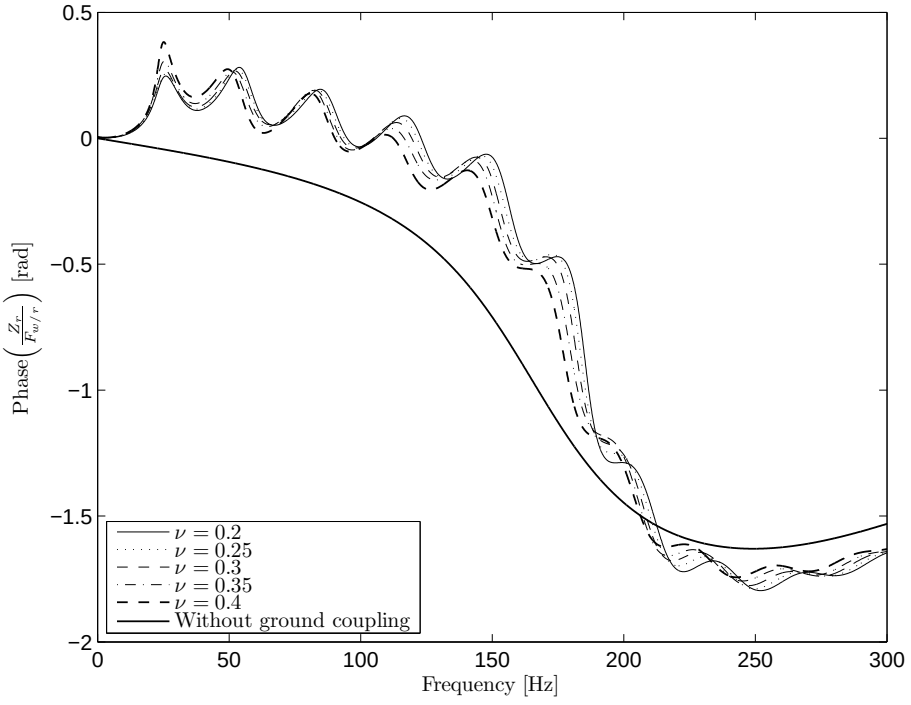


FIGURE C.62: Phase of the rail receptance for five different Poisson's ratios of the subgrade and for the superstructure parameters in Case 4 (see Tables 4.1, 4.2 and 4.3). The other mechanical parameters of the subgrade are equal to the Quaternary ground type (see Table 3.1).

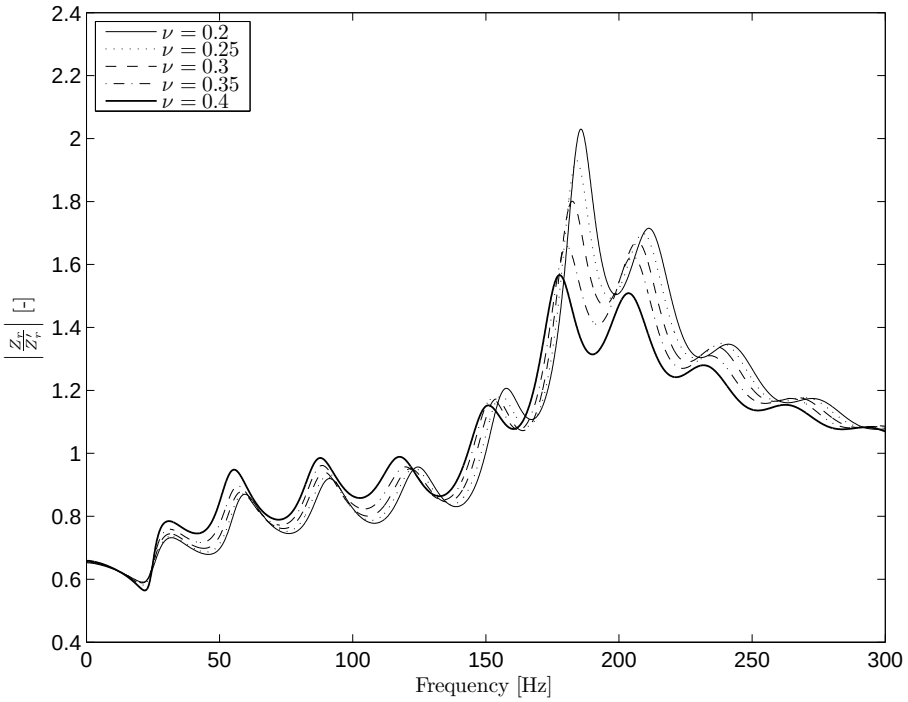


FIGURE C.63: Adimensional module of the rail receptance for five different Poisson's ratios of the subgrade and for the superstructure parameters in Case 4 (see Tables 4.1, 4.2 and 4.3). The other mechanical parameters of the subgrade are equal to the Quaternary ground type (see Table 3.1).

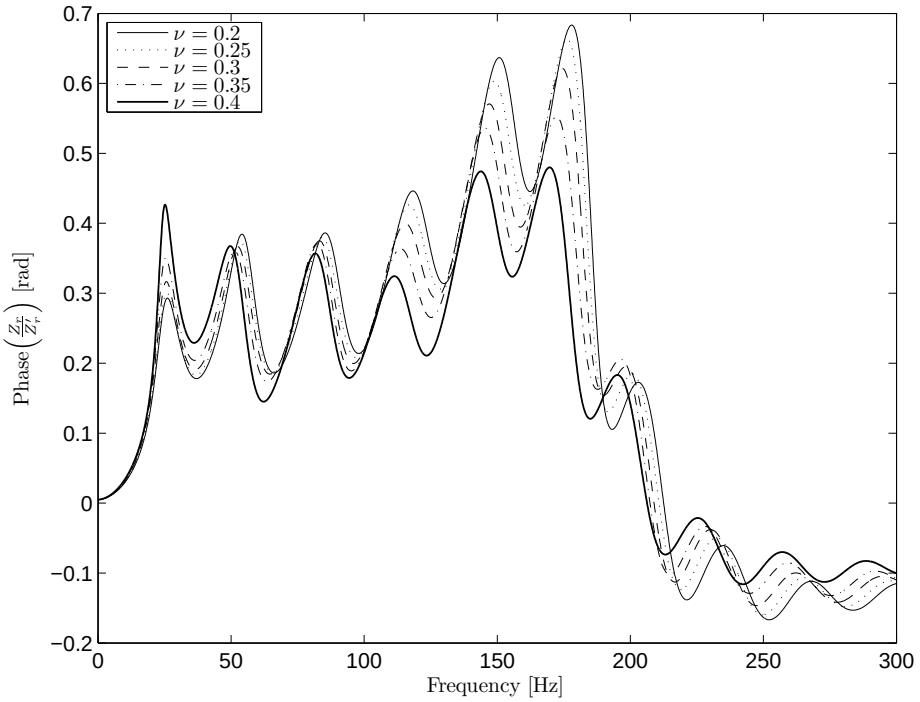


FIGURE C.64: Adimensional phase of the rail receptance for five different Poisson's ratios of the subgrade and for the superstructure parameters in Case 4 (see Tables 4.1, 4.2 and 4.3). The other mechanical parameters of the subgrade are equal to the Quaternary ground type (see Table 3.1).

### C.1.5 Effects of the Young's modulus

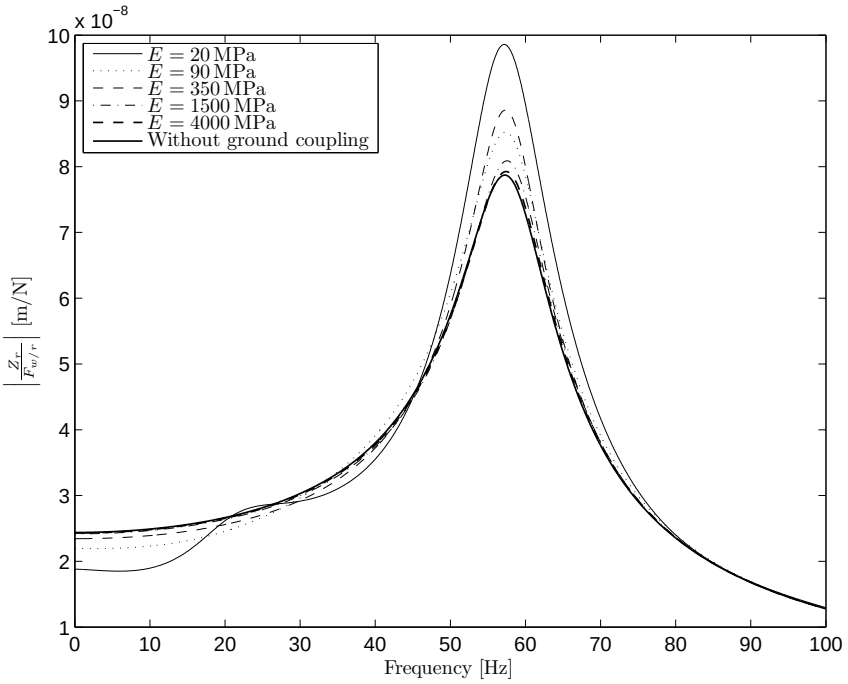


FIGURE C.65: Module of the rail receptance for five different Young's modulus of the subgrade and for the superstructure parameters in Case 1 (see Tables 4.1, 4.2 and 4.3). The other mechanical parameters of the subgrade are equal to the Quaternary ground type (see Table 3.1).

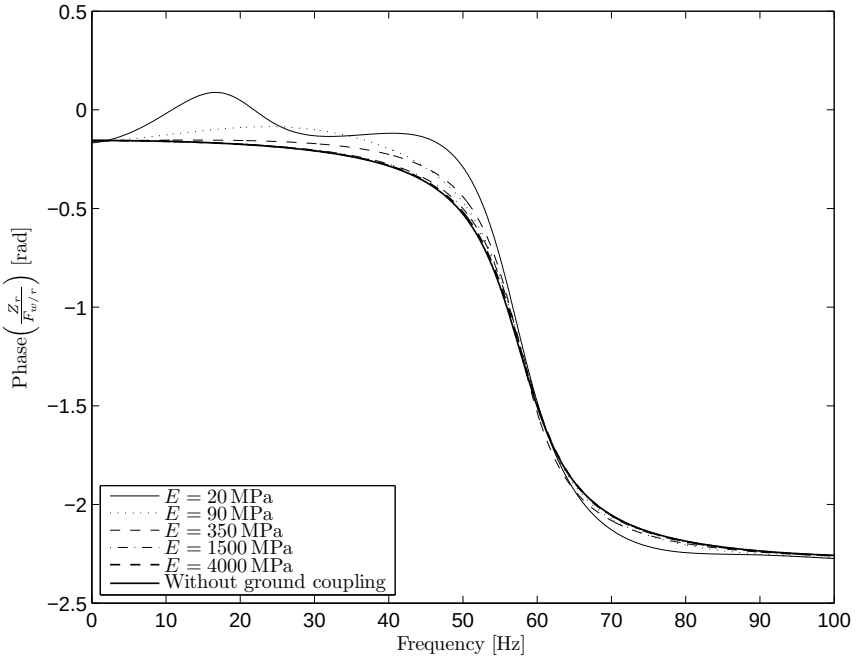


FIGURE C.66: Phase of the rail receptance for five different Young's modulus of the subgrade and for the superstructure parameters in Case 1 (see Tables 4.1, 4.2 and 4.3). The other mechanical parameters of the subgrade are equal to the Quaternary ground type (see Table 3.1).

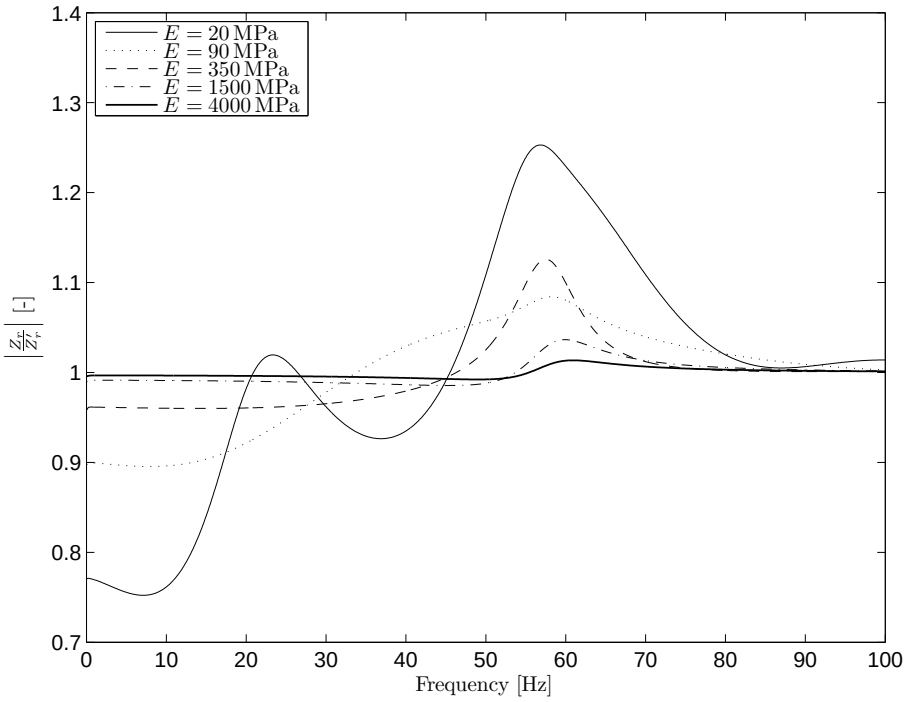


FIGURE C.67: Adimensional module of the rail receptance for five different Young's modulus of the subgrade and for the superstructure parameters in Case 1 (see Tables 4.1, 4.2 and 4.3). The other mechanical parameters of the subgrade are equal to the Quaternary ground type (see Table 3.1).

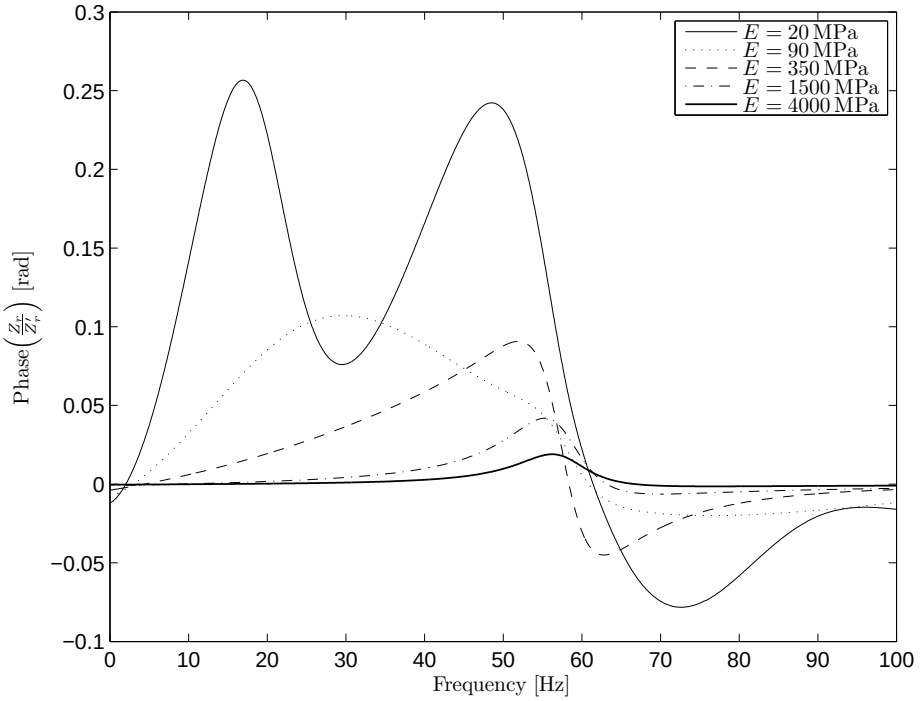


FIGURE C.68: Adimensional phase of the rail receptance for five different Young's modulus of the subgrade and for the superstructure parameters in Case 1 (see Tables 4.1, 4.2 and 4.3). The other mechanical parameters of the subgrade are equal to the Quaternary ground type (see Table 3.1).

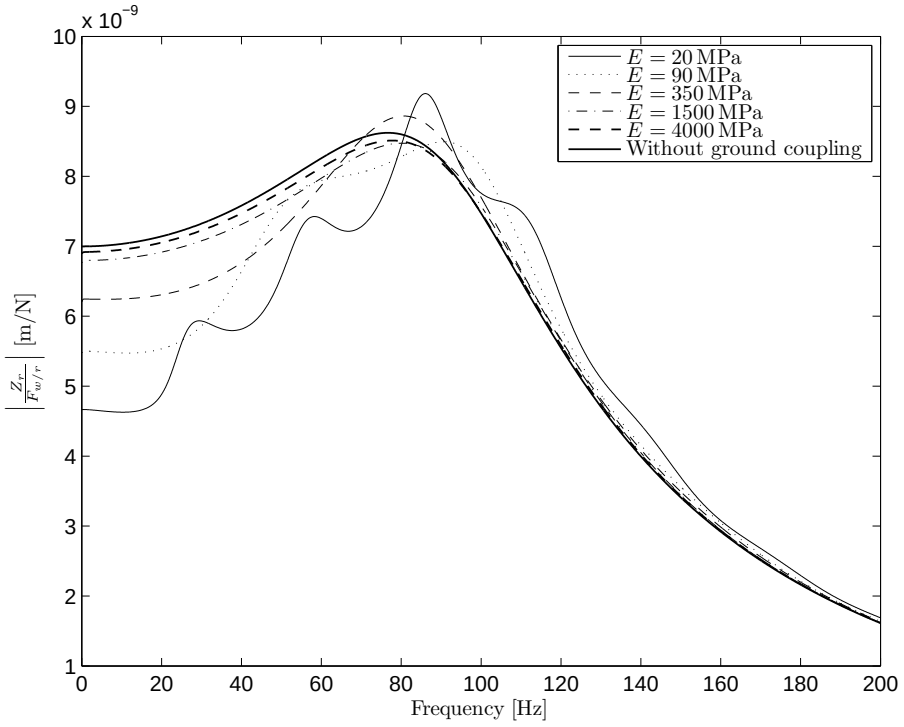


FIGURE C.69: Module of the rail receptance for five different Young's modulus of the subgrade and for the superstructure parameters in Case 2 (see Tables 4.1, 4.2 and 4.3). The other mechanical parameters of the subgrade are equal to the Quaternary ground type (see Table 3.1).

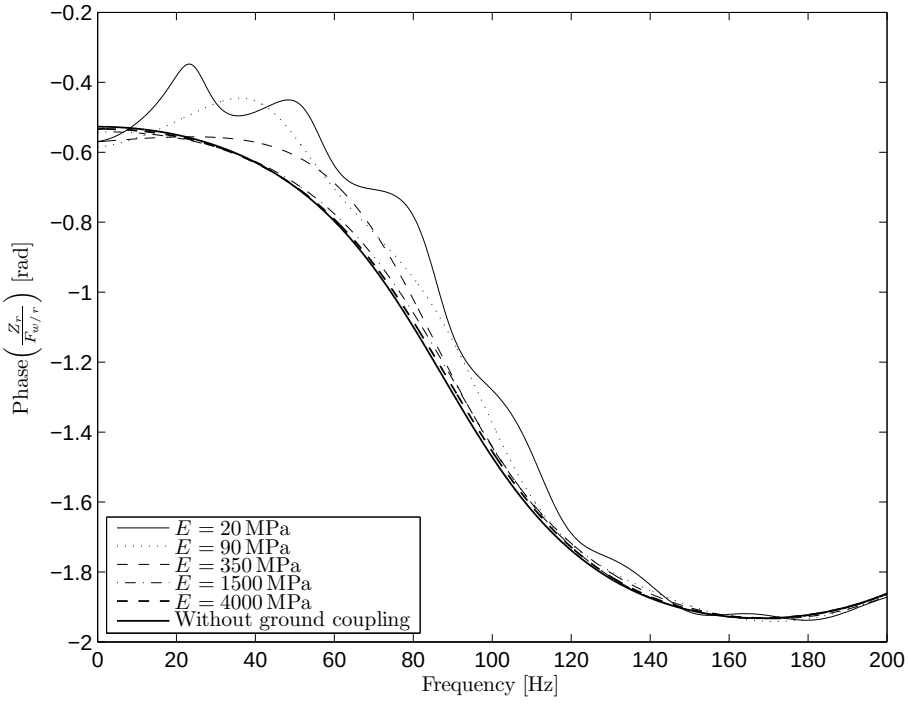


FIGURE C.70: Phase of the rail receptance for five different Young's modulus of the subgrade and for the superstructure parameters in Case 2 (see Tables 4.1, 4.2 and 4.3). The other mechanical parameters of the subgrade are equal to the Quaternary ground type (see Table 3.1).

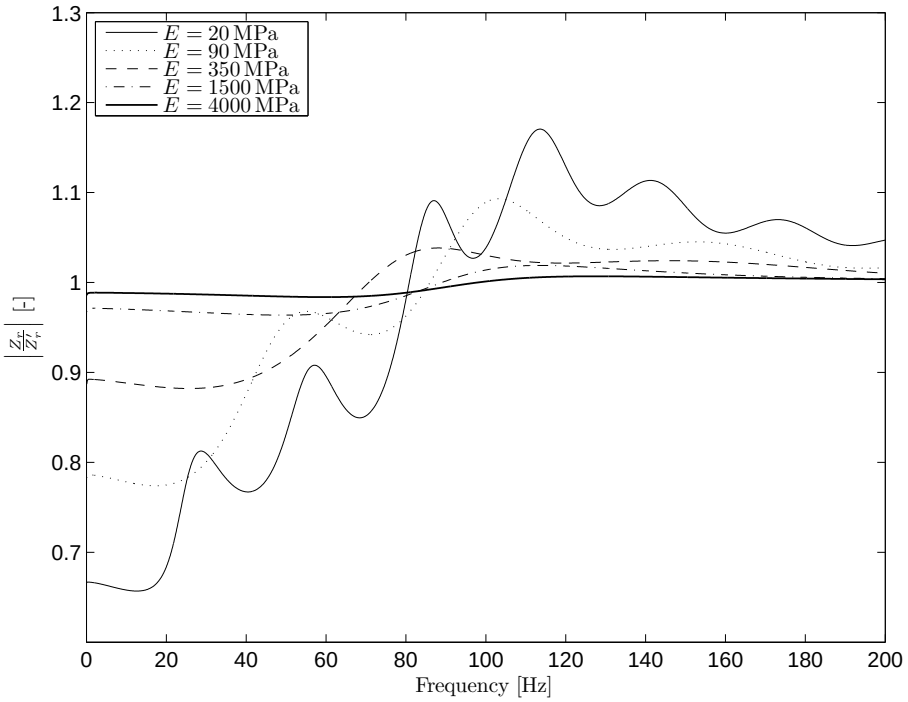


FIGURE C.71: Adimensional module of the rail receptance for five different Young's modulus of the subgrade and for the superstructure parameters in Case 2 (see Tables 4.1, 4.2 and 4.3). The other mechanical parameters of the subgrade are equal to the Quaternary ground type (see Table 3.1).

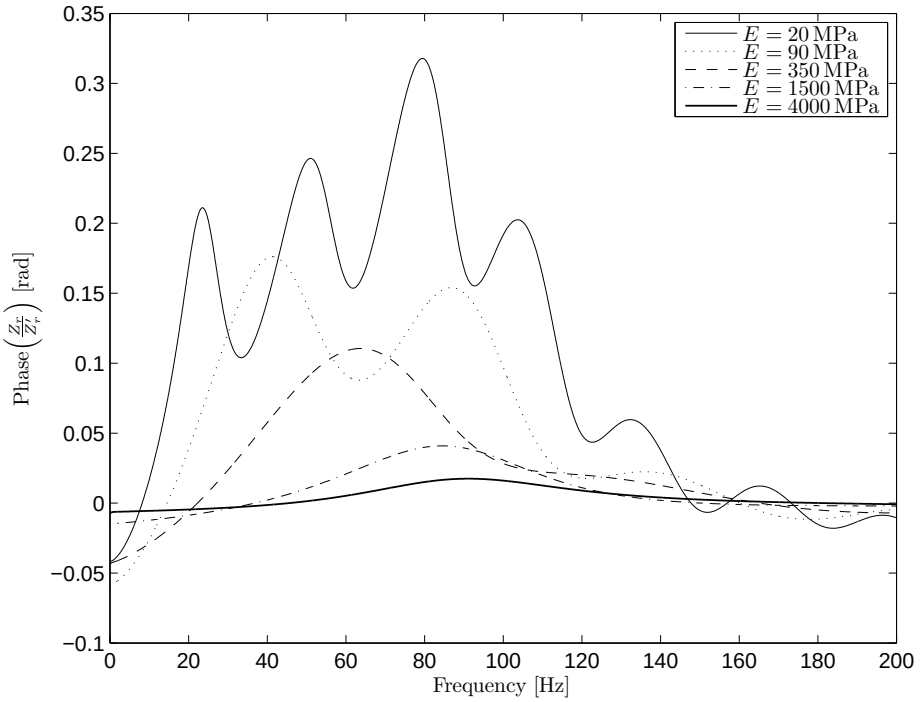


FIGURE C.72: Adimensional phase of the rail receptance for five different Young's modulus of the subgrade and for the superstructure parameters in Case 2 (see Tables 4.1, 4.2 and 4.3). The other mechanical parameters of the subgrade are equal to the Quaternary ground type (see Table 3.1).

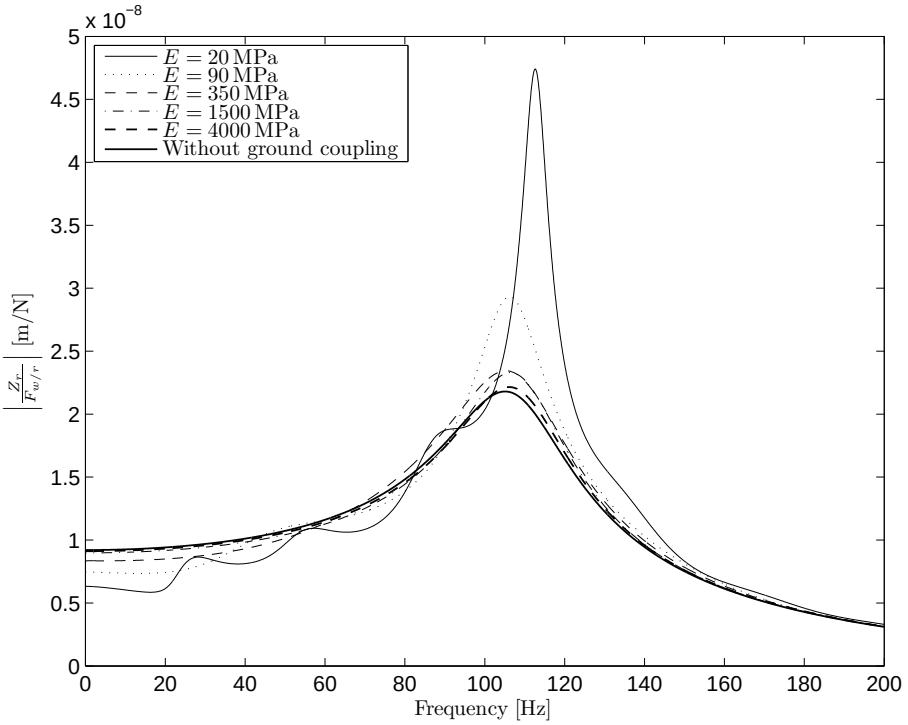


FIGURE C.73: Module of the rail receptance for five different Young's modulus of the subgrade and for the superstructure parameters in Case 3 (see Tables 4.1, 4.2 and 4.3). The other mechanical parameters of the subgrade are equal to the Quaternary ground type (see Table 3.1).

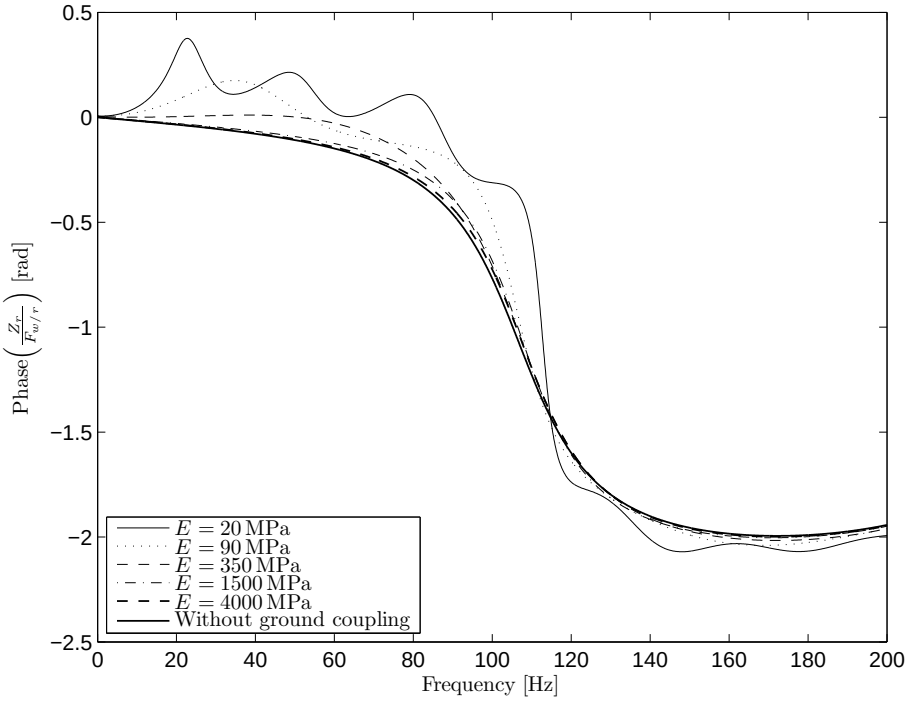


FIGURE C.74: Phase of the rail receptance for five different Young's modulus of the subgrade and for the superstructure parameters in Case 3 (see Tables 4.1, 4.2 and 4.3). The other mechanical parameters of the subgrade are equal to the Quaternary ground type (see Table 3.1).

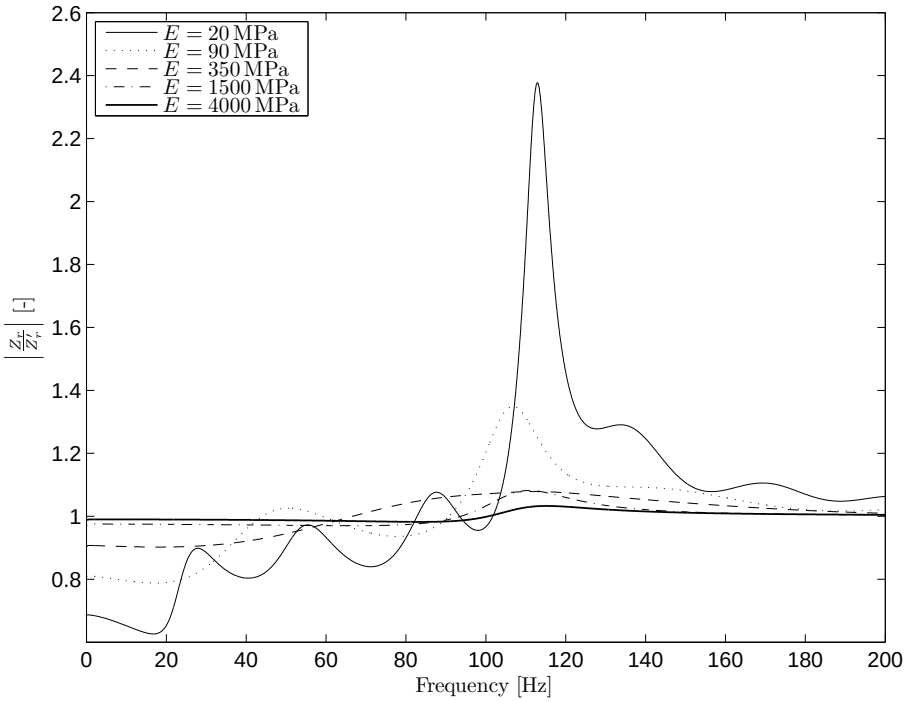


FIGURE C.75: Adimensional module of the rail receptance for five different Young's modulus of the subgrade and for the superstructure parameters in Case 3 (see Tables 4.1, 4.2 and 4.3). The other mechanical parameters of the subgrade are equal to the Quaternary ground type (see Table 3.1).

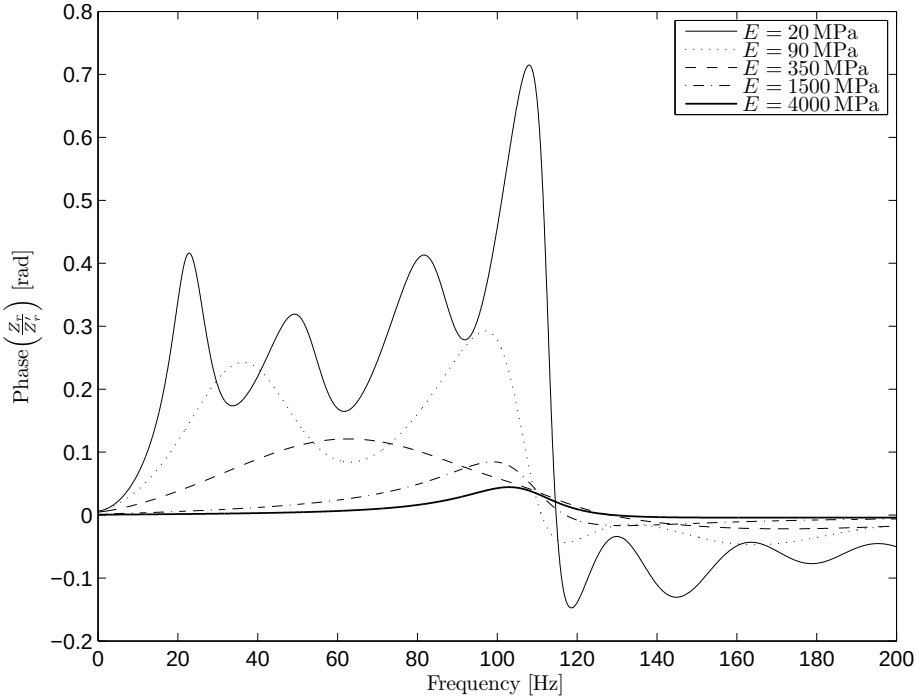


FIGURE C.76: Adimensional phase of the rail receptance for five different Young's modulus of the subgrade and for the superstructure parameters in Case 3 (see Tables 4.1, 4.2 and 4.3). The other mechanical parameters of the subgrade are equal to the Quaternary ground type (see Table 3.1).

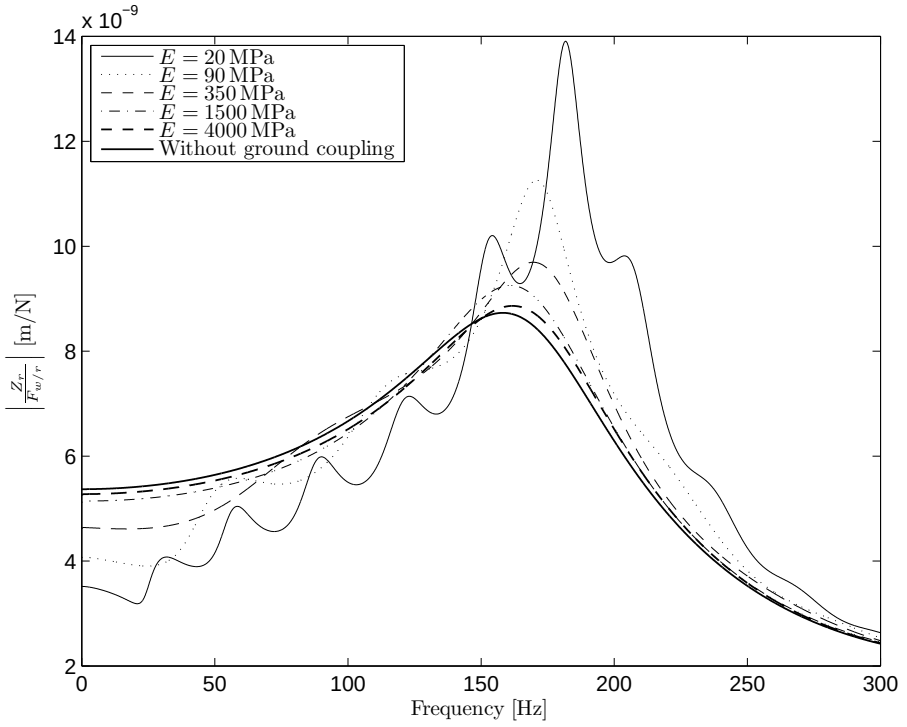


FIGURE C.77: Module of the rail receptance for five different Young's modulus of the subgrade and for the superstructure parameters in Case 4 (see Tables 4.1, 4.2 and 4.3). The other mechanical parameters of the subgrade are equal to the Quaternary ground type (see Table 3.1).

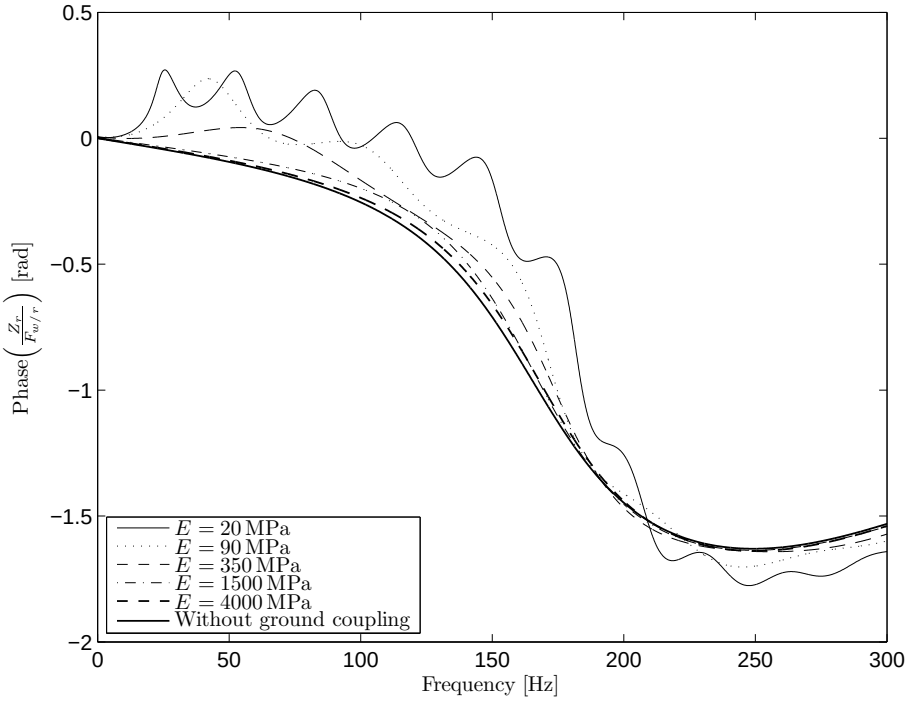


FIGURE C.78: Phase of the rail receptance for five different Young's modulus of the subgrade and for the superstructure parameters in Case 4 (see Tables 4.1, 4.2 and 4.3). The other mechanical parameters of the subgrade are equal to the Quaternary ground type (see Table 3.1).

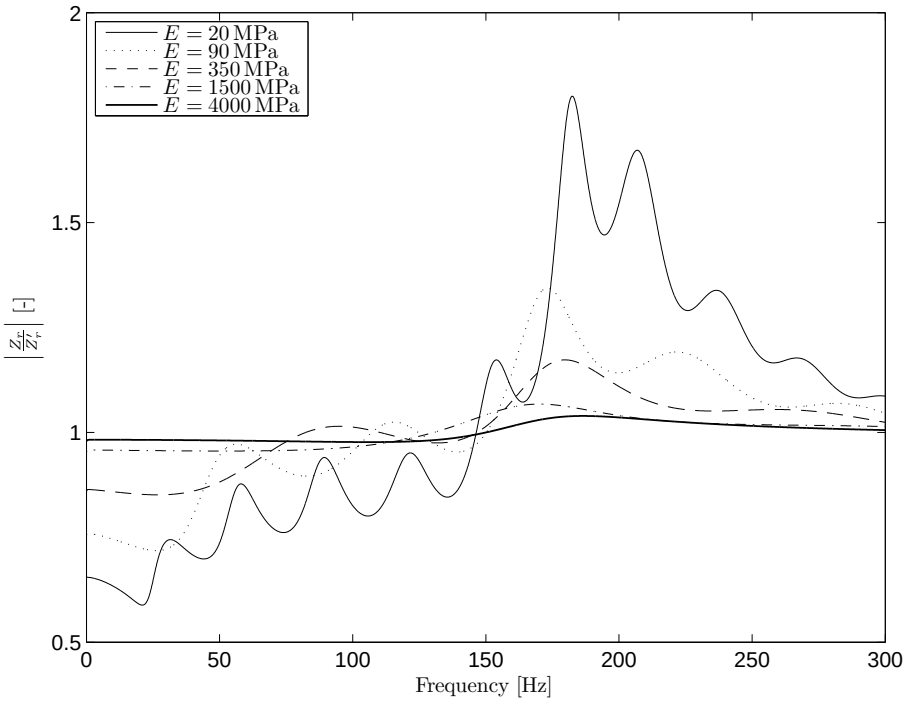


FIGURE C.79: Adimensional module of the rail receptance for five different Young's modulus of the subgrade and for the superstructure parameters in Case 4 (see Tables 4.1, 4.2 and 4.3). The other mechanical parameters of the subgrade are equal to the Quaternary ground type (see Table 3.1).

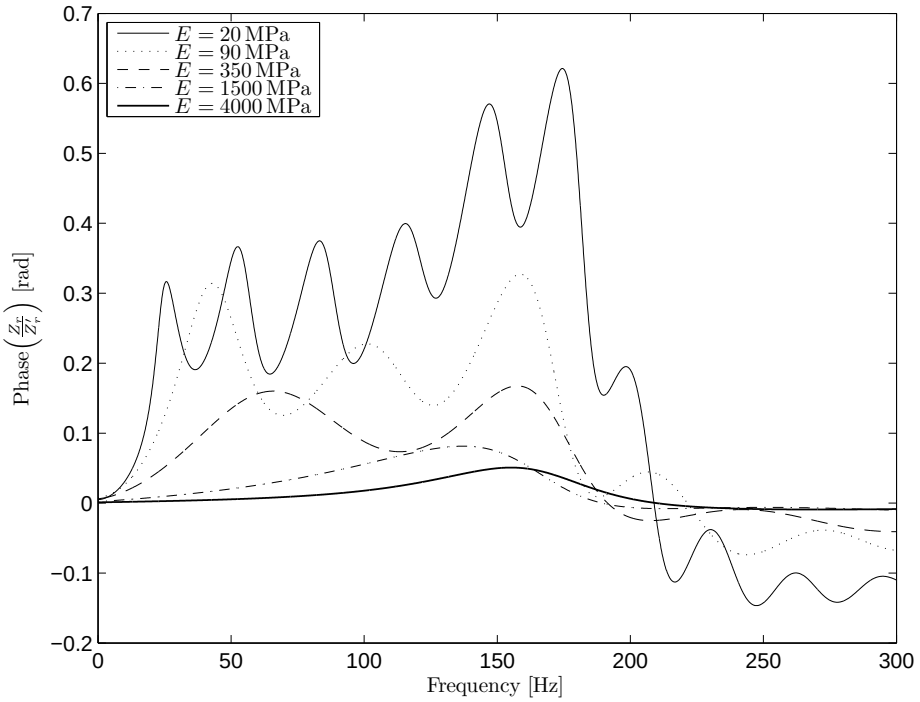


FIGURE C.80: Adimensional phase of the rail receptance for five different Young's modulus of the subgrade and for the superstructure parameters in Case 4 (see Tables 4.1, 4.2 and 4.3). The other mechanical parameters of the subgrade are equal to the Quaternary ground type (see Table 3.1).

### C.1.6 Effects of the superstructure width

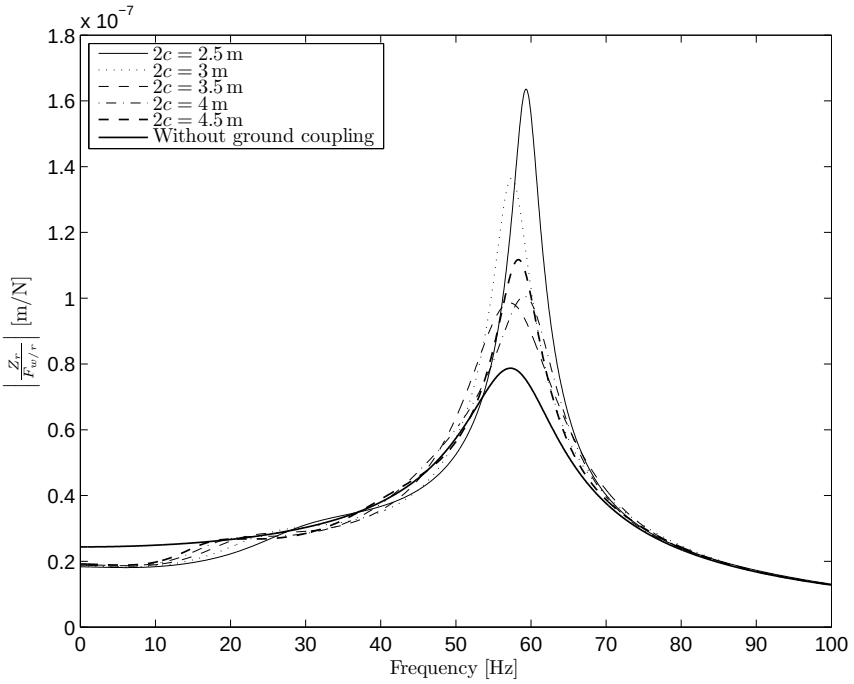


FIGURE C.81: Module of the rail receptance for five different widths of the contact area between the superstructure and the subgrade and for the superstructure parameters in Case 1 (see Tables 4.1, 4.2 and 4.3). The other mechanical parameters of the subgrade are equal to the Quaternary ground type (see Table 3.1).

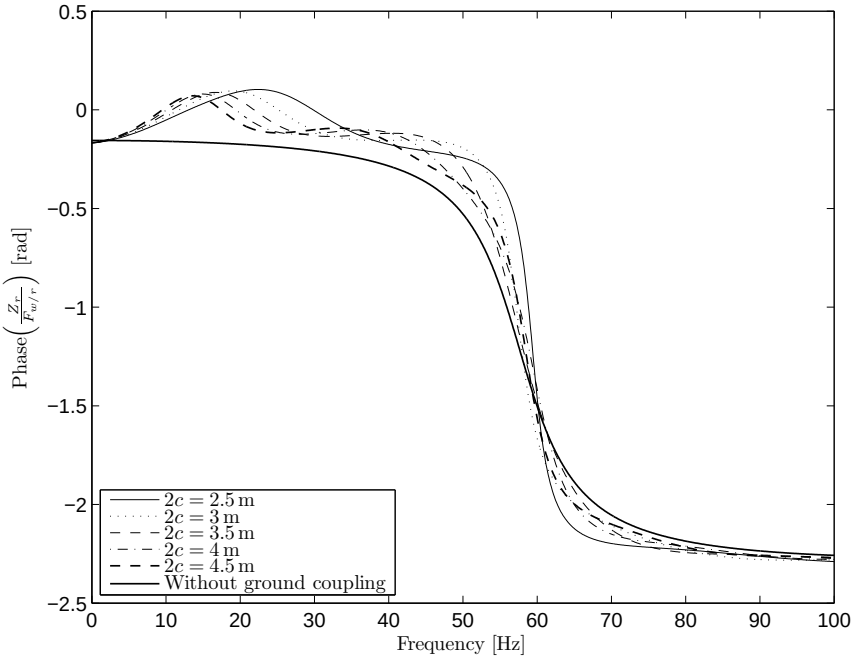


FIGURE C.82: Phase of the rail receptance for five different widths of the contact area between the superstructure and the subgrade and for the superstructure parameters in Case 1 (see Tables 4.1, 4.2 and 4.3). The other mechanical parameters of the subgrade are equal to the Quaternary ground type (see Table 3.1).

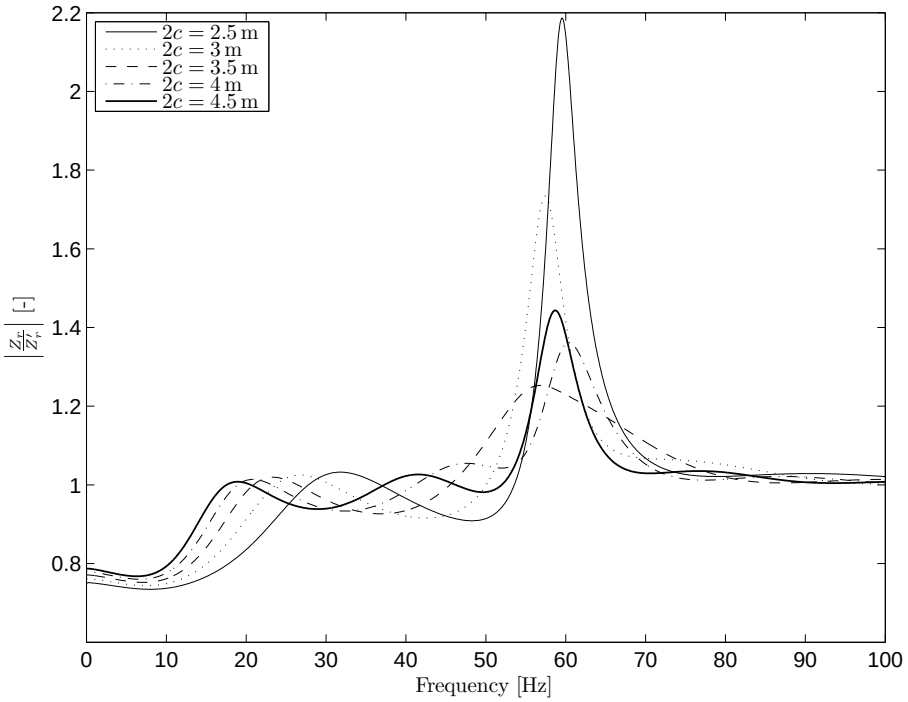


FIGURE C.83: Adimensional module of the rail receptance for five different widths of the contact area between the superstructure and the subgrade and for the superstructure parameters in Case 1 (see Tables 4.1, 4.2 and 4.3). The other mechanical parameters of the subgrade are equal to the Quaternary ground type (see Table 3.1).

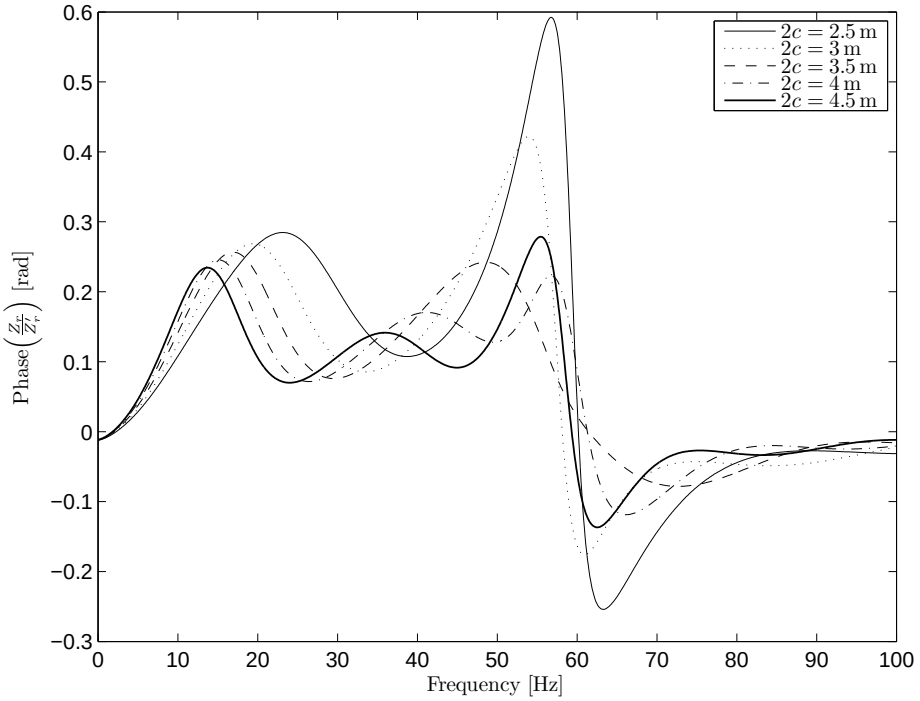


FIGURE C.84: Adimensional phase of the rail receptance for five different widths of the contact area between the superstructure and the subgrade and for the superstructure parameters in Case 1 (see Tables 4.1, 4.2 and 4.3). The other mechanical parameters of the subgrade are equal to the Quaternary ground type (see Table 3.1).

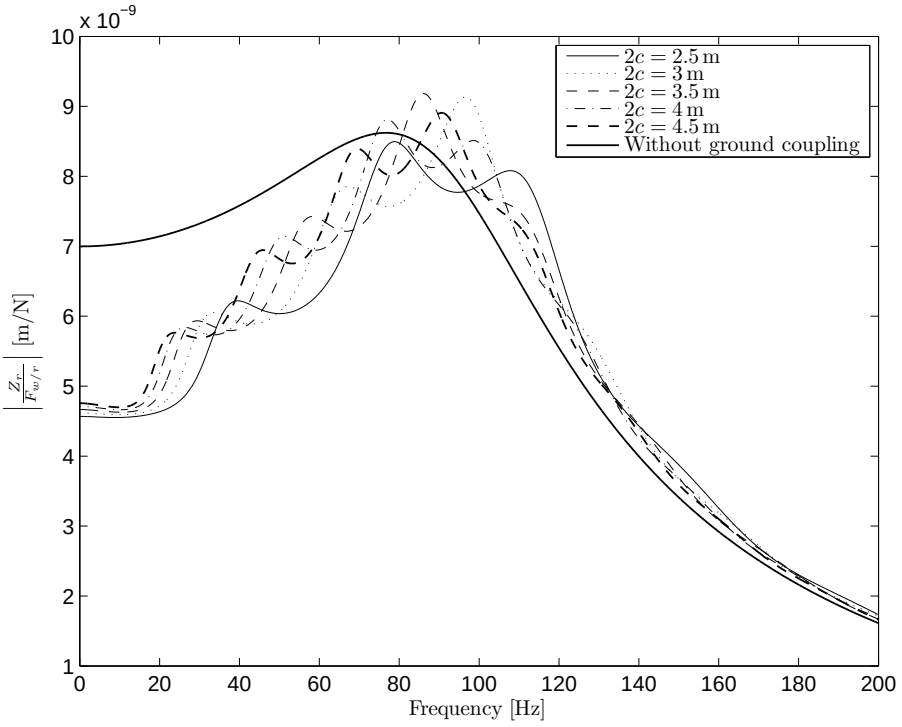


FIGURE C.85: Module of the rail receptance for five different widths of the contact area between the superstructure and the subgrade and for the superstructure parameters in Case 2 (see Tables 4.1, 4.2 and 4.3). The other mechanical parameters of the subgrade are equal to the Quaternary ground type (see Table 3.1).

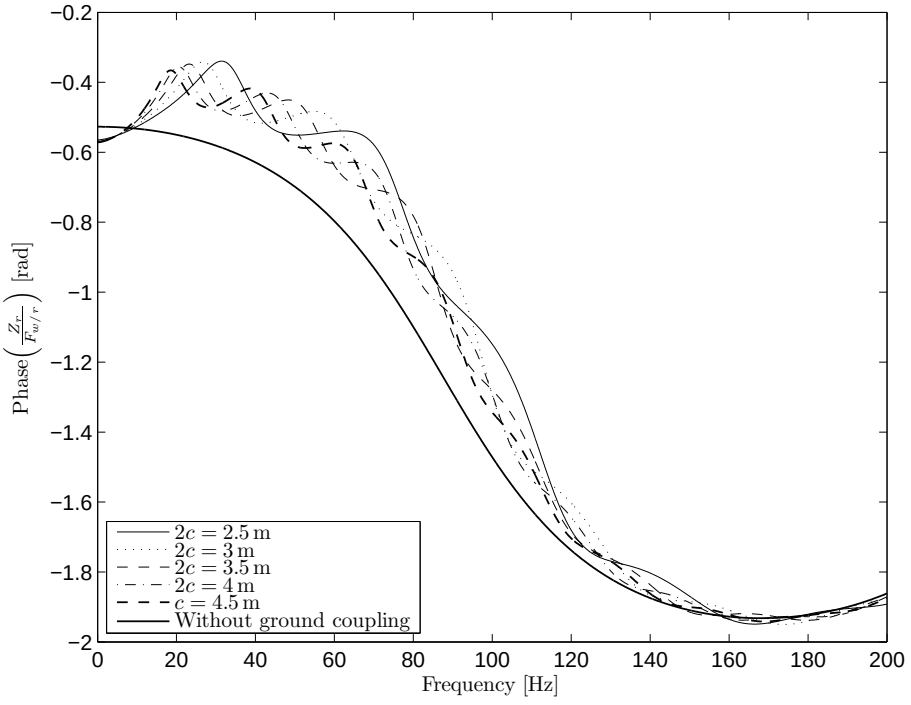


FIGURE C.86: Phase of the rail receptance for five different widths of the contact area between the superstructure and the subgrade and for the superstructure parameters in Case 2 (see Tables 4.1, 4.2 and 4.3). The other mechanical parameters of the subgrade are equal to the Quaternary ground type (see Table 3.1).

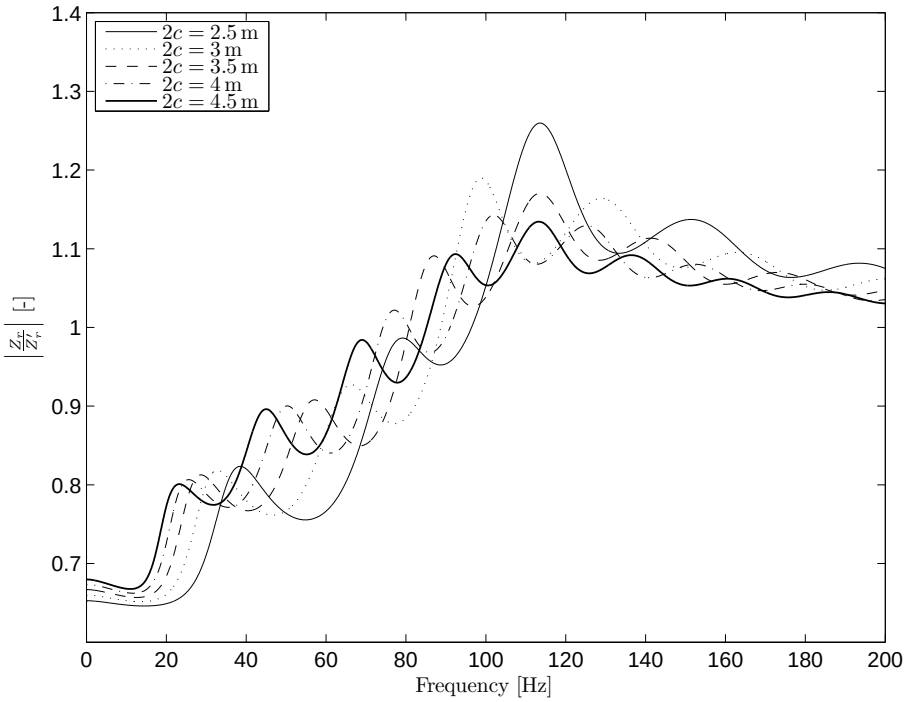


FIGURE C.87: Adimensional module of the rail receptance for five different widths of the contact area between the superstructure and the subgrade and for the superstructure parameters in Case 2 (see Tables 4.1, 4.2 and 4.3). The other mechanical parameters of the subgrade are equal to the Quaternary ground type (see Table 3.1).

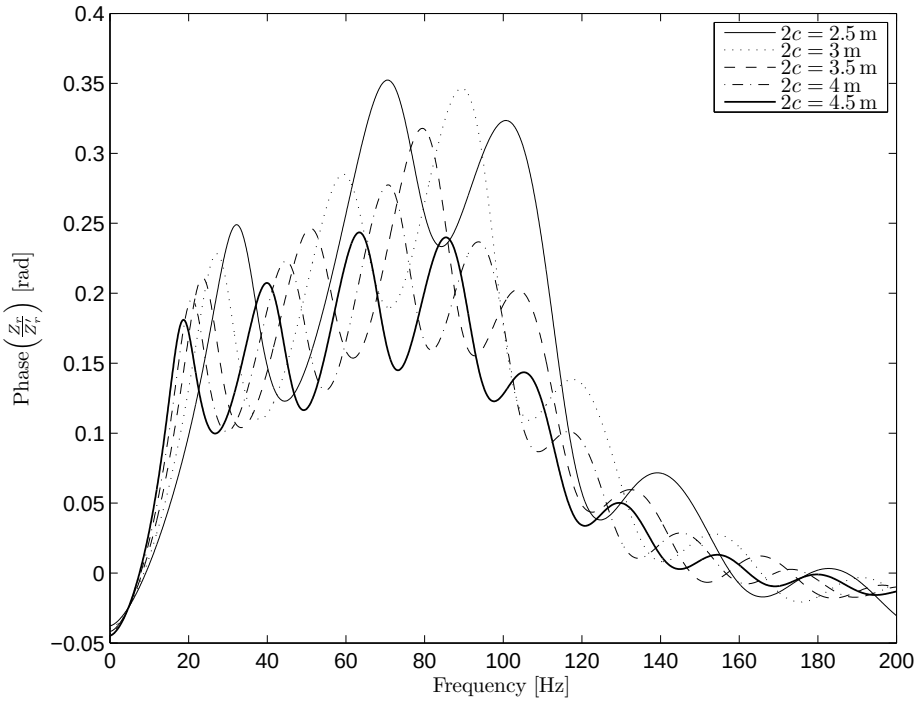


FIGURE C.88: Adimensional phase of the rail receptance for five different widths of the contact area between the superstructure and the subgrade and for the superstructure parameters in Case 2 (see Tables 4.1, 4.2 and 4.3). The other mechanical parameters of the subgrade are equal to the Quaternary ground type (see Table 3.1).

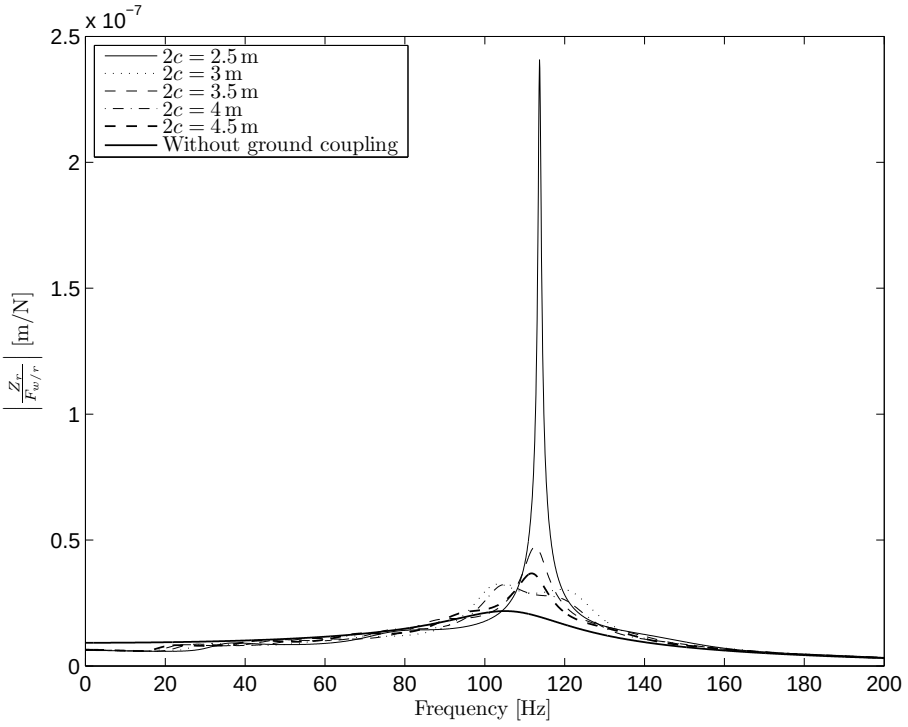


FIGURE C.89: Module of the rail receptance for five different widths of the contact area between the superstructure and the subgrade and for the superstructure parameters in Case 3 (see Tables 4.1, 4.2 and 4.3). The other mechanical parameters of the subgrade are equal to the Quaternary ground type (see Table 3.1).

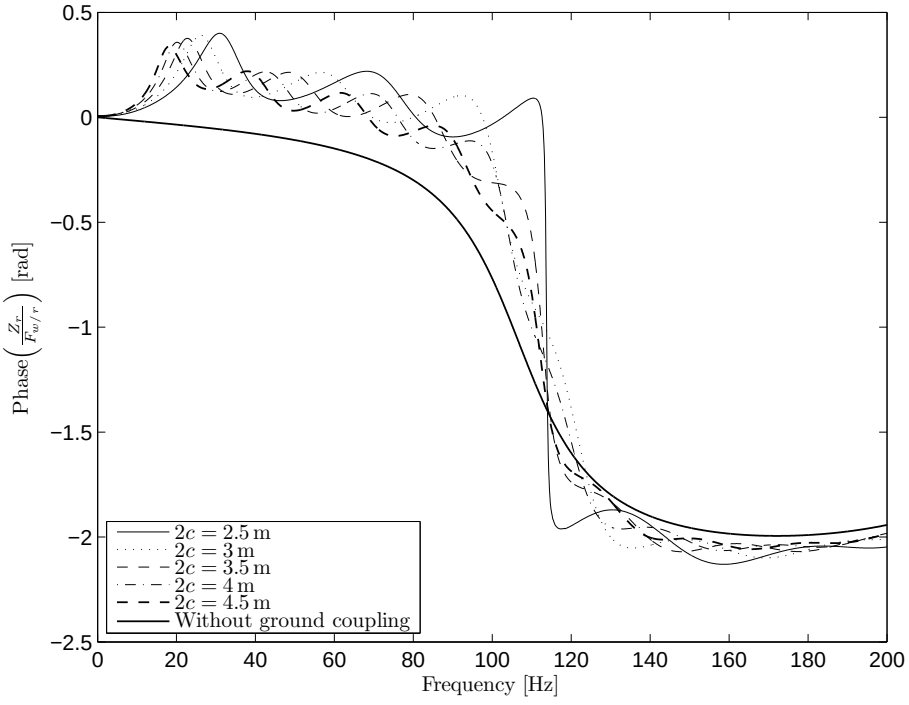


FIGURE C.90: Phase of the rail receptance for five different widths of the contact area between the superstructure and the subgrade and for the superstructure parameters in Case 3 (see Tables 4.1, 4.2 and 4.3). The other mechanical parameters of the subgrade are equal to the Quaternary ground type (see Table 3.1).

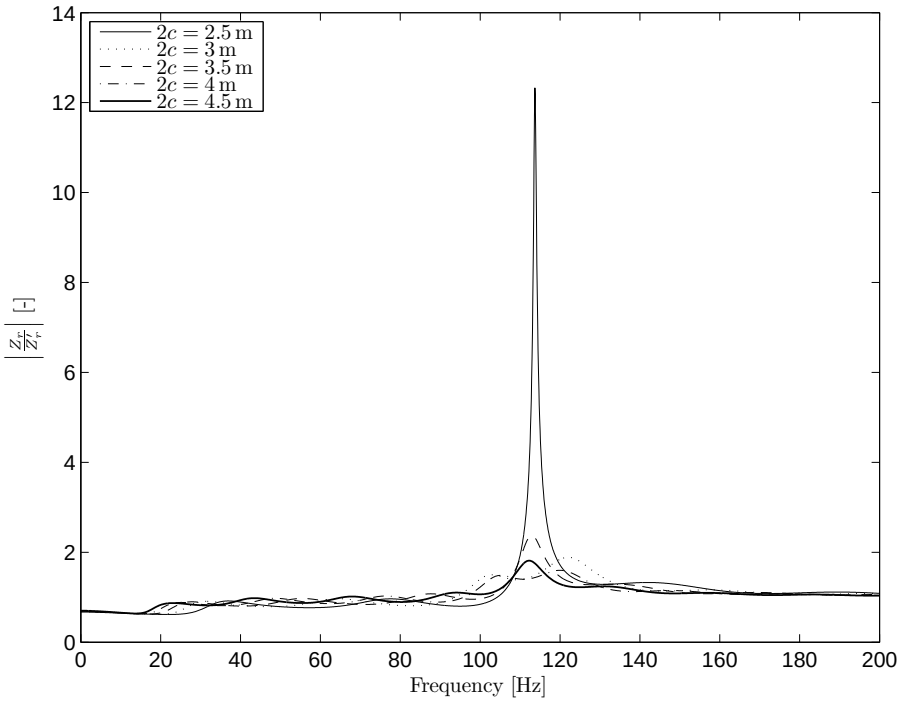


FIGURE C.91: Adimensional module of the rail receptance for five different widths of the contact area between the superstructure and the subgrade and for the superstructure parameters in Case 3 (see Tables 4.1, 4.2 and 4.3). The other mechanical parameters of the subgrade are equal to the Quaternary ground type (see Table 3.1).

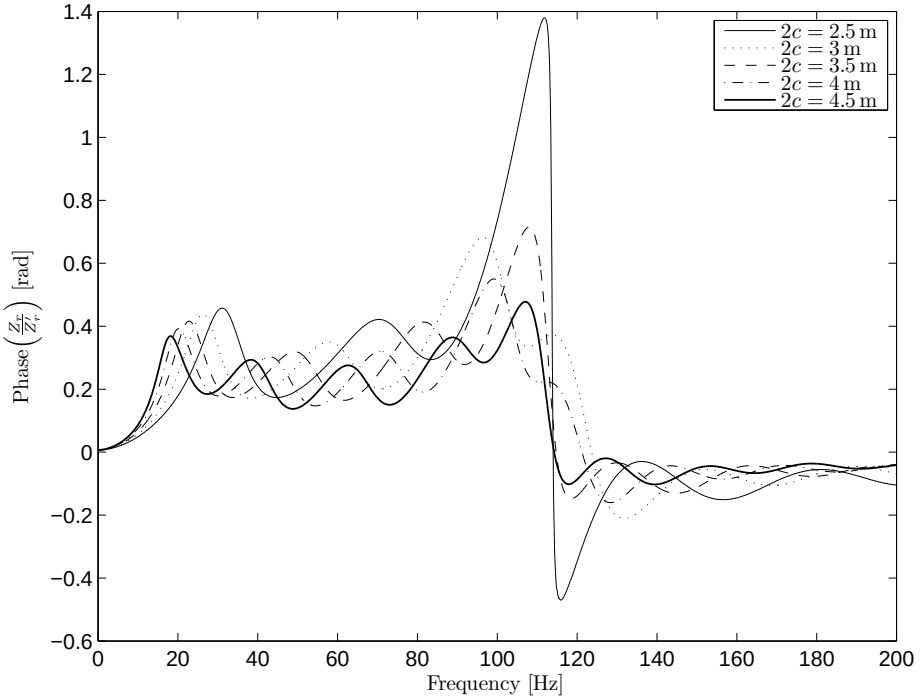


FIGURE C.92: Adimensional phase of the rail receptance for five different widths of the contact area between the superstructure and the subgrade and for the superstructure parameters in Case 3 (see Tables 4.1, 4.2 and 4.3). The other mechanical parameters of the subgrade are equal to the Quaternary ground type (see Table 3.1).

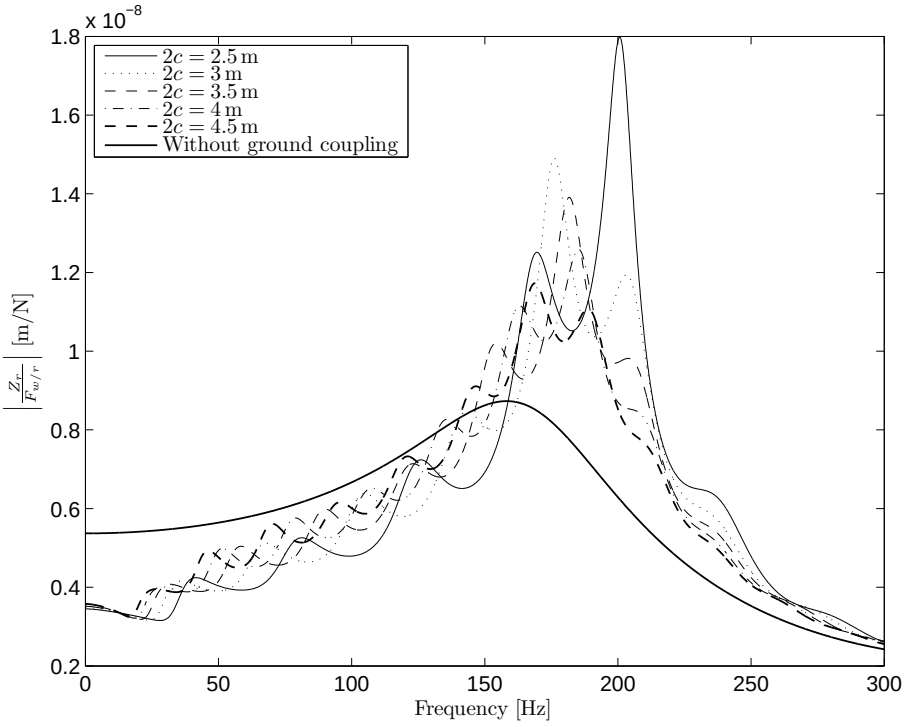


FIGURE C.93: Module of the rail receptance for five different widths of the contact area between the superstructure and the subgrade and for the superstructure parameters in Case 4 (see Tables 4.1, 4.2 and 4.3). The other mechanical parameters of the subgrade are equal to the Quaternary ground type (see Table 3.1).

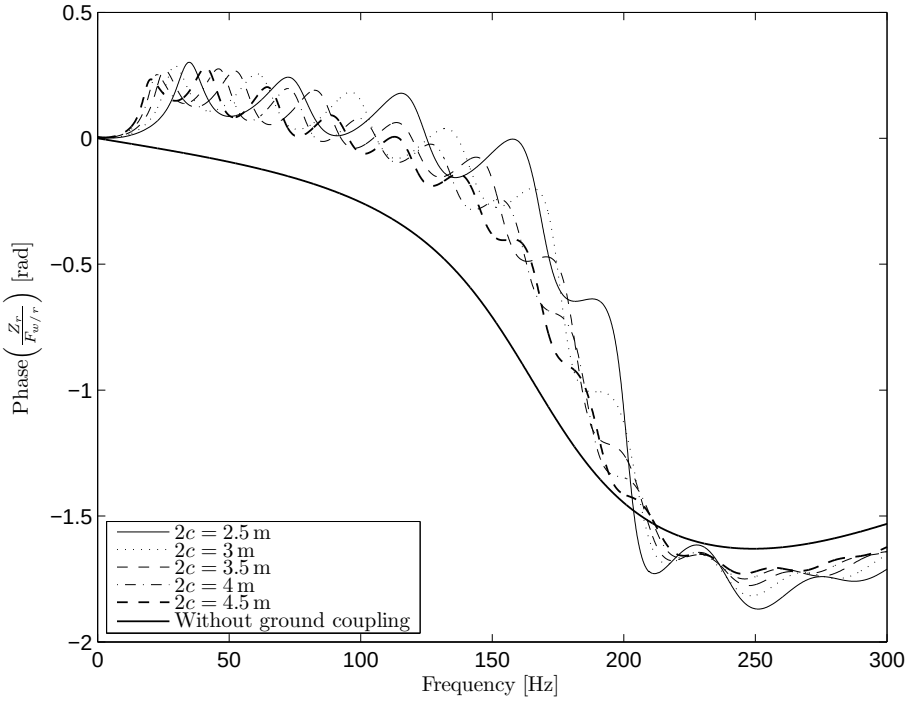


FIGURE C.94: Phase of the rail receptance for five different widths of the contact area between the superstructure and the subgrade and for the superstructure parameters in Case 4 (see Tables 4.1, 4.2 and 4.3). The other mechanical parameters of the subgrade are equal to the Quaternary ground type (see Table 3.1).

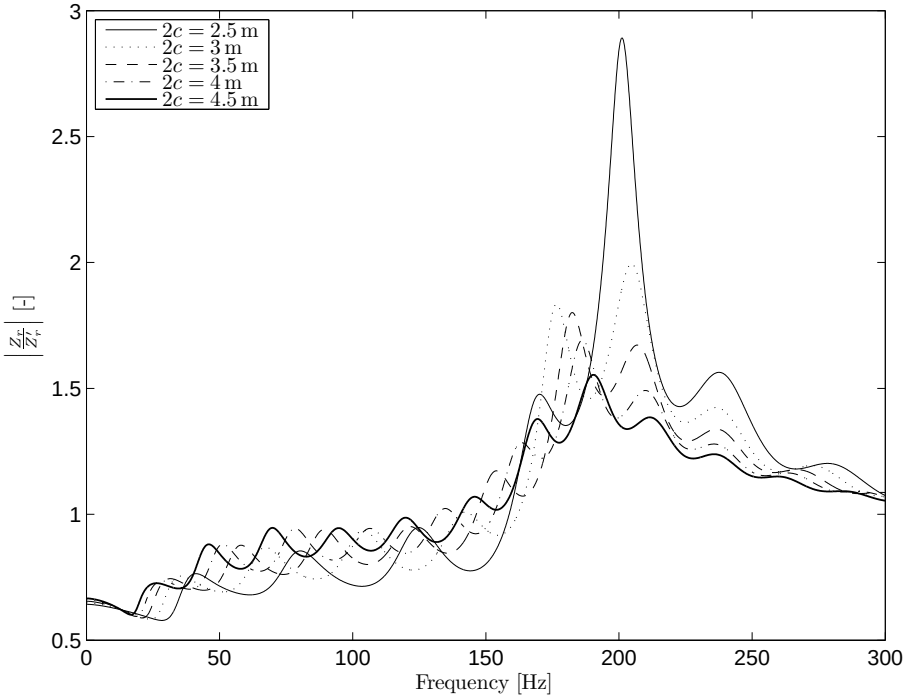


FIGURE C.95: Adimensional module of the rail receptance for five different widths of the contact area between the superstructure and the subgrade and for the superstructure parameters in Case 4 (see Tables 4.1, 4.2 and 4.3). The other mechanical parameters of the subgrade are equal to the Quaternary ground type (see Table 3.1).

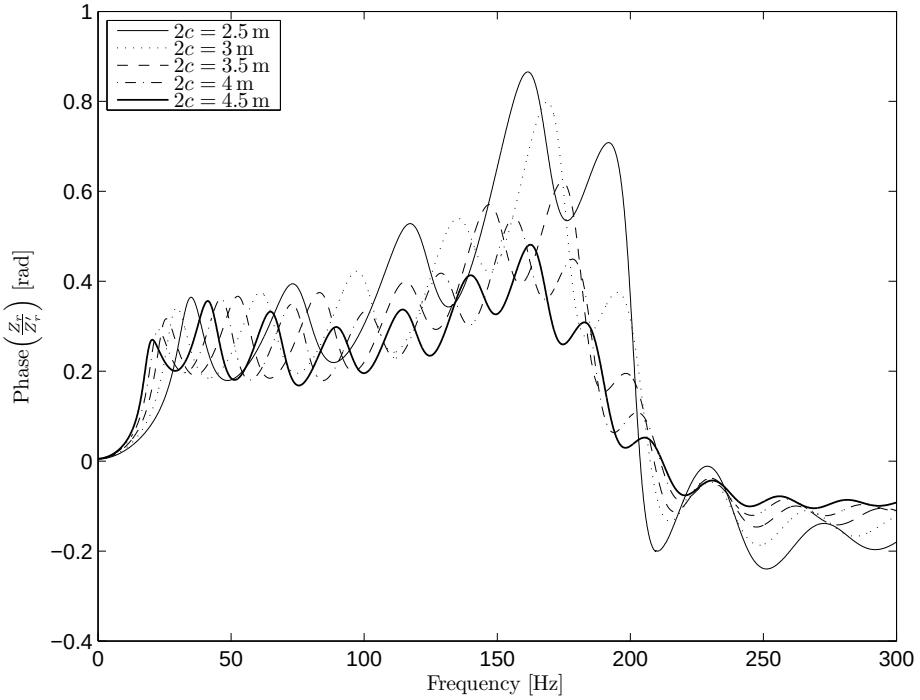


FIGURE C.96: Adimensional phase of the rail receptance for five different widths of the contact area between the superstructure and the subgrade and for the superstructure parameters in Case 4 (see Tables 4.1, 4.2 and 4.3). The other mechanical parameters of the subgrade are equal to the Quaternary ground type (see Table 3.1).

## C.2 Equivalent model parameters

### C.2.1 Equivalent model with constant parameters

| **Equivalent model parameters** | | | | |
|---|---|---|---|---|
| Parameters | Case 1 | Case 2 | Case 3 | Case 4 |
| $m'_r$ [kg] | 80.45 | 98.41 | 75.88 | 66.68 |
| $m'_s$ [kg] | 288.57 | 217.9 | 245.4 | 217 |
| $k'_F$ [N/m] | $3.447 \cdot 10^8$ | $8.125 \cdot 10^8$ | $4.638 \cdot 10^8$ | $4.489 \cdot 10^8$ |
| $k'_B$ [N/m] | $5.081 \cdot 10^7$ | $1.872 \cdot 10^8$ | $1.617 \cdot 10^8$ | $4.105 \cdot 10^8$ |
| $c'_F$ [N s/m] | $2.716 \cdot 10^4$ | $3.476 \cdot 10^3$ | $4.57 \cdot 10^4$ | $7.07 \cdot 10^4$ |
| $c'_B$ [N s/m] | $3.012 \cdot 10^4$ | $2.529 \cdot 10^5$ | $6.62 \cdot 10^4$ | $1.504 \cdot 10^5$ |

TABLE C.1: Equivalent model parameters obtained for Cases 1, 2, 3 and 4 (see Tables 4.1, 4.2 and 4.3) and for a quaternary subgrade (see Table 3.1). Constant parameters.

### C.2.2 Equivalent model with frequency dependence parameters

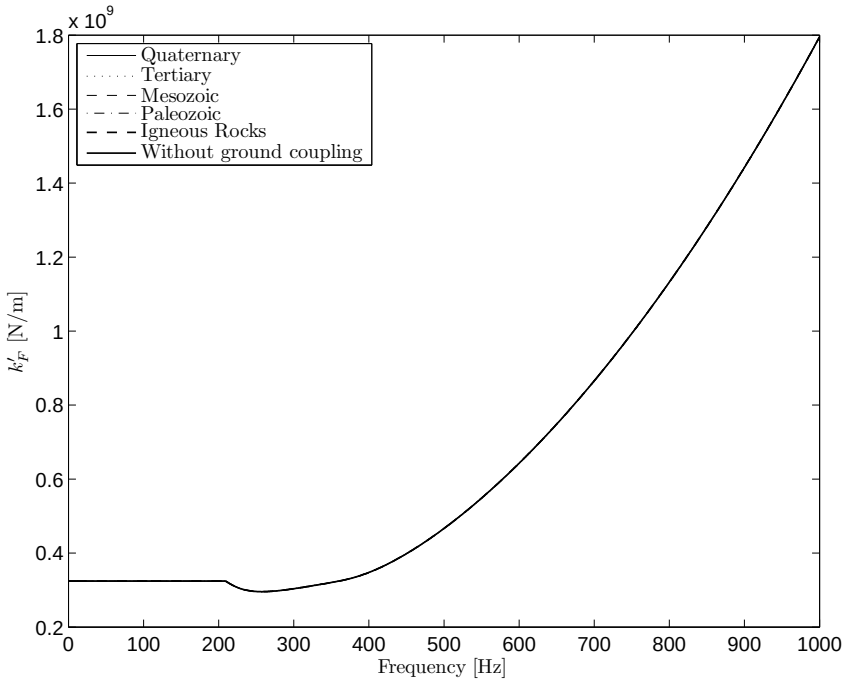


FIGURE C.97: Fasteners equivalent stiffness as a function of the frequency for Case 1 (see Tables 4.1, 4.2 and 4.3) and for five different subgrade parameters of the Table 3.1.

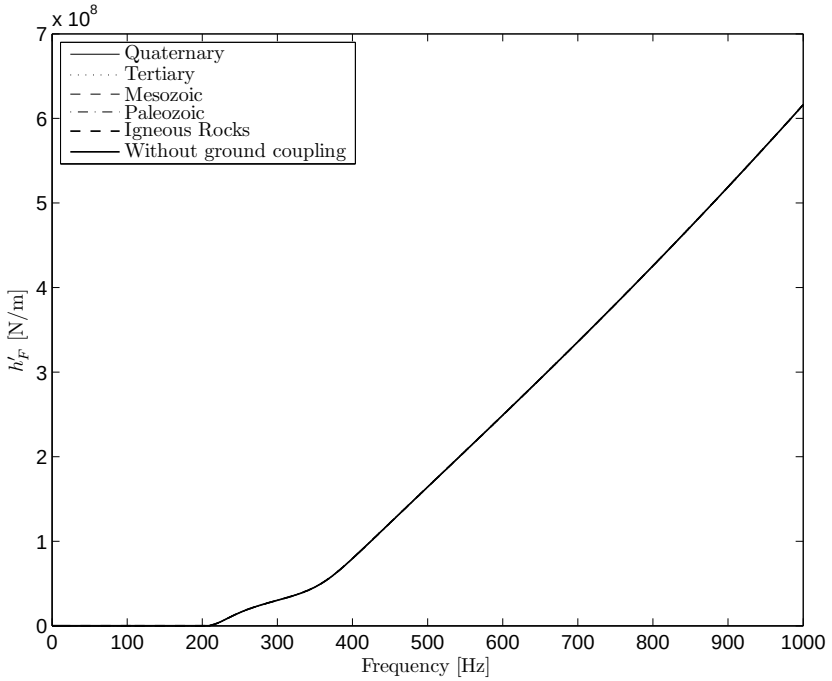


FIGURE C.98: Fasteners equivalent structural damping as a function of the frequency for Case 1 (see Tables 4.1, 4.2 and 4.3) and for five different subgrade parameters of the Table 3.1.

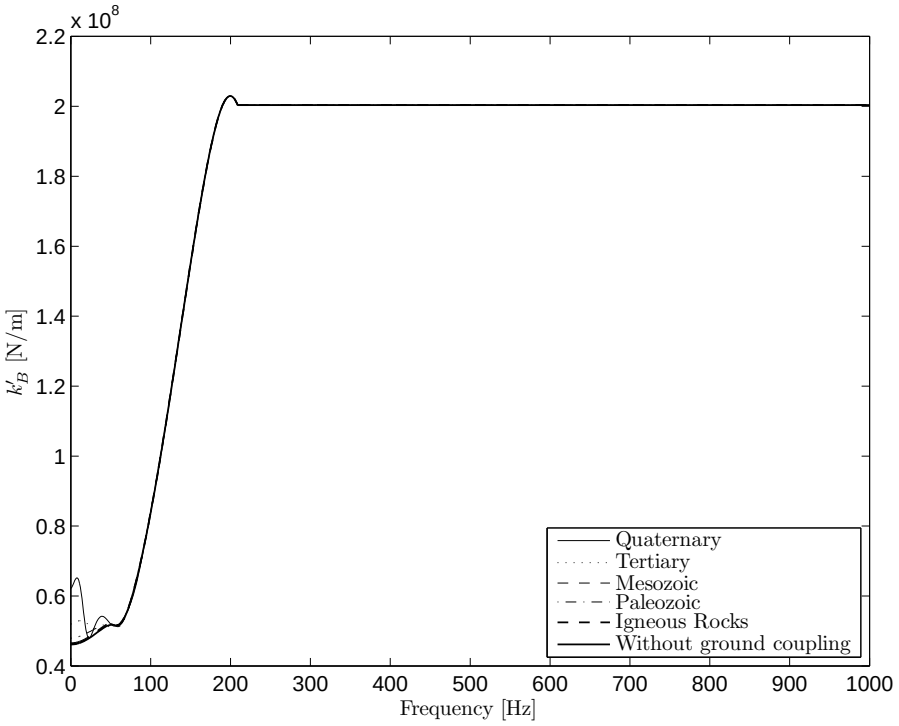


FIGURE C.99: Ballast equivalent stiffness as a function of the frequency for Case 1 (see Tables 4.1, 4.2 and 4.3) and for five different subgrade parameters of the Table 3.1.

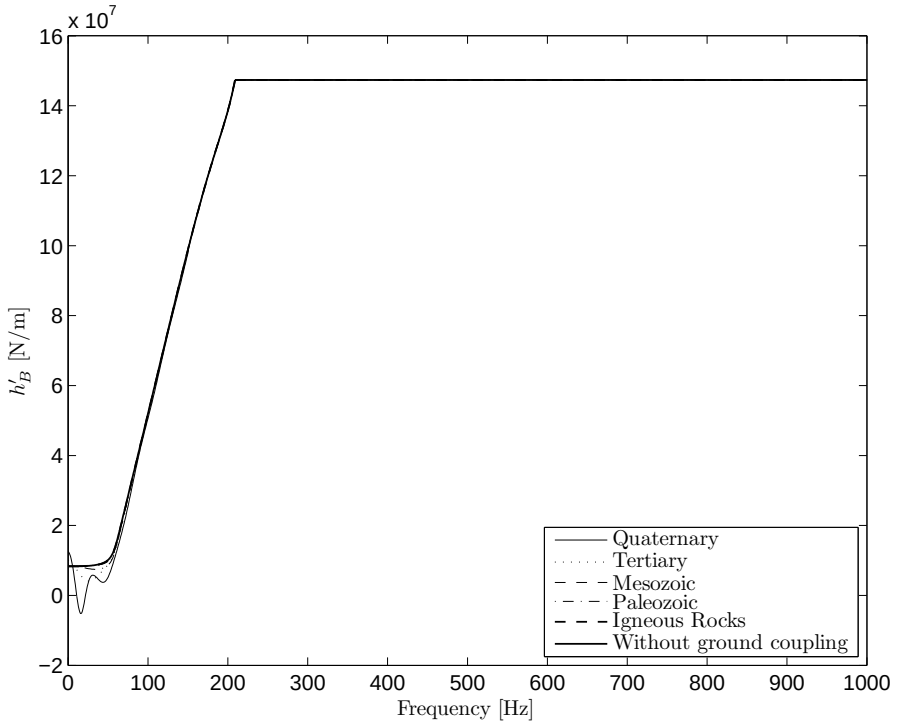


FIGURE C.100: Ballast equivalent structural damping as a function of the frequency for Case 1 (see Tables 4.1, 4.2 and 4.3) and for five different subgrade parameters of the Table 3.1.

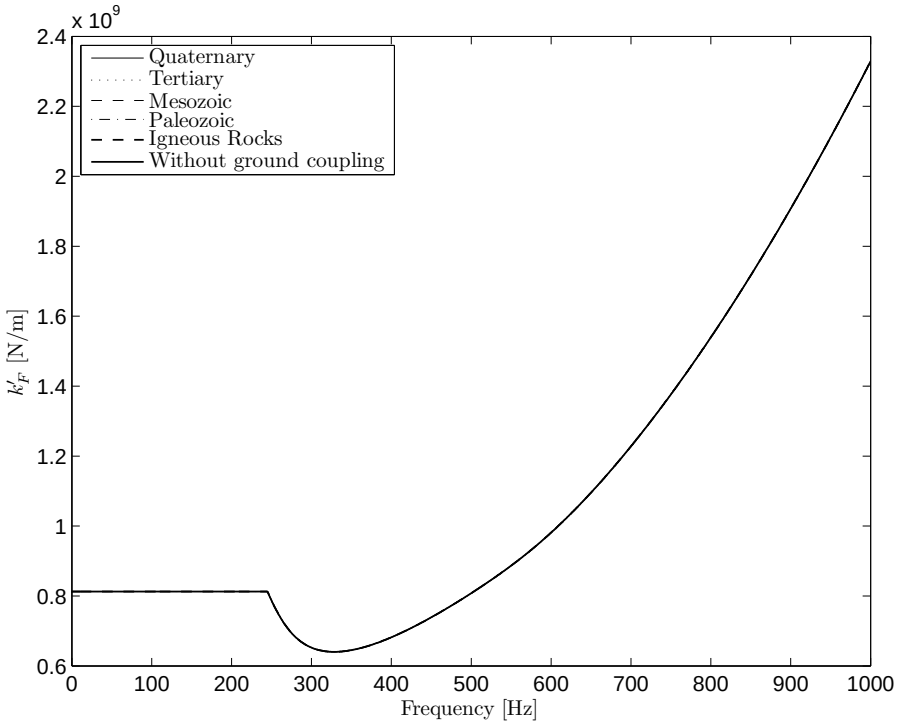


FIGURE C.101: Fasteners equivalent stiffness as a function of the frequency for Case 2 (see Tables 4.1, 4.2 and 4.3) and for five different subgrade parameters of the Table 3.1.

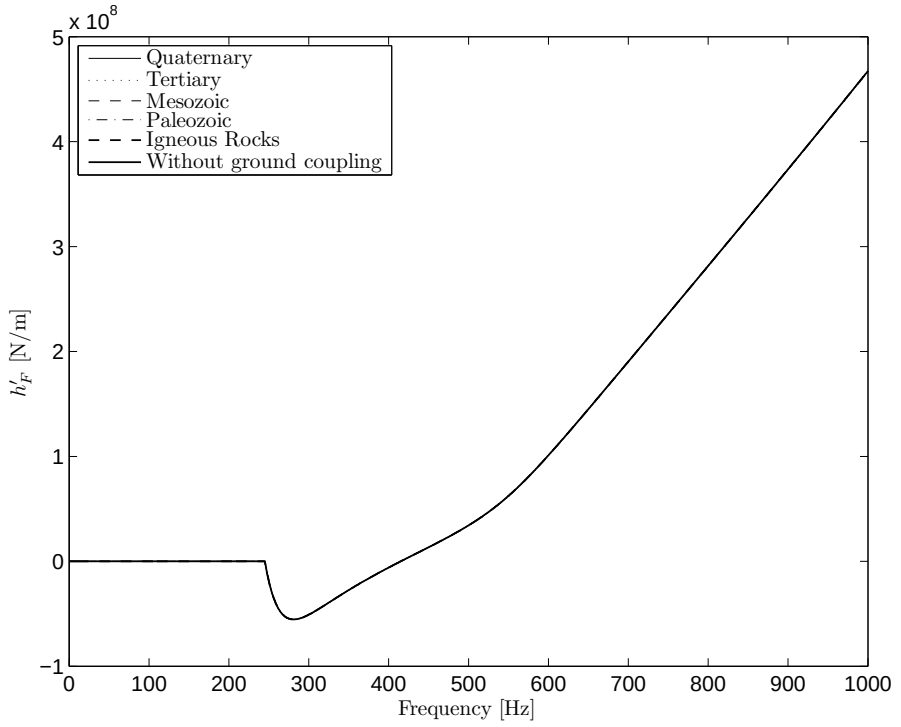


FIGURE C.102: Fasteners equivalent structural damping as a function of the frequency for Case 2 (see Tables 4.1, 4.2 and 4.3) and for five different subgrade parameters of the Table 3.1.

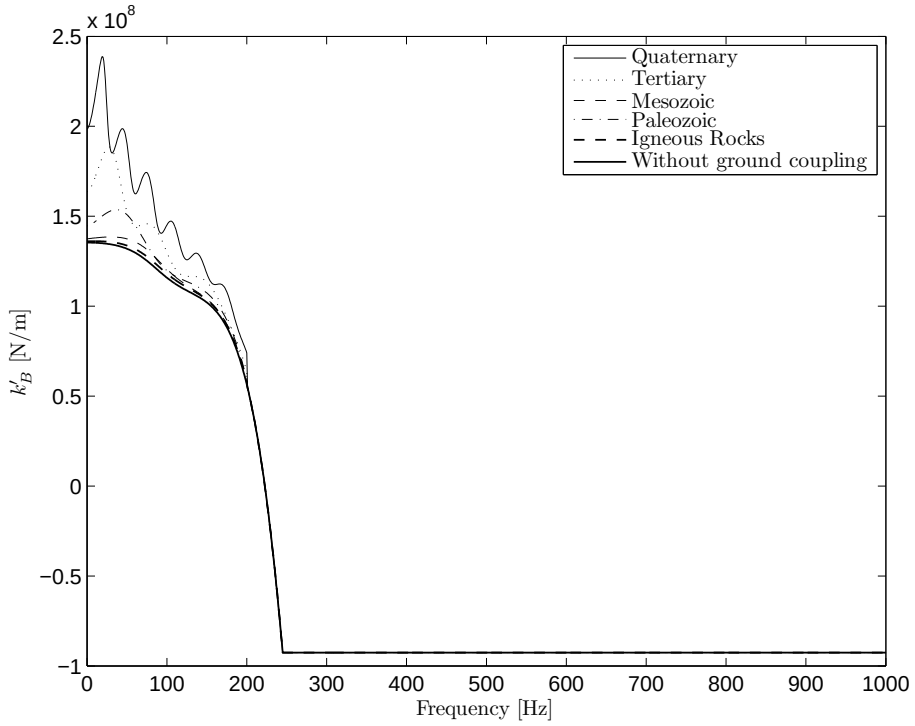


FIGURE C.103: Ballast equivalent stiffness as a function of the frequency for Case 2 (see Tables 4.1, 4.2 and 4.3) and for five different subgrade parameters of the Table 3.1.

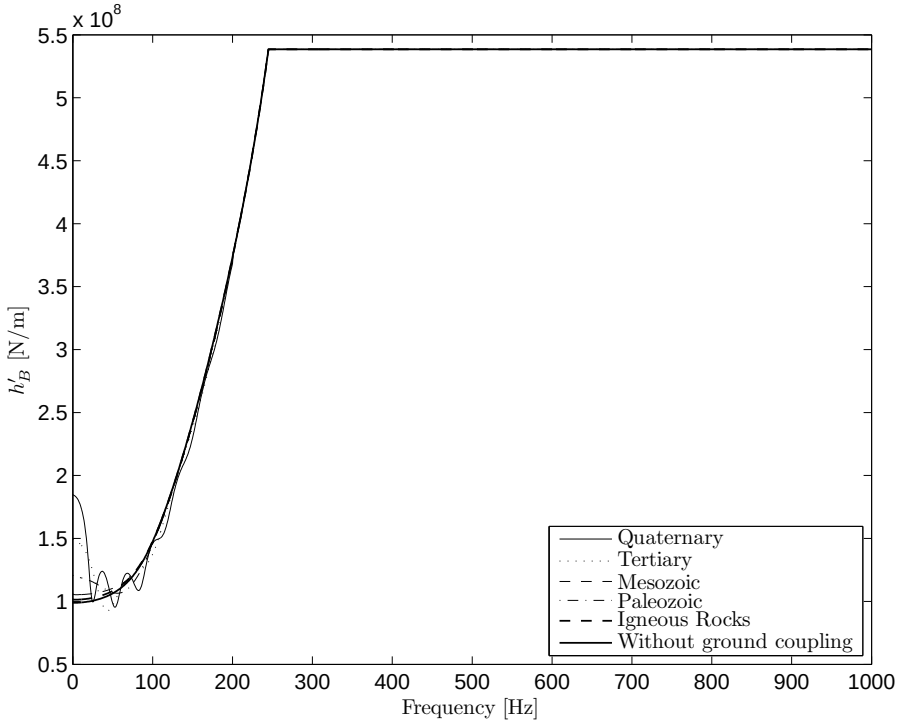


FIGURE C.104: Ballast equivalent structural damping as a function of the frequency for Case 2 (see Tables 4.1, 4.2 and 4.3) and for five different subgrade parameters of the Table 3.1.

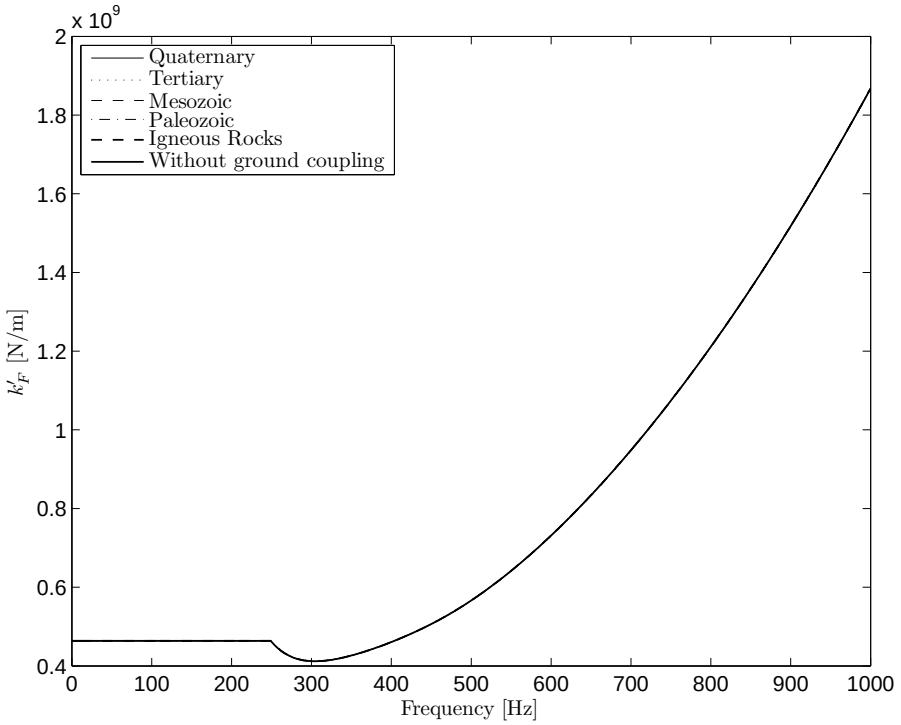


FIGURE C.105: Fasteners equivalent stiffness as a function of the frequency for Case 3 (see Tables 4.1, 4.2 and 4.3) and for five different subgrade parameters of the Table 3.1.

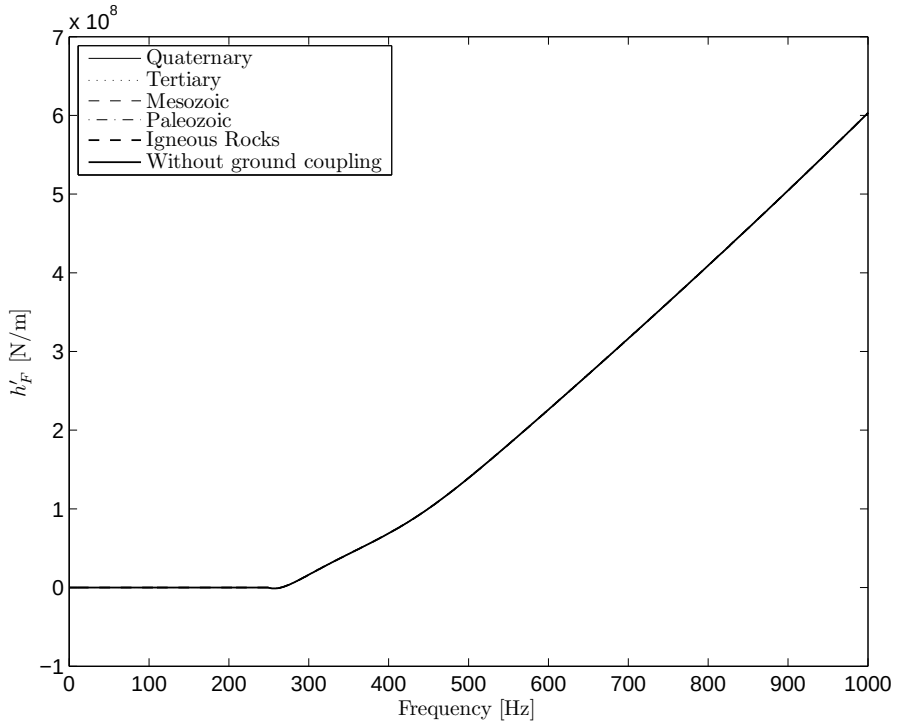


FIGURE C.106: Fasteners equivalent structural damping as a function of the frequency for Case 3 (see Tables 4.1, 4.2 and 4.3) and for five different subgrade parameters of the Table 3.1.

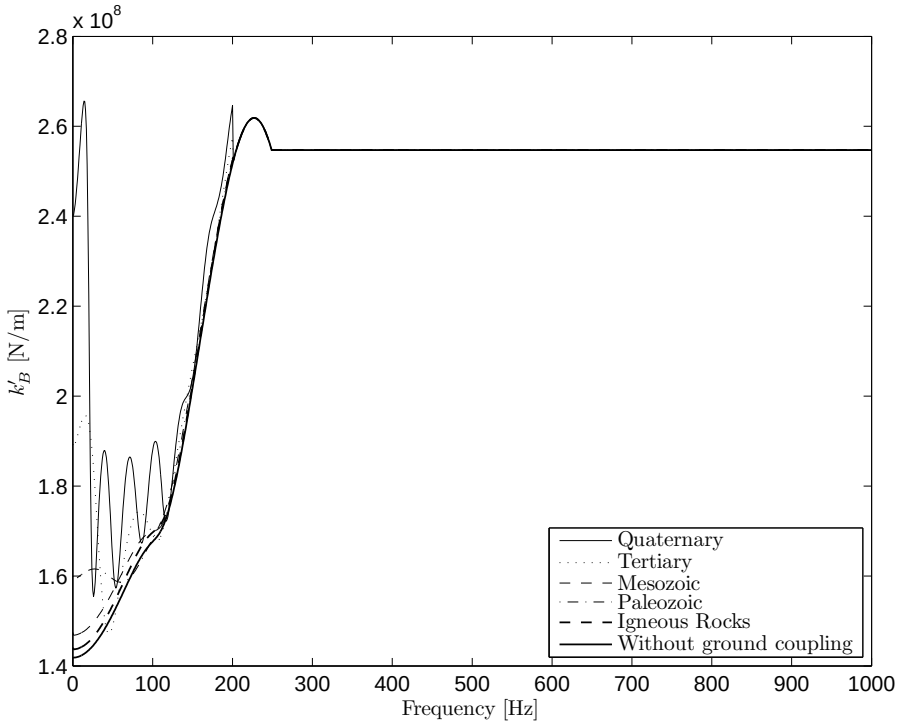


FIGURE C.107: Ballast equivalent stiffness as a function of the frequency for Case 3 (see Tables 4.1, 4.2 and 4.3) and for five different subgrade parameters of the Table 3.1.

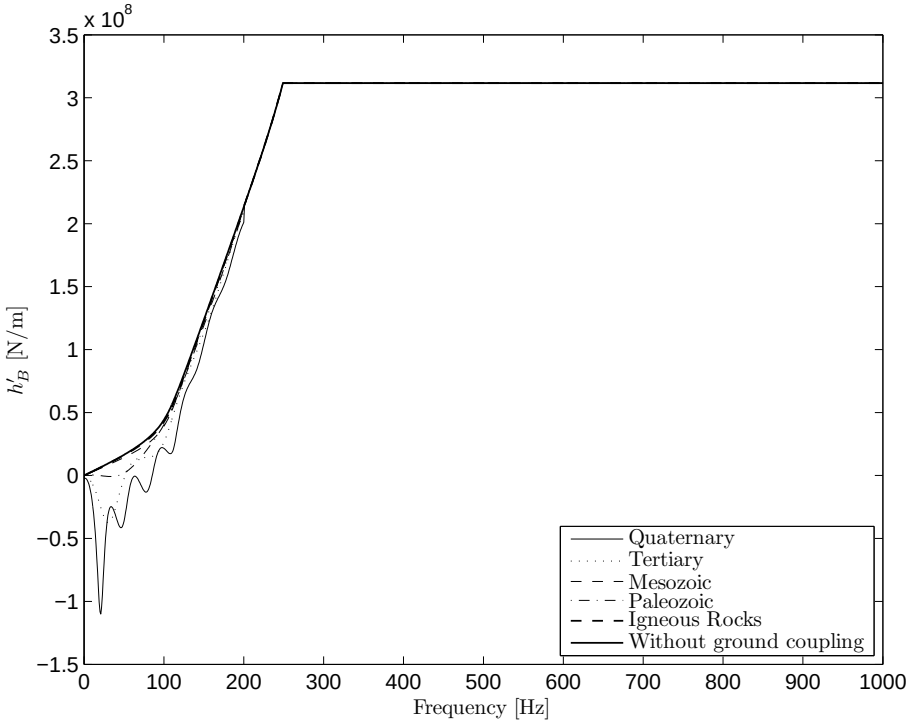


FIGURE C.108: Ballast equivalent structural damping as a function of the frequency for Case 3 (see Tables 4.1, 4.2 and 4.3) and for five different subgrade parameters of the Table 3.1.

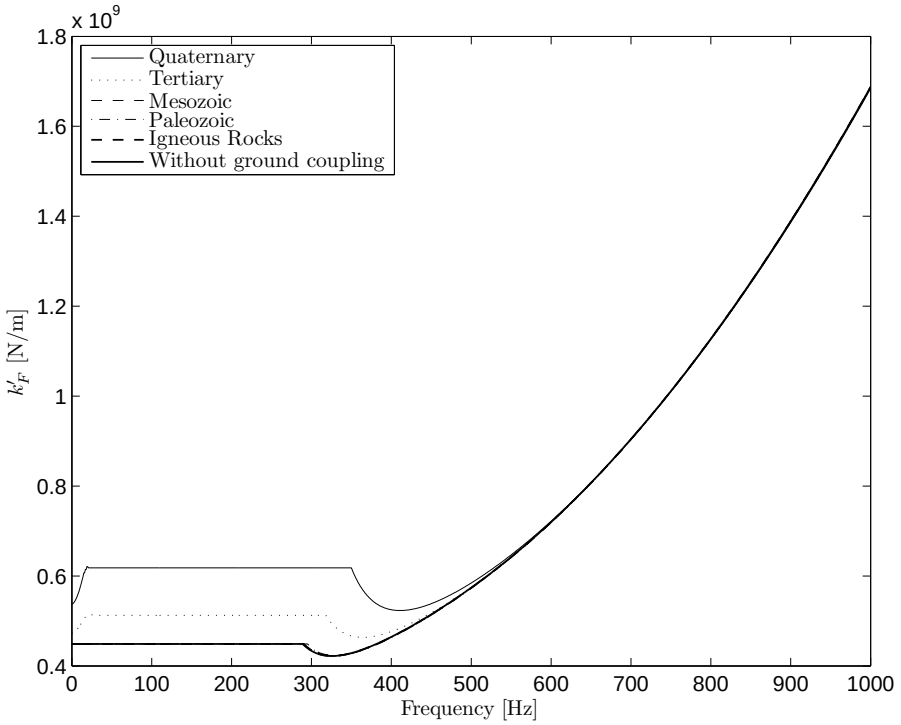


FIGURE C.109: Fasteners equivalent stiffness as a function of the frequency for Case 4 (see Tables 4.1, 4.2 and 4.3) and for five different subgrade parameters of the Table 3.1.

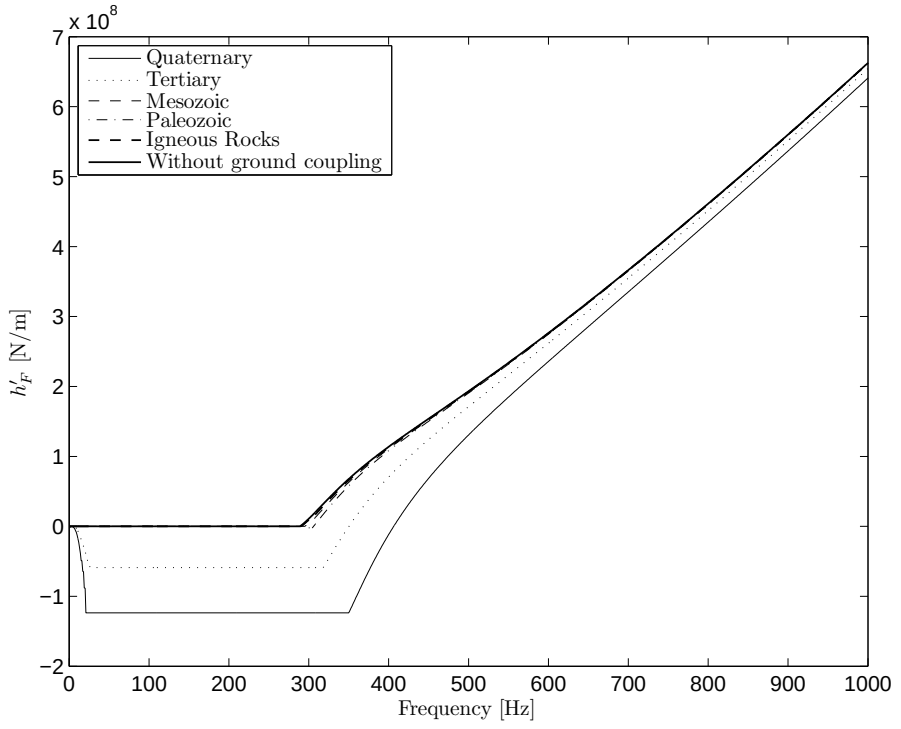


FIGURE C.110: Fasteners equivalent structural damping as a function of the frequency for Case 4 (see Tables 4.1, 4.2 and 4.3) and for five different subgrade parameters of the Table 3.1.

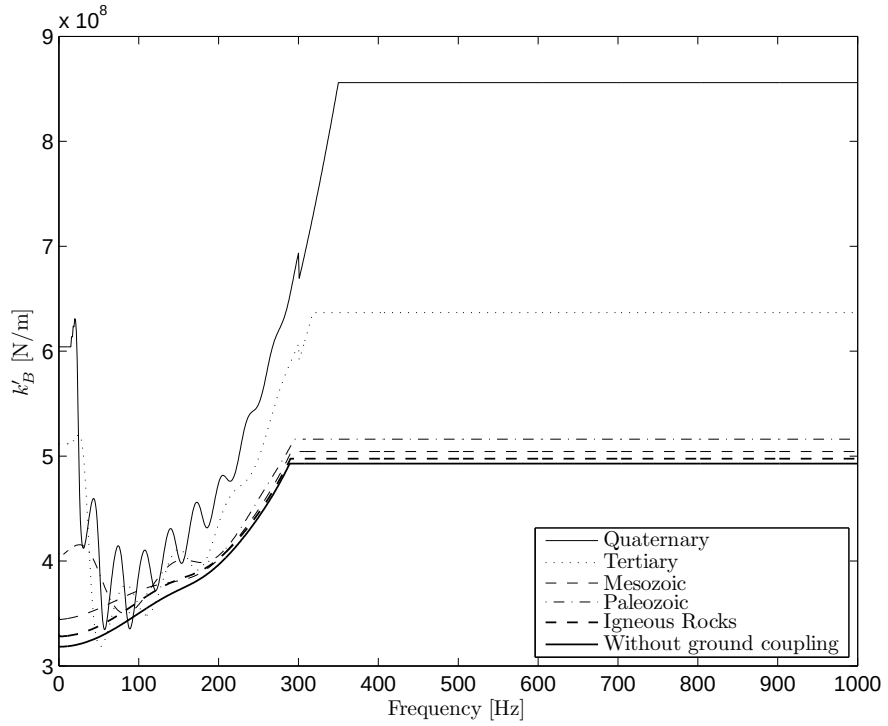


FIGURE C.111: Ballast equivalent stiffness as a function of the frequency for Case 4 (see Tables 4.1, 4.2 and 4.3) and for five different subgrade parameters of the Table 3.1.

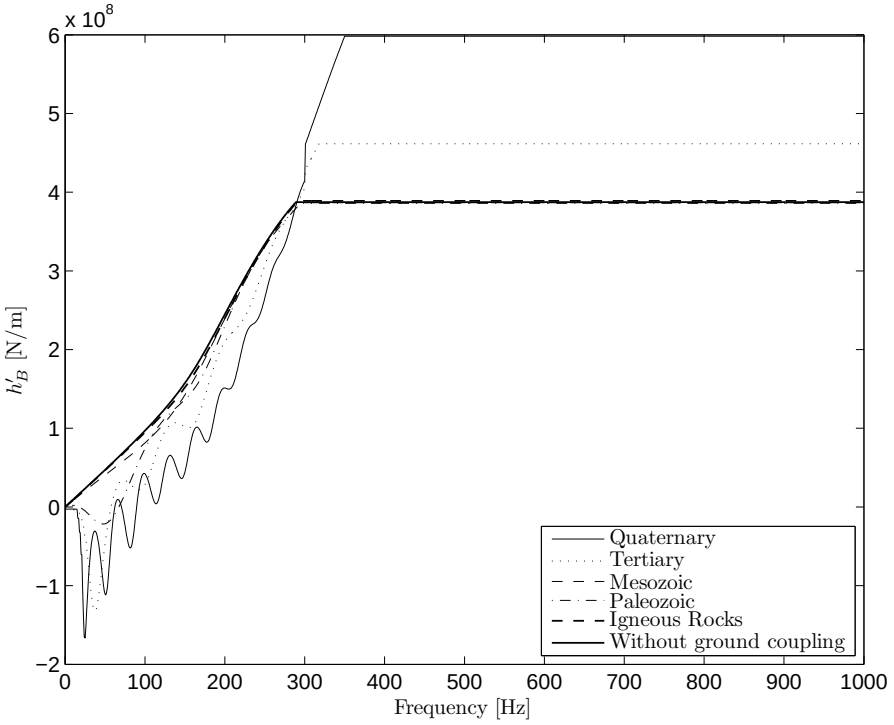


FIGURE C.112: Ballast equivalent structural damping as a function of the frequency for Case 4 (see Tables 4.1, 4.2 and 4.3) and for five different subgrade parameters of the Table 3.1.

## C.3 Subgrade influence on the response of the wheel/rail contact dynamics

### C.3.1 Subgrade influence on the wheel response

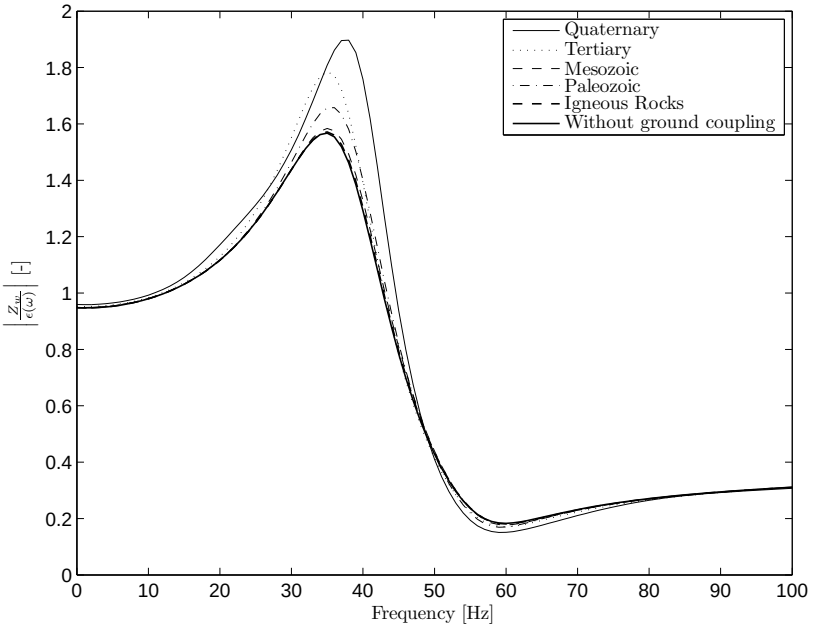


FIGURE C.113: Module of the transfer function between the wheel vertical displacement and the roughness excitation for Case 1 (see Tables 4.1, 4.2 and 4.3) and for five different subgrade parameters of the Table 3.1.

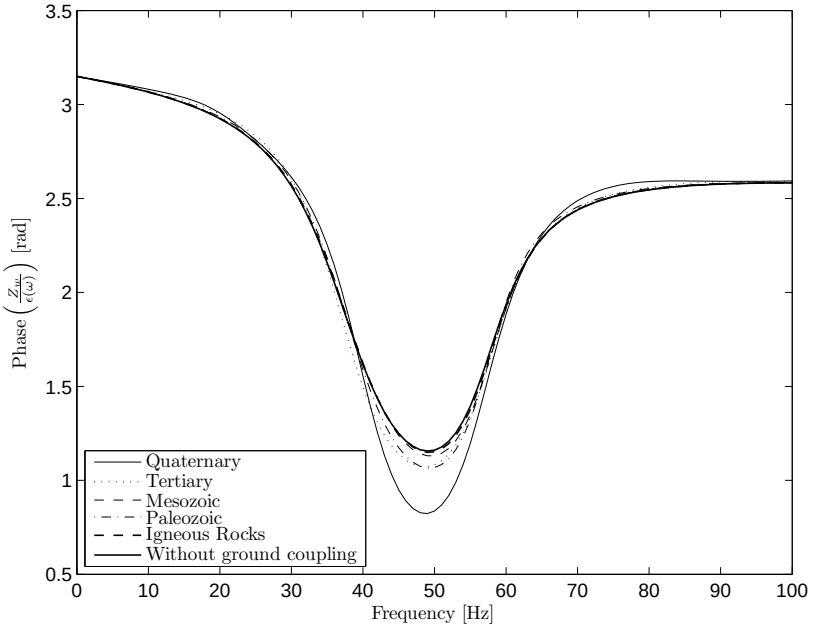


FIGURE C.114: Phase of the transfer function between the wheel vertical displacement and the roughness excitation for Case 1 (see Tables 4.1, 4.2 and 4.3) and for five different subgrade parameters of the Table 3.1.

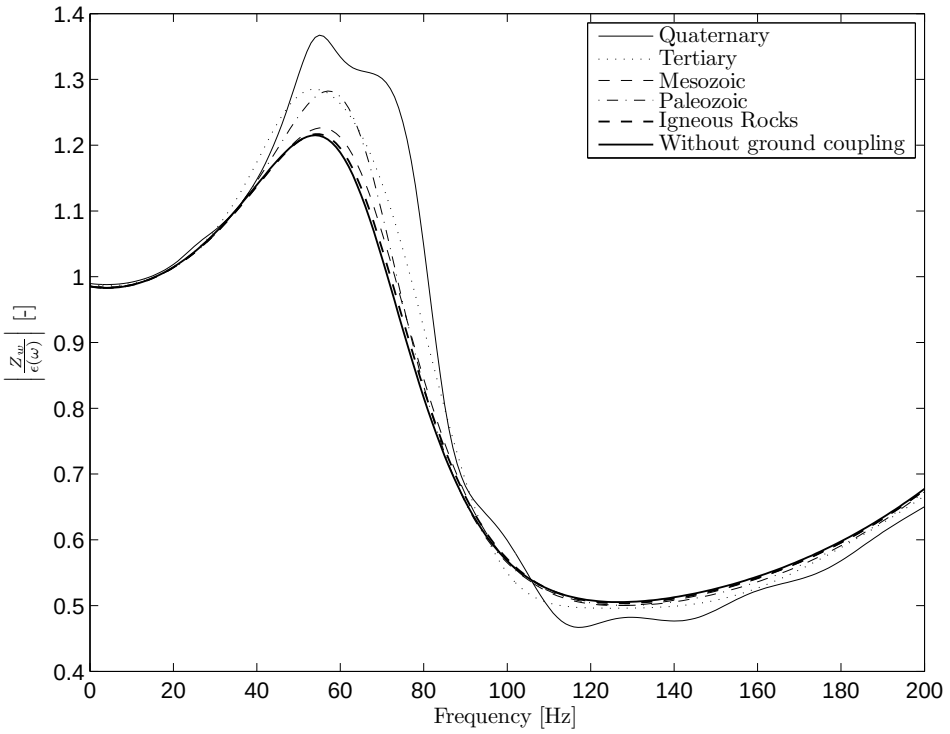


FIGURE C.115: Module of the transfer function between the wheel vertical displacement and the roughness excitation for Case 2 (see Tables 4.1, 4.2 and 4.3) and for five different subgrade parameters of the Table 3.1.

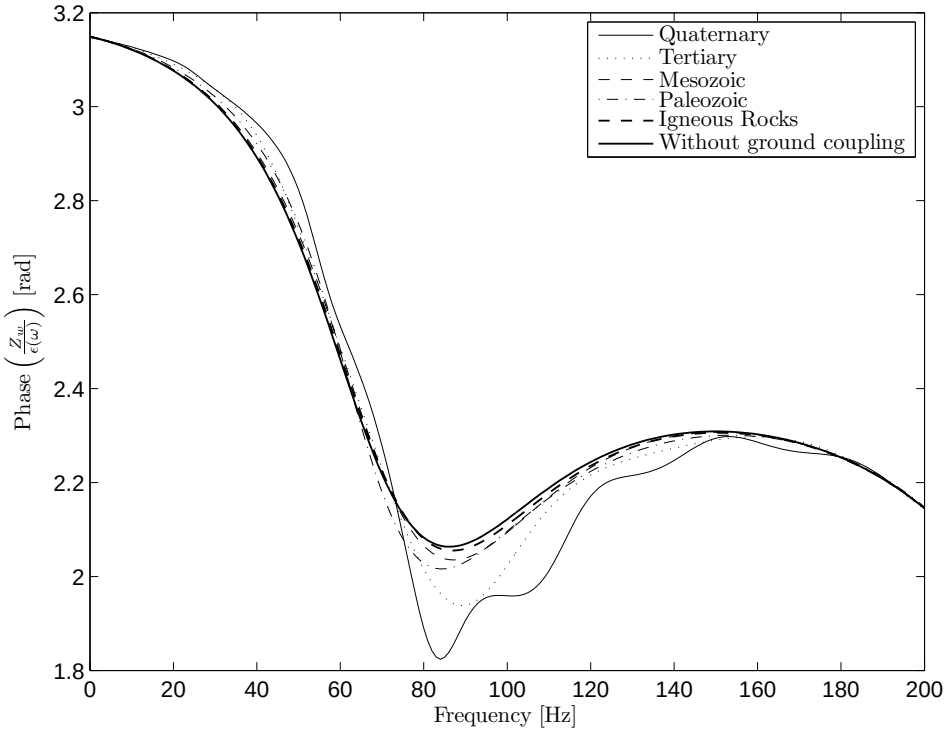


FIGURE C.116: Phase of the transfer function between the wheel vertical displacement and the roughness excitation for Case 2 (see Tables 4.1, 4.2 and 4.3) and for five different subgrade parameters of the Table 3.1.

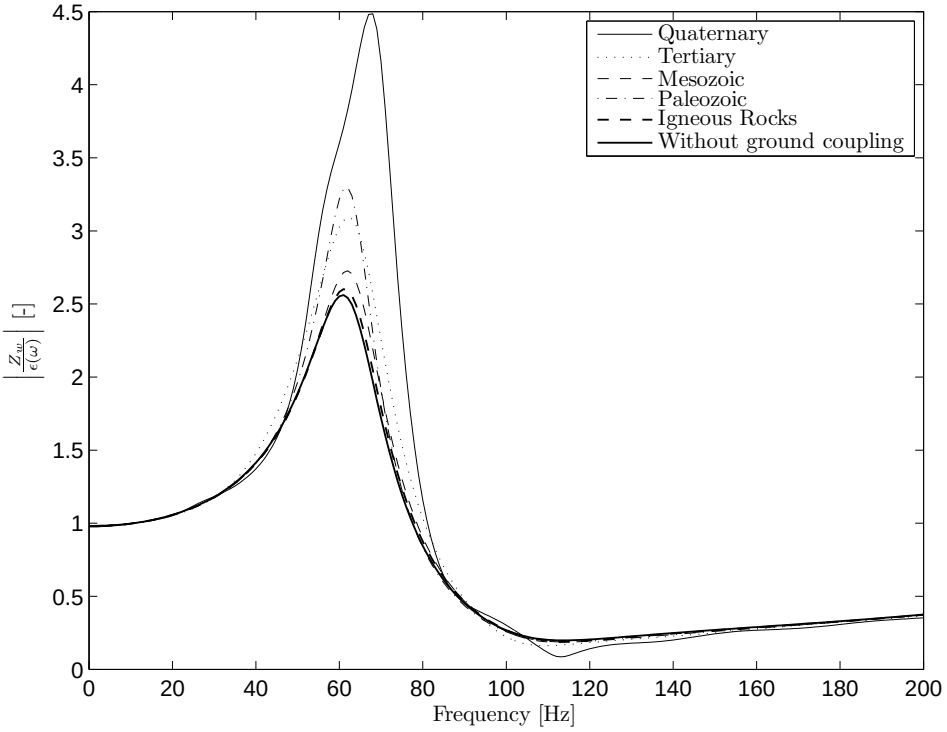


FIGURE C.117: Module of the transfer function between the wheel vertical displacement and the roughness excitation for Case 3 (see Tables 4.1, 4.2 and 4.3) and for five different subgrade parameters of the Table 3.1.

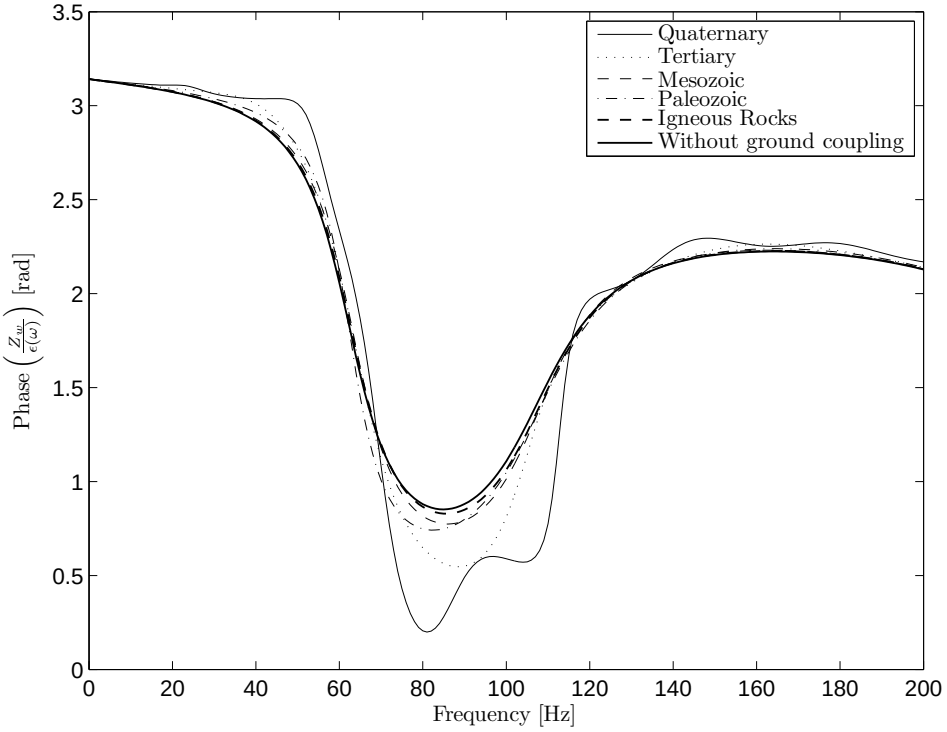


FIGURE C.118: Phase of the transfer function between the wheel vertical displacement and the roughness excitation for Case 3 (see Tables 4.1, 4.2 and 4.3) and for five different subgrade parameters of the Table 3.1.

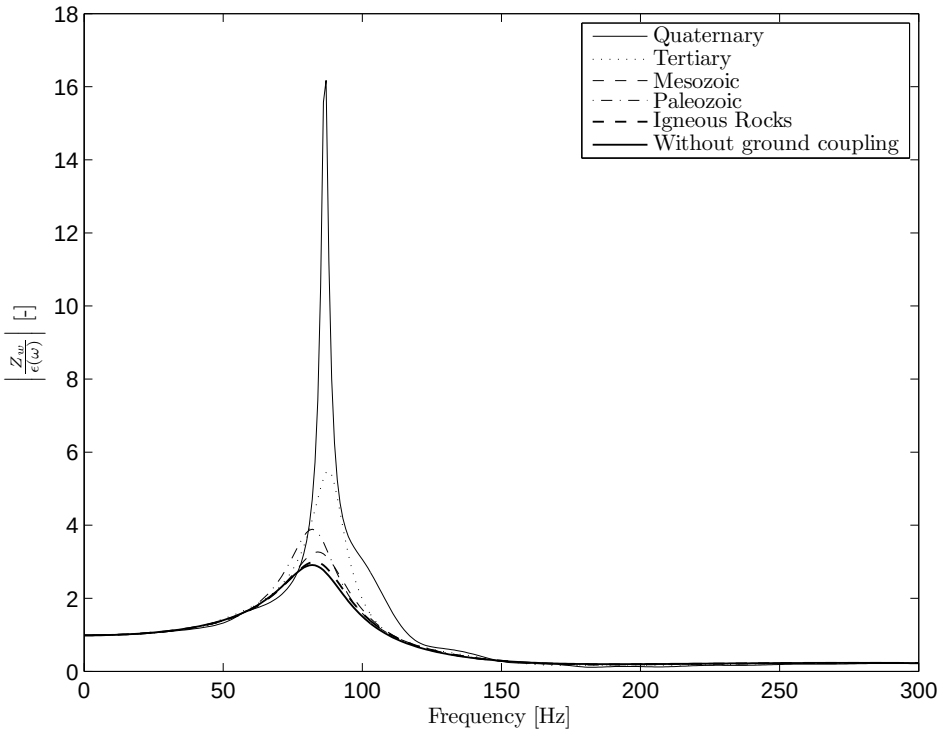


FIGURE C.119: Module of the transfer function between the wheel vertical displacement and the roughness excitation for Case 4 (see Tables 4.1, 4.2 and 4.3) and for five different subgrade parameters of the Table 3.1.

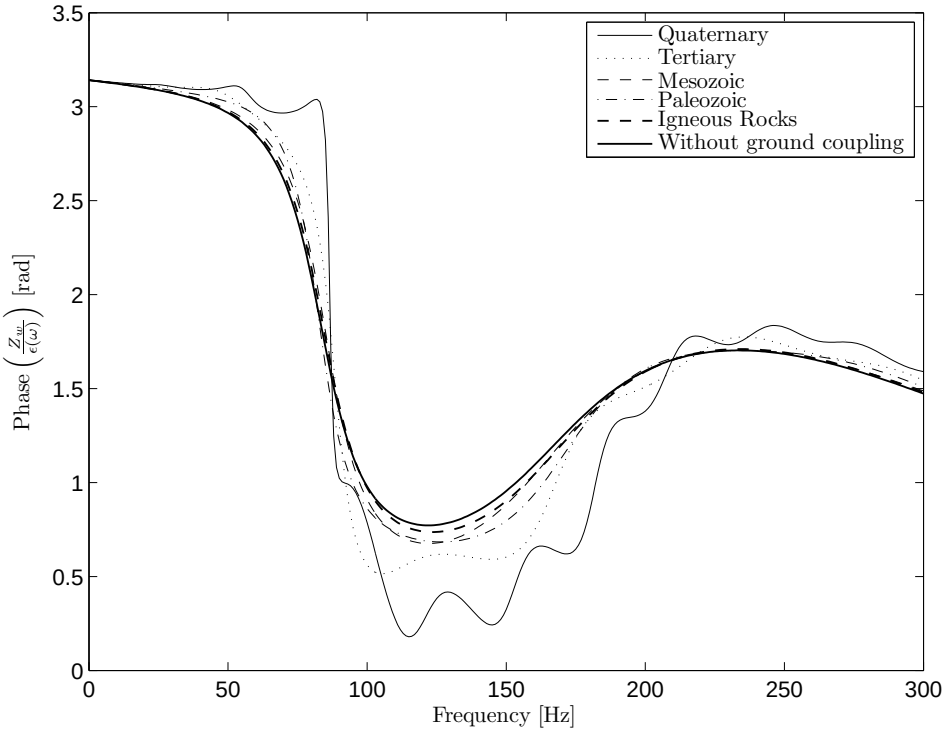


FIGURE C.120: Phase of the transfer function between the wheel vertical displacement and the roughness excitation for Case 4 (see Tables 4.1, 4.2 and 4.3) and for five different subgrade parameters of the Table 3.1.

### C.3.2 Subgrade influence on the rail response

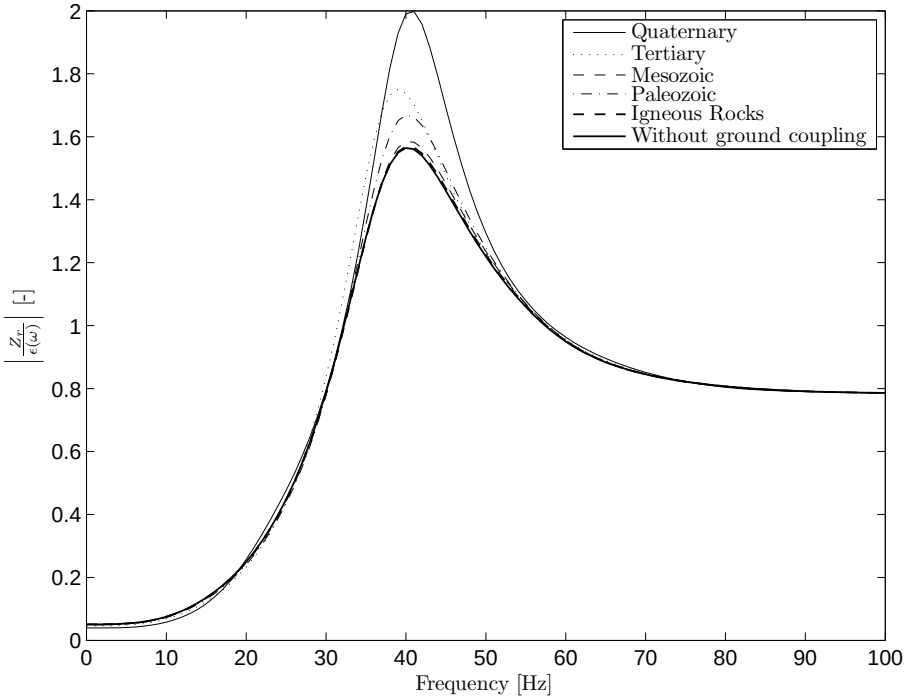


FIGURE C.121: Module of the transfer function between the rail vertical displacement and the roughness excitation for Case 1 (see Tables 4.1, 4.2 and 4.3) and for five different subgrade parameters of the Table 3.1.

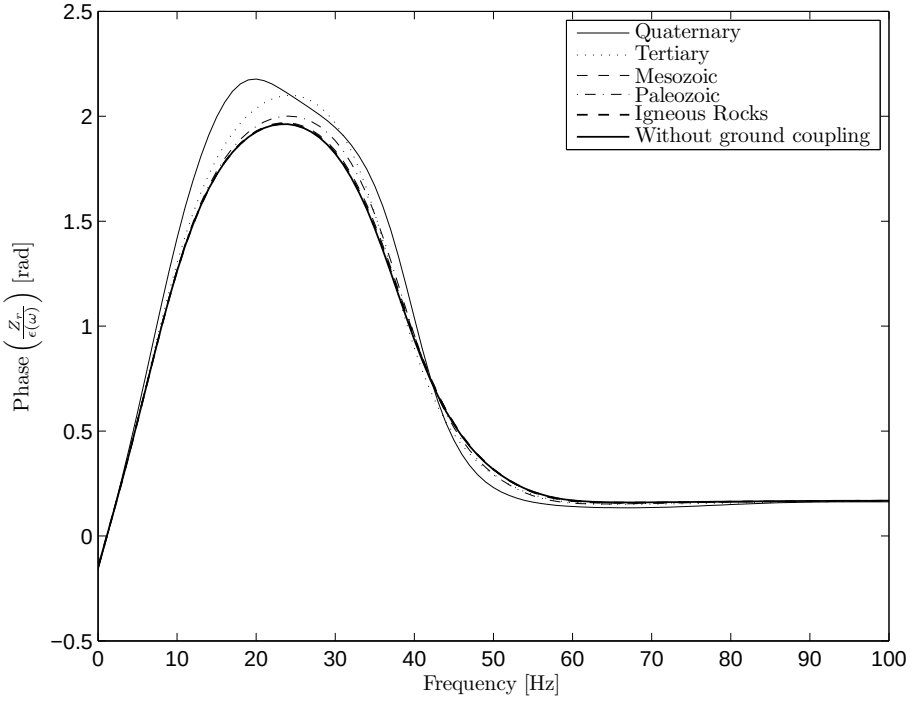


FIGURE C.122: Phase of the transfer function between the rail vertical displacement and the roughness excitation for Case 1 (see Tables 4.1, 4.2 and 4.3) and for five different subgrade parameters of the Table 3.1.

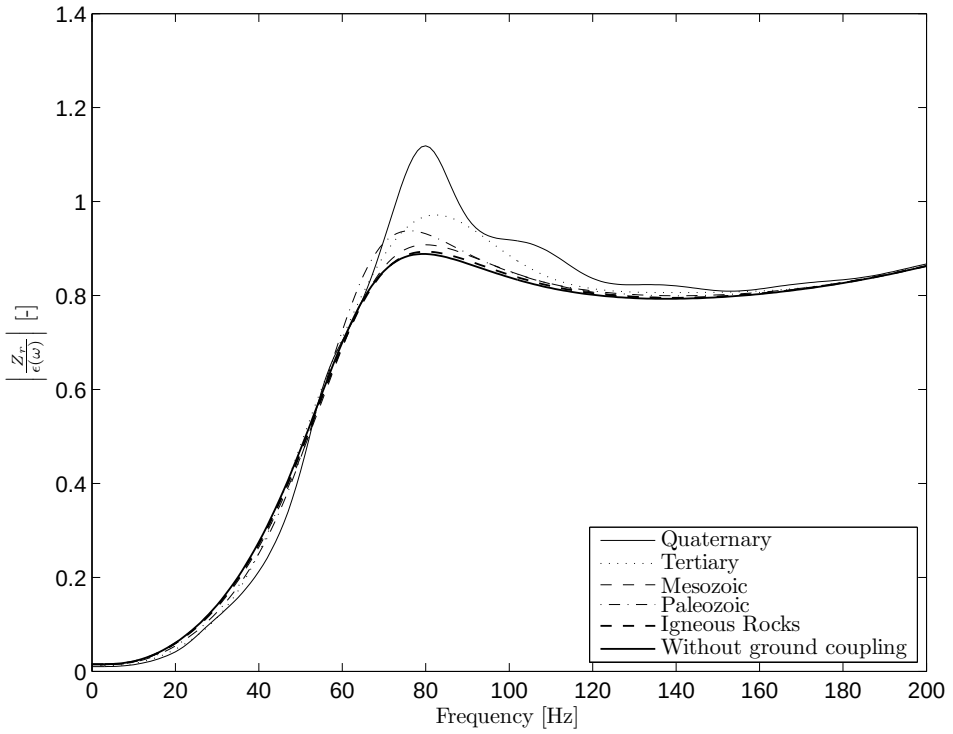


FIGURE C.123: Module of the transfer function between the rail vertical displacement and the roughness excitation for Case 2 (see Tables 4.1, 4.2 and 4.3) and for five different subgrade parameters of the Table 3.1.

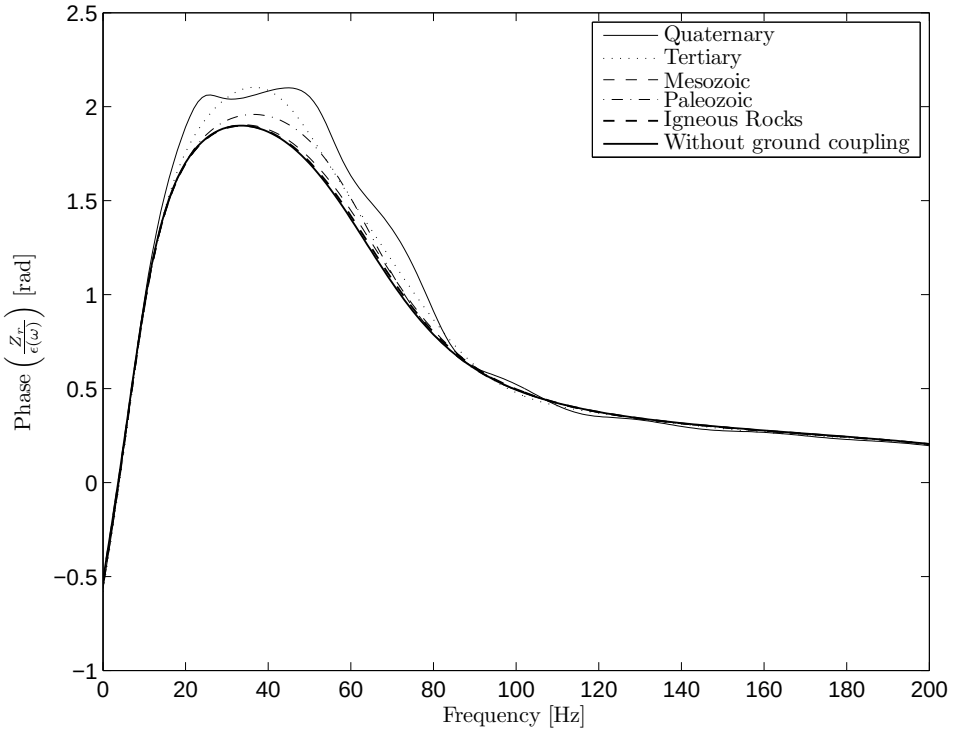


FIGURE C.124: Phase of the transfer function between the rail vertical displacement and the roughness excitation for Case 2 (see Tables 4.1, 4.2 and 4.3) and for five different subgrade parameters of the Table 3.1.

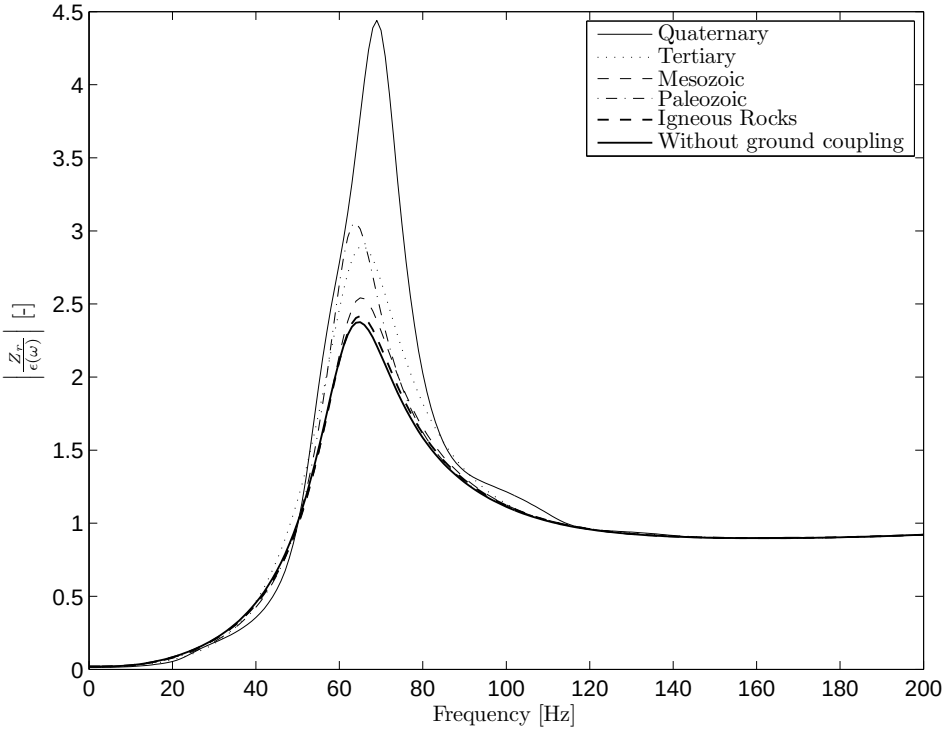


FIGURE C.125: Module of the transfer function between the rail vertical displacement and the roughness excitation for Case 3 (see Tables 4.1, 4.2 and 4.3) and for five different subgrade parameters of the Table 3.1.

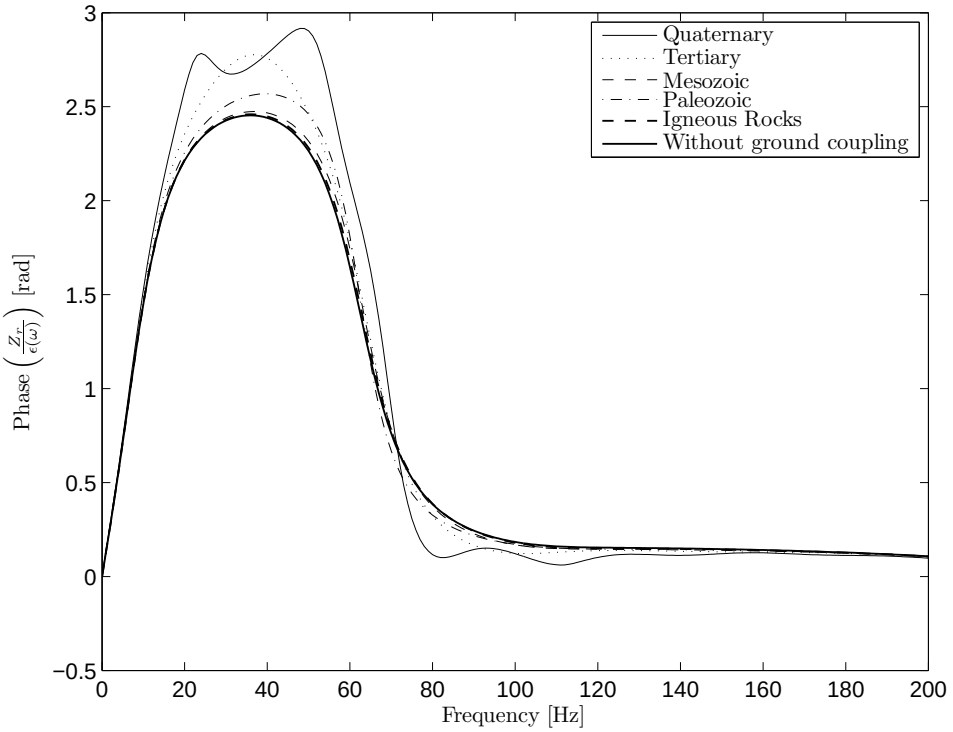


FIGURE C.126: Phase of the transfer function between the rail vertical displacement and the roughness excitation for Case 3 (see Tables 4.1, 4.2 and 4.3) and for five different subgrade parameters of the Table 3.1.

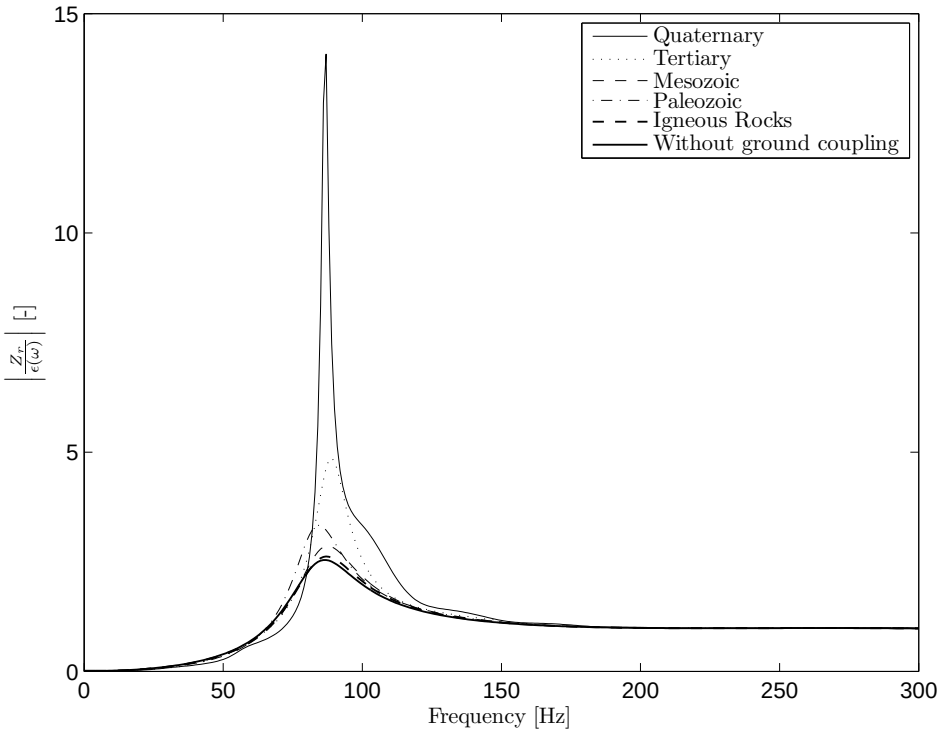


FIGURE C.127: Module of the transfer function between the rail vertical displacement and the roughness excitation for Case 4 (see Tables 4.1, 4.2 and 4.3) and for five different subgrade parameters of the Table 3.1.

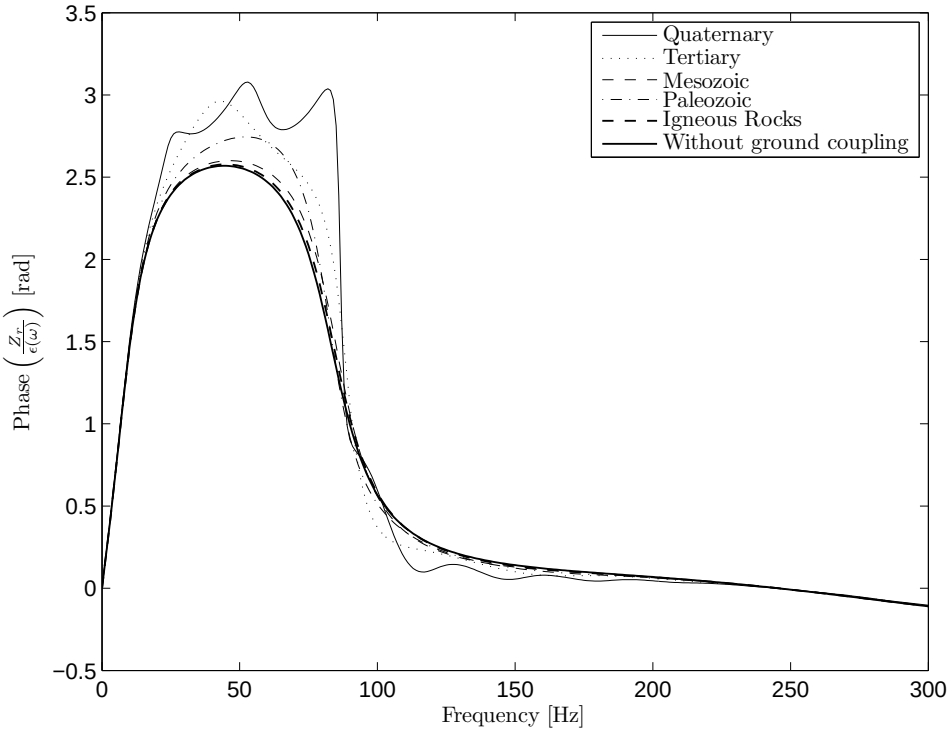


FIGURE C.128: Phase of the transfer function between the rail vertical displacement and the roughness excitation for Case 4 (see Tables 4.1, 4.2 and 4.3) and for five different subgrade parameters of the Table 3.1.

### C.3.3 Subgrade influence on the wheel/rail contact force

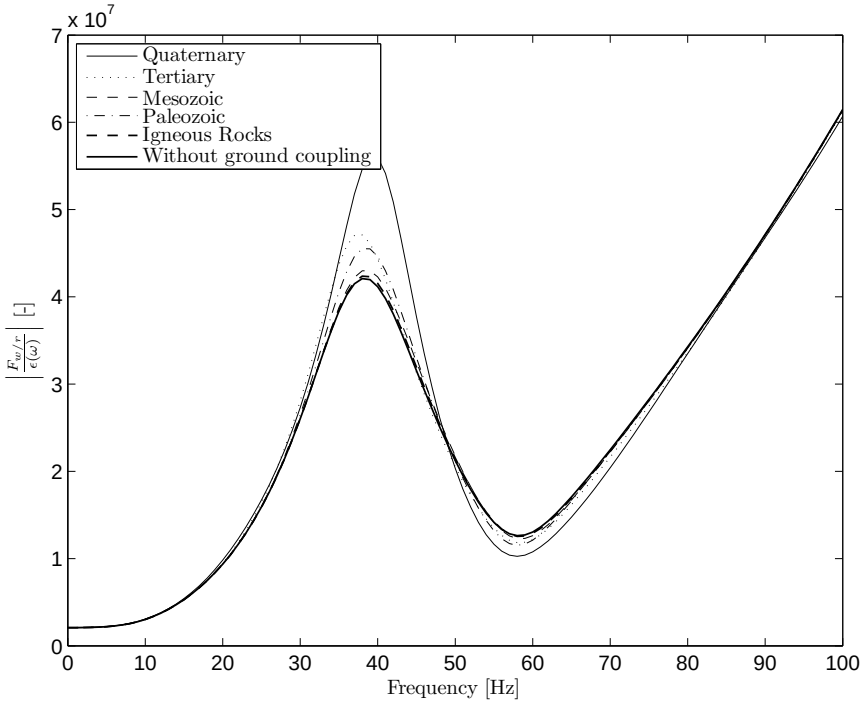


FIGURE C.129: Module of the transfer function between the wheel/rail dynamic contact force and the roughness excitation for Case 1 (see Tables 4.1, 4.2 and 4.3) and for five different subgrade parameters of the Table 3.1.

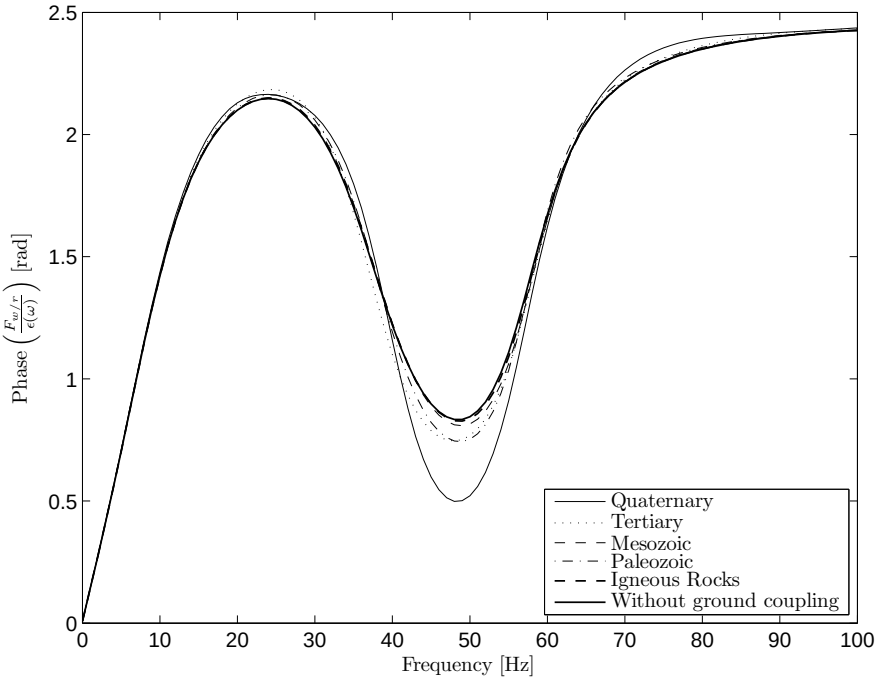


FIGURE C.130: Phase of the transfer function between the wheel/rail dynamic contact force and the roughness excitation for Case 1 (see Tables 4.1, 4.2 and 4.3) and for five different subgrade parameters of the Table 3.1.

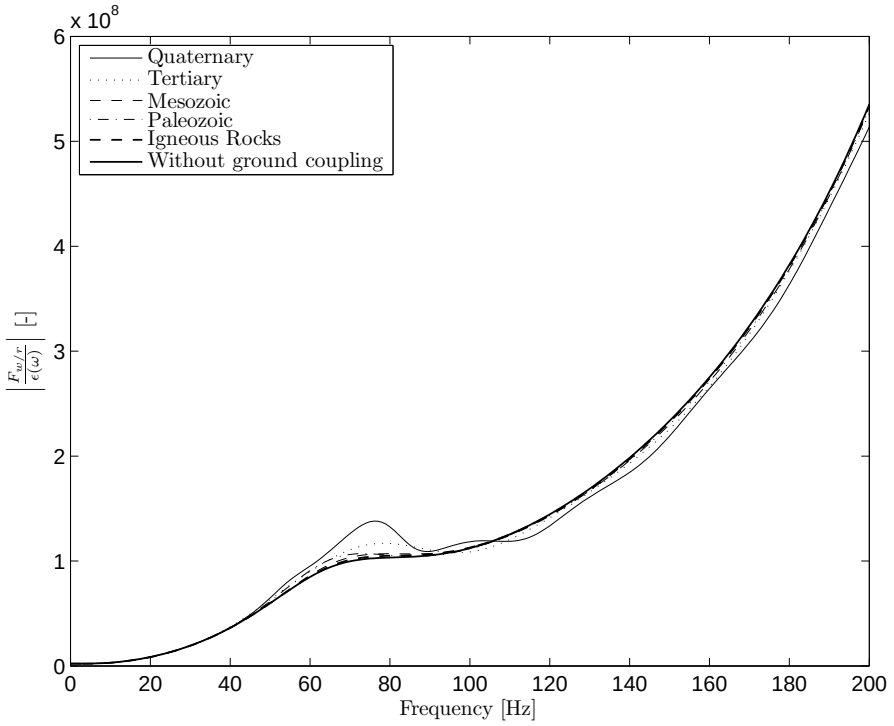


FIGURE C.131: Module of the transfer function between the wheel/rail dynamic contact force and the roughness excitation for Case 2 (see Tables 4.1, 4.2 and 4.3) and for five different subgrade parameters of the Table 3.1.

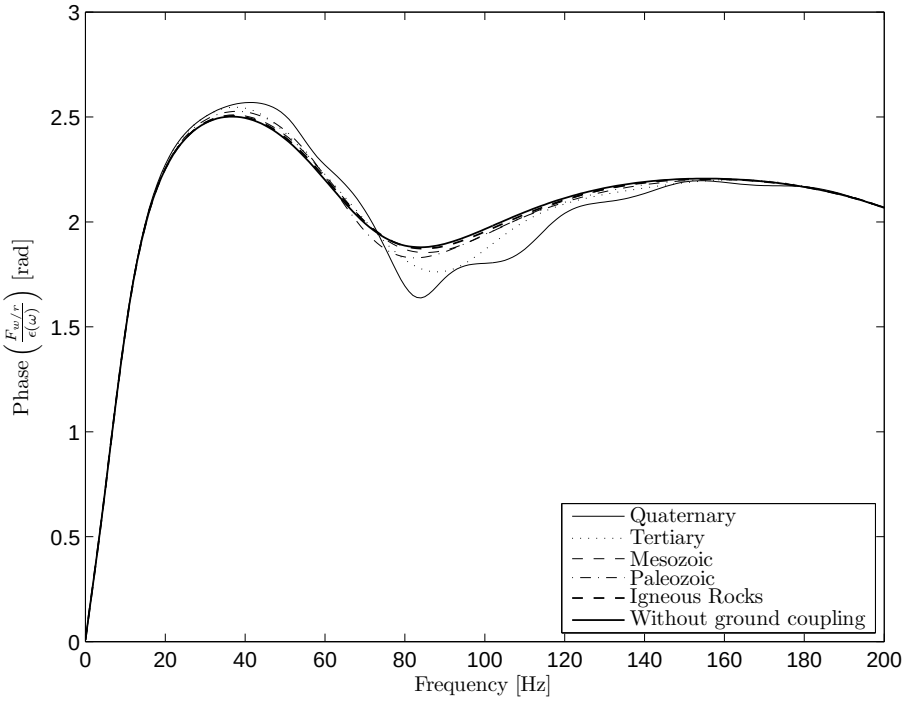


FIGURE C.132: Phase of the transfer function between the wheel/rail dynamic contact force and the roughness excitation for Case 2 (see Tables 4.1, 4.2 and 4.3) and for five different subgrade parameters of the Table 3.1.

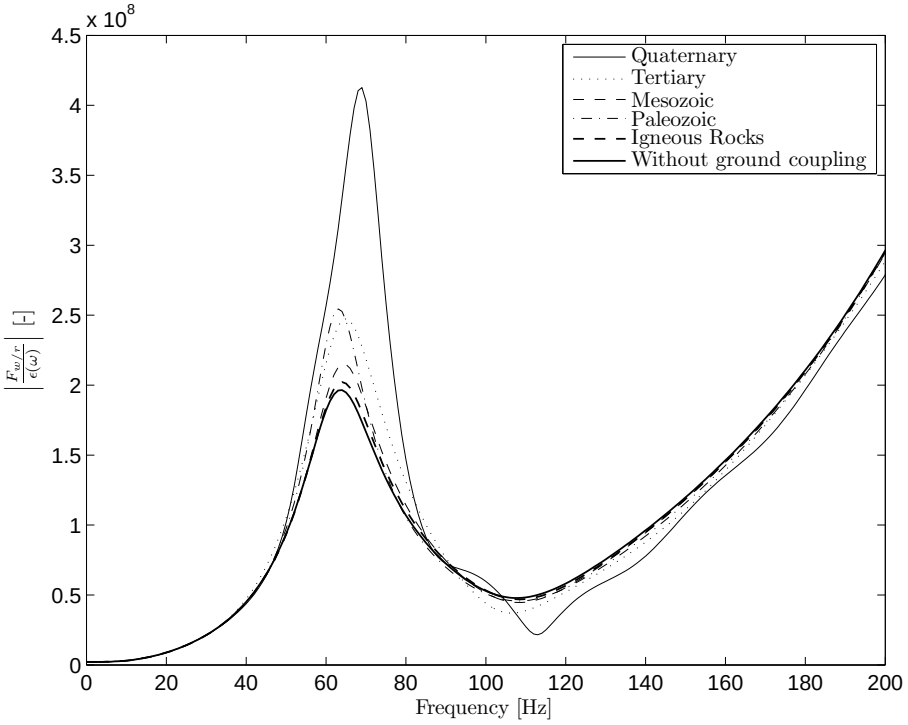


FIGURE C.133: Module of the transfer function between the wheel/rail dynamic contact force and the roughness excitation for Case 3 (see Tables 4.1, 4.2 and 4.3) and for five different subgrade parameters of the Table 3.1.

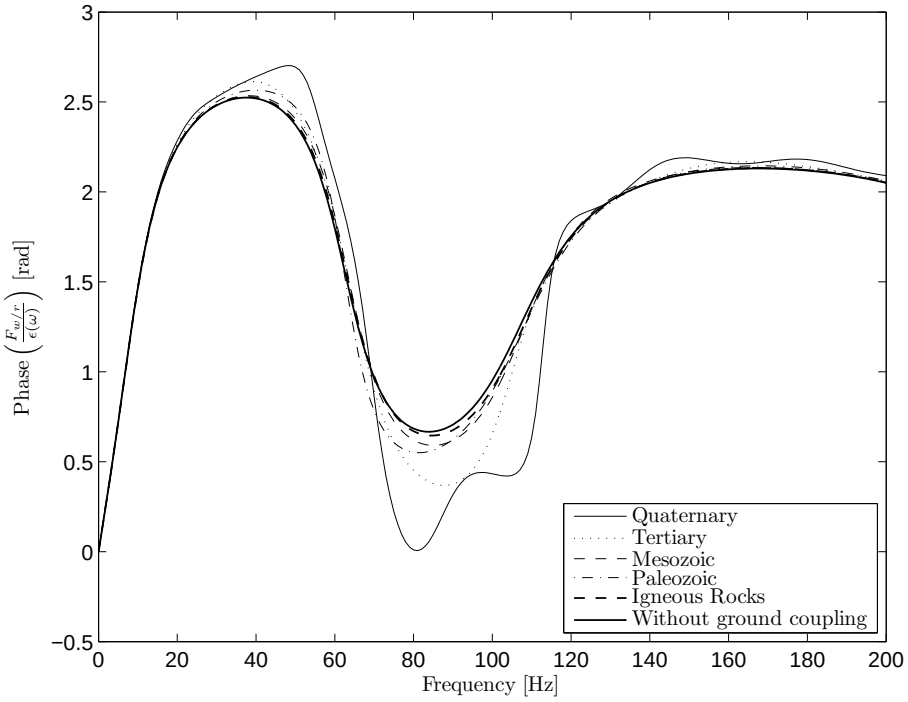


FIGURE C.134: Phase of the transfer function between the wheel/rail dynamic contact force and the roughness excitation for Case 3 (see Tables 4.1, 4.2 and 4.3) and for five different subgrade parameters of the Table 3.1.

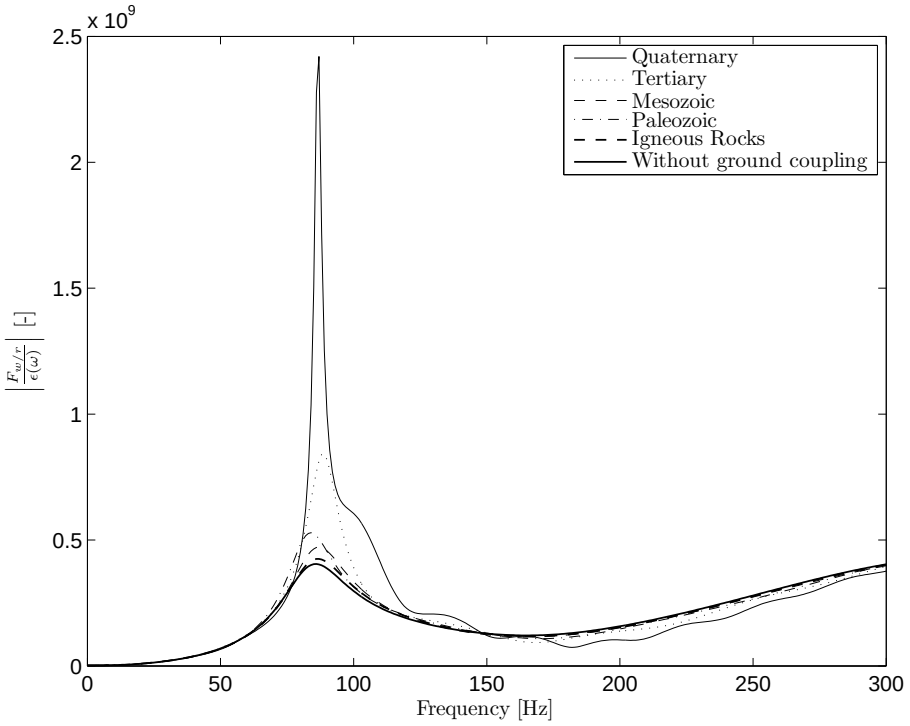


FIGURE C.135: Module of the transfer function between the wheel/rail dynamic contact force and the roughness excitation for Case 4 (see Tables 4.1, 4.2 and 4.3) and for five different subgrade parameters of the Table 3.1.

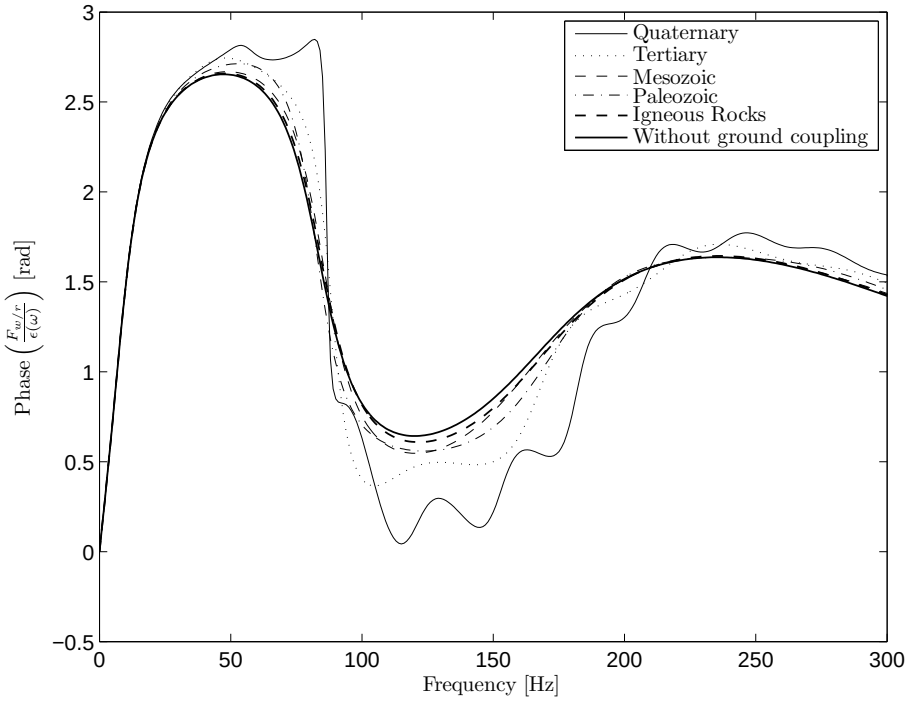


FIGURE C.136: Phase of the transfer function between the wheel/rail dynamic contact force and the roughness excitation for Case 4 (see Tables 4.1, 4.2 and 4.3) and for five different subgrade parameters of the Table 3.1.

# Appendix D

# Determination of the superstructure/subgrade contact width

In Chapter 4, the superstructure for a single railway is assumed as an infinite strip load, of width $2c$, that acts on the surface of the subgrade. In this appendix the possible range of values of this width is deduced for the case of ballasted tracks.

As shown in [199], it can be assumed that the load transmitted from a sleeper to the ballast approximately coincides with a cone distribution. The stresses of the ballast are uniformly distributed over this cone region and they are null outside the cone. The dimensions of this cone in the subgrade contact determine the effective contact area between the ballast and the subgrade.

In Fig. D.1 the variables involved in the problem are presented, where $\alpha_B$ is the ballast stress distribution angle, $d_B$ is the depth of the ballast, $l_e$ is the effective supporting length of half sleeper on the ballast, $l_{es}$ is the effective supporting length of half sleeper on the subgrade and $l_c$ is the distance between the centres of the rail heads.

For this model, the width of the ballast/subgrade interaction area is

$$2c = 2d_B \tan\alpha_B + l_e + l_c = l_{es} + l_c \tag{D.1}$$

In Table D.1, the possible values of the variables inside Eq. (D.1) are presented.

where the variation of $l_{es}$ are calculated using $l_{es} = 2d_B \tan\alpha_B + l_e$ and where $d_B$ also contains the sub-ballast.

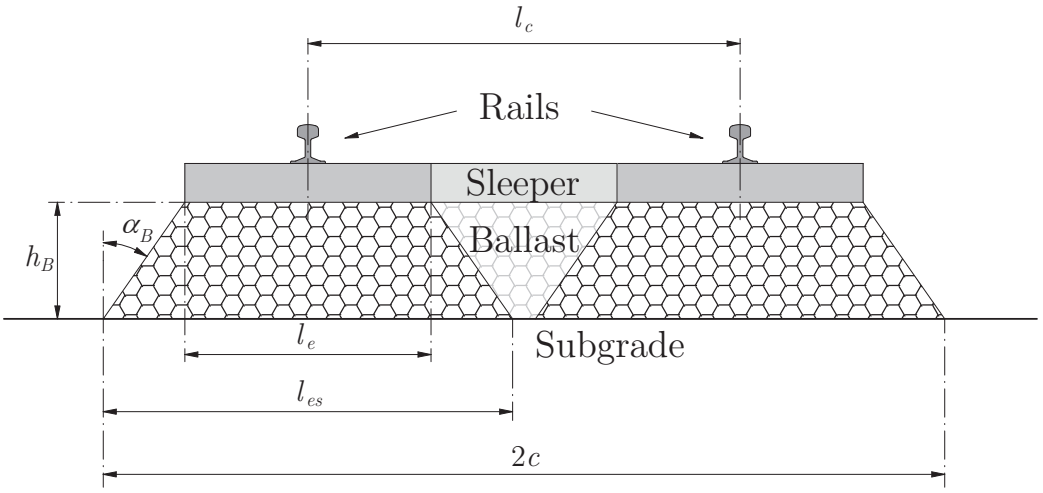


FIGURE D.1: Stresses transmitted through the ballast in the cross-sectional area of the track.

| Variable | Range of values |
|---|---|
| $\alpha_B$ | 30°-45° |
| $d_B$ | 0.3-0.7 m |
| $l_e$ | 0.7-1.27 m |
| $l_{es}$ | 1-2.7 m |
| $l_c$ | 1.505-1.743 m |

TABLE D.1: Range of values of the variables inside Eq. (D.1). Source: [3]

From these ranges of values, the width of the effective superstructure/subgrade interaction area ranges approximately between 2.5 and 4.5 m, by the application of Eq. (D.1).

# Bibliography


[1] J. Otero. *Contribución de las vibraciones producidas por el contacto rueda-carril y su transmisión al entorno.* PhD thesis, Technical University of Catalonia (UPC), 2009.

[2] W.M. Zhai and Z. Cai. Dynamic interaction between a lumped mass vehicle and a discretely supported continuous rail track. *Computers and Structures*, 63(5): 987–997, 1997.

[3] A. López Pita. *Infraestructuras ferroviarias.* Edicions UPC, Barcelona, 1st edition, 2006.

[4] *ISO 14837-1:2005 Mechanical vibration. Ground-borne noise and vibration arising from rail systems. Part 1: General Guidance.* International Organization for Standardization, 2005.

[5] A. Zach. Vibration insulation research results in switzerland. *Journal of Sound and Vibration*, 231(3):877–882, 2000.

[6] *Directive 2002/49/EC. Assessment and management of envionmental noise.* European Parliament, 2002. Council of 25 of June 2002 relating to the assessment and management of environmental noise.

[7] C. Madshus, B. Beassason, and L. Harvik. Prediction model for low frequency vibration from high speed railways on soft grounds. *Journal of Sound and Vibration*, 193(1):195–203, 1996.

[8] H. Kuppelwieser and A. Ziegler. A tool for predicting vibration and structure-borne noise immissions caused by railways. *Journal of Sound and Vibration*, 193 (1):261–267, 1996.

[9] C. With, M. Bahrekazemi, and A. Bodare. Validation of an empirical model for prediction of train-induced ground vibrations. *Soil dynamics and Earthquake engineering*, 26(11):983–990, 2006.

[10] R.A. Hood, R.J. Greer, M. Breslin, and P.R. Williams. The calculation and assessment of ground-borne noise and perceptible vibration from trains in tunnels. *Journal of Sound and Vibration*, 193(1):215–225, 1996.

[11] H.E.M. Hunt. Modelling of rail vehicles and track for calculation of ground-vibration transmission into buildings. *Journal of Sound and Vibration*, 193(1): 185–194, 1996.

[12] C.J.C. Jones and J.R. Block. Prediction of ground vibration from freight trains. *Journal of Sound and Vibration*, 193(1):205–213, 1996.

[13] C.E. Hanson, D.A. Towers, and L.D. Meister. *Transit noise and vibration impact assessment*. U.S. Department of Transportation, Federal transit administration, 2006.

[14] H.H. Hung and Y.B. Yang. A review of researches on ground-borne vibrations with emphasis on those induced by trains. *Proceedings of National Science Council*, 25 (1):1–16, 2001.

[15] T.G. Gutowski and C.L. Dym. Propagation of ground vibration. *Journal of Sound and Vibration*, 49(2):179–193, 1976.

[16] G. Lombaert and G. Degrande. Ground-borne vibration due to static and dynamic axle loads of Intercity and high-speed trains. *Journal of Sound and Vibration*, 319 (3-5):1036–1066, 2009.

[17] S. Gupta and G. Degrande. Modelling of continuous and discontinuous floating slab tracks in a tunnel using a periodic approach. *Journal of Sound and Vibration*, 329(1):1101–1125, 2010.

[18] X. Sheng, C.J.C. Jones, and D.J. Thompson. A comparison of a theoretical model for quasi-statically and dynamically induced environmental vibration from trains with measurements. *Journal of Sound and Vibration*, 267(3):621–635, 2003.

[19] C. Madshus and A.M. Kaynia. High-speed railway lines on soft ground: Dynamic behaviour at critical train speed. *Journal of Sound and Vibration*, 231(3):689–701, 2000.

[20] K.L. Knothe and S.L. Grassie. Modelling of railway track and vehicles/track interaction at high frequencies. *Vehicle System Dynamics*, 22(3-4):209–262, 1993.

[21] A. Johansson, J.C.O. Nielsen, R. Bolmsvik, AA. Karlsträm, and R. Lundén. Under sleeper pads - Influence on dynamic train-track interaction. *WEAR*, 265(9-10): 1479–1487, 2008.

[22] S. Kaewunruen and A.M. Remennikov. Field trials for dynamic characteristics of railway track and its components using impact excitation technique. *NDT and E International*, 40(7):510–519, 2007.

[23] C. Guigou-Carter, M. Villot, B. Guillerme, and C. Petit. Analytical and experimental study of sleeper SAT S 312 in slab track Sateba system. *Journal of Sound and Vibration*, 293(3-5):878–887, 2006.

[24] J. Maes, H. Sol, and P. Guillaume. Measurements of the dynamic railpad properties. *Journal of Sound and Vibration*, 293(3-5):557–565, 2006.

[25] M. Heckl, G. Hauck, and R. Wettschureck. Structure-borne sound and vibration from rail traffic. *Journal of Sound and Vibration*, 193(1):175–184, 1996.

[26] G. Degrande and G. Lombaert. An efficient formulation of Krylov's prediction model for train induced vibrations based on the dynamic reciprocity theorem. *Journal of Acoustical Society of America*, 110(3):1379–1390, 2001.

[27] E. Celebi. Three-dimensional modelling of train-track and sub-soil analysis for surface vibrations due to moving loads. *Applied Mathematics and Computation*, 179(1):209–230, 2006.

[28] X. Sheng, C.J.C. Jones, and M. Petyt. Ground vibration generated by load moving along railway track. *Journal of Sound and Vibration*, 228(1):129–156, 1999.

[29] X. Sheng, C.J.C. Jones, and M. Petyt. Ground vibration generated by a harmonic load acting on a railway track. *Journal of Sound and Vibration*, 225(1):3–28, 1999.

[30] K. Knothe and Y. Wu. Receptance behaviour of railway track and subgrade. *Archive of Applied mechanics*, 68(7-8):457–470, 1998.

[31] V.V. Krylov, A.R. Dawson, M.E. Heelis, and A.C. Collop. Rail movement and ground waves caused by high-speed trains approaching track-soil critical velocities. *Proceedings of the Institution of Mechanical Engineers, Part F-Journal of Rail and Rapid Transit*, 214(2):107–116, 2000.

[32] S. Bruni, I. Anastasopoulos, S. Alfi, A. Van Leuven, and G. Gazetas. Effects of train impacts on urban turnouts: Modelling and validation through measurements. *Journal of Sound and Vibration*, 324(3-5):666–689, 2009.

[33] *ISO 2631-1:1997 Mechanical vibration and shock. Evaluation of human exposure to whole-body vibration. Part 1: General requeriments.* International Organization for Standardization, 1997.

[34] *ISO 2631-2:2003 Mechanical vibration and shock. Evaluation of human exposure to whole-body vibration. Part 2: Vibration in buildings (1 Hz to 80 Hz)*. International Organization for Standardization, 2003.

[35] T.X. Wu and D.J. Thompson. A double Timoshenko beam model for vertical vibration analysis of railway track at high frequencies. *Journal of Sound and Vibration*, 224(2):329–348, 1999.

[36] D.J. Thompson. Wheel-rail noise generation, part 1: Introduction and interaction model. *Journal of Sound and Vibration*, 161(3):387–400, 1993.

[37] D.J. Thompson. Wheel-rail noise generation, part 2: Wheel vibration. *Journal of Sound and Vibration*, 161(3):401–419, 1993.

[38] D.J. Thompson. Wheel-rail noise generation, part 3: Rail vibration. *Journal of Sound and Vibration*, 161(3):421–446, 1993.

[39] D.J. Thompson. *Wheel-rail noise: theoretical modelling of the generation of vibrations*. PhD thesis, University of Southampton, 1990.

[40] D.J. Thompson, B. Hemsworth, and N. Vincent. Experimental validation of TWINS prediction program for rolling noise, Part 1: Description of the model and method. *Journal of Sound and Vibration*, 193(1):123–135, 1996.

[41] D.J. Thompson, P. Fodiman, and H. Mahé. Experimental validation of TWINS prediction program for rolling noise, Part 2: Results. *Journal of Sound and Vibration*, 193(1):137–147, 1996.

[42] R.A. Clark, P.A. Dean, J.A. Elkins, and S.G. Newton. An investigation into the dynamic effects of railway vehicles running on corrugated rails. *Journal of Mechanical Engineering Science*, 24(1):65–76, 1982.

[43] P. Van den Broek and G. De Roeck. The vertical receptance of track including soil-structure interaction. structural dynamics. In *Structural dynamics*, volume 1-2, pages 837–842, 1999. 4th European Conference on Structural Dynamics (EURODYN 99), Prague, Czech Republic.

[44] L. Auersch. The excitation of ground vibration by rail traffic: theory of vehicle-track-soil interaction and measurements on high-speed lines. *Journal of Sound and Vibration*, 284(1-2):103–677, 2005.

[45] X. Sheng, C.J.C. Jones, and D.J. Thompson. A theoretical model for ground vibration from trains generated by vertical track irregularities. *Journal of Sound and Vibration*, 272(3-5):937–965, 2004.

[46] G. Lombaert, G. Degrande, and D. Cloteau. Numerical modelling of free field traffic-induced. *Soil Dynamics and Earthquake Engineering*, 19(7):473–488, 2000.

[47] G. Lombaert, G. Degrande, J. Kogut, and S. François. The experimental validation of a numerical model for the prediction of railway induced vibrations. *Journal of Sound and Vibration*, 297(3-5):512–535, 2006.

[48] S.N. Verichev and A.V. Metrikine. Instability of vibrations of a mass that moves uniformly along a beam on a periodically inhomogeneous foundation. *Journal of Sound and Vibration*, 260(5):901–925, 2003.

[49] H.A. Dieterman and A.V. Metrikine. The equivalent stiffness of a half-space interacting with a beam. critical velocities of a moving load along the beam. *European Journal of Mechanics A/Solids*, 15(1):67–90, 1996.

[50] A.V. Metrikine and H.A. Dieterman. The equivalent vertical stiffness of an elastic half-space interacting with a beam, including the shear stresses at the beam-half-space interface. *European Journal of Mechanics A/Solids*, 16(3):515–527, 1997.

[51] A.V. Metrikine and S.N. Verichev. Instability of vibrations of a moving two-mass oscillator on a flexibly supported timoshenko beam. *Journal of Sound and Vibration*, 272(3-5):937–965, 2004.

[52] A.V. Metrikine and K. Popp. Vibration of a periodically supported beam on an elastic half-space. *European Journal of Mechanics A/Solids*, 18(4):679–701, 1999.

[53] K.L. Metrikine and K. Grassie. Instability of vibrations of an oscillator moving along a beam on an elastic half-space. *European Journal of Mechanics A/Solids*, 18(2):331–349, 1993.

[54] A.V. Metrikine, S.N. Verichev, and J. Blaauwendraad. Stability of a two-mass oscillator moving on a beam supported by a visco-elastic half-space. *International Journal of solids and structures*, 42(3-4):1187–1207, 2005.

[55] S.L. Grassie, R.W. Gregory, D. Harrison, and K.L. Johnson. The dynamic response of railway track to high frequency vertical excitation. *Journal of Mechanical Engineering Science*, 24(2):77–90, 1982.

[56] J.C.O. Nielsen and A. Igeland. Vertical dynamic interaction between train and track-influence of wheel and track imperfections. *Journal of Sound and Vibration*, 187(5):825–839, 1995.

[57] D.A. Hills, D. Nowell, and A. Sackfield. *Mechanics of elastic contacts*. Butterworth-Heinemann Ltd., Oxford, 1993.

[58] T.X. Wu and D.J. Thompson. Vibration analysis of railway track with multiple wheels on the rail. *Journal of Sound and Vibration*, 239(1):69–97, 2001.

[59] A.M. Remennikov and Kaewunruen. A review of loading conditions for railway track structures due to train and track vertical interaction. *Structural control and Health monitoring*, 15(2):207–234, 2008.

[60] M.J.M.M. Steenbergen. Quantification of dynamic wheel-rail contact forces at short rail irregularities and application to measured rail welds. *Journal of Sound and Vibration*, 312(4-5):606–629, 2008.

[61] D.J. Dings and M.G. Dittrich. Roughness on dutch railway wheels and rails. *Journal of Sound and Vibration*, 193(1):103–112, 1996.

[62] P. Remington and J. Webb. Estimation of wheel/rail interaction forces in the contact area due to roughness. *Journal of Sound and Vibration*, 193(1):83–102, 1996.

[63] E. Fernández. *Contribució a l'estudi de la detecció i l'análisi de les vibracions produïdes pels bogis d'un ferrocarril*. PhD thesis, Technical University of Catalonia (UPC), 2000.

[64] S.H. Crandall and W.Q. Zhu. Random vibration: A survey of recent developments. *Journal of Applied Mechanics-Transactions of the ASME*, 50(4B):953–962, 1983.

[65] C.J. Dodds and J.D. Robson. Description of road surface-roughness. *Journal of Sound and Vibration*, 31(2):175–183, 1973.

[66] K.M.A. Kamash and J.D. Robson. Application of isotropy in road surface modelling. *Journal of Sound and Vibration*, 57(1):89–100, 1978.

[67] D.E. Newland. *An introduction to random vibration, spectral and wavelet analysis*. Dover Publications Inc., New York., 3rd edition, 1993.

[68] L. Sun. Simulation of pavement roughness and iri based on power spectral density. *Mathematics and Computers in simulation*, 61(2):77–88, 2003.

[69] *ISO 3095:2005 Railway applications - Acoustics - Measurement of noise emitted by railbound vehicles*. International Organization for Standardization, 2005.

[70] *ISO 3381:2005 Railway applications - Acoustics - Measurement of noise inside railbound vehicles*. International Organization for Standardization, 2005.

[71] B.E Croft, Jones C.J.C., and D.J. Thompson. Modelling the effect of rail dampers on wheel-rail interaction forces and rail roughness growth rates. *Journal of Sound and Vibration*, 323(4-5):17–32, 2009.

[72] T.D. Armstrong and D.J. Thompson. Use a reduced scale model for the study of wheel/rail interaction. *Proceedings of the Institution of mechanical engineers. Part F-Journal of Rail and Rapid Transit*, 220(3):235–246, 2006.

[73] A. Shinozuka and C.M. Jan. Digital simulation of random processes and its applications. *Journal of Sound and Vibration*, 25(1):111–128, 1972.

[74] S. Cardona, E. Fernández-Díaz, M.A. de los Santos, and J.L. Tejedo. Simple model for the time history of the ground vibrations generated by underground trains as the means of monitoring the riding quality of the wheels of a bogie. *Vehicle system dynamics*, 33(6):421–434, 2000.

[75] J. Otero, J. Martínez, M.A. de los Santos, and S. Cardona. Modelo global de la dinmica de contacto rueda-carril para determinar la vibracin de un punto del carril al paso de un tren. *Scientia et Technica*, 13(34):207–212, 2007.

[76] J. Martínez, M.A. de los Santos, and S. Cardona. A convolution method to determine the dynamic response in a railway track submitted to a moving vertical excitation. *Machine Vibration*, 4:142–146, 1995.

[77] M.A. de los Santos, J. Martínez, and S. Cardona. A convolution application to determine the dynamic response of a railway track. *Mechanical systems and Signal processing*, 9(6):707–708, 1995.

[78] F.G. Graff. *Wave motion in elastic solids*. Dover publications Inc., 1975.

[79] H. Lamb. On the propagation of tremors over the surface of an elastic solid. *Philosophical transactions of the Royal Society of London Series A-Containing papers of a mathematical or physical character*, 203:1–42, 1904.

[80] W.M. Ewing, W.S. Jardetzky, and F. Press. *Elastic waves in layered media*. McGraw-Hill, 1957.

[81] N.A. Haskell. Radiation pattern of surface waves from point sources in a multilayered medium. *Bulletin of the Seismological Society of America*, 54(1):377–393, 1964.

[82] Schröder C.T. and R.S. Waymond. On the complex conjugate roots of the Rayleigh equation: The leaky surface wave. *Journal of the Acoustical Society of America*, 110(6):2867–2877, 2001.

[83] G.F. Miller and H. Pursey. On the partition of energy between elastic waves in a semi-infinite solid. *Proceedings of the royal society of London Series A-Mathematical and physical sciences*, 233(1192):55–69, 1955.

[84] G.F. Miller and H. Pursey. The field and radiation impedance of mechanical radiators on the free surface of semi-inifinite isotropic solid. *Proceedings of the royal society of London Series A-Mathematical and physical sciences*, 233(1155): 521–541, 1954.

[85] S. Tamura. Comparison of body and Rayleigh wave displacements generated by a vertical point force on a layered elastic medium. In *Eleventh World Conference on Earthquake Engineering*, 1996. Paper No. 1722.

[86] Lord Rayleigh. On waves propagated along the surface of an elastic solid. *Proceedings of London Mathematical Society*, s1-17(1):4–11, 1885.

[87] J.D. Achenbach. *Wave propagation in elastic solids*. Elsevier Science Publishers B.V., 1973.

[88] U. Holzlöhner. Vibrations of the elastic half-space due to vertical surface loads. *Earthquake engineering and Structural dynamics*, 8(5):405–414, 1980.

[89] U. Holzlöhner. Vibrations of elastic half-spaces in stresses applied to a rectangular surface. *Ingenieur Archiv*, 38(6):370–&, 1969.

[90] D.D. Barkan. *Dynamics of Bases and Foundations*. McGraw-Hill, 1962.

[91] W.T. Thomson. Transmission of elastic waves through a stratified solid medium. *Journal of Applied Physics*, 21(2):89–93, 1950.

[92] N.A. Haskell. The dispersion of surface waves on multilayered media. *Bulletin of Seismological Society of America*, 41(3):17–34, 1953.

[93] D.G. Harkrider. Surface waves in multilayered elastic media. Part 1. Rayleigh and Love waves from buried sources in a multilayered elastic half-space. *Bulletin of the Seismological Society of America*, 54(2):627–679, 1964.

[94] R.Y.S. Pak and B.B. Guzina. Three-dimensional Green's functions for a multilayered half-space in displacement potentials. *Journal of Engineering Mechanics-ASCE*, 128(4):449–461, 2002.

[95] L. Knopoff. A matrix method for elastic wave problems. *Bulletin of Seismological Society of America*, 51(4):431–438, 1964.

[96] J.W. Dunkin. Computation of modal solutions in layered, elastic media at high frequencies. *Bulletin of the Seismological Society of America*, 55(2):335–358, 1965.

[97] F. Schwab. Surface-wave computations: Knopoff's method. *Bulletin of the Seismological Society of America*, 60(5):1491–1520, 1970.

[98] F. Schwab and L. Knopoff. Surface-wave dispersion computations. *Bulletin of Seismological Society of America*, 60(2):321–344, 1970.

[99] F.A. Schwab. Fast surface wave and free mode computations. *Methods in Computational Physics*, 11:87–180, 1972.

[100] E.N. Thrower. Computations of dispersion of elastic waves in layered media. *Journal of Sound and Vibration*, 2(3):210–&, 1965.

[101] T.H. Watson. A note on fast computation of rayleigh wave dispersion in the multilayered elastic half-space. *Bulletin of the Seismological Society of America*, 60(1):161–166, 1970.

[102] E. Kausel and J.M. Roësset. Stiffness matrices for layered soils. *Bulletin of the Seismological Society of America*, 71(6):1743–1761, 1981.

[103] J.H. Ginsberg. *Mechanical and structural vibrations. Theory and applications.* John Wiley and Sons, Inc., 2001.

[104] M.A. Biot. Fundamentals of generalized rigidity matrices for multi-layered media. *Bulletin of Seismological Society of America*, 73(3):749–763, 1983.

[105] J.E. Luco and R.J. Apsel. On the Green's functions for a layered half-space. Part I. *Bulletin of the Seismological Society of America*, 73(4):909–929, 1983.

[106] J.E. Luco and R.J. Apsel. On the Green's functions for a layered half-space. Part II. *Bulletin of the Seismological Society of America*, 73(4):931–951, 1983.

[107] G.J. Rix, C.G. Lai, and Spang Jr. In situ measurement of damping ratio using surface waves. *Journal of Geotechnical and Geoenvironmental engineering*, 126(5): 472–480, 2000.

[108] D.V. Jones and M. Petyt. Ground vibration in the vicinity of a rectangular load on a half-space. *Journal of Sound and Vibration*, 166(1):141–159, 1993.

[109] J.J. Liao and C.D. Wang. Elastic solutions for a transversely isotropic half-space subjected to a point load. *International Journal for Numerical and Analytical Methods in Geomechanics*, 22(6):425–447, 1998.

[110] M.G. Neigauz and G.V. Shkadinskaya. Method for calculating surface Rayleigh waves in a vertically inhomogeneous half-space. *Computational Seismology*, pages 88–92, 1972.

[111] C. Vrettos. Green's functions for vertical point load on an elastic half-space with depth-degrading stiffness. *Engineering Analysis with Boundary Elements*, 32(12): 1037–1045, 2008.

[112] C.D. Wang, Tzeng C.S., E. Pan, and J.J. Liao. Displacements and stresses due to a vertical point load in an inhomogeneous transversely isotropic half-space. *International Journal of Rock Mechanics and Mining Sciences*, 40(5):667–685, 2003.

[113] A. El Bahrawy. Point force excitation of surface-waves along the doubly corrugated traction-free boundary of an elastic half-space. *Journal of the Acoustical Society of America*, 96(5):3167–3176, 1994.

[114] W.T. Read. Stress analysis for compressible viscoelastic materials. *Journal of Applied Physics*, 21(7):671–674, 1950.

[115] R.M. Christensen. *Theory of viscoelasticity - An introduction.* Ed. Academic Press, 1971.

[116] F.J. Rizzo and D.J. Shippy. An application of the correspondence principle of linear viscoelasticity. *SIAM Journal of Applied Mathematics*, 21(2):321–330, 1971.

[117] I. Emri and N.W. Tschoegl. Generating line spectra from experimental responses. Part I. Relaxation modulus and creep compliance. *Rheologica Acta*, 32(3):311–321, 1993.

[118] N.W. Tschoegl and I. Emri. Generating line spectra from experimental responses. Part II. Storage and loss functions. *Rheologica Acta*, 32(3):322–327, 1993.

[119] N.W. Tschoegl and I. Emri. Generating line spectra from experimental responses. Part III. Interconversion between relaxation and retardation behaviour. *Rheologica Acta*, 18(1-2):117–127, 1992.

[120] N.W. Tschoegl and I. Emri. Generating line spectra from experimental responses. Part IV. Application to experimental data. *Rheologica acta*, 33(1):60–70, 1994.

[121] I. Emri and N.W. Tschoegl. Generating line spectra from experimental responses. Part V: Time-dependent viscosity. *Rheologica Acta*, 36(3):303–306, 1997.

[122] K. Knopoff, K. Aki, C.B. Archambeau, A. Ben-Menahem, and J.A. Hudson. Attenuation of dispersed waves. *Journal of Geophysical Research*, 69(8):1655–1657, 1964.

[123] G.L. Lai. *Simultaneous inversion of Rayleigh phase velocity and attenuation for near-surface site characterization.* PhD thesis, Georgia Institute of Technology - School of Civil and Environmental Engineering, 1998.

[124] H.M. Zhang and X.F. Chen. Self-adaptive Filon's integration method and its application to computing synthetic seismograms. *Chinese Physics Letters*, 18(3): 313–315, 2001.

[125] L.N. Frazer and J.F. Gettrust. On a generalization of Filon's method and the computation of the oscillatory integrals of seismology. *Geophysical Journal of the Royal Astronomical Society*, 76(2):461–481, 1984.

[126] R.J. Apsel. *Dynamic Green's functions for layered media and applications to boundary-value problems*. PhD thesis, Universtiy of California, San Diego, 1979.

[127] M. Schevenels. *The impact of uncertain dynamic soil characteristics on the prediction of ground vibration*. PhD thesis, Katholieke Universiteit Leuven, 2007.

[128] L.F. Shampine. Vectorized adaptive quadrature in MATLAB. *Journal of Computational and Applied Mathematics*, 211(2):131–140, 2008.

[129] W. Gander and W. Gautschi. Adaptive quadrature - Revisited. *BIT Numerical Mathematics*, 40(1):84–101, 2000.

[130] R.A. Phinney. Theoretical calculation of spectrum 1st arrivals in layered mediums. *Journal of Geophysical Research*, 70(20):5107–&, 1965.

[131] E.A. Flinn. A modification of Filon's mehtod of numerical integration. *Journal of the ACM*, 7(2):181–184, 1960.

[132] H. Hirayama. A numerical integration method for oscillatory functions over an infinite interval by substitution and Taylor series. In Constanda, C. and Nashed, Z. and Rollins, D., editor, *Integral Methods in Science and Engineering: Theoretical and Practical Aspects*, pages 99–104, 2006. International Conference on Integral Methods in Science and Engineering (IMSE 2004), Orlando, FL, 2004.

[133] S.M. Chase and L.D. Fosdick. An algorithm for Filon quadrature. *Communications of the ACM*, 12(8):453–&, 1969.

[134] R. Piessens and F. Poleunis. A numerical method for the integration of oscillatory functions. *BIT Numerical Mathematics*, 11(3):317–327, 1971.

[135] J.D. Talman. Numerical Fourier and Bessel transforms in logarithmic variables. *Journal of Computational Physics*, 29(1):35–48, 1978.

[136] A.J.S. Hamilton. Uncorrelated modes of the nonlinear Power Spectrum. *Monthly Notices of the Royal Astronomical Society*, 312(2):257–284, 2000.

[137] Q.H. Liu and N. Nguyen. An accurate algorithm for nonuniform fast Fourier transforms (NUFFT's). *IEEE Microwave and Guided Wave Letters*, 8(1):18–20, 1998.

[138] A.E. Siegman. Quasi fast Hankel transform. *Optics Letters*, 1(1):13–15, 1977.

[139] G.P. Agrawal and M. Lax. End correction in the quasi-fast Hankel transform for optical-propagation problems. *Optics Letters*, 6(4):171–173, 1981.

[140] L. Yu, M.C. Huang, M.Z. Chen, W.Z. Chen, W.D. Huang, and Z.Z. Zhu. Quasi-discrete Hankel transform. *Optics Letters*, 23(6):409–411, 1998.

[141] M. Guizar-Sicairos and J.C. Gutierrez-Vega. Computation of quasi-discrete Hankel transforms of integer order for propagating optical wave fields. *Journal of the Optical Society of America A-Optics Image Science and Vision*, 21(1):53–58, 2004.

[142] J. Markham and J.A. Conchello. Numerical evaluation of Hankel transforms for oscillating functions. *Journal of the Optical Society of America A-Optics Image Science and Vision*, 20(4):621–630, 2003.

[143] Q.H. Liu and Z.Q. Zhang. Nonuniform fast Hankel transform (NUFHT) algorithm. *Applied Optics*, 38(32):6705–6708, 1999.

[144] Q.H. Liu and Z.Q. Zhang. Nonuniform fast Hankel transform (NUFHT) algorithm: errata. *Applied Optics*, 39(11):1842, 2000.

[145] S. Gupta, W.F. Liu, G. Degrande, G. Lombaert, and W.N. Liu. Prediction of vibrations induced by underground railway traffic in beijing. *Journal of Sound and Vibration*, 310(3):608–630, 2008.

[146] D. Clouteau, M. Arnst, T.M. Al-Hussaini, and G. Degrande. Freefield vibrations due to dynamic loading on a tunnel embedded in a stratified medium. *Journal of Sound and Vibration*, 283(1-2):173–199, 2005.

[147] M.F.M. Hussein, H.E.M. Hunt, L. Rikse, S. Gupta, D. Degrande, J.P. Talbot, S. Franois, and M. Schevenels. Using the PiP model for fast calculation of vibration from a railway tunnel in a multi-layered half-space. *Noise and vibration mitigation for rail transportation systems, Notes on numerical fluid mechanics and multidisciplinary design*, 99:136–142, 2008.

[148] S. Gupta, Y. Stanus, G. Lombaert, and G. Degrande. Influence of tunnel and soil parameters on vibrations from underground railways. *Journal of Sound and Vibration*, 327:70–91, 2008.

[149] Y.B. Yang and H.H. Hung. Soil vibrations caused by underground moving trains. *Journal of Geoenvironmental engineering*, 134(11):1633–1644, 2008.

[150] P. Chatterjee, G. Degrande, D. Clouteau, T. Al-Hussaini, M. Arnst, R. Othman, and K.U. Leuven. Numerical modelling of ground borne vibrations from underground railway traffic. Technical report, Report of the CONVURT Project, 2003.

[151] W. Gardien and H.G. Stuit. Modelling of soil vibrations from railway tunnels. *Journal of Sound and Vibration*, 267(3):605–619, 2003.

[152] E. Kausel. Thin-layer method: formulation in time domain. *International Journal for Numerical Methods in Engineering*, 37(6):927–941, 1994.

[153] A.T. Peplow and S. Finnveden. Calculation of vibration transmission over bedrock using a waveguide finite element model. *International Journal for Numerical and Analytical Methods in Geomechanics*, 32(6):701–719, 2008.

[154] G. Bornitz. *Über die Ausbreitung der von Groszkolbenmaschinen erzeugten Bodenschwingungen in die Tiefe (About the propagation of ground vibrations generated by piston engines in depth)*. J. Springer, 1931.

[155] D.S. Kim and J.S. Lee. Propagation and attenuation characteristics of various ground vibrations. *Soil dynamics and earthquake engineering*, 19(2):115–125, 2000.

[156] C.L. Dym. Attenuation of ground vibration. *Sound and Vibration*, 10(4):32–34, 1976.

[157] H. Amick. A frequency-dependent soil propagation model. In *Conference on Optomechanical engineering and vibration control*, Denver, July 20-23 1999.

[158] G.R. Watts. The generation and propagation of vibration in various soils produced by the dynamic loading of road pavements. *Journal of Sound and Vibration*, 156 (2):191–206, 1992.

[159] H. Amick and M. Gendreau. Construction vibrations and their impact on vibration-sensitive facilities. Technical report, ASCE Construction Congress 6, Orlando, Florida, February 22, 2000.

[160] P.B. Wei, H. Xia, and J.G. Chen. Validation of an empirical prediction model for train-induced ground vibrations. In *Proceedings of 3rd International Symposium on Environmental Vibrations-Prediction, Monitoring, Mitigation and Evaluation*, 2007. ISEV 2007 Conference, Taipei, Taiwan.

[161] H.P. Verhas. Prediction of the propagation of train-induced ground vibrations. *Journal of Sound and Vibration*, 66(3):371–376, 1979.

[162] V.V. Krylov. Generation of ground vibrations by superfast trains. *Applied Acoustics*, 44(2):149–164, 1995.

[163] V.V. Krylov. On the theory of railway-induced ground vibrations. *Journal of Physique IV*, 4(C5):769–772, 1994.

[164] V.V. Krylov. Spectra of low-frequency ground vibrations generated by high-speed trains on layered ground. *Journal of low frequency noise vibration and active control*, 16(4):257–270, 1997.

[165] V.V. Krylov. Generation of ground vibration boom by high-speed trains. In *Noise and Vibration from high-speed trains*, pages 251–283, London, 2001. Thomas Telford Ltd.

[166] V.V. Krylov. Effects of track properties on ground vibrations generated by high-speed trains. *Acta Acustica*, 228(1):129–156, 1999.

[167] V.V. Krylov. Vibrational impact of high-speed trains. I. Effect of track dynamics. *Journal of Acoustical Society of America*, 100(5):3121–3134, 1996.

[168] J.D. Frýba. *Vibration of solids and structures under moving loads.* International Publishing, Groningen, 1972.

[169] D.V. Jones and M. Petyt. Ground vibration in the vicinity of a strip load - A two-dimensional half-space model. *Journal of Sound and Vibration*, 147(1):155–166, 1991.

[170] D.V. Jones and M. Petyt. Ground vibration in the vicinity of a strip load: An elastic layer on a rigid foundation. *Journal of Sound and Vibration*, 152(3):501–515, 1992.

[171] D.V. Jones and M. Petyt. Ground vibration in the vicinity of a strip load: An elastic layer on an elastic half-space. *Journal of Sound and Vibration*, 161(1):1–18, 1993.

[172] D.V. Jones and M. Petyt. Ground vibration in the vicinity of a rectangular load acting on a viscoelastic layer over a rigid foundation. *Journal of Sound and Vibration*, 203(2):307–319, 1997.

[173] D.V. Jones, D. Le Houédec, A.T. Peplow, and M. Petyt. Ground vibration in the vicinity of a moving harmonic rectangular load on a half-space. *European Journal of Mechanics A/Solids*, 17(1):153–166, 1998.

[174] G. Lefeuve-Mesgouez, D. Le Houédec, and A.T. Peplow. Ground vibration in the vicinity of a high-speed moving harmonic strip load. *Journal of Sound and Vibration*, 231(5):1289–1309, 2000.

[175] T. Bierer and C. Bode. A semi-analytical model in time domain for moving loads. *Soil Dynamics and Earthquake engineering*, 27(12):1073–1081, 2007.

[176] D. Aubry, D. Cloteau, and G. Bonnet. Modelling of wave propagation due to fixed or mobile dynamic sources. In Chouw N. and G. Schimd, editors, *Workshop Wave '94, Wave propagation and Reduction of Vibrations*, 1994.

[177] J. Jonsson. Comments on "Ground vibration generated by load moving along railway track". *Journal of Sound and Vibration*, 236(2):359–361, 2000.

[178] X. Sheng, C.J.C. Jones, M. Petyt, and D.J. Thompson. Comments on "Ground vibration generated by load moving along railway track" - Authors' reply. *Journal of Sound and Vibration*, 236(2):362–366, 2000.

[179] X. Sheng, C.J.C. Jones, and D.J. Thompson. Prediction of ground vibration from trains using the wavenumber finite and boundary element methods. *Journal of Sound and Vibration*, 293(3-5):575–586, 2006.

[180] J. O'Brien and D.C. Rizos. A 3D BEM-FEM methodology for simulation of high speed train induced vibrations. *Soil Dynamics and Earthquake Engineering*, 25 (4):289–301, 2005.

[181] P. Galvín and J. Domínguez. Experimental and numerical analyses of vibrations induced by high-speed trains on the Córdoba-Málaga line. *Soil Dynamics and Earthquake engineering*, 29(4):641–657, 2009.

[182] M.G. Floquet. Sur les équations différentielles linéaires à coefficients périodiques. *Annales Scientifiques de l'É.N.S*, 12:47–88, 1883.

[183] H. Chebli, D. Cloteau, and L. Schmitt. Dynamic response of high-speed ballasted railway tracks: 3D periodic model and in situ measurements. *Soil and dynamics earthquake engineering*, 28(2):118–131, 2008.

[184] D. Cloteau, M.L. Elhabre, and D Aubry. Periodic BEM and FEM-BEM coupling - Application to seismic behaviour of very long structures. *Computational Mechanics*, 25(6):567–577, 2000.

[185] D. Clouteau, D. Aubry, M.L. Elhabre, and E. Savin. Periodic and stochastic BEM for large structures embedded in an elastic half-space. *Mathematical aspects of boundary element methods*, 414:91–102, 2000.

[186] G. Lombaert and G. Degrande. Experimetal validation of a numerical prediction model for free field traffic induced vibrations by in situ experiments. *Soil and dynamics earthquake engineering*, 21(6):485–497, 2001.

[187] A. Ditzel, G.C. Herman, and G.G. Drijkoningen. Seismograms of moving trains: Comparison of theory and measurements. *Journal of Sound and Vibration*, 248 (4):635–652, 2001.

[188] Y. Kitamura and S. Sakurai. Dynamic stiffness for rectangular rigid foundations on a semi-infinite elastic medium. *International Journal for Numerical and Analytical Methods in Geomechanics*, 3(2):159–171, 1979.

[189] R. Arcos, J. Romeu, A. Balastegui, and T. Pàmies. Determination of the near field distance for point and line sources acting on the surface of an homogeneous and viscoelastic half-space. *Soil Dynamics and Earthquake Engineering*, 31(7): 1072–1074, 2011.

[190] X. Sheng, M. Li, C.J.C. Jones, and D.J. Thompson. Using the fourier-series approach to study interactions between moving wheels and a periodically supported rail. *Journal of Sound and Vibration*, 303(3-5):873–894, 2007.

[191] J.C.O. Nielsen. High-frequency vertical wheel-rail contact forces. Validation of a prediction model by field testing. *WEAR*, 265(9-10):1465–1471, 2008.

[192] D.J. Ewins. *Modal Testing. Theory, practice and application.* Research Studies Press Ltd., Baldock, Hertfordshire, England, 2000.

[193] J.A. Inaudi and J.M. Kelly. Linear hysteretic damping and the Hilbert transform. *Journal of Engineering Mechanics-ASCE*, 121(5):626–632, 1995.

[194] S.H. Crandall. *Dynamic response of systems with structural damping.* Air Space and Instruments. McGraw-Hill, 1987.

[195] N. Makris. Time domain analysis of generalized viscoelastic models. *Soil Dynamics and Earthquake Engineering*, 14(5):375–386, 1995.

[196] P.J. Remington. Wheel rail rolling noise, 1: Theoretical analysis. *Journal of the Acoustical Society of America*, 81(6):1805–1823, 1987.

[197] T. Mazilu. Prediction of the interaction between a simple moving vehicle and an infinite periodically supported rail - Green's functions approach. *Vehicle system dynamics*, 48(9):1021–1042, 2010.

[198] E. Kausel and J.M. Roësset. Frequency domain analysis of undamped systems. *Journal of Engineering Mechanics-ASCE*, 118(4):721–734, 1992.

[199] W.M. Zhai, K.Y Wang, and J.H. Lin. Modelling and experiment of railway ballast vibrations. *Journal of Sound and Vibration*, 270(4-5):673–683, 2004.